

Parametrically Activated Interactions in Circuit Quantum Electrodynamical Systems

Koenig, J.D.

DOI

[10.4233/uuid:5df3acc3-2e8e-4962-8702-5814d3cbe04c](https://doi.org/10.4233/uuid:5df3acc3-2e8e-4962-8702-5814d3cbe04c)

Publication date

2025

Document Version

Final published version

Citation (APA)

Koenig, J. D. (2025). *Parametrically Activated Interactions in Circuit Quantum Electrodynamical Systems*. [Dissertation (TU Delft), Delft University of Technology]. <https://doi.org/10.4233/uuid:5df3acc3-2e8e-4962-8702-5814d3cbe04c>

Important note

To cite this publication, please use the final published version (if applicable). Please check the document version above.

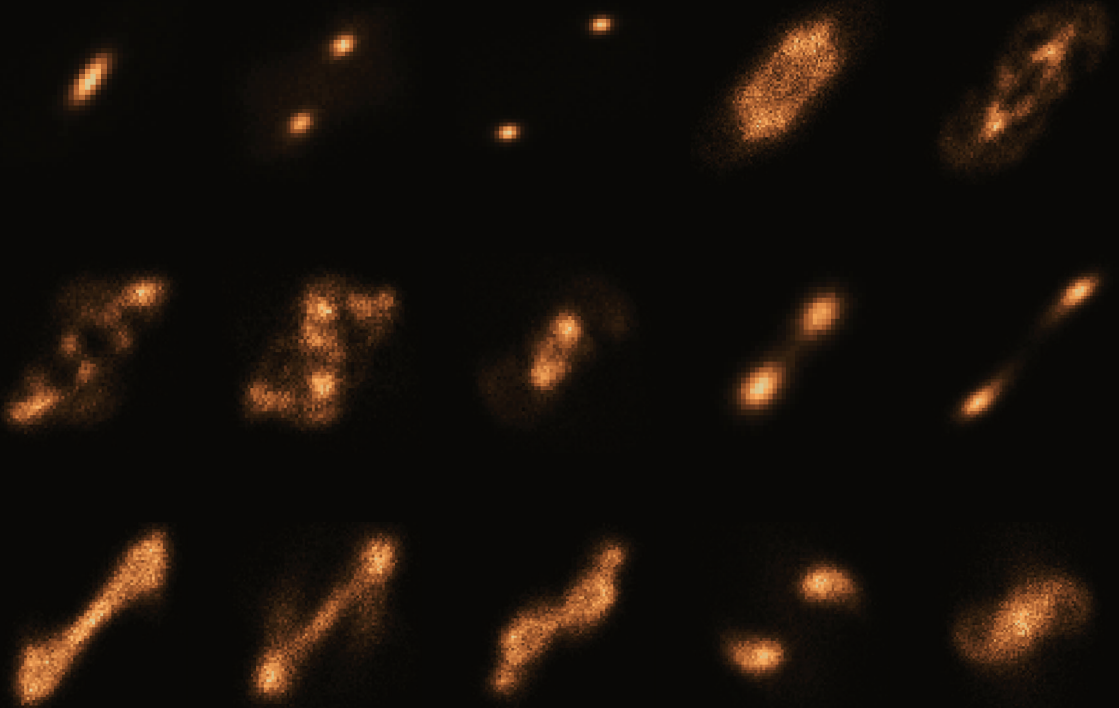
Copyright

Other than for strictly personal use, it is not permitted to download, forward or distribute the text or part of it, without the consent of the author(s) and/or copyright holder(s), unless the work is under an open content license such as Creative Commons.

Takedown policy

Please contact us and provide details if you believe this document breaches copyrights. We will remove access to the work immediately and investigate your claim.

**PARAMETRICALLY ACTIVATED
INTERACTIONS IN CIRCUIT
QUANTUM ELECTRODYNAMICAL SYSTEMS**



JACOB DANIEL KOENIG

PARAMETRICALLY ACTIVATED INTERACTIONS IN CIRCUIT QUANTUM ELECTRODYNAMICAL SYSTEMS

PARAMETRICALLY ACTIVATED INTERACTIONS IN CIRCUIT QUANTUM ELECTRODYNAMICAL SYSTEMS

Dissertation

for the purpose of obtaining the degree of doctor

at Delft University of Technology

by the authority of the Rector Magnificus, prof.dr.ir. T.H.J.J. van der Hagen

chair of the Board for Doctorates

to be defended publicly on

Wednesday 9 April 2025 at 15:00 o'clock

by

Jacob Daniel KOENIG

Bachelor of Science in Physics and Astronomy,

University of Waterloo, Canada

born in Toronto, Canada

This dissertation has been approved by the promotor.

Composition of the doctoral committee:

Rector Magnificus,	chairperson
Prof. dr. G.A. Steele,	Delft University of Technology, promotor
Prof. dr. B.M. Terhal,	Delft University of Technology, promotor

Independent members:

Prof. dr. P.G. Steeneken,	Delft University of Technology, The Netherlands
Prof. dr. Y. Nakamura,	University of Tokyo, Japan
Prof. dr. Z. Leghtas,	Ecole Normale Supérieure, France
Univ.-Prof. dr. G. Kirchmair,	University of Innsbruck, Austria
Prof. dr. O. Zilberberg,	University of Konstanz, Germany
Prof. dr. ir. H.S.J. van der Zant,	Delft University of Technology, reserve member



Keywords: Kerr nonlinear oscillator, superconducting, qubit, transmon, tunable coupler, Duffing, cQED, circuit QED, parametric

Printed by: Gildeprint, Enschede

Front & Back: Quadrature histogram data obtained from measurements of a parametrically driven superconducting Duffing oscillator.

Copyright © 2025 by Jacob Daniel Koenig

ISBN 978-94-6384-747-6

An electronic version of this dissertation is available at
<http://repository.tudelft.nl/>.

To my family and friends,

*I learned that just beneath the surface there's another world,
and still different worlds as you dig deeper.*

David Lynch

4.6.2	Circuit Quantization	77
4.6.3	Extraction of Couplings.	81
5	Spectroscopic Observation of a Few-Photon Parametric State in a Kerr Nonlinear Oscillator	85
5.1	Introduction	86
5.2	Device and Bichromatic Driving	86
5.3	Spectroscopy of a Parametric Phase State	88
5.4	Occurrence of a Dynamical Phase Transition	90
5.5	Conclusion	95
5.5.1	Contributions	96
5.6	Supplementary Information	97
5.6.1	Experimental Setup	97
5.6.2	Effective Model.	98
6	Biased Switching Dynamics in a Parametrically Driven Kerr Nonlinear Oscillator	103
6.1	Introduction	104
6.2	Device, Bichromatic Driving, and Bistability.	104
6.3	Output Field Measurements of a Parametric Phase State.	107
6.4	Stochastic Switching and Phase Control	108
6.5	Conclusion	111
6.5.1	Contributions	112
6.6	Supplementary Information	113
6.6.1	Experimental Setup	113
6.6.2	Effective Model and Stability Analysis	115
7	Chaotic Behaviour of a Strongly Parametrically Driven Duffing Oscillator	119
7.1	Introduction	120
7.2	Devices and Chaotic Behaviour in Duffing Oscillators	120
7.3	Emergence of Chaotic Signatures	124
7.4	Confluence of Period-Halving and Doubling Bifurcation Cascades	125
7.5	Conclusion	128
7.5.1	Contributions	128
7.6	Supplementary Information	130
7.6.1	Experimental Setup	130
8	Conclusion	133
8.1	Findings	134
8.2	Outlook	135
	Appendices	137
A.1	Solutions to the Parametrically Driven Duffing Oscillator	137
B.2	Additional Datasets of Parametrically Driven Duffing Nonlinear Oscillators	140
B.2.1	Stability Diagrams	140
B.2.2	Shared Spectroscopic Features of Parametric States for Detuning and Power Sweeps of Duffing and Kerr Oscillators	141
B.2.3	Response Snapshots of a Parametrically Driven Duffing Oscillator for Various Drive Parameters	143

B.2.4	Response Map of a Parametrically Driven Duffing Oscillator for Various Drive Parameters.	160
	Acknowledgements	167
	Curriculum Vitæ	171
	List of Publications	173
	Bibliography	174

SUMMARY

In this thesis observations on the application of parametric drives to superconducting quantum circuits in disparate parameter regimes are presented. By the nonlinear inductance of the Josephson junction, a variety of interactions in circuit quantum electrodynamical systems comprised of strongly, moderately, and weakly nonlinear oscillators are realized.

Chapter 1 contains an introduction to classical and quantum information and introduces superconducting circuits as a platform for quantum information processing. An outline of the contents of the thesis is also provided.

In **Chapter 2** a theoretical foundation for the later chapters is established, spanning from the classical harmonic oscillator to circuit quantum electrodynamical systems and parametric driving. The transmon qubit, junction-embedded coplanar waveguide, tunable coupler, and Josephson junction array resonator are introduced and some methods for realizing parametrically activated interactions in such systems are discussed.

Chapter 3 focuses on the steps necessary for constructing a superconducting quantum circuit. The design, simulation, and fabrication methods necessary for creating the experimental devices of later chapters are discussed.

In **Chapter 4** results of the parametrically activated interactions between two tunably coupled transmon qubits by flux modulation of a SQUID are presented. When the coupling SQUID is modulated at the sum or difference frequencies of the transmons, level repulsion and attraction are observed spectroscopically. The viability of the platform for analog quantum simulations is discussed and the experimental results are compared to analytical models and numerical simulations of the quantum master equation.

In **Chapter 5** spectroscopic signatures of a few-photon Kerr parametric oscillator are observed upon the application of an all-microwave bichromatic drive to a Josephson junction-embedded coplanar waveguide resonator. Semiclassical analytical, numerical, and quantum master equation simulations are performed and compared with the experimental results. An effective model based on semiclassical methods proves insufficient in modelling the behaviour of the system, indicating the presence of quantum effects.

In **Chapter 6** a weakly nonlinear Josephson junction array resonator is bichromatically driven into a parametric phase state. Stochastic switching between the two non-equilibrium stationary states of the system is observed and the time between stochastic switching events is determined for a range of drive strengths. An additional microwave drive resonant with the frequency of parametric response is applied and the system is biased into one of the phase states. The biasing and change in switching time as a function of drive power and phase is shown. The contributions of classical and quantum effects to the occurrence of switching events is discussed.

In **Chapter 7** measurements of a strongly parametrically driven Duffing oscillator are presented. As the system is strongly driven at a variety of large negative detunings, signatures of chaotic behaviour are observed in the output field spectrum and quadrature histograms. The observed features are discussed and compared to known markers of chaotic behaviour in classical parametrically driven Duffing oscillators.

Chapter 8 concludes the thesis, providing a review of the contents and findings of the previous chapters. The thesis ends with an outlook and suggestions for potential future topics of study.

1

INTRODUCTION

*My basic view of things is
not to have any basic view of things.*

Ingmar Bergman

In this chapter we discuss classical and quantum information from a historical perspective, introduce superconducting quantum circuits as quantum information processors, and summarize the structure of the thesis.

1.1. CLASSICAL AND QUANTUM INFORMATION

What do we think of when we think of *information*? Perhaps we envision a stack of papers, a file folder, a computer hard drive, or a complicated network of nodes and connective lines. Etymologically, we can argue that it means to "bring into form," but what is being brought into form, and what form does it take? Is it necessary to communicate information, or does information exist whether or not we inform anyone of anything?

I was first introduced to *information* in a formal sense during my undergraduate studies. I was taught to think about information from a physical perspective vis-à-vis the work of Claude Shannon, which enables one to quantify what we do and do not know about a set of *things* [1]. The very act of quantifying "things that we do and do not know" or "knowledge" or "information" allows us to work with these concepts as mathematical quantities. For example, we may consider how much information is contained in a coin. If we flip the coin, the result is either heads or tails. According to Shannon, the information we have gained by flipping the coin and observing the result is 1 *bit* of information. We can think of the coin as being an object which encodes 1 bit of information.

Similarly, if we wish to transfer information to communicate with others, we can very simply turn off or on a bright lamp. When the lamp is on, it communicates some predetermined message to another person conventionally in the affirmative, while if the lamp is off, it communicates a message conventionally in the negative. Alternatively, we can use the dots and dashes of Morse code in order to communicate information to others. While the choice of dot or dash is binary, the content of a message is determined by how it has been decided that we map dots and dashes to letters. In the mapping to the Latin alphabet, the information content of the message scales with the amount of dashes, dots, and pauses. In the same way, we can convert zeroes and ones to other numbers with binary representations. Suddenly, a collection of coins facing heads or tails can be used to communicate messages which contain information.

If information can be encoded and communicated, one may also wonder whether information can be processed to perform tasks. We have at hand a means by which we can prepare information in binary states (0 or 1), and we wish to configure a collection of information in such a way that it can be processed in order to complete a task. One can, for instance, decide that some action should be performed provided that certain information has been received. For example, if we receive a 0, we can return a 1. If we receive a 1, we can return a 0. Alternatively, with two bits, if we receive 00, we can return 0. If we receive 01 or 10, we return 0. Lastly, if we receive 11, we return 1. Such *Boolean functions* as the NOT and AND gates described above can be used to construct *logic gates*, which transform binary inputs into binary outputs. If one constructs a system with two lamps in which when the first lamp is turned on, the second turns off, and when the first lamp is turned off, the second turns on, a circuit with a NOT gate has been realized. If we wish to be more efficient, one can construct a system of electronic components such as transistors, resistors, capacitors, and diodes connected in a circuit which can perform all known logical operations on binary inputs, with light replaced by specific voltages. If one continues building circuits of logic gates, in the end, a classical digital computer will be constructed.

The amount of time between when humans first utilized information processors and when we finally began to generally understand them was thousands of years. Indeed, the task of

constructing machines which can be presented with information, perform operations given that information, and return processed information as a human would is a monumental task. Between the invention of the abacus and the punched card computer, a significant portion of all of recorded human history transpired [2]. As a species, we did not properly understand what computers were or could be in the modern understanding until the 19th and 20th centuries [3–5]. Now, with devices containing billions of transistors in the hands of most of the population of the world, computation seems an afterthought. It is now natural that one should be able to compute virtually anything that the average person wishes within seconds of conceiving the very thought of doing so. The vast majority of humanity are able to interface with such complex machinery in order to complete exceedingly sophisticated tasks, all the while treating these devices as perfectly opaque black boxes conceived by unknown individuals in the previous century.

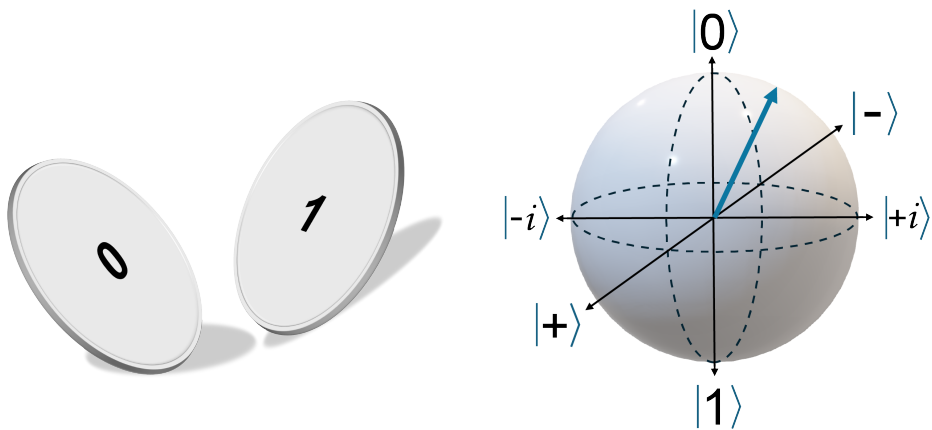


Figure 1.1: In contrast to a classical bit, a quantum bit is the state of a two-level quantum system. The state of the system can be represented as a point on or in the Bloch sphere which illustrates the space of possible quantum states [6].

In the late 19th and early 20th centuries, some of humanity’s brightest minds discovered that the natural world was not sufficiently modellable by what is now known as *classical physics* [7–10]. Towards the end of the 20th century, following the early development of the modern gate-based digital computer, the problem of simulating the natural (quantum) world was posited [11–13]. If one is to use computers as a tool to understand the universe, and if the universe is quantum mechanical, should those computers be quantum mechanical? What would happen if we exchanged our transistors encoding information in the classical binary states 0 and 1 with quantum systems such as electrons and photons with which we could encode information in complex-valued quantum states? Through the rest of the 20th century, the groundwork for quantum computation would be laid, with much theoretical and experimental work done on what it would mean to construct a *quantum bit*, execute quantum algorithms, and discover what could be achieved by doing so relative to using classical bits [14–78].

By the turn of the millennium, it was understood that a system of coupled quantum bits could be used to perform any quantum information processing task which could be achieved by unitary operations - which in turn meant that, at the very least, such systems could simulate and compute anything that a classical computer could [13, 41, 50]. It was also shown that certain computational and simulational tasks could be performed with algorithms on qubits more efficiently than with any known algorithms on classical bits [37, 47, 50]. While such a *universal quantum computer* could hypothetically be built, it was (and still is) an entirely different task to actually build one. Firstly, which quantum systems are the most efficient, accurate, and economical for encoding information and performing such universal processing tasks? If the criterion is that we encode information in quantum states, shall we use photons, electrons, atoms, ions, anyons, or something else [26, 43, 44, 61, 69, 75–77, 79–82]? After determining a platform, in which basis should one encode information?

Classically, the basis seems natural given the platform - for a coin, heads or tails, and a lamp, on or off. When it comes to the case of the photon, shall we encode information in its polarization, spin, or energy? The choice of encoding depends on the efficiency and reliability with which information can be processed, which depends on the lifetimes of the quantum states and the fidelity of gates executed on those systems. Once information is encoded, errors will inevitably occur in the preparation of states, execution of gates, and readouts of registers. How should these errors be corrected? Much of the past few decades of research in quantum information processing has been concerned with these questions, and it seems to be the case that this will continue for the foreseeable future.

1.2. SUPERCONDUCTING QUANTUM CIRCUITS

The quantum information processing platform that I have chosen to devote my study to is the superconducting qubit. In Chapter 2, we discuss the superconducting qubit in more detail, but here, suffice to say that we can think of the superconducting qubit as an *artificial atom*. Such an artificial atom has a set of discrete energy levels that the electrons of the atom can occupy. An electron will transition to a higher energy level if the atom absorbs a photon of energy matching the difference between the two levels. Conversely, a photon can be emitted from an atom if an electron occupying a higher energy level transitions to a lower level, with the emitted photon having energy equal to the difference between the transitioned levels. In both atoms and artificial atoms, such transition dynamics have been observed in great detail [83, 84]. A natural choice for an artificial atom is one for which we can engineer and control the transitions between individual energy levels, preferably with single photon and electron resolution.

The origin of the superconducting qubit can be traced at least back to experimentation on the quantum nature of Josephson junctions revealing macroscopic quantum tunnelling and energy level quantization [18, 19, 85, 86]. As for the choice of artificial atom, the critical component was found when a Josephson junction cooled to cryogenic temperatures and irradiated with (microwave) photons of the appropriate energy (frequency) caused transitions between quantized energy levels [19]. The energy levels were defined by a nonlinear potential, such that the transition frequencies between levels were unequal - a key ingredient for building a superconducting qubit, as will be discussed in Chapter 2. A mere three years after the most well-known treatise on early quantum computation was published, what would become the

key ingredient for the most popular quantum computing platform of the early 21st century was revealed [12, 19]. While the first superconducting qubit, the "Cooper-pair box", was proposed only a few years after the quantized energy level experiment, it would not be until the last years of the millennium that the superconducting qubit truly took form once quantum oscillations and control of coherent state evolution were demonstrated [71, 76, 87].

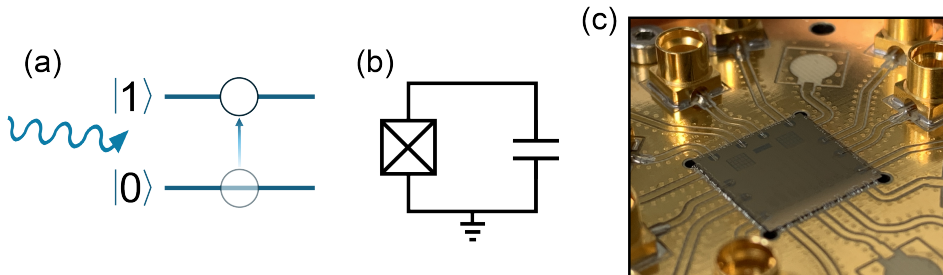


Figure 1.2: Artificial atoms and superconducting quantum circuits. (a) A two-level system excited by a resonant microwave drive. (b) The circuit representation of a superconducting qubit (the *transmon*). The inductance and capacitance of the Josephson junction are represented by a square with a cross. (c) An image of a chip containing superconducting quantum circuits wirebonded to a printed circuit board.

In the years that followed, several alternative superconducting qubit designs were proposed and their viability for quantum computation was experimentally demonstrated [55, 71, 76, 88–111]. Mechanisms for control, readout, and coupling of superconducting qubits generally coalesced around the framework of circuit quantum electrodynamics, in which networks of resonators and qubits formed by capacitors, inductors, and Josephson junctions are used to perform quantum gates and read out qubit states [111–118]. It is within this framework that the experiments outlined in Chapters 4 - 7 were performed; superconducting quantum devices formed by Josephson junctions, capacitors, and inductors, coupled to transmission-line resonators and irradiated with microwave signals.

A few additional threads of progress have also been developing since the late 1990s, even within the field of superconducting quantum circuits specifically. The first is concerned with whether the basis consisting of the ground and excited states of a superconducting qubit is the most optimal way to encode information. An alternative approach is to encode information in bosonic modes and continuous variables; this field of research has been the focus of increased study in the 21st century with numerous exciting experimental developments demonstrating the viability of quantum information processing with Schrödinger cat states, grid states, and GKP states with quantum circuits and on other platforms [119–133]. Much theoretical and experimental progress has also been made with quantum error detection and correction towards fault-tolerant quantum computation, regardless of the choice of platform or basis of encoding [51, 134–158].

1.3. THESIS OUTLINE

In Chapter 1 we have introduced the concept of quantum information and superconducting quantum devices. In Chapter 2 we discuss more deeply the theoretical background necessary

for understanding the later chapters, encompassing harmonic and anharmonic oscillators, circuit quantum electrodynamics, and parametric driving. In Chapter 3 we discuss how one goes about conceiving of, designing, simulating, and fabricating superconducting quantum circuits. In Chapter 4 we present our findings on the parametrically activated interactions between two strongly nonlinear Kerr oscillators realized by flux modulation of a tunable coupler. We discuss the circuit in detail theoretically and show that the device can be operated in distinct parameter regimes which can be used to investigate a variety of physical phenomena. In particular, we observe level repulsion and attraction between the two nonlinear oscillators, with the spectroscopic signatures of two-mode squeezing observable in a regime where the nonlinear cross-Kerr coupling is dominant. In Chapter 5 we report on the observation of a parametric state in a moderately nonlinear Kerr oscillator generated by an all-microwave bichromatic driving scheme. We investigate the response of the oscillator to bichromatic driving for a variety of pump parameters and observe response signatures which indicate the few-photon oscillator state is not adequately described by semiclassical methods. In Chapter 6 we demonstrate the parametric driving of a quantum Kerr nonlinear oscillator into multistability and show phase control over the system in the bistable state with the application of an additional weak resonant drive. We investigate the switching dynamics for a variety of parametric pump parameters and observe a change in the characteristic stochastic switching time over several orders of magnitude. We further observe a suppression of the switching time as the oscillator is driven out of the parametric response region due to nonlinear effects. In Chapter 7 we parametrically drive a quantum Duffing oscillator beyond bistability into chaos, observing a variety of chaotic signatures in the output field spectrum and quadrature histograms. In Chapter 8 we conclude, providing a review of the contents of the thesis, main findings, and outlook. The relevant data for this thesis can be found at the following DOI: <https://doi.org/10.4121/0d0ef8aa-43d9-46ab-8afd-e02b76f2469a.v1>.

2

THEORETICAL BACKGROUND

The fish you don't catch is always the biggest.

Abe Kōbō

In this chapter we begin with the simple harmonic oscillator, building up a base of knowledge until we eventually cover quantum anharmonic oscillators, transmon qubits, circuit quantum electrodynamics, and the parametrically driven Duffing oscillator. This chapter establishes a foundation from which the reader can better understand the underlying physics of the later research chapters containing tunable couplers and parametrically driven quantum nonlinear oscillators.

2.1. HARMONIC OSCILLATORS AND ENGINEERABLE QUANTUM (AN)HARMONIC OSCILLATORS

2.1.1. EVERYDAY OSCILLATORS

SIMPLE HARMONIC OSCILLATORS

While it may be common knowledge among physicists that a child being pushed on a swing is described by many of the same fundamental equations as the motion of celestial bodies and the dynamics of charges in electrical circuits, this understandably comes as a surprise to the non-physicist. How should it be that such an everyday, commonplace activity has such a deep correspondence with the most advanced technologies we have developed as a species over the course of thousands of years? Most students would likely never expect that when first introduced during high school to the famous equation [159]

$$\vec{F} = m\vec{a} \quad (2.1)$$

that this simple expression is not far removed from the vast majority of the mathematics behind quantum circuits.

We can start with the simple harmonic oscillator, defined as a system in which an object displaced from its equilibrium position is acted upon by a restoring force which returns the object to the equilibrium position. For example, in the absence of friction, a mass attached to the end of a stretched spring can be described by

$$\vec{F} = m\vec{a} = m \frac{d^2 \vec{x}}{dt^2} = -k\vec{x} \quad (2.2)$$

where k is a characteristic parameter of the spring (the *spring constant*), which relates the force exerted on the spring to how far it is displaced [160]. One may think of this as a measure of the stiffness of the spring. If we wish to uncover the position of the spring at any given point in time, we can straightforwardly solve the differential equation for x under some initial conditions (for example, that the spring is initially stretched to a position x_0 and released from rest) and determine that

$$x(t) = x_0 \cos(\omega_0 t) \quad (2.3)$$

where the natural frequency of the oscillator is given by $\omega_0 = \sqrt{k/m}$. Thus, at any given point in time, the position of the mass is entirely parametrized by the frequency at which it oscillates, which in turn depends on the mass of the object and the stiffness of the spring. A heavy object with a loose spring will oscillate at a lower frequency (and thus move more slowly) than a light object with a stiff spring.

We can solve this problem alternatively with the Lagrangian formulation, in which instead of describing the system initially in terms of the forces present, we consider the kinetic and potential energies

$$\mathcal{L} = \mathcal{T} - \mathcal{U} \quad (2.4)$$

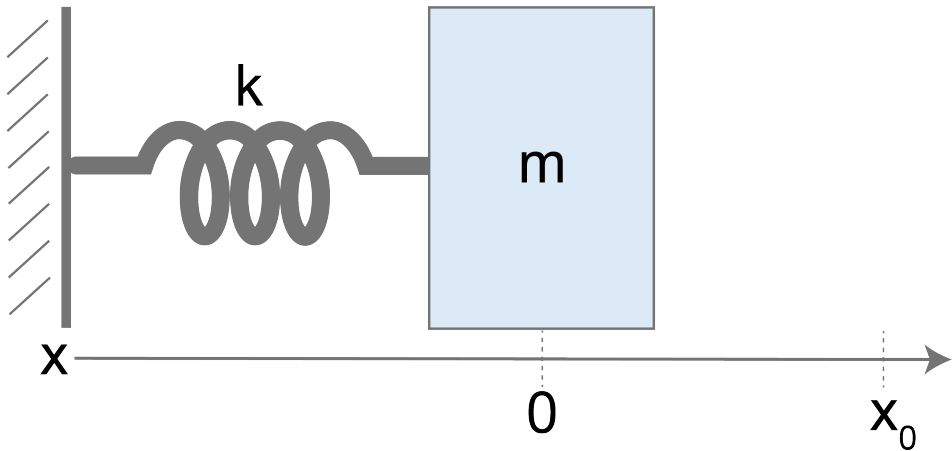


Figure 2.1: A diagram depicting a mass-spring system at equilibrium. When the mass is placed at the position x_0 , the spring is stretched and the system has potential energy. When the mass is released, it oscillates back and forth as potential energy and kinetic energy are exchanged.

where for the mass-spring system, we have $\mathcal{T} = \frac{1}{2}m\left(\frac{dx}{dt}\right)^2$ and $\mathcal{U} = \frac{1}{2}kx^2$. What this equation tells us is that when the mass is displaced from equilibrium (when the spring is stretched or compressed), the potential energy of the system is maximal, and when the mass is passing through equilibrium where the spring is neither stretched nor compressed, the kinetic energy is maximal. The energy in the system oscillates between being stored as potential energy and released as kinetic energy.

We can apply the Euler-Lagrange equation to Eq. 2.4 as

$$\frac{d}{dt} \left(\frac{\partial \mathcal{L}}{\partial \dot{x}} \right) = \frac{\partial \mathcal{L}}{\partial x} \quad (2.5)$$

from which we recover our differential equation $m \frac{d^2x}{dt^2} = -kx$ as in Eq. 2.2. As we will later see, describing our physical systems in terms of energies rather than forces will prove to be a more natural approach, especially as we move towards unravelling the dynamics of quantum circuits.

LC RESONATORS

As another more directly pertinent oscillator, it is useful to consider the flow of charge carriers q in an electrical circuit containing a charged capacitor and an inductor arranged in parallel. The charged capacitor with capacitance C has a potential difference V across its two plates, which generates an electric field in the gap of distance d , given by $E = \frac{V}{d}$ where $V = \frac{q}{C}$. As the charge carriers move through the circuit due to the potential difference, they pass through the inductor with inductance L , which generates a magnetic field B with flux $\Phi_B = L \frac{dq}{dt}$ and induces a voltage given by $V = -\frac{d\Phi_B}{dt}$.

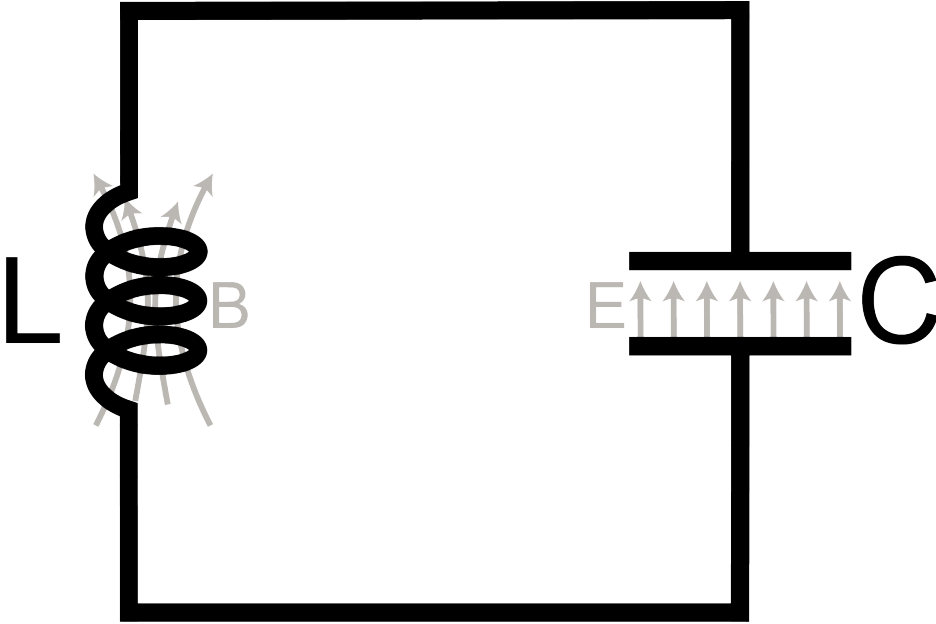


Figure 2.2: A diagram depicting an LC oscillator. Energy in the circuit oscillates between being stored in the electric field E between the charged plates of the capacitor and in the magnetic field B generated by charge carriers flowing through the inductor.

Thus, from the capacitor and inductor, we have

$$\frac{dq(t)}{dt} = -C \frac{dV(t)}{dt} \quad (2.6)$$

$$V(t) = L \frac{d^2q}{dt^2}. \quad (2.7)$$

We can form a Lagrangian with the knowledge that $T = \frac{1}{2}L(\frac{dq}{dt})^2$ and $U = \frac{1}{2}qV$ and solve the Euler-Lagrange equation to obtain

$$L \frac{d^2q}{dt^2} = -\frac{q}{C} \quad (2.8)$$

which has a clear resemblance in form to Eq. 2.2. Similarly to the oscillations of the position of the mass on a spring, the charge $q(t) = q_0 \cos(\omega_0 t)$ oscillates between the inductor and capacitor at the resonant frequency $\omega_0 = \frac{1}{\sqrt{LC}}$.

In reality, springs and electrical circuits are not such idealized objects. These systems are made of materials, and those materials have their own properties. Further, they are not closed systems non-interacting with their environment. For example, how might our solutions differ if the spring we use is rusty and slowly loses a small amount of stiffness as it oscillates? What happens if we give the object a little push each time it extends to its maximum? How do the resistive losses of the wires in our circuit change our equations? What if our object attached

to the spring is an opened parachute that catches the wind as it returns to equilibrium? What if we attach two springs together with different spring constants? Our simple toy problems can very rapidly complicate themselves if we consider factors such as nonlinearities, couplings, and driven oscillations, as we will see in later chapters.

RESONATORS AND MODES

If you have ever found that you can blow air into a glass bottle in just the right way to produce a loud ringing sound, you have already encountered a resonator [161]. The geometry of the bottle determines the frequency of sound waves that can be hosted, and blowing into the bottle causes the air inside to vibrate. Similarly, subjecting a wine glass to sound waves of a specific frequency (typically on the order of a few kHz) will cause the rim of the glass to vibrate at that resonant frequency.

In the case of a cylindrical tube closed at one end and open at the other, the *quarter-wavelength* or $\lambda/4$ resonator can host a series of standing waves with frequencies increasing as $f_n = n \frac{v_s}{4d}$, where n are positive integers, v_s is the speed of sound in the tube, and d is the length of the tube. While before our exercise with the mass-spring system showed one natural frequency, here our open-ended tube hosts a series of *normal modes* of different frequencies, each separated by integer multiples of the speed of sound divided by the length of the pipe.

Conversely, a guitar string is fixed at both ends and hosts modes as in a *half-wavelength* or $\lambda/2$ resonator closed at both ends, with frequencies given by $f_n = n \frac{v_s}{2d}$ where d is the length of the string. When the string is strummed, a near-instantaneous "kick" is delivered, and a combination of these modes are excited with the frequencies dependent on the tension of the string set by the tuning peg and the position of the user's fingers holding down the string which modifies the effective length of the resonator.

I think that most non-physicists would be surprised to learn that there are strong correspondences between such common activities as plucking a guitar string or bouncing a mass on a spring and the quantum computers that they read about in the news or see in science fiction media. All of the complicated quantum mechanical experiments outlined in later chapters are fundamentally concerned with nonlinear LC oscillators and coplanar waveguide resonators, which have resonance frequencies and normal modes that we excite in ways not dissimilar to these simple classical systems. The modes may be hosted on "tubes" much thinner than a human hair, and we may excite them with microwave signals rather than by blowing air or plucking a string, but much of the physics underpinning these devices is the same as we experience in our everyday lives.

2.1.2. THE DRIVEN, DAMPED, NONLINEAR OSCILLATOR

If we want to discuss our qubit of choice (the superconducting transmon qubit) in any detail, it is instructive to first expand our understanding of the simple harmonic oscillator to include damping, driving, and nonlinearity. Much of the experimental work in this thesis is concerned with driven, damped, anharmonic oscillators so it is useful to introduce each of these ingredients in our construction of the experimental problems at hand.

We introduce the following equation, known widely as the Duffing equation, which describes

the motion of forced Duffing oscillators as

$$\frac{d^2x}{dt^2} + \alpha x + \delta \frac{dx}{dt} + \beta x^3 = F \cos(\omega t) \quad (2.9)$$

which can be seen to closely resemble Eq. 2.2, with the addition of a term proportional to the speed of the oscillator by a damping constant δ and a cubic nonlinearity in position with constant β , as well as a periodic driving force with amplitude F at frequency ω . Neglecting the applied force and damping, we can determine the kinetic and potential energies and write the Lagrangian of the undriven oscillator as

$$\mathcal{L} = T - U = \frac{1}{2}m\left(\frac{dx}{dt}\right)^2 - \frac{1}{2}m\alpha x^2 - \frac{1}{4}m\beta x^4 \quad (2.10)$$

which shows that this oscillator exists in a potential with quadratic and quartic contributions. Later, we will show a correspondence between this potential and quantum circuits containing Josephson junctions.

A commonly cited damping mechanism of an oscillator is friction (as an object slides along a surface or through a non-vacuum medium such as air or oil), with the damped oscillator characterized by whether δ is equal to 0, between 0 and 1, equal to 1, or greater than 1. In the case of a damped oscillator, where we also consider $\beta = F = 0$, our example in Eq. 2.2 of the mass-spring system would change to

$$m\frac{d^2x}{dt^2} + \delta\frac{dx}{dt} = -kx \quad (2.11)$$

and the solution would be modified with a decaying exponential set by the damping rate given by

$$x(t) = x_0 e^{-\frac{\delta}{2m}t} \cos(\omega t) \quad (2.12)$$

where now $\omega = \sqrt{\omega_0^2 - (\frac{\delta}{2m})^2}$. In the case of an LC oscillator with resistive losses, the damping of the oscillations in the circuit is due to the resistance R , with the quality factor $Q = \frac{1}{R} \sqrt{\frac{L}{C}}$ of the oscillator set by the degree of damping.

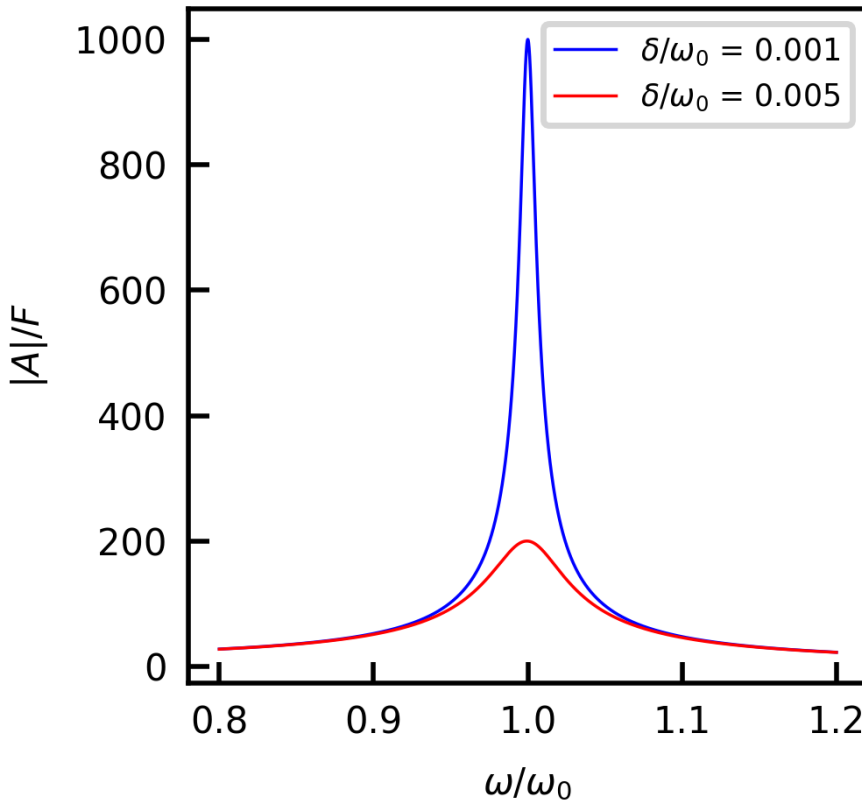


Figure 2.3: The steady-state response amplitude as a function of frequency, as defined in Eq. 2.15 with $m=0.1$ kg. The response has a Lorentzian shape with linewidth determined by the damping factor δ .

If we extend Eq. 2.11 to now include a periodic driving force as

$$m \frac{d^2 x}{dt^2} + kx + \delta \frac{dx}{dt} = F \cos(\omega t) \quad (2.13)$$

we find that the problem quickly becomes more complicated, with the solutions strongly dependent on the degree of damping. If we instead consider the driving force to be complex with $F(t) = F e^{i\omega t}$ which maintains $\text{Re}[F(t)] = F \cos(\omega t)$, we can apply a general trial solution of the form $x(t) = A e^{i(\omega t + \phi)}$ to solve for the steady-state solution. It is then straightforward to express A in terms of the other parameters as

$$A = \frac{F e^{-i\omega t}}{m(\omega_0^2 - \omega^2) + i\delta\omega} \quad (2.14)$$

and since we take A and x to be real, we have

$$A = \frac{F}{\sqrt{m^2(\omega_0^2 - \omega^2)^2 + \delta^2\omega^2}} \quad (2.15)$$

$$\phi = -\arctan\left(\frac{\delta\omega}{k - m\omega^2}\right) \quad (2.16)$$

and we can write $x(t) = A \cos(\omega t + \phi) + x_t$ where additive transient terms of the solution x_t are dependent on the initial conditions and degree of damping relative to the force amplitude and frequency.

The system becomes much more complicated when we add the cubic nonlinearity βx^3 and derive solutions to Eq. 2.9. Following Ref. [162], we can propose a trial solution

$$x(t) = a \cos(\omega t) + b \sin(\omega t) \quad (2.17)$$

which, when combined with Eq. 2.9 and after dropping the higher order harmonics, which play a negligible role, yields

$$\begin{aligned} (-\omega^2 a + \omega \delta b + \alpha a + \frac{3}{4}\beta a^3 + \frac{3}{4}\beta a b^2 - F) \cos(\omega t) &= (\omega^2 b + \omega \delta a - \frac{3}{4}\beta b^3 - \alpha b \\ &\quad - \frac{3}{4}\beta a^2 b) \sin(\omega t) \end{aligned} \quad (2.18)$$

which we can solve to obtain

$$((\omega^2 - \alpha - \frac{3}{4}\beta(a^2 + b^2))^2 + \delta^2 \omega^2)(a^2 + b^2) = F^2. \quad (2.19)$$

We can reparametrize the solution to

$$x(t) = z \cos(\omega t - \phi) \quad (2.20)$$

where $z = \sqrt{a^2 + b^2}$ and $\phi = \arctan\left(\frac{b}{a}\right)$. We can then find the characteristic Duffing response by plotting $\frac{z}{F}$ versus $\frac{\omega}{\sqrt{\alpha}}$, or in other words, the force-normalized amplitude response of the oscillator as a function of frequency of forcing relative to the "stiffness" (and in turn, the natural frequency ω_0) of the oscillator.

At certain forcing frequencies and amplitudes the response of the oscillator is multi-valued and it can further be shown that the system exhibits hysteresis, in that the response depends on whether the forcing frequency is increasing or decreasing as it is swept. These are characteristic properties of the quantum circuits containing Josephson junctions under investigation in later chapters. We will discuss the parametrically driven Duffing oscillator specifically in Sec. 2.3, which is more directly relevant to our results in Chapters 4 - 7.

2.1.3. NONLINEAR LC RESONATORS

SUPERCONDUCTIVITY, JOSEPHSON JUNCTIONS, AND SQUIDS

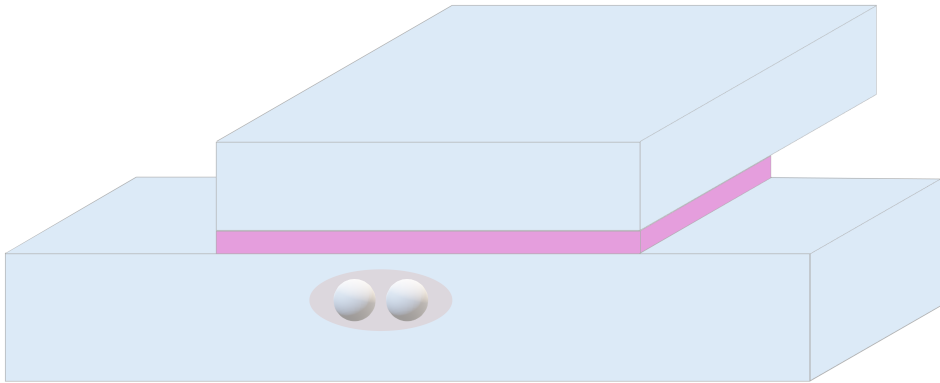


Figure 2.4: An example of a Josephson junction, with the superconducting material (blue) surrounding a thin insulating layer (purple). Two electrons forming a Cooper pair are shown in the superconducting material.

In order to construct quantum circuits, we require two components: a patternable layer of superconducting metal for bulk structures (such as coplanar waveguide resonators and qubit electrodes) and Josephson junctions (which themselves contain thin films of superconducting metal sandwiching an insulating layer).

Superconductors are materials which exhibit zero electrical DC resistance and repel magnetic fields when brought below their critical temperature T_c , which is typically at or below tens of Kelvin. For the materials used in the experiments outlined later in this thesis, thin-film NbTiN and Al, the critical temperatures are around 10 K and 1.2 K, respectively. To reach such low temperatures, simply placing the devices in liquid nitrogen is insufficient, and so the use of helium dilution refrigerators is necessary to reach milli-Kelvin temperatures far below the critical temperatures of the device's superconductors and satisfying the condition $\hbar\omega \gg k_B T$ to ensure the lack of thermal excitations on the order of the frequencies of the modes we are interested in.

When a material superconducts, the electrons in the material tend to form weakly bonded "Cooper pairs," which easily break apart at higher temperatures. Curiously, while electrons are spin-1/2 fermions, Cooper pairs are bosons, so they are not restricted to separate quantum states as electrons are. Thus, rather than considering single charge carriers moving through a circuit, we are concerned with the quantum states associated with the presence and movement of Cooper pairs, especially across Josephson junctions.

A Josephson junction is an element formed by separating two superconductors from each other with an insulating layer. For the junctions in the devices discussed in this thesis, the superconductors are Al, and the insulating layer is AlO_x . On the left and right sides of the junction, the quantum state of the Cooper pairs in the superconductors can be expressed as

$$\psi_i = \psi_i e^{i\phi_i} \quad (2.21)$$

where i can be l, r representing the left and right sides respectively, ψ_i is the amplitude (related to the number of charge carriers), and ϕ_i is the phase of the wavefunction. The junction acts as a small capacitor, where instead of charges separated with a potential difference, there are Cooper pairs, which yield a difference in energy across the junction $\Delta U = 2eV$.

Following Ref. [163], we can apply the Schrödinger equation to obtain a system of equations given by

$$\hbar \frac{\partial}{\partial t} (\psi_l e^{i\phi_l}) = eV \psi_l e^{i\phi_l} + K \psi_r e^{i\phi_r} \quad (2.22)$$

$$\hbar \frac{\partial}{\partial t} (\psi_r e^{i\phi_r}) = -eV \psi_r e^{i\phi_r} + K \psi_l e^{i\phi_l} \quad (2.23)$$

which can be rearranged to obtain

$$\frac{\partial}{\partial t} (\psi_l^2) = \frac{2}{\hbar} K \psi_l \psi_r \sin(\delta) \quad (2.24)$$

$$\frac{\partial}{\partial t} (\psi_r^2) = -\frac{2}{\hbar} K \psi_l \psi_r \sin(\delta) \quad (2.25)$$

$$\frac{\partial}{\partial t} (\phi_l) = -\frac{K}{\hbar} \frac{\psi_r}{\psi_l} \cos(\delta) - \frac{eV}{\hbar} \quad (2.26)$$

$$\frac{\partial}{\partial t} (\phi_r) = \frac{K}{\hbar} \frac{\psi_l}{\psi_r} \cos(\delta) + \frac{eV}{\hbar} \quad (2.27)$$

where $\delta = \phi_r - \phi_l$ is the phase difference across the junction or the Josephson phase and K is the amplitude of the coupling between the two sides of the junction. A consequence of these equations and the presence of Cooper pairs is that current may flow (as Cooper pairs tunnel) through the junction without an applied voltage. Supposing that the amplitudes on either side of the barrier are equal, we can solve the above equations to obtain the Josephson equations given by

$$I(t) = I_c \sin(\delta(t)) \quad (2.28)$$

$$\frac{\partial \delta}{\partial t} = \frac{2eV(t)}{\hbar} = \frac{2\pi V(t)}{\Phi_0} \quad (2.29)$$

where $\Phi_0 = \frac{h}{2e}$ is the superconducting flux quantum. Further, by making use of the fact that $V = L \frac{dI}{dt}$, we can rearrange the above to find the inductance of the junction given by

$$L(\delta) = \frac{\Phi_0}{2\pi I_c \cos(\delta)} \quad (2.30)$$

where the Josephson inductance is $L_J = L(0) = \frac{\Phi_0}{2\pi I_c}$, and we can determine the energy stored in the junction as

$$E(\delta) = -\frac{I_c \Phi_0}{2\pi} \cos(\delta) \quad (2.31)$$

from which we can define the Josephson energy as $E_J = E(0) = \frac{I_c \Phi_0}{2\pi}$ where the energy is calculated from $E = \int I(t)V(t)dt$. It is important to note the relationship between the time-dependent voltage and Josephson phase in Eq. 2.29 has consequences for the Josephson inductance and energy. If we integrate both sides of Eq. 2.29 with respect to time, we can find

that $\delta(t) = \frac{2\pi}{\Phi_0} \int V(t)dt$ while we know from Sec. 2.1.1 that an inductor follows the relation $V(t) = -\frac{d\Phi}{dt}$. The dependence of the phase difference on magnetic flux is explored below during the discussion on SQUIDS.

From these, we can see that the current flowing across the junction is maximal at a critical current I_c and modulated by the phase difference across the junction. We can also note that the voltage across the junction is strictly determined by the rate of change of the phase difference across the junction, so we may have a flow of current with no voltage due to quantum tunnelling. From the above, we can surmise that at very low temperatures, we can have very small currents flow across a junction due to the change in phase of Cooper pairs in two superconductors separated by an insulating layer. As we show later, we can use the charge and phase as quantum operators in our quantization of circuits containing Josephson junctions.

Lastly, there is yet another interesting set of effects that manifest when two Josephson junctions are placed in parallel, making a superconducting loop with two spatially separate insulating barriers. The phase difference across the loop is then dependent on the quantized flux threading the loop, given by

$$\delta = 2\pi \frac{\Phi_a}{\Phi_0}. \quad (2.32)$$

Thus, the total current of the element is $I = I_1 + I_2$, which can be combined with Eq. 2.28 to find the total flux-dependent critical current of the loop

$$I_c(\Phi_a) = \sqrt{(I_{c1} - I_{c2})^2 + 4I_{c1}I_{c2} \cos\left(2\pi \frac{\Phi_a}{\Phi_0}\right)^2} \quad (2.33)$$

which shows that the critical current of a superconducting loop, or Superconducting Quantum Interference Device (SQUID) is modulated by a cosine dependence on the magnetic flux threading the loop relative to the magnetic flux quantum. Given that the critical current is flux-dependent, it also follows that the Josephson inductance and Josephson energy of the SQUID also inherit flux-dependence through the critical current. For two identical junctions, the simple substitution $I_c \rightarrow 2I_c |\cos(2\pi \frac{\Phi_a}{\Phi_0})|$ can be used.

QUANTUM (AN)HARMONIC OSCILLATORS

If we revisit the case of the LC oscillator, replacing the linear inductance with the nonlinear inductor which is the Josephson junction, we can effectively realize the basis for much of the past few decades of research in superconducting qubits. However, before taking the step of creating an anharmonic quantum oscillator, we may first start by quantizing the linear LC oscillator.

If we consider the results of Eq. 2.6 - 2.8, we can construct a Lagrangian for an LC oscillator as

$$\mathcal{L} = \frac{1}{2}L\left(\frac{dq}{dt}\right)^2 - \frac{1}{2}qV = \frac{1}{2}\frac{\Phi^2}{L} - \frac{1}{2}\frac{q^2}{C} \quad (2.34)$$

where we make use of the fact that $V = q/C$ and $\Phi = L\frac{dq}{dt}$. We may then apply the Legendre transform to obtain the Hamiltonian for the system as

$$\mathcal{H} = \frac{1}{2}\frac{\Phi^2}{L} + \frac{1}{2}\frac{q^2}{C}. \quad (2.35)$$

and treat the charge and flux parameters as quantum operators with the following commutation relation

$$[\hat{\Phi}, \hat{q}] = i\hbar \quad (2.36)$$

where if we define

$$\hat{\Phi} = \sqrt{\frac{\hbar}{2\omega C}} (\hat{a}^\dagger + \hat{a}) \quad (2.37)$$

$$\hat{q} = \sqrt{\frac{\hbar\omega C}{2}} (\hat{a}^\dagger - \hat{a}) \quad (2.38)$$

we can obtain the standard form of the quantum harmonic oscillator

$$\hat{\mathcal{H}} = \hbar\omega \left(\hat{a}^\dagger \hat{a} + \frac{1}{2} \right) \quad (2.39)$$

where again $\omega = \frac{1}{\sqrt{LC}}$ and \hat{a}^\dagger, \hat{a} are the creation and annihilation operators respectively.

We are now ready to replace the linear inductance of the quantized LC oscillator with the nonlinear inductance provided by the Josephson junction. Recalling that the phase-dependent Josephson inductance is defined as in Eq. 2.30, with the phase-flux relation given by Eq. 2.32, we can write the inductive potential energy of the circuit as $-E_J \cos(\delta)$. We may now exchange the inductive potential energy of Eq. 2.35 with our nonlinear inductive potential energy and write our new Hamiltonian as

$$\mathcal{H} = 4E_C \hat{n}^2 - E_J \cos(\hat{\delta}) \quad (2.40)$$

where $E_C = \frac{e^2}{2C}$ is the charging energy and $\hat{\delta} = 2\pi \frac{\hat{\Phi}}{\Phi_0}$, $\hat{n} = \frac{\hat{q}}{2e}$ are the phase and charge number operators respectively, and we take $E_J \gg E_C$ which allows us to neglect an offset charge arising from coupling of the oscillator to the environment [118].

Simply by replacing the linear inductive energy with that of the energy stored in the Josephson junction, we have now arrived at a very powerful equation from which we can adjust and expand to uncover the dynamics of the quantum circuits that will be discussed in this thesis. For example, by maintaining that the Josephson energy is far larger than the charging energy, we can Taylor expand the cosine potential and retain terms to fourth order, yielding

$$\mathcal{H} = 4E_C \hat{n}^2 + \frac{1}{2} E_J \hat{\delta}^2 - \frac{1}{24} E_J \hat{\delta}^4 \quad (2.41)$$

which, together with the definitions

$$\hat{\delta} = \left(\frac{2E_C}{E_J} \right)^{1/4} (\hat{b}^\dagger + \hat{b}) \quad (2.42)$$

$$\hat{n} = i \left(\frac{E_J}{32E_C} \right)^{1/4} (\hat{b}^\dagger - \hat{b}) \quad (2.43)$$

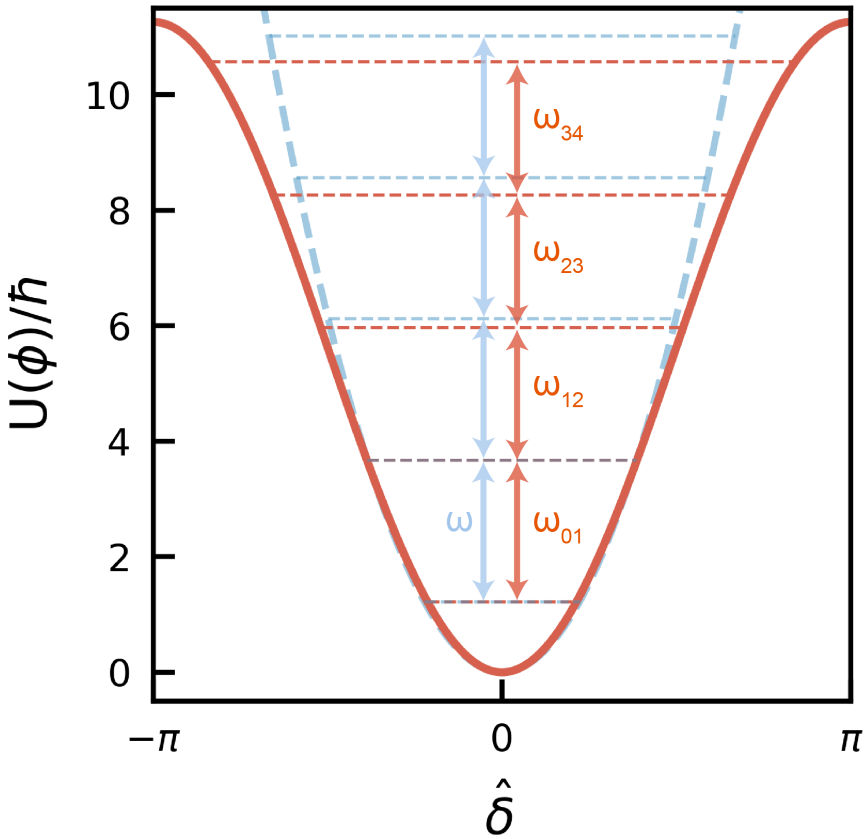


Figure 2.5: The energy potential for a quantum harmonic (blue) and anharmonic (red) oscillator. The harmonic oscillator shown contains only a quadratic dependence on phase, and the anharmonic potential contains the full cosine dependence as in Eq. 2.40. The spacing between each energy level of the harmonic potential is equal ($\hbar\omega$) while the energy level spacings for the anharmonic potential are non-equidistant and depend on the nonlinearity of the oscillator.

allows us to write the Hamiltonian of a superconducting qubit (the "transmon" [111]) as

$$\mathcal{H} = \sqrt{8E_C E_J} \hat{b}^\dagger \hat{b} - \frac{E_C}{12} (\hat{b}^\dagger + \hat{b})^4 \quad (2.44)$$

for which the first term is as in Eq. 2.39, and the second bestows our device with a quartic nonlinearity. This oscillator will be discussed further in Sec. 2.2.

We can further simplify our Hamiltonian by expanding out the fourth order term and dropping terms which are fast-rotating by applying the Rotating Wave Approximation (RWA), under the argument that in a frame rotating at ω , (provided that $\hbar\omega \gg \frac{E_C}{4}$) the contributions of these fast-rotating terms to the dynamics of the system average out. In this situation, we can arrive

at the simplified Kerr Hamiltonian

$$\mathcal{H}/\hbar \approx \omega \hat{b}^\dagger \hat{b} + K \hat{b}^\dagger \hat{b}^\dagger \hat{b} \hat{b} \approx \omega \hat{b}^\dagger \hat{b} + \frac{\alpha}{2} \hat{b}^\dagger \hat{b}^\dagger \hat{b} \hat{b} \quad (2.45)$$

where $\hbar\omega = \sqrt{8E_C E_J} - E_C$ is the frequency of the transmon and $K = -\frac{E_C}{2\hbar}$ is the self-Kerr nonlinearity, where again provided that $E_J \gg E_C$, we may take $\alpha \approx -E_C/\hbar$ to be the anharmonicity of the oscillator.

When the nonlinearity (anharmonicity) is sufficiently large relative to the strengths of the drives we apply to excite our oscillator, we are justified in truncating our Hilbert space to a *computational subspace* usually consisting of the ground and first excited states, which realizes a qubit [118]. In the case that we restrict ourselves to only the first two energy levels of the transmon, we may then exchange our creation and annihilation operators for the Pauli operators $\{\sigma_X, \sigma_Y, \sigma_Z\}$ and obtain the spin-like qubit Hamiltonian

$$\mathcal{H}_q = \frac{\hbar}{2} \hat{\sigma}_Z. \quad (2.46)$$

The transmon qubit is a very commonly constructed and robust device, given that it may be realized by simply placing a Josephson junction in parallel to a capacitor. These devices are often realized on nanofabricated chips by defining one or two electrodes separated from a ground plane by a small gap to realize a capacitance, connected only via a Josephson junction. By tuning the critical current of the junction and the capacitance of the electrode(s), the frequency and nonlinearity of the qubit can be directly engineered.

If the reader has noticed a resemblance between Eq. 2.10 and Eq. 2.41, this is not a coincidence – nonlinear LC oscillators based on Josephson junctions, in the parameter regime where $\frac{I_c \Phi_0}{2\pi} \gg \frac{e^2}{2C}$, are very well-described as Duffing oscillators [111].

2.2. CIRCUIT QUANTUM ELECTRODYNAMICS

2.2.1. RESONATORS AND QUBITS

While even today, there is still not yet a consensus on which platform is best to realize quantum computing, within the superconducting qubit community, there were several viable candidates in the early 2000s for the ideal qubit. The charge qubit, followed by the flux and phase qubits, had numerous studies presented in high profile publications, but it would end up being a tweak to the charge qubit that brought the transmon qubit to virtually take over the field [55, 71, 76, 88–98, 100–110]. While the *circuit quantum electrodynamics* (circuit QED) foundation was laid a few years earlier, the field would blossom with the marriage of the transmon qubit and the readout resonator [111–117].

Drawing from the field of cavity quantum electrodynamics (cavity QED), it was posited that the *artificial atom* of the superconducting qubit together with the transmission line resonator would be a suitable architecture for quantum computing [112, 164–167]. While originally embedded in the waveguide itself, in general, coupling a superconducting qubit to a coplanar waveguide (CPW) resonator (or even a 3D cavity) will realize a Jaynes-Cummings interaction and yield a qubit-photon interaction in the same way as the atoms in cavity QED [114, 115, 168].

THE TRANSMISSION LINE RESONATOR

The storage and relaying of microwave frequency electromagnetic signals is often achieved by the use of transmission lines. A transmission line is a distributed circuit element which supports the transmission of electromagnetic energy along its length and hosts a variety of transverse electromagnetic (TEM) modes of propagation. If one wishes to construct a resonator-transmission system in an integrated circuit platform, transmission line resonators are a natural choice to achieve such a goal, given the decades of history of microfabrication of such structures. Further, they can be constructed with superconducting materials and cooled down to cryogenic temperatures, a key ingredient required for operating these devices as coherent quantum systems.

In the following, we draw from the derivations of Ref. [169, 170]. We can characterize the system as a series of distributed inductors and capacitors of infinitesimal length Δx , through which currents can be passed and voltages can be applied. Given the distributed nature of the circuit, the currents and voltages at any given point along the line can vary given the large discrepancy between the total length of the line l between $[-l/2, l/2]$ and each individual distributed element with resistance, conductance, inductance, and capacitance scaled by the length segment Δx given by R , G , L and C respectively.

In the case of a lossless transmission line where $R = G = 0$, we can define the characteristic impedance of the line to be

$$Z_0 = \sqrt{\frac{L}{C}} \quad (2.47)$$

where the steady-state voltage and current as a function of position along the line are given by

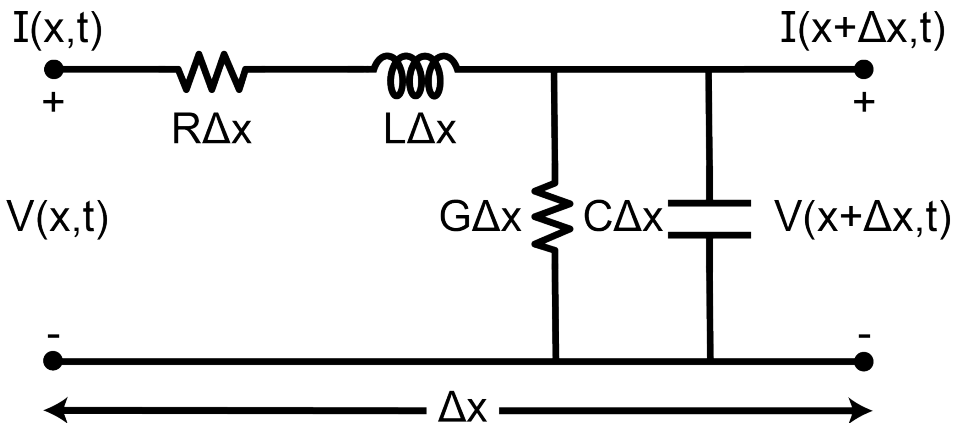


Figure 2.6: A circuit diagram adapted from Ref. [169]. Displayed are the resistance, conductance, inductance, capacitance, voltage, and current for a segment Δx of a transmission line.

$$V(x) = V_0^+ e^{-i\beta x} + V_0^- e^{i\beta x} \quad (2.48)$$

$$I(x) = \frac{1}{Z_0} (V_0^+ e^{-i\beta x} - V_0^- e^{i\beta x}) \quad (2.49)$$

where $\beta = \omega\sqrt{LC}$ is the imaginary component of the propagation constant $\gamma = \alpha + i\beta$, ω is the frequency of the wave propagating along the line, "+" denotes propagation in the positive x direction, and "-" in the negative x direction. We can also define the wavelength and phase velocity of the line as $\lambda = \frac{2\pi}{\beta} = \frac{2\pi}{\omega\sqrt{LC}}$ and $v_p = \frac{\omega}{\beta} = \frac{1}{\sqrt{LC}}$ respectively.

If the transmission line is terminated at one end by a load with impedance Z_L , we can better understand how this system can be considered as a resonator. If we place a load Z_L at position $x = 0$, we can use Eq. 2.48, 2.49 to determine that

$$Z_L = V(0)/I(0) = \frac{V_0^+ + V_0^-}{V_0^+ - V_0^-} Z_0 \quad (2.50)$$

where the incident wave is propagating in the $+x$ direction and originating from $x < 0$. We can then take the ratio of the voltages of the returning (negatively propagating) and incident (positively propagating) waves to find the voltage reflection coefficient

$$\Gamma = \frac{V_0^-}{V_0^+} = \frac{Z_L - Z_0}{Z_L + Z_0} \quad (2.51)$$

and reparametrize the voltage and current in the line in terms of the incident wave and the reflection coefficient as

$$V(x) = V_0^+ (e^{-i\beta x} + \Gamma e^{i\beta x}) \quad (2.52)$$

$$I(x) = \frac{V_0^+}{Z_0} (e^{-i\beta x} - \Gamma e^{i\beta x}). \quad (2.53)$$

Given that the voltage and current vary along the line and depend on the load impedance, we can also define the input impedance or impedance at the beginning of the line at $x = -l/2$ in terms of the characteristic impedance and reflection coefficient as

$$Z_{in} = V(-l/2)/I(-l/2) = Z_0 \frac{1 + \Gamma e^{-i\beta l}}{1 - \Gamma e^{-i\beta l}} = Z_0 \frac{Z_L + iZ_0 \tan(\beta \frac{l}{2})}{Z_0 + iZ_L \tan(\beta \frac{l}{2})}. \quad (2.54)$$

We now have the tools necessary to analyze the cases in which the line is *short* ($Z_L = 0$, $\Gamma = -1$) and *open* ($Z_L \rightarrow \infty$, $\Gamma = 1$). We can plot the voltages and currents as a function of position for both cases using Eq. 2.52, 2.53 and find that there are voltage anti-nodes and current nodes at integer multiples of the quarter-wavelength for the short line and at integer multiples of the half-wavelength for the open line.

We can also consider the case where the terminating load is, in fact, another transmission line with characteristic impedance Z_1 , in which case the reflection coefficient is $\Gamma = \frac{Z_1 - Z_0}{Z_1 + Z_0}$ and we can define the transmission coefficient as $T = 1 + \Gamma$ which represents the voltage fraction of

the incident wave which carries on through into the second line rather than reflecting back in the negative direction. If the characteristic impedances of both lines are equal, all of the incident waves are transmitted, and none is reflected ($T = 1$, $\Gamma = 0$), while if the second line's impedance is infinitely smaller than the first, the incident wave is entirely reflected ($T = 0$, $\Gamma = 1$).

If we follow the same treatment above instead for a lossy transmission line where $R_l \neq 0$ and $G_l \neq 0$, where before the arguments of our exponentials were $i\beta$, we can exchange $i\beta$ for the full propagation constant

$$\gamma = \alpha + i\beta = \sqrt{(R + i\omega L)(G + i\omega C)} \quad (2.55)$$

where α is the attenuation constant of the line, and re-define the characteristic impedance as

$$Z_0 = \sqrt{\frac{R + i\omega L}{G + i\omega C}}. \quad (2.56)$$

With the above, we may now finally examine the short $\lambda/4$ and open $\lambda/2$ transmission line resonators, which are the most relevant for the content in later sections of this thesis. Following our definitions in Eq. 2.48, 2.49, 2.54 under the exchange $i\beta \rightarrow \gamma$, we can define the input impedances of the short and open transmission lines of total length $l = \lambda/4$ and $l = \lambda/2$ as

$$Z_{in,s} = Z_0 \tanh\left(\gamma \frac{\lambda}{4}\right) \quad (2.57)$$

$$Z_{in,o} = Z_0 \coth\left(\gamma \frac{\lambda}{2}\right). \quad (2.58)$$

If we consider small losses, such that $\tanh(\alpha) \approx \alpha$, we can simplify the above to

$$Z_{in,s} = \frac{1}{\frac{\alpha l}{Z_0} + 2iC(\omega - \omega_0)} \quad (2.59)$$

$$Z_{in,o} = \frac{Z_0}{\alpha l + i\pi\left(\frac{\omega}{\omega_0} - 1\right)} \quad (2.60)$$

which are equal to the input impedances of equivalent parallel RLC circuits with resonance frequencies $\omega_0 = 1/\sqrt{LC}$, resistances $R = \frac{Z_0}{\alpha l}$, inductances $L = \frac{1}{\omega_0^2 C}$, capacitances

$$C_s = \frac{\pi}{4\omega_0 Z_0} \quad (2.61)$$

$$C_o = \frac{\pi}{2\omega_0 Z_0} \quad (2.62)$$

and quality factors $Q = \omega_0 RC = \frac{\beta}{2\alpha}$.

THE COPLANAR WAVEGUIDE RESONATOR

While transmission line resonators may be realized in a variety of configurations (i.e. microstrip, stripline, slotline, coaxial line, etc.), we will consider the most commonly used integrated 2D transmission line resonator in circuit QED; the coplanar waveguide (CPW) resonator. The CPW is formed by arranging a layer of (super)conductive metal of thickness t on top of a substrate of thickness h with relative permittivity (dielectric constant) ϵ_r .

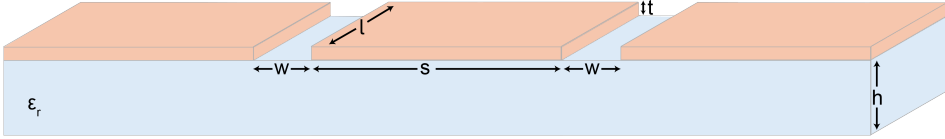


Figure 2.7: A diagram displaying a coplanar waveguide resonator as described in the main text. A superconducting thin film is laid on top of a substrate with the width (s) and length (l) of the center trace, gap width (w), film thickness (t), substrate height (h), and relative permittivity (ϵ_r) indicated.

The layer of metal is then etched such that a center trace of width s and length l is beset on each side by gaps of width w , separating the conductor from the rest of the metal layer. The center conductor then forms a capacitance with the rest of the metal layer and has a linear geometric inductance determined by l , s , and w . Following Ref. [170–173], conformal mapping techniques can be used to determine the inductance and capacitance of the resonator in relation to its geometry. If we define the ratio of the complete elliptic integral of the first kind to its complementary function as

$$\frac{K(k)}{K(k')} = \begin{cases} \pi / \left(\ln \left(2 \frac{1+\sqrt{k'}}{1-\sqrt{k'}} \right) \right) & \text{for } 0 \leq k \leq 0.7 \\ \frac{1}{\pi} \ln \left(2 \frac{1+\sqrt{k'}}{1-\sqrt{k'}} \right) & \text{for } 0.7 \leq k \leq 1 \end{cases} \quad (2.63)$$

where $k' = \sqrt{1-k^2}$ and $k = \frac{s}{s+2w}$, we can write the characteristic impedance of the line as

$$Z_0 = \frac{30\pi}{\sqrt{\epsilon_l}} \frac{K(k')}{K(k)} \quad (2.64)$$

where ϵ_l is the effective dielectric constant given by

$$\epsilon_l = 1 + \frac{\epsilon_r - 1}{2} \frac{K(k')K(k_1)}{K(k)K(k'_1)} \quad (2.65)$$

with $k_1 = \sinh\left(\frac{\pi s}{4h}\right) / \sinh\left(\frac{\pi(s/2+w)}{2h}\right)$.

From these, we can determine the fundamental frequency, inductance per unit length, and capacitance per unit length of the $l = \lambda/2$ waveguide resonator as

$$\frac{\omega_0}{2\pi} = \frac{c}{2l\sqrt{\epsilon_l}} = \frac{v_p}{2l} = \frac{1}{2l\sqrt{L_l C_l}} \quad (2.66)$$

and for the $l = \lambda/4$ waveguide resonator we obtain

$$\frac{\omega_0}{2\pi} = \frac{c}{4l\sqrt{\epsilon_l}} = \frac{v_p}{4l} = \frac{1}{4l\sqrt{L_l C_l}} \quad (2.67)$$

with

$$L_l = \frac{\mu_0}{4} \frac{K(k')}{K(k)} \quad (2.68)$$

$$C_l = 4\epsilon_0 \epsilon_l \frac{K(k)}{K(k')} \quad (2.69)$$

where μ_0, ϵ_0 are the vacuum permeability and permittivity, respectively.

If a CPW is coupled on one side to the end of a transmission line with characteristic impedance $Z_0 = 50\Omega$ via a capacitor C_e , we can find that

$$\frac{\omega_0}{2\pi} = 1/\sqrt{L(C + C_e)} \quad (2.70)$$

$$Q_e \approx \frac{C + C_e}{\omega_0 C_e^2 Z_0} \quad (2.71)$$

$$Q_i \approx \omega_0 R(C + C_e) \quad (2.72)$$

where R is the parallel resistance of the CPW and Q_e, Q_i are the external and internal quality factors with $Q = 1/(\frac{1}{Q_i} + \frac{1}{Q_e})$. Following a similar procedure as in the previous subsection, we can then determine the reflection coefficient for the system in this *reflection geometry* to be

$$\Gamma_r(\omega) = \frac{\kappa_i - \kappa_e + 2i(\omega - \omega_0)}{\kappa_i + \kappa_e + 2i(\omega - \omega_0)} \quad (2.73)$$

where $\{\kappa_e, \kappa_i\} = \{\omega_0/Q_e, \omega_0/Q_i\}$ are the external and internal loss rates of the CPW.

If we instead arrange the CPW to be capacitively *side-coupled* to a transmission line rather than capacitively terminating the line, one can show that the external quality factor changes with respect to the reflection geometry expression in Eq. 2.71 as $Q_e \rightarrow 2Q_e$ [174, 175]. In this case, the transmission coefficient becomes

$$T_{sc}(\omega) = 1 + \Gamma_{sc}(\omega) = \frac{\kappa_i + 2i(\omega - \omega_0)}{\kappa_i + \kappa_e + 2i(\omega - \omega_0)}. \quad (2.74)$$

Devices constructed for circuit QED experiments are commonly designed to be in the reflection or side-coupled transmission geometries, where the CPW is driven and probed through its capacitive coupling to the transmission line serving as a measurement feedline which is in turn connected via coaxial cables to measurement instruments.

THE RESONATOR-TRANSMON PARADIGM

If we proceed with the transmon Hamiltonian from Eq. 2.41 and the linear LC resonator Hamiltonian from Eq. 2.39, we can introduce a coupling term between the two if we suppose that they are capacitively coupled to each other, which yields

$$\mathcal{H} = \hbar\omega_r \left(\hat{a}^\dagger \hat{a} + \frac{1}{2} \right) + 4E_C (\hat{n} + \hat{n}_r)^2 - E_J \cos(\hat{\delta}) \quad (2.75)$$

where we now include the additional charge due to the capacitive coupling of the qubit to the resonator C_c , given by $\hat{n}_r = \frac{C_c \hat{q}_r}{2eC_r}$ where \hat{q}_r is as in Eq. 2.38, and C_r is the capacitance of the resonator itself. Here, we consider only the fundamental mode of the resonator, supposing that the transmon mode is far detuned from all other resonator modes, which are then negligible. Expanding the Hamiltonian and renormalizing the resonator frequency, we can again apply the RWA to arrive at the following

$$\mathcal{H} \approx \hbar\omega_r \hat{a}^\dagger \hat{a} + \hbar\omega_q \hat{b}^\dagger \hat{b} - \frac{E_C}{2} \hat{b}^\dagger \hat{b}^\dagger \hat{b} \hat{b} + \hbar g (\hat{a}^\dagger \hat{b} + \hat{a} \hat{b}^\dagger) \quad (2.76)$$

where $g = \omega_r \frac{C_c}{C_q} \left(\frac{E_J}{2E_C} \right)^{1/4} \sqrt{\frac{\pi e^2}{h}} \sqrt{\frac{L_r}{C_r}}$ and the final coupling term is known as the *beam-splitter* or *photon-hopping* interaction. If again we enforce that the transmon nonlinearity be sufficiently large, we can exchange to Pauli operators and obtain the Jaynes-Cummings Hamiltonian

$$\mathcal{H} \approx \hbar\omega_r \hat{a}^\dagger \hat{a} + \frac{\hbar}{2} \omega_q \hat{\sigma}_Z + \hbar g (\hat{a}^\dagger \hat{\sigma}_- + \hat{a} \hat{\sigma}_+) \quad (2.77)$$

where $\hat{\sigma}_\pm = \frac{1}{2}(\hat{\sigma}_X \pm i\hat{\sigma}_Y)$ are the raising and lowering operators, which when coupled through \hat{a}^\dagger and \hat{a} serve to mediate excitations between the qubit and resonator modes. The magnitude of the coupling strength g in relation to other parameters enables the ability to operate the qubit-resonator system in a variety of different regimes, with one in particular (the "dispersive regime") allowing for non-destructive readout of the qubit state.

COUPLING REGIMES

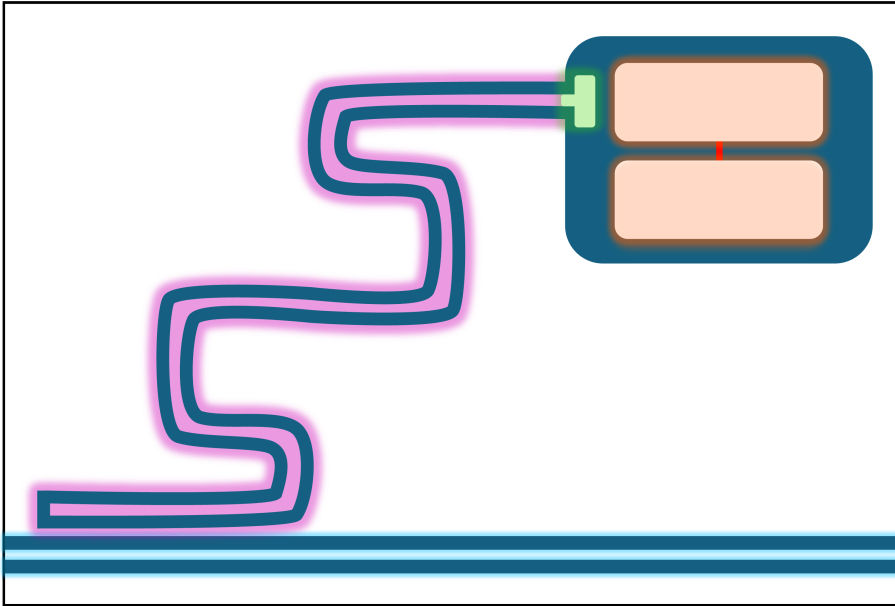


Figure 2.8: An illustration showing a highlighted measurement feedline (blue), readout resonator (purple), coupling pad segment (green), transmon electrodes (orange), and Josephson junction (red). The resonator is arranged in a side-coupled transmission configuration with capacitive coupling C_e to the feedline. The size of the coupling segment and its proximity to the transmon electrodes can be adjusted to tune the coupling capacitance C_c between the resonator and qubit.

The resonator-transmon system can be engineered to serve a variety of purposes. For instance, if we wish to bestow upon our linear resonator a degree of nonlinearity inherited from its interaction with the transmon, how strong must the coupling g be, and how far should they be detuned Δ from each other in frequency? In another case, if we wish to only have the resonator be used to non-destructively probe the state of our qubit, what should these values be? To answer these questions, we must also consider the role that the environment plays in the approach that we have taken thus far. Indeed, our resonator-transmon system is implicitly connected to some measurement apparatuses with which we may drive and probe the state of our system. Additionally, our device does not exist in a perfect world without dielectric losses, parasitic modes, two-level systems living in and on our materials, charge and flux noise, and all of the coupling mechanisms associated with these channels ignored when we made the demarcation between the resonator-transmon system and the rest of the universe.

We can start by defining the coupling strength of our resonator to the environment (everything which is not our transmon) with $\kappa = \kappa_e + \kappa_i$, where κ_e is the engineered external coupling to the measurement feedline (such as via a coupling capacitor C_e) and κ_i is the total "internal" loss rate associated with couplings to neither the transmon nor the measurement chain (as in the case of a parallel resistor as discussed above). In this thesis, κ_e is always set by the capacitive or inductive coupling of the resonator to a transmission line, through which we may measure

the device as each port of the transmission line is, in turn, connected via coaxial cables to our measurement devices, such as signal generators, vector network analyzers (VNA) or spectrum analyzers. We may also define the loss rate of the transmon as γ , which characterizes the rate at which the transmon exchanges energy with elements of the environment which are not the fundamental resonator mode.

We can then define quality factors of the resonator and transmon similarly as in Sec. 2.1.2 by $Q_r = \frac{\omega_r}{\kappa}$ and $Q_q = \frac{\omega_q}{\gamma}$. The resonator may be further characterized in terms of the ratio of the external to total loss rate, $\eta = \frac{\kappa_e}{\kappa} = \frac{Q_r}{Q_e}$ where $Q_r = 1/(\frac{1}{Q_e} + \frac{1}{Q_i})$ as before. We can then characterize the resonator as being overcoupled, critically coupled, or undercoupled to our measurement transmission line by whether $\eta > 0.5$, $= 0.5$, or < 0.5 , respectively. For our purposes, it is preferable to engineer devices to be in the overcoupled regime, such that the majority of the photons in the resonator are interacting with either our measurement chain or the transmon.

Measurements of transmission line parameters are not always as straightforward as the discussions above may indicate. Impedance mismatches and *Fano interference* caused by the presence of multiple background paths and insufficient isolation between measurement ports which interfere with resonant signals can lead to distortions in the real and imaginary components of reflection and transmission coefficients as functions of frequency [176, 177]. The determination of accurate external and internal quality factors of devices can prove difficult, in particular for overcoupled devices [177]. Developing calibrated design and simulation workflows which consistently produce devices with reliable external quality factors, as well as engineering microwave environments which reduce impedance mismatches and improve isolation can help to alleviate these issues.

If we wish to uncover the behaviour of the system in different coupling regimes, it is illustrative to return to the Jaynes-Cummings Hamiltonian in Eq. 2.77. The coupling between the resonator and qubit leads to a change in the energy landscape from the *bare* (uncoupled) spectrum to the *dressed* (coupled) spectrum, in which energy levels are split proportional to the degree of coupling when the bare energy levels are degenerate [112, 118]. If we define the joint system state as $|\sigma, n\rangle$ where n denotes the number of excitations in the resonator mode and $|\sigma\rangle$ may be $|g\rangle$ or $|e\rangle$ to represent the qubit being in the ground or excited state respectively, we can determine the dressed energy levels of the system as

$$E_{\pm, n} = \hbar\omega_r n \pm \frac{\hbar}{2} \sqrt{4ng^2 + \Delta^2} \quad (2.78)$$

where $\Delta = \omega_q - \omega_r$ is the frequency detuning between the resonator and qubit, $|\pm, n\rangle$ represents the state split to higher (+) or lower (-) energy relative to the level with n total excitations, and $E_{g,0} = -\frac{\hbar}{2}\omega_q$ is the ground state of the system. Given the above, when the detuning between the qubit and resonator is made to be zero, the levels which would be degenerate in the bare spectrum instead have their degeneracy lifted by $2g\sqrt{n}$ for joint states in which the resonator and transmon share n total excitations.

Thus, the Jaynes-Cummings interaction enables one to create maximally entangled states between the qubit and resonator when resonant and induce vacuum Rabi oscillations between the $|g, 1\rangle$ and $|e, 0\rangle$ states at the Rabi frequency $\frac{E}{\pi}$. When this coupling is larger than the

total loss rates of the qubit γ and resonator κ , one can resolve the energy level splitting and operate the system in the *strong coupling* regime where $g \gg \kappa, \gamma$.

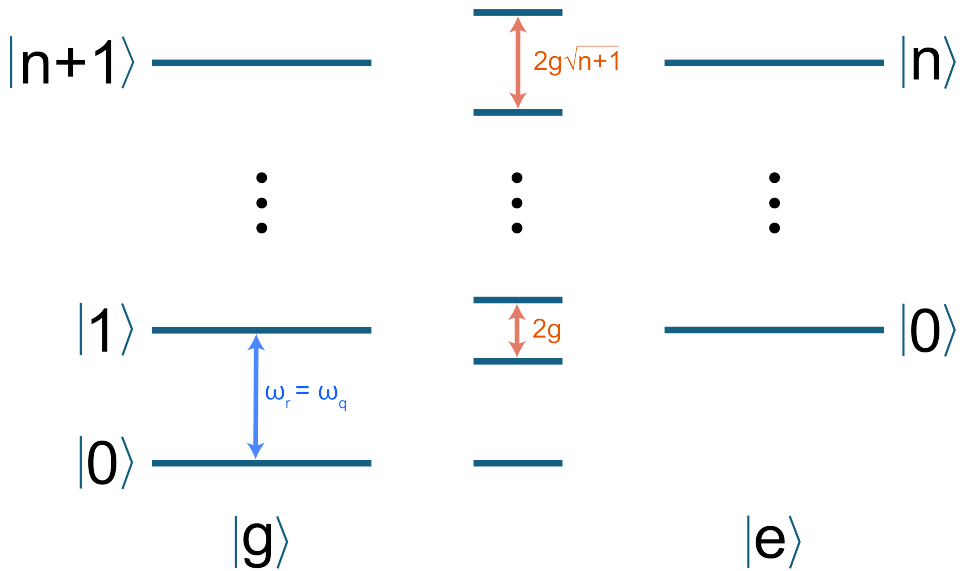


Figure 2.9: An energy level diagram showing the dressed (center) and bare (left, right) spectra for the Jaynes-Cummings Hamiltonian when the qubit and resonator are made resonant ($\Delta = 0$) [112]. The states $\{|g\rangle, |e\rangle\}$ represent the ground and excited states of the qubit, while $|n\rangle$ represents the number of excitations in the resonator. For a joint system state with n total quanta of energy, the level degeneracy in the dressed spectrum is lifted by $2g\sqrt{n}$.

However, in the case where the coupling g is made to be *ultra-strong*, where it approaches or even exceeds the resonance frequencies of the oscillators ω_q, ω_r , several assumptions that we have made about our system up to this point break down [178–180]. For example, our applications of the RWA are no longer valid, and we must now not only consider counter-rotating terms of the Hamiltonian such as $\hbar g(\hat{a}^\dagger \hat{\sigma}_+ + \hat{a} \hat{\sigma}_-)$, but the justification for truncating the transmon to a two-level system also breaks down, and we must consider the interactions between the higher-level transitions of the joint system.

DISPERSIVE READOUT

If one instead wishes to do operations on and perform readout of the qubit state, it is then preferable to operate the system in a regime where the qubit and resonator are not resonant ($\Delta \neq 0$) but still with sufficiently large coupling g to control and probe the state of the qubit via the resonator. To better understand the effects of the coupling and detuning on the system dynamics, we may expand the square root of Eq. 2.78 in g/Δ and retain terms to fourth order to obtain

$$E_{\pm, n} \approx \hbar\omega_r n \pm \frac{\hbar}{2} \left(\Delta + 2n \frac{g^2}{\Delta} - 2n^2 \frac{g^4}{\Delta^3} \right) \quad (2.79)$$

which holds for a small number of excitations n and $g < \Delta$. If we instead restrict ourselves to $g \ll \Delta$ in the large-detuning limit and maintain a small number of excitations defined by

$$n_{crit} = \left(\frac{\Delta}{2g}\right)^2 \quad (2.80)$$

we can retain only terms of the expansion to second order and find that rather than having degenerate eigenenergies with splitting $2g\sqrt{n}$, the energy levels are shifted down by g^2/Δ if the qubit is in the ground state and up by the same amount if the qubit is in the excited state. The transition frequency of the qubit is shifted to

$$\omega_q \rightarrow \omega_q + \frac{g^2}{\Delta} \left(n + \frac{1}{2}\right) \quad (2.81)$$

which is composed of the photon-dependent Stark shift $n\frac{g^2}{\Delta}$ and the Lamb shift $\frac{g^2}{2\Delta}$ [115, 181, 182]. Conversely, we can interpret this change in the energy level landscape as the resonator frequency experiencing a corresponding shift where

$$\omega_r \rightarrow \omega_r + \hat{\sigma}_Z \frac{g^2}{\Delta}. \quad (2.82)$$

This qubit-state-dependent shift of the resonator frequency in the dispersive regime is the basis for the quantum non-demolition (QND) mapping of the qubit state onto the cavity [118, 183, 184]. This can be seen by the commutativity of $\hat{\sigma}_Z$ with the dispersive Hamiltonian which modifies Eq. 2.77 to yield

$$H_{disp} \approx \frac{\hbar}{2} \left(\omega_q + \frac{g^2}{\Delta}\right) \hat{\sigma}_Z + \left(\hbar\omega_r + \hbar\frac{g^2}{\Delta} \hat{\sigma}_Z\right) \hat{a}^\dagger \hat{a}. \quad (2.83)$$

If we recall that our transmon is not a perfect two-level system but rather an anharmonic oscillator with anharmonicity $\alpha = -E_C/\hbar$, we can incorporate a correction from a higher order term in the perturbative expansion of the Jaynes-Cummings Hamiltonian which takes into account the effects of the coupling of the resonator to the second excited state of the transmon with

$$H_{disp} \approx \frac{\hbar}{2} \left(\omega_q + \frac{g^2}{\Delta}\right) \hat{\sigma}_Z + \left(\hbar\left(\omega_r + \chi\frac{\Delta}{\alpha}\right) + \hbar\chi\hat{\sigma}_Z\right) \hat{a}^\dagger \hat{a} \quad (2.84)$$

where we define $\chi = \frac{\alpha}{\Delta} \frac{g^2}{\Delta + \alpha}$ as the *dispersive shift* of the cavity frequency dependent on the qubit state [111, 118, 185]. Depending on the sign of Δ (whether the qubit is higher or lower frequency relative to the resonator) as well as how large the detuning is relative to the anharmonicity, the sign of χ can change from negative to positive. The region in which χ is positive is known as the *straddling regime* as it exists for only a relatively narrow parameter range where the cavity frequency is between the first and second transition frequencies of the transmon with $0 < \Delta < E_C$ [111].

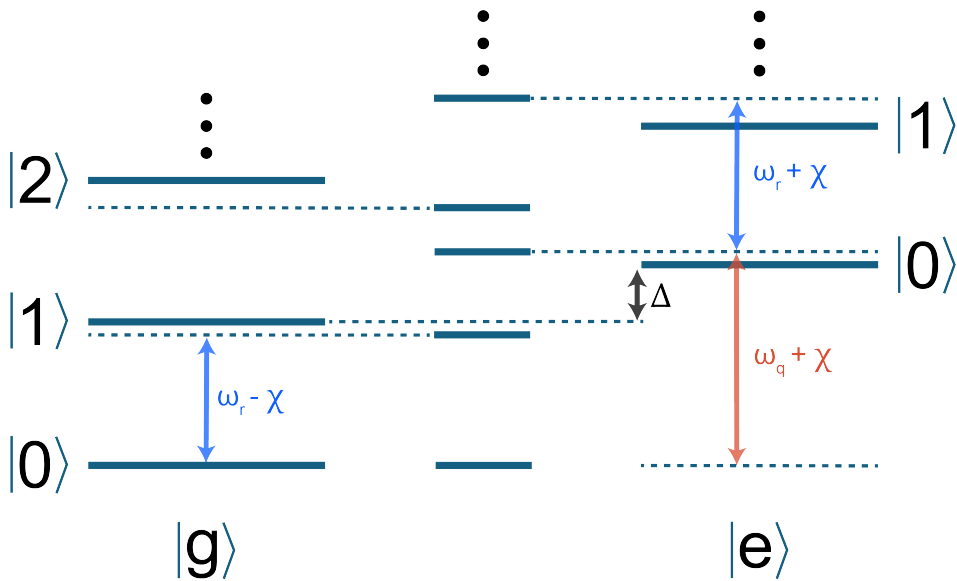


Figure 2.10: An energy level diagram showing the dressed (center) and bare (left, right) spectra for the Jaynes-Cummings Hamiltonian when the system is in the dispersive regime [118]. The states $\{|g\rangle, |e\rangle\}$ represent the ground and excited states of the qubit, while $|n\rangle$ represents the number of excitations in the resonator. The qubit transition frequency is increased by χ while the resonator transition frequency is shifted by $\pm\chi$ dependent on the state of the qubit.

Lastly, if we insist that the dispersive shift χ be much larger than the decay rates κ, γ , we can enter the *strong dispersive regime* of circuit QED. In this coupling regime, the qubit spectrum forms an array of photon number peaks which can be used to determine the resonator photon number distribution, and the resonator frequency shift is large enough to resolve the qubit state even at the single photon level [117, 184, 186].

If we return to Eq. 2.79 once more and include the fourth order term, it can be shown that in the case of sufficiently strong coupling, the resonator frequency shift becomes dependent on the number of photons in the resonator, proportional to $n \frac{g^4}{\Delta^3}$. Thus, in this *anharmonic strong dispersive* limit, the resonator is sufficiently coupled to the qubit to inherit nonlinearity from it, in which case the resonator itself should be treated as a Kerr oscillator with its own self-Kerr nonlinearity [187–189].

2.2.2. JOSEPHSON CAVITIES

JUNCTION-EMBEDDED COPLANAR WAVEGUIDE RESONATORS

Recalling the quantized nonlinear LC oscillator, we can investigate how the system changes when we consider there to be both linear and nonlinear inductances in the circuit. We may first consider an LC resonator in which the capacitance, linear geometric inductance, and nonlinear Josephson inductance are all in parallel with each other. We can revisit Eq. 2.35 and Eq. 2.40

and write the circuit of our new *nonlinear resonator* Hamiltonian as

$$\mathcal{H} = 4E_C \hat{n}^2 + \frac{1}{2} \frac{\hat{\Phi}^2}{L} - E_J \cos\left(2\pi \frac{\hat{\Phi}}{\Phi_0}\right). \quad (2.85)$$

We can again Taylor expand the cosine potential, retain terms to fourth order, and find

$$\mathcal{H} = 4E_C \hat{n}^2 + \frac{1}{2} \left(\frac{1}{L} + \frac{1}{L_J}\right) \hat{\Phi}^2 - \frac{2}{3} \left(\frac{\pi}{\Phi_0}\right)^4 E_J \hat{\Phi}^4 \quad (2.86)$$

which is simply our previous nonlinear LC oscillator Hamiltonian where the inductance in the quadratic term has been modified to

$$L \rightarrow 1/(1/L + 1/L_J). \quad (2.87)$$

This straightforward derivation is unfortunately not the full picture if we wish to realize such a nonlinear oscillator by, for example, embedding a Josephson junction within a CPW resonator [190]. While the individual modes of transmission line resonators can be represented by lumped-element LC circuits, the full system is best described as an infinite series of inductances and capacitances per unit length L_l , C_l for a resonator of length $2l$, as discussed in Sec. 2.2.1.

Further, while we have until now neglected the small capacitance of the Josephson junction C_J , we must consider how both the capacitance and inductance of the junction change the normal modes of the resonator. When introducing a Josephson junction to the transmission line, we must rather consider a discretized representation in which the junction placed at some position modifies the boundary conditions of the system as a function of its position, given that now the energy stored in the system is distributed between the nonlinear junction and the linear resonator dependent on the normal mode amplitudes along the length of the resonator [191]. This distribution can be parameterized in terms of the capacitive and inductive participation ratios $\eta_{c,m}$ and $\eta_{l,m}$, which take into account the contributions of the linear and nonlinear parts to the modified normal modes of the system.

Following Ref [191], it can be shown that the wavevector of the nonlinear resonator modes $k_m = \omega_m/v$ where $v = 1/\sqrt{L_l C_l}$ for mode m can be determined by solving the transcendental equation

$$k_m = \frac{1}{l} \left[-(k_m l)^2 \frac{C_J}{C_l l} + \frac{L_l l}{L} \right] [\tan(k_m(x_J - l) + \phi_m^+) - \tan(k_m(x_J + l) - \phi_m^-)] \quad (2.88)$$

where the junction is positioned at x_J , the inductance and capacitance per unit length on either side of the junction are considered to be equal, and $\phi_m^{(+,-)}$ are phases parameterized by any external coupling capacitance the waveguide may have at either endpoint which tend to $\frac{\pi}{2}$ as the coupling capacitance goes to zero [191]. For our purposes, we will consider systems which are capacitively coupled on only one end with capacitance C_e to a transmission line which yields an external loss rate as discussed in Sec. 2.2.1.

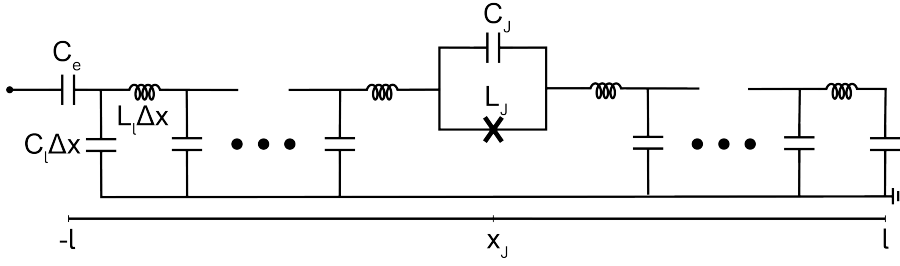


Figure 2.11: A discretized circuit representation of a junction-embedded CPW capacitively coupled on one side to a feedline [191]. The junction is placed at position x_J along a CPW of length $2l$, bridging a gap in the center conductor of the CPW.

While we may determine the frequencies of the modes from the above equation, if we wish to uncover the nonlinearities we must determine the capacitive and inductive participation ratios of the modes of the system. We can define them as

$$\eta_{C,m} = C_J / C_m \quad (2.89)$$

$$\eta_{L,m} = L_m / L_J \quad (2.90)$$

where $C_m = C_{tot} / \Delta u_m^2$ and $L_m = \Delta u_m^2 / (\omega_m^2 C_{tot})$ are determined by the total capacitance of the system C_{tot} and the mode amplitude difference across the junction Δu_m which is calculated for each mode by solving Eq. 2.88 and obtaining the amplitude of the mode at positions immediately on either side of the junction $\{x_J^+, x_J^-\}$. In most cases, we have $C_J \ll C_m$ and so we may take $\eta_{C,m} \rightarrow 0$, in which case the parameter we are most interested in is the inductive participation ratio $\eta_{L,m}$.

We can then find the self-Kerr nonlinearity of a given mode as $K_{mm} = -E_{C,m} \eta_{L,m} / (2\hbar)$ where $E_{C,m} = e^2 / (2C_m)$ and the cross-Kerr coupling between pairs of modes is $K_{mn} = 2\sqrt{K_{mm}K_{nn}}$ which shifts each mode in frequency. While it may seem that the system is directly parameterized by the total capacitance C_{tot} , junction inductance L_J , and position x_J , the calculation for the mode amplitude difference Δu_m is non-trivial and varies strongly with mode number and the boundary conditions of the waveguide. For instance, for the fundamental mode of the system, the self-Kerr nonlinearity converges to $K_{00} = -e^2 / (4C_{tot}\hbar)$ for $L_J \gg L/l$ rather than continuing to grow as L_J is increased. In this limit of dominant Josephson inductance, we can see how the nonlinearity converges to that of a transmon. Indeed, if the total linear inductance is negligible, we recover the transmon qubit, where each section of the CPW center conductor on either side of the junction is effectively an electrode of the transmon. The quintessential double-island transmon qubit can be approximated as a junction-embedded CPW in the limit that the waveguide is made exceptionally short, reducing the linear inductance and capacitance. This recalls the early cavity in-line Cooper-pair box and transmon designs [111, 112, 114, 192].

If we take the limit where $K_{mm} \gg \kappa$, we can recover the initial nonlinear resonator Hamiltonian in Eq. 2.85 where E_C and L are adjusted according to Δu_m for each mode and the Hamiltonian resembles that of a transmon with a non-negligible parallel linear inductance

contribution. Alternatively, in the limit where $K_{mm} < \kappa$, we can realize a weakly nonlinear device which can be well-operated as a parametric amplifier. In the intermediate regime where $K_{mm} \approx \kappa$, we can operate the device as a few-photon quantum parametric oscillator which exhibits photon blockade and can be driven into small coherent and cat states. Later, in Chapter 5, we investigate the dynamics of a junction-embedded CPW in the intermediate or mesoscopic nonlinearity regime subject to parametric driving.

DIMERIZED JOSEPHSON JUNCTION ARRAYS

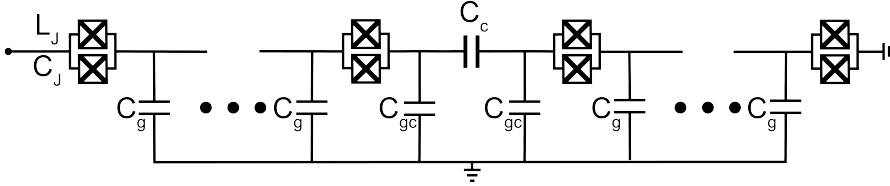


Figure 2.12: A discretized circuit representation of a dimerized Josephson junction array resonator, adapted from Ref. [193]. The square enclosing a cross represents a junction with inductance L_J in parallel with capacitance C_J . Each SQUID has a capacitance to ground C_g , forming a series of islands on either side of a large capacitor with capacitance C_c with capacitance to ground C_{gc} . The resonator is galvanically connected to an external port for measurement at one end and shorted to ground at the other end.

Another useful system to consider is the Josephson junction array resonator, in which a series of N SQUIDs are connected together, each with identical Josephson capacitances and inductances C_J, L_J and capacitances to ground C_g . Following Ref. [193], such a system has a set of normal modes defined by the number of junctions and the values of the capacitances and inductances, as expected for a nonlinear LC oscillator. However, we can additionally separate the array into two halves by adding a large coupling capacitor to the center, with coupling capacitance C_c and capacitance to ground C_{gc} , which *dimerizes* the system, splitting each of the normal modes into two hybridized dimer modes separated from each other by the strength of their coupling, which depends on C_c . Provided that no applied drives induce interactions between the two modes of the circuit, each can be treated as an individual Kerr nonlinear oscillator. Such a system is a natural platform for investigating systems of coupled KNOs as well, in which multiple parametrically driven modes could be used together with coupling drives to investigate the dynamics of linearly coupled Kerr parametric oscillators (KPOs).

This system can be considered in some sense as a variation on the junction-embedded CPW discussed above, under the exchange of series linear inductors L_I to a series of nonlinear junctions with L_J, C_J , and by exchanging the CPW's junction in the center with a large capacitor C_c . We may even similarly define an inductive participation ratio $\gamma_L = L_{J,tot}/(L_{J,tot} + L_S)$ for the fundamental mode where $L_{J,tot}$ is the total nonlinear inductance of the junctions in series while L_S is the linear flux-independent stray geometric and kinetic inductance contributions of the superconducting metal composing the device. In the lumped element model, the frequency of the fundamental mode can then be written as

$$\omega_o(\Phi) = \frac{1}{\sqrt{C_{tot}(L_{J,tot}(\Phi) + L_S)}} \quad (2.91)$$

where C_{tot} is the total capacitance of the device.

However, as we saw with the junction-embedded CPW, the simple approach of the lumped element model is not always applicable. If we wish to determine the Hamiltonian and normal modes of this circuit composed of a series of inductors and capacitors, it is better to start with the Lagrangian written as

$$\mathcal{L} = \frac{1}{2} \vec{\Phi}^T \mathbf{C} \vec{\Phi} - \frac{1}{2} \vec{\Phi}^T \mathbf{L}^{-1} \vec{\Phi} \quad (2.92)$$

where the superconducting phase across the n^{th} junction island ϕ_n determines the node flux $\Phi_n = \frac{\hbar \phi_n}{2e}$ where the node fluxes along the chain can be collected into the flux vector $\vec{\Phi}^T = [\Phi_0 \ \cdots \ \Phi_N]$ and \mathbf{C} , \mathbf{L} are the capacitance and inductance matrices respectively. The Hamiltonian can then be written after performing a Legendre transformation as

$$\mathcal{H} = \frac{1}{2} \vec{Q}^T \mathbf{C} \vec{Q} + \frac{1}{2} \vec{\Phi}^T \mathbf{L}^{-1} \vec{\Phi} \quad (2.93)$$

where $Q_n = \frac{\partial \mathcal{L}}{\partial \Phi_n}$ are the components of the charge vector \vec{Q} . The normal mode frequencies ω_m of the circuit are then determined by solving the eigenequation

$$\mathbf{C}^{-\frac{1}{2}} \mathbf{L}^{-1} \mathbf{C}^{-\frac{1}{2}} \vec{\psi}_m = \omega_m^2 \vec{\psi}_m \quad (2.94)$$

and the eigenvectors $\vec{\psi}_m$ are related to the flux node vector by

$$\vec{\Phi} = \sum_m \mathbf{C}^{-\frac{1}{2}} \vec{\psi}_m \sqrt{\frac{\hbar}{2\omega_m}} (\hat{a}^\dagger + \hat{a}). \quad (2.95)$$

Thus, after determining the inductance and capacitance matrices of the circuit, a Lagrangian can be derived, and after quantizing the circuit, retaining terms to fourth order, and applying the RWA as in Sec. 2.1.3, the system can be represented as a series of cross-Kerr coupled nonlinear oscillators with Hamiltonian given by

$$\mathcal{H}/\hbar = \sum_{m=0}^{N-1} (\omega_m \hat{a}_m^\dagger \hat{a}_m - \frac{K_{mm}}{2} \hat{a}_m^\dagger \hat{a}_m^\dagger \hat{a}_m \hat{a}_m) - \sum_{m \neq n}^{N-1} \frac{K_{mn}}{2} \hat{a}_m^\dagger \hat{a}_m \hat{a}_n^\dagger \hat{a}_n \quad (2.96)$$

where

$$K_{mm} = 2 \frac{\hbar \pi^4}{\Phi_0^4} \frac{E_J \eta_{mmmm}}{C_j^2 \omega_m^2} \quad (2.97)$$

$$K_{mn} = 4 \frac{\hbar \pi^4}{\Phi_0^4} \frac{E_J \eta_{mnnn}}{C_j^2 \omega_m \omega_n} \quad (2.98)$$

where η_{mnnn} is a scaling factor determined from the capacitance matrix and $\vec{\psi}_m$, $\vec{\psi}_n$. By changing N , L_j , and the capacitances, the frequencies and nonlinearities of the device normal modes can be engineered into a variety of parameter regimes, as in the case of the junction-embedded CPW above.

Upon measuring the device spectroscopically, due to the dimerization of each mode induced by the linear coupling of the central capacitor, rather than measuring a mode with frequency ω_m , two modes split by $2J_m$ are observed instead. If the spacing between modes $\Delta_{m,n} =$

$\omega_n - \omega_m$ is large relative to the strength of hybridization J_m induced on each individual mode, we can treat any given dimer as a system of two linearly coupled harmonic oscillators with Hamiltonian

$$\mathcal{H}/\hbar = \omega_1 \hat{a}_1^\dagger \hat{a}_1 + \omega_2 \hat{a}_2^\dagger \hat{a}_2 + J_m (\hat{a}_1^\dagger \hat{a}_2 + \hat{a}_1 \hat{a}_2^\dagger) \quad (2.99)$$

where the observed dimer frequencies are

$$\omega_{m,\pm} = \frac{\omega_1 + \omega_2}{2} \pm \sqrt{\left(\frac{\omega_1 - \omega_2}{2}\right)^2 + J_m^2}. \quad (2.100)$$

Similarly to the case of the junction-embedded CPW, circuits formed by Josephson junction arrays can also be engineered to be operated as parametric amplifiers, with the self-Kerr non-linearity K_{mm} made to be much smaller than the loss rates of each mode κ_m . However, here, a unique driving scheme exists which results in nondegenerate parametric amplification via four-wave-mixing for the dimerized Josephson junction array, in which a strong pump placed between any dimer modes $\omega_{m,\pm}$ will result in gain at both dimer frequencies which coincide with the signal and idler frequencies [193, 194]. This is in contrast to degenerate parametric amplification, in which the signal and idler frequencies fall within the linewidth of a single driven mode [194].

2.2.3. TUNABLE COUPLERS

TUNABLE COUPLINGS WITH SQUIDS

In our discussions of transmon qubits and resonators, we have so far only considered the linear, capacitive coupling and the various regimes associated with the coupling strength relative to other system parameters. However, we may consider what happens when we not only couple two oscillators together capacitively, but also via the nonlinear inductance of the Josephson junction.

We can begin by considering two single-island transmon qubits capacitively coupled by C_C , for which the system Hamiltonian can be written as

$$\mathcal{H} = \hbar\omega_1 \hat{a}^\dagger \hat{a} - \frac{E_{C1}}{2} \hat{a}^\dagger \hat{a}^\dagger \hat{a} \hat{a} + \hbar\omega_2 \hat{b}^\dagger \hat{b} - \frac{E_{C2}}{2} \hat{b}^\dagger \hat{b}^\dagger \hat{b} \hat{b} + J[(\hat{a}^\dagger \hat{b}^\dagger + \hat{a} \hat{b}) - (\hat{a}^\dagger \hat{b} + \hat{a} \hat{b}^\dagger)] \quad (2.101)$$

where the last term gives the capacitive coupling $J = 4E_C^C \hat{n}_1 \hat{n}_2$, \hat{n}_i is the charge number operator for each transmon, and the modified charge energies are given by

$$E_{C1} = \frac{e^2}{2} \frac{C_C + C_2}{C_1 C_2 + C_C(C_1 + C_2)} \quad (2.102)$$

$$E_{C2} = \frac{e^2}{2} \frac{C_C + C_1}{C_1 C_2 + C_C(C_1 + C_2)} \quad (2.103)$$

$$E_C^C = \frac{e^2 C_C}{C_1 C_2 + C_C(C_1 + C_2)} \quad (2.104)$$

so we can write the coupling as

$$J = -E_C^C \left(\frac{E_{J1} E_{J2}}{4E_{C1} E_{C2}} \right)^{1/4} \quad (2.105)$$

which describes the capacitively coupled two-transmon system.

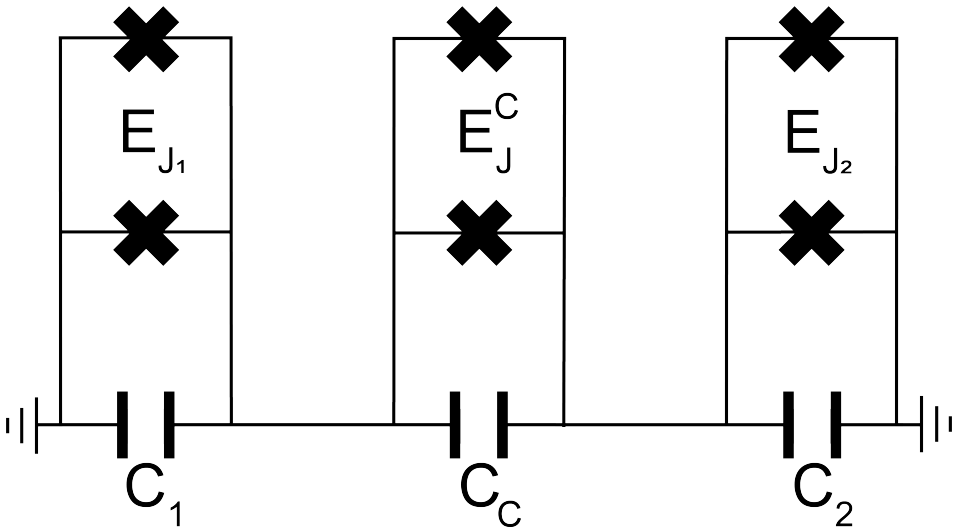


Figure 2.13: A circuit representation of a SQUID tunable coupling between two single-island transmon qubits. Each transmon i has its own capacitance C_i and maximal Josephson energy E_J^i . The transmons are coupled by a flux-tunable SQUID inductance with Josephson energy E_J^C and a fixed capacitance C_C . The negligible junction capacitances are not shown.

If we now additionally couple the transmons via a flux-tunable SQUID placed in parallel to the coupling capacitor, the Hamiltonian gains a nonlinear inductive potential term as $\mathcal{H} \rightarrow \mathcal{H} + \mathcal{H}_S$ where

$$\mathcal{H}_S = -E_J^C \cos(\hat{\delta}_2 - \hat{\delta}_1) \quad (2.106)$$

where E_J^C is the Josephson energy of the coupling SQUID. We can Taylor expand this cosine potential and again retain terms to fourth order, finding that the effect of the SQUID is to modify the linear coupling, add a nonlinear cross-Kerr coupling, and shift the frequencies of the oscillators as we make the following exchanges

$$E_{Ji} \rightarrow E_{Ji} + E_J^C \quad (2.107)$$

$$J_{1,2} = \pm(4E_{J1}E_{J2}E_{C1}E_{C2})^{1/4} \left(\frac{E_J^C}{\sqrt{E_{J1}E_{J2}}} \mp \frac{C_C}{\sqrt{(C_1 + C_C)(C_2 + C_C)}} \right) \quad (2.108)$$

and define the cross-Kerr coupling strength as

$$V = -2E_J^C \sqrt{\frac{E_{C1}E_{C2}}{E_{J1}E_{J2}}} \quad (2.109)$$

to finally obtain the system Hamiltonian

$$\mathcal{H} = \hbar\omega_1 \hat{a}^\dagger \hat{a} - \frac{E_{C1}}{2} \hat{a}^\dagger \hat{a}^\dagger \hat{a} \hat{a} + \hbar\omega_2 \hat{b}^\dagger \hat{b} - \frac{E_{C2}}{2} \hat{b}^\dagger \hat{b}^\dagger \hat{b} \hat{b} + J_1(\hat{a}^\dagger \hat{b} + \hat{a} \hat{b}^\dagger) + J_2(\hat{a}^\dagger \hat{b}^\dagger + \hat{a} \hat{b}) + V \hat{a}^\dagger \hat{a} \hat{b}^\dagger \hat{b} \quad (2.110)$$

where we now have

$$\omega_i = \sqrt{8E_{J_i}E_{C_i}} - E_{C_i} + \frac{V}{2}. \quad (2.111)$$

The presence of the SQUID tunable coupler in the circuit allows the user of the device to tune the transmon frequencies and strengths of the various couplings via the flux-dependent $E_J^C(\Phi)$ and also enables the selective activation of certain couplings under parametric driving, as will be explored in Chapter 4 for a circuit with two double-island transmons. While often the off-resonant $\hat{a}^\dagger \hat{b}^\dagger + \hat{a} \hat{b}$ *two-mode squeezing* interaction is neglected, here it is retained due to the fact that we will be able to activate it under parametric flux modulation of the coupler SQUID.

TUNABLE COUPLINGS WITH SNAILS

Another useful tool that we have at our disposal when designing quantum circuits is the Superconducting Nonlinear Asymmetric Inductive Element (SNAIL) [195]. The SNAIL is, in some sense, an extension of the SQUID, in which one arm of the superconducting loop contains n junctions with energy E_J and the other arm contains only one junction with energy ηE_J where η is a scaling factor. The effect of this modification is to create an asymmetric potential dependent on n and η , which can be chosen to engineer previously difficult-to-control system parameters, especially those related to nonlinear interactions such as the cross-Kerr and optomechanical couplings. The inductive energy of the SNAIL is given by

$$U_L = -E_J \left[\eta \cos(\hat{\delta}) + n \cos\left(\frac{\Phi - \hat{\delta}}{n}\right) \right] \quad (2.112)$$

where Φ is the applied flux through the superconducting loop in units of $\frac{2\pi}{\Phi_0}$ and $\hat{\delta}$ is the phase operator, with the above potential valid for $E_J \gg \frac{e^2}{2C_J}$ and $\frac{C_J}{n^2} \gg C_g$ where C_J is the capacitance of each junction and C_g is the capacitance of the SNAIL electrode(s) to ground.

The utility of the SNAIL in quantum circuits becomes apparent after Taylor expanding the inductive potential about a minimal phase difference δ_m and defining the effective phase operator $\tilde{\delta} = \hat{\delta} - \delta_m$, in which case we can reorganize the inductive potential in order of $\tilde{\delta}$ as

$$U_L = c_1 \tilde{\delta} + c_2 \tilde{\delta}^2 + c_3 \tilde{\delta}^3 + c_4 \tilde{\delta}^4 \quad (2.113)$$

where

$$c_1 = E_J (\eta \sin(\delta_m) - \sin\left(\frac{\Phi - \delta_m}{n}\right)) \quad (2.114)$$

$$c_2 = \frac{E_J}{2} (-\eta \cos(\delta_m) + \frac{1}{n} \cos\left(\frac{\Phi - \delta_m}{n}\right)) \quad (2.115)$$

$$c_3 = \frac{E_J}{6} (-\eta \sin(\delta_m) + \frac{1}{n^2} \sin\left(\frac{\Phi - \delta_m}{n}\right)) \quad (2.116)$$

$$c_4 = \frac{E_J}{24} \left(-\eta \cos(\delta_m) - \frac{1}{n^3} \cos\left(\frac{\Phi - \delta_m}{n}\right) \right). \quad (2.117)$$

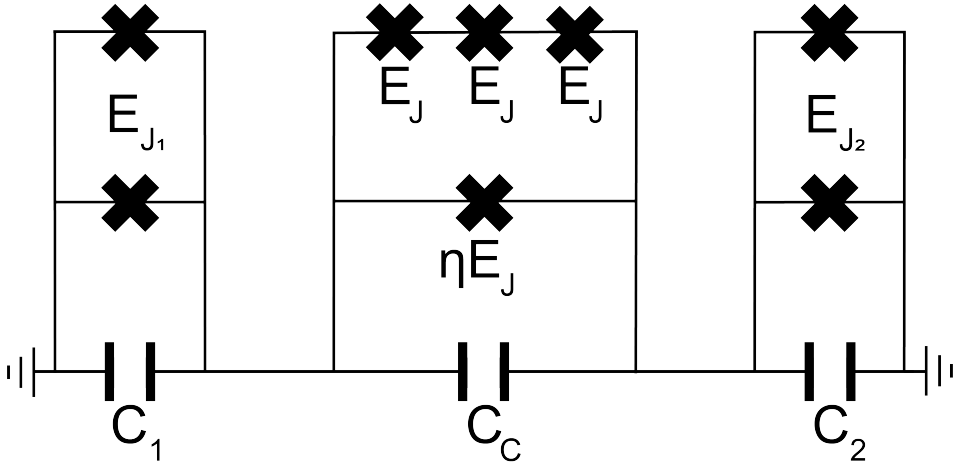


Figure 2.14: A circuit representation of a SNAIL tunable coupling between two single-island transmon qubits for the case $n = 3$. Similarly to the SQUID tunable coupler, each transmon i has its own capacitance C_i and maximal Josephson energy E_J^i . The transmons are coupled by a flux-tunable SNAIL inductance, with each junction having Josephson energy E_J and a fixed capacitance C_C . The small junction capacitances and individual capacitances of the SNAIL electrodes to ground are not shown.

We can immediately see that in comparison to the inductive potential from Eq. 2.41, we now have terms which are linear and cubic in $\tilde{\delta}$. Further, given that each of the parameters c_i have two terms with two degrees of freedom, we would expect to be able to engineer a wide variety of inductive potentials.

Similarly to the case of the SQUID coupler, we may take two transmons and couple them together via a capacitor C_C and a SNAIL with inductive energy U_L and exchanging $\tilde{\delta} \rightarrow \tilde{\delta}_2 - \tilde{\delta}_1$, as before. Following the same procedure, while the full Hamiltonian is extensive, some of the more interesting terms indicate that we will again have interactions $(\hat{a}^\dagger \hat{b} + \hat{a} \hat{b}^\dagger)$ and $(\hat{a}^\dagger \hat{b}^\dagger + \hat{a} \hat{b})$ which scale with c_2 , as well as interactions $(\hat{a}^{\dagger 2} \hat{b} + \hat{a}^2 \hat{b}^\dagger)$, $(\hat{a}^{\dagger 2} \hat{b}^\dagger + \hat{a}^2 \hat{b})$, and $\hat{a}^\dagger \hat{a}(\hat{b}^\dagger + \hat{b})$ (plus equivalent terms under exchange of \hat{a} , \hat{b}) which scale with c_3 . While many of the higher-order interactions are typically far off-resonant and negligible, there are driving schemes which can activate these terms. The term $\hat{a}^\dagger \hat{a}(\hat{b}^\dagger + \hat{b})$ often arises in the field of quantum optomechanics, in which the occupation of one mode drives the coupled mode in a *radiation pressure* or *photon pressure* interaction, which is useful for designing quantum circuits which emulate the physics of optomechanical systems [196, 197]. In a similar manner to the parametric driving with a SQUID coupler shown in Chapter 4, one would be able to activate these SNAIL-enabled interaction terms by the use of flux modulation.

One of the more frequently stated use-cases for SNAIL-based devices is the ability to minimize c_4 in order to remove the cross-Kerr interaction in circuits which is often unwanted, especially when one is trying to perform two-qubit gates specifically enabled by linear couplings between

qubits. Interestingly, with the appropriate choice of E_J , n , and η , it is possible to design c_4 to be positive, zero, or negative, which means that one may engineer devices with positive self-Kerr nonlinearities as well [195, 198, 199]. Lastly, parametric amplifiers based on SNAILS rather than SQUIDs have also been proposed, given the possibilities enabled by the engineerable asymmetric inductive potential [200, 201].

2

2.3. PARAMETRIC DRIVING

2.3.1. PARAMETRICALLY DRIVEN OSCILLATORS

THE VERTICALLY DRIVEN PENDULUM

While we previously discussed driven oscillators in Sec. 2.1.2, we only considered systems linearly driven at and around the resonant frequency of the oscillator. However, it is just as possible for us to drive an oscillator by varying a parameter of the system. For instance, for the case of a mass-spring system, instead of forcing along its axis of movement resonantly, what happens if we vary the spring constant of the system as a function of the resonance frequency? Or, what happens if the damping varies periodically?

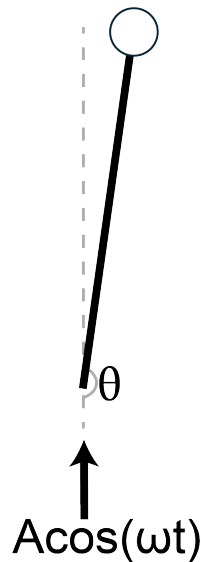


Figure 2.15: A diagram depicted a vertically driven pendulum. An oscillating drive $A \cos(\omega t)$ is applied, which modulates the position of the pivot point of the pendulum at a frequency ω .

A nice example is the classic pendulum, in which the most commonly observed stable position is for the mass at the end of the pendulum to be positioned downwards at $\theta = 0$ due to the force of gravity. However, if the system is driven not along its axis of rotation but rather if the pivot point of the pendulum itself is driven to oscillate up and down at a given frequency, a stable point at $\theta = \pi$ can emerge for certain values of driving amplitude and frequency.

Following Ref. [202–206], the equation of motion of the vertically driven pendulum is given as

$$\frac{d^2\theta}{dt^2} + (\omega_0^2 + A \cos(\omega t)) \sin(\theta) = 0 \quad (2.118)$$

which is the form of a damped parametric oscillator. For small θ such that $\sin \theta \approx \theta$, the differential equation has the form of the well-known Mathieu equation for which the solutions are Mathieu functions [207–210]. With the addition of a damping term $\gamma \frac{d\theta}{dt}$, the above equation can be rewritten under the substitution $\theta = \phi e^{-\gamma t/2}$ as

$$\frac{d^2\phi}{dt^2} + (\omega_0^2 - \gamma^2/4 + A \cos(\omega t))\phi = 0. \quad (2.119)$$

This particular system is stabilized upside-down at $\theta = \pi$ for $A > \sqrt{2\omega_0^2 \frac{(\omega^2 + \omega_0^2)^2 + \gamma^2 \omega^2}{\omega^2 + \omega_0^2}}$. Conversely, we can consider the problem as one of destabilizing a downwards-oriented pendulum if we consider those driving parameters which cause $\theta = 0$ to be an unstable point. The system can be mapped out entirely in terms of the drive parameters A and ω to identify where regions of stability and instability (also known as *Arnold tongues*) exist [211–213].

The regions in which the system is unstable are those in which the *parametric resonance condition* of integer n^{th} order is met. With damping, the instability regions are pushed to stronger drive amplitudes and stable frequencies with stronger driving are made possible when those same drive parameters would lead to instability in the undamped case.

THE PARAMETRICALLY DRIVEN DUFFING OSCILLATOR

In our description of the parametrically driven Duffing oscillator, we can build on Eq. 2.119 by following Ref. [214]. We start by adding the Duffing nonlinearity term from Sec. 2.1.2, as well as a nonlinear damping term, yielding the equation of motion for 2ω driving as

$$\frac{d^2x}{dt^2} + \omega_0^2(1 - \lambda \cos(2\omega t))x + \gamma \frac{dx}{dt} + \alpha x^3 + \eta x^2 \frac{dx}{dt} = 0 \quad (2.120)$$

where $\lambda = A/\omega_0^2$ is the scaled driving amplitude, η is the nonlinear damping coefficient, α is the Duffing nonlinearity, and γ is the linear damping coefficient. We can recast this equation in terms of dimensionless parameters under the substitutions $y = \sqrt{\frac{\alpha}{\omega_0}} x$ and $\tau = \omega_0 t$ to obtain

$$\frac{d^2y}{d\tau^2} + (1 - \lambda \cos(2\Omega\tau))y + \tilde{\gamma} \frac{dy}{d\tau} + y^3 + \tilde{\eta} y^2 \frac{dy}{d\tau} = 0 \quad (2.121)$$

where $\Omega = \omega/\omega_0$, $\tilde{\gamma} = \gamma/\omega_0$, $\tilde{\eta} = \eta\omega_0/|\alpha|$ are all rescaled dimensionless parameters.

While the above equation is nontrivial to solve, there do exist several stable solutions from which we can derive stability diagrams as a function of drive amplitude and frequency, as in the case of the vertically driven pendulum. One can apply the van der Pol transformation and *averaging theorem* to this equation to obtain two *slow-flow* equations in rotating frame coordinates (u, v) . We then have $x = u \cos(\omega t) - v \sin(\omega t)$ which can be solved to determine the steady states of the oscillator, where $\frac{du}{dt} = \frac{dv}{dt} = 0$ and the amplitude response is given by $|X| = \sqrt{u^2 + v^2}$. This averaging approach is analogous to our previous application of the RWA, in that we are deriving equations that describe the dynamics of our system on long timescales

and neglecting any contributions that average out over multiple periods of oscillations. One can then obtain the coupled equations

$$\frac{du}{dt} = -\frac{1}{2\Omega} [\tilde{\gamma}\Omega u + v(\Delta_0 + \frac{\lambda}{2}) + \frac{3}{4}(u^2 + v^2)v + \Omega \frac{\tilde{\eta}}{4}(u^2 + v^2)u] \quad (2.122)$$

$$\frac{dv}{dt} = -\frac{1}{2\Omega} [\tilde{\gamma}\Omega v + u(-\Delta_0 + \frac{\lambda}{2}) - \frac{3}{4}(u^2 + v^2)u + \Omega \frac{\tilde{\eta}}{4}(u^2 + v^2)v] \quad (2.123)$$

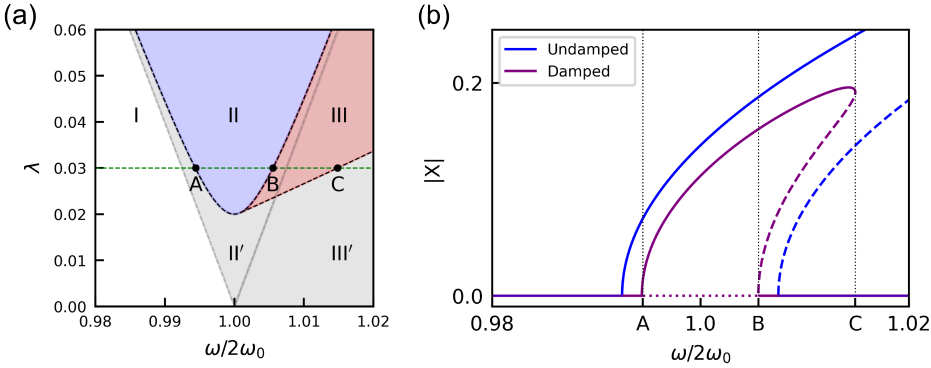


Figure 2.16: Characteristic response of the parametrically driven Duffing oscillator. a) A phase diagram with different parametric response regions indicated for $\tilde{\eta} = 0.5$ and $\tilde{\gamma} = 0.01$. In Region I, the system has one zero-amplitude solution (monostable). In Region II (bistable), there are two stable phase states and one unstable (the zero-amplitude) solutions. In Region III (tristable) there are three stable (the zero-amplitude and two stable phase states), and two unstable solutions. Regions II' and III' are the bistable and tristable regions in the absence of dissipation. b) The oscillator response for driving amplitude $\lambda = 0.03$, indicated by the green dashed line in a). The damped oscillator with $\tilde{\eta} = 0.5$ and $\tilde{\gamma} = 0.01$ is bistable between points A and B and tristable between B and C. Between A and B, the zero-amplitude response is represented by a dotted line, which indicates that it is not a stable solution in the bistable region. At low driving frequencies, both oscillator steady-states are given by the zero-amplitude solution alone. The tristable region for the undamped oscillator ($\tilde{\eta} = \tilde{\gamma} = 0$) extends beyond the point C.

where $\Delta_0 = 1 - \Omega^2$. The above slow-flow equations are valid for small damping, nonlinearity, and drive amplitude relative to the oscillator resonance frequency, which, in the case of the several gigahertz frequency Duffing oscillators studied in later sections, generally holds true. Luckily, there are several analytical solutions to the equation $\frac{du}{dt} = \frac{dv}{dt} = 0$, including one trivial zero-amplitude solution in which $u = v = 0$. The five (lengthy) expressions for the amplitude responses are shown in Appendix A.1.

The simplest stability region (for the zero-amplitude solution) is defined by drive amplitudes $\lambda < \lambda_{th}$ where

$$\lambda_{th} = 2\sqrt{(\Omega\tilde{\gamma})^2 + \Delta_0^2} \quad (2.124)$$

which bears a strong resemblance to the parametric threshold at which gain diverges for Josephson Parametric Amplifiers (JPAs)

$$\lambda_{th,JPA} = \sqrt{k^2/4 + \Delta^2} \quad (2.125)$$

where there, $\Delta = \omega_0 - \omega/2$ and κ is the total loss rate [215]. When operating such a device to produce gain, the JPA is parametrically driven close to, but below, the parametric threshold such that gain is produced before instability.

Beyond λ_{th} , the zero-amplitude state becomes unstable, and the oscillator undergoes a pitchfork bifurcation, yielding two bistable solutions separated from each other in phase space by π radians [216]. Given the presence of nonlinear damping and Duffing nonlinearity, there exists another parametric threshold defined by

$$\lambda_{th,\eta} = \frac{2\Omega|3\gamma + \eta(\Omega^2 - 1)|}{\sqrt{\eta^2\Omega^2 + 9}} \quad (2.126)$$

which occurs for detuned parametric drives with the same sign as that of the nonlinearity, in which the zero-amplitude state exists along with the bistable states, while there also exists a pair of unstable states π shifted in phase. This region is known as the tristable regime, given that the two bistable states and the zero-amplitude state are stable solutions.

The ability to generate multistable states in parametrically driven Duffing oscillators is of key importance for later chapters, in which we parametrically drive our quantum circuits beyond these thresholds. For example, in Chapter 6 we explore the bistable regime and demonstrate control over the dynamics of the bifurcating system while in Chapter 7 we drive a Duffing oscillator through the multistable regimes described above and into chaos.

2.3.2. MODULATED NONLINEAR INDUCTANCE IN A QUANTUM CIRCUIT

BICHROMATIC DRIVING AND FLUX MODULATION

While one may implement a parametric drive on a pendulum by oscillating its pivot point vertically, if we instead wish to parametrically drive superconducting quantum circuits, a straightforward way to do so is via the nonlinear inductance of the Josephson junction [215]. Given Eq. 2.28 -2.30, we can express the nonlinear inductance of the junction in terms of the current and flux as

$$L = L_J \left[1 + \frac{1}{6} \left(\frac{I}{I_c} \right)^2 + \dots \right] = L_J \left[1 + \frac{1}{2} \left(2\pi \frac{\Phi}{\Phi_0} \right)^2 + \dots \right] \quad (2.127)$$

where we may then modulate the nonlinear inductance via control over the current and/or flux. Given that the quantum circuits discussed so far have inductance-dependent frequencies, current or flux driving of these devices at $I = I_a \cos(\omega_d t + \phi)$ or $\Phi = \Phi_a \cos(\omega_d t + \phi)$ will lead to a time-dependent modulation of the oscillator inductance (and thus frequency) as a function of ω_d .

We may first consider the case of modulating the inductance of a Josephson junction-based Kerr oscillator with resonance frequency ω_0 and self-Kerr nonlinearity K as in Eq. 2.45. If we choose to apply two microwave drives with frequencies ω_1 and ω_2 , such that $\Delta_{12} = \omega_1 - \omega_2$ and $\delta = \omega_0 - \frac{(\omega_1 + \omega_2)}{2}$ (thus, $\omega_1 + \omega_2 = 2\omega_0$ for $\delta = 0$), one of the results of this pumping scheme is to generate a *two-photon pumping* term $\frac{\epsilon_2}{2} \hat{a}^{\dagger 2} + \frac{\epsilon_2^*}{2} \hat{a}^2$ where $\epsilon_2 = 4K\alpha_1\alpha_2$ is the parametric pump strength and α_i are the classical pump field amplitudes [215]. Compared to a single microwave drive on resonance at ω_0 , in this *bichromatic driving* scheme (named due to the presence of two drives of different frequencies), we are able to separate the pumps from the oscillator spectrally [215, 217]. This simplifies analysis of the oscillator response for large values of Δ_{12} relative to ϵ_2 , given that we may set our measurement bandwidth to capture only the system

dynamics of interest and exclude the presence of our applied drives and higher-order effects, which would not be straightforward if we instead applied a single near-resonant microwave drive to realize a parametric pump.

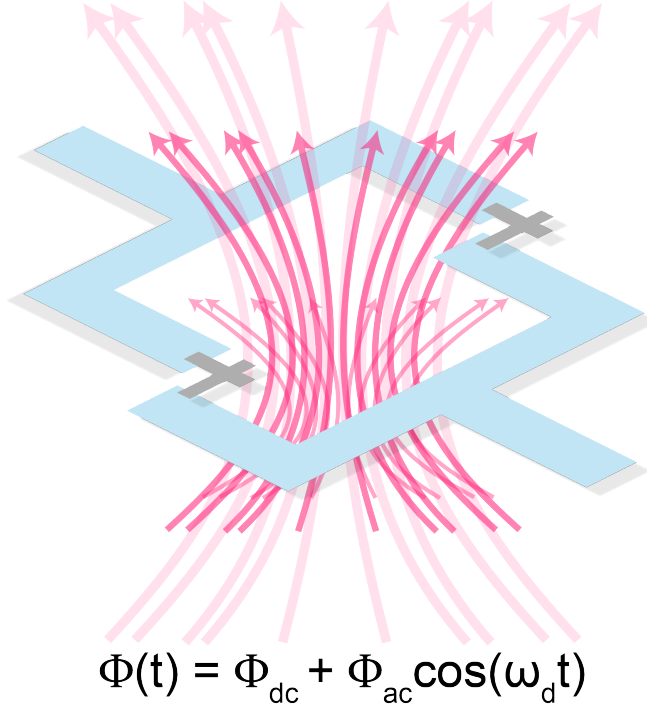


Figure 2.17: An illustration of a SQUID loop being parametrically driven via flux modulation. The loop formed by superconducting metal (blue) and two Josephson junctions in parallel (grey) is threaded by a magnetic field with a static component and a time-dependent component. The time-dependent component modulates the amplitude of the flux threading the loop at a frequency ω_d .

Similarly, if the flux we apply to the oscillator's SQUID loop is composed of a static and time-dependent component $\Phi(t) = \Phi_{dc} + \Phi_{ac} \cos(\omega_d t)$ and we set the modulation frequency $\omega_d = 2\omega_0$, we will again generate a two-photon pumping term with $\epsilon_2 = -2E_J \Phi_{ac} \sin(\Phi_{dc}) \frac{E_C}{\omega_0}$ [215]. In the case of a SQUID tunable coupler connecting two frequency-detuned oscillators ω_A and ω_B , flux modulation of the coupler at the sum and difference frequencies $\omega_A \pm \omega_B$ can selectively activate either the beam-splitter or two-mode squeezing interactions respectively, as will be shown in Chapter 4. In the case of a SNAIL coupler, the flux can be modulated at various frequencies to activate higher-order interactions, such as the optomechanical photon-pressure coupling and to induce multi-photon transitions between the oscillators.

In the language of the classical parametrically driven Duffing oscillator, the consequence of applying these microwave and flux drives in such a way to modulate the inductance of the oscillator at twice its resonance frequency is to drive the system towards first-order parametric resonance. The application of this two-photon pump to quantum Duffing (or Kerr) oscilla-

tors can be used to generate gain or, upon stronger driving, push the oscillator beyond the parametric threshold into multistable regimes. In Chapters 5, 6, and 7, we show the driving of a quantum circuit below, into, and beyond the multistable regimes discussed above and demonstrate phase control of the oscillator state in the bistable regime.

3

DEVICE DESIGN AND FABRICATION

*Thou shouldst not have been old
till thou hadst been wise.*

William Shakespeare

In this chapter we outline the process necessary for building a quantum circuit. In order to construct a quantum circuit, one must progress through multiple levels of abstraction - from the device as a quantum system (the Hamiltonian level), to the device as a circuit (the circuit representation level), to the device as a multidimensional simulacrum with defined physical properties (the multiphysical model level), and lastly to the device as a material object (the fabrication level). As we move from abstraction to reality, the idealities we impose on the mathematical modeling of our system at the Hamiltonian level are always at risk of degrading if we fail to account for the effects of additional physical processes at subsequent levels. The goal is to have at the end of the process fabricated a quantum circuit from which one can acquire measurement data unveiling exciting physical phenomena that can be analyzed and interpreted with mathematical models.

3.1. DESIGN AND SIMULATION

3.1.1. QUTIP

The first step in designing a quantum circuit is determining which physical parameters to engineer. While we may now know what the resonance frequency and anharmonicity of a transmon qubit are for a given set of capacitances and inductances, we should first decide what we want those values to actually be. For example, we may wish to understand the system consisting of a CPW capacitively coupled to an external feedline on one side and a transmon qubit on the other. In this case, the system Hamiltonian is as in Eq. 2.76, given by

$$\mathcal{H} = \hbar\omega_r \hat{a}^\dagger \hat{a} + \hbar\omega_q \hat{b}^\dagger \hat{b} - \frac{E_C}{2} \hat{b}^\dagger \hat{b}^\dagger \hat{b} \hat{b} + \hbar g (\hat{a}^\dagger \hat{b} + \hat{a} \hat{b}^\dagger) \quad (3.1)$$

along with total resonator and transmon loss rates κ , γ respectively. How do the transmon and resonator exchange interactions over time with the inclusion of collapse operators? If we want to understand the dynamics of this system and explore the consequences of varying the ratios of these parameters, it is useful to first simulate it before starting to construct the circuit itself.

Alternatively, we may want to simulate the interactions between two transmons which are connected via a SQUID tunable coupler, as in Eq. 2.110

$$\mathcal{H} = \hbar\omega_1 \hat{a}^\dagger \hat{a} - \frac{E_{C1}}{2} \hat{a}^\dagger \hat{a}^\dagger \hat{a} \hat{a} + \hbar\omega_2 \hat{b}^\dagger \hat{b} - \frac{E_{C2}}{2} \hat{b}^\dagger \hat{b}^\dagger \hat{b} \hat{b} + J_1 (\hat{a}^\dagger \hat{b} + \hat{a} \hat{b}^\dagger) + J_2 (\hat{a}^\dagger \hat{b}^\dagger + \hat{a} \hat{b}) + V \hat{a}^\dagger \hat{a} \hat{b}^\dagger \hat{b}. \quad (3.2)$$

As another example, in order to produce a Josephson cavity which can be driven with a two-photon pump beyond the parametric threshold, what should the resonance frequency, non-linearity, and linewidth be? Then, in the frame of the resonant two-photon pump, we have

$$\mathcal{H}_{rot} = K \hat{a}^\dagger \hat{a}^\dagger \hat{a} \hat{a} + \epsilon_2 (\hat{a}^{\dagger 2} + \hat{a}^2). \quad (3.3)$$

What responses do we expect to be displayed on laboratory instruments upon measuring such devices?

The Quantum Toolbox in Python (QuTiP) is a Python library which contains a variety of objects and functions which are useful for simulating quantum systems [218]. QuTiP can be straightforwardly used to take a Hamiltonian and construct energy level diagrams, investigate the time evolution with loss channels and time-dependent drives, and visualize the state of a system in many ways, such as on the Bloch sphere, with Wigner functions or by its emission spectrum. In this thesis, QuTiP was always used when designing new devices in order to understand what parameters we should be targeting once we start the fabrication process and to have a foundation for what to expect upon measurement.

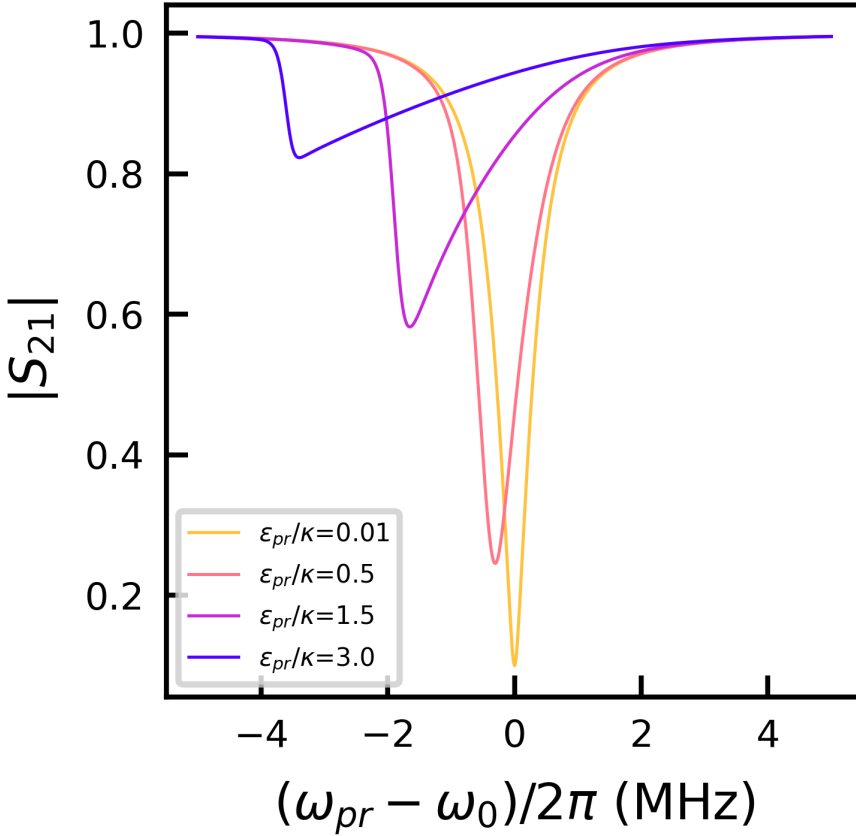


Figure 3.1: The simulated transmission coefficient $|S_{21}|$ for a Kerr oscillator under a range of applied probe powers side-coupled to a measurement feedline.

We now proceed with a few illustrative examples. We can start by simulating the expected transmission coefficient when probing the state of a Kerr oscillator in a side-coupled transmission geometry. This system may be realized by an on-chip $Z_0 = 50\Omega$ transmission line to which a junction-embedded CPW is capacitively coupled at one end and shorted to ground via a junction at the other. In this case, we consider a fundamental mode frequency of $\omega_0 = 5$ GHz and a self-Kerr nonlinearity of $K = -200$ kHz, with $\kappa_e = 0.9$ MHz and $\kappa_i = 0.1$ MHz. We can write the system Hamiltonian in the rotating frame of a weak probe tone of strength ϵ_{pr} and frequency ω_{pr} by

$$\mathcal{H} = (\omega_0 - \omega_{pr})\hat{a}^\dagger\hat{a} + K\hat{a}^\dagger\hat{a}^\dagger\hat{a}\hat{a} + i\epsilon_{pr}(\hat{a}^\dagger - \hat{a}) \quad (3.4)$$

and solve for the steady-state of the system under single-photon loss \hat{a} at rate κ_{tot} implemented as a Lindbladian collapse operator [219]. We could also consider the collapse operators of an oscillator coupled to a thermal bath, but here we assume that $\hbar\omega \gg k_B T$ and thus the thermal occupation of the mode we are interested in is $n_{th} = (e^{\hbar\omega/k_B T} - 1)^{-1} \approx 0$, as

would be the case for GHz circuits thermalized to the $\approx 10\text{-}20$ mK plates of dilution refrigerators. We can then sweep ω_{pr} about ω_0 and calculate the expectation value of \hat{a} and find $|S_{21}| = 1 - \langle \hat{a} \rangle \frac{\kappa_e}{2\epsilon_{pr}}$, given the simulated steady-state of the system ρ_{ss} , which is displayed in Fig. 3.1 for various probe powers [220]. QuTiP then yields the theoretically expected response - as the probe power increases (and thus, the number of photons in the oscillator increases as a function of the proximity of the probe to the oscillator frequency), the resonance frequency shifts proportional to the self-Kerr nonlinearity and at strong enough driving the oscillator exhibits a "shark fin" shape indicative of bifurcation. We may relate the probe strength to power via

$$\epsilon_{pr} = \sqrt{\frac{\kappa_e P_{pr}}{\hbar \omega_{pr}}} \quad (3.5)$$

where P_{pr} is the incident power at the device and can be related to the number of photons in the oscillator mode by

$$\langle n \rangle = \frac{\kappa_e}{\left(\frac{\kappa_{tot}}{2}\right)^2 + (\omega_{pr} - \omega_0)^2} \langle n_{pr} \rangle \quad (3.6)$$

where $\langle n_{pr} \rangle = \frac{P_{pr}}{\hbar \omega_{pr}}$ is the number of photons applied at the device input [221, 222]. Thus, a simple QuTiP simulation can quickly be used to aid in preparing one's experimental setup to facilitate delivering an appropriate amount of photons to the circuit given a set of design parameters, but can also be used as an analysis tool to determine unknown device parameters upon measurement (in this instance, with a VNA).

Our second example is that of the Kerr oscillator under a two-photon drive, as in Eq. 3.3. We can use QuTiP to calculate the expectation value of the photon number operator and Wigner function of the simulated state as a function of time $\rho(t)$, again under single-photon loss at rate κ_{tot} . The Wigner function is a quasi-probability distribution which describes the state of a quantum system in phase space, with quadratures x and p [223, 224]. Working in units where $\omega_0 = 5$ and the two-photon drive frequency is set to $\omega_d = 2\omega_0$, we set $\kappa_{tot} = 1/1000$, $K = -\kappa_{tot}/2$, and $\epsilon_2 = -5K$ and obtain the mode's photon number expectation value $\langle n \rangle$ as well as the Wigner function associated with $\rho(t)$ shown in Fig. 3.2, 3.3.

This system is closely related to the parametrically driven Duffing oscillator, as can be seen by the Wigner function of the steady state of the system in the bottom-right panel of Fig. 3.2. The oscillator steady-state under sufficiently strong two-photon driving is that of a parametrically driven Duffing oscillator in the bistable regime, represented by two displaced coherent states of equal amplitude and opposite phase.

Given our choice of parameters, the approximation of the Duffing oscillator as a Kerr oscillator here holds true. Indeed, we can shift our drive ω_d from resonance with $2\omega_0$ to being detuned by a negative value δ to observe a tristable state and to observe the zero-amplitude state we may either decrease our two-photon pump strength or detune to sufficiently positive frequencies (the opposite sign of the nonlinearity), as shown in Fig. 3.4. We may also replace the self-Kerr term with the full Duffing nonlinearity $K'(\hat{a}^\dagger + \hat{a})^4$ and set $K' = -\kappa_{tot}/12$ and obtain similar results to the bistable Kerr oscillator.

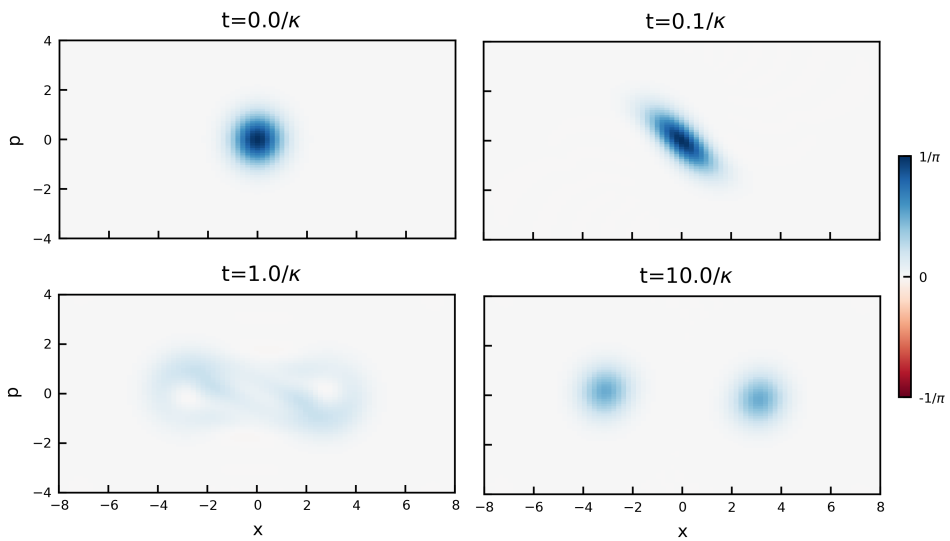


Figure 3.2: The Wigner function of a Kerr nonlinear oscillator over the course of its time evolution under two-photon driving.

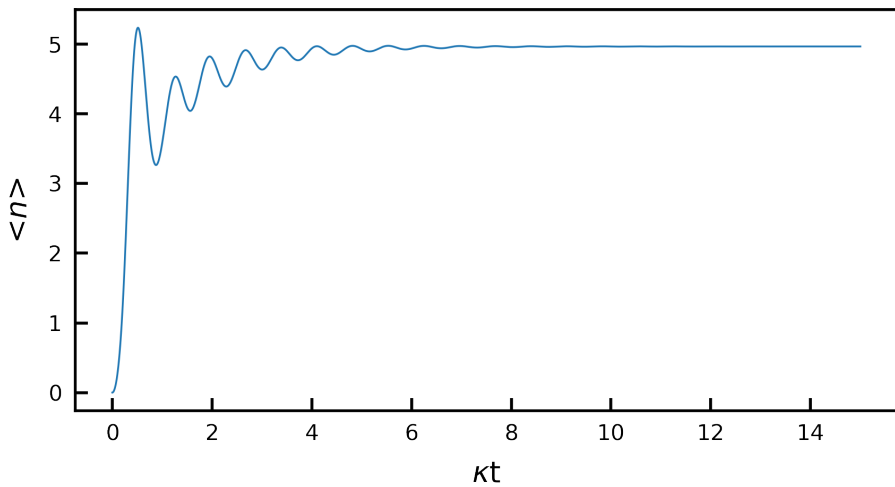


Figure 3.3: The time-dependent expectation value of the photon number operator of a parametrically driven Kerr nonlinear oscillator.

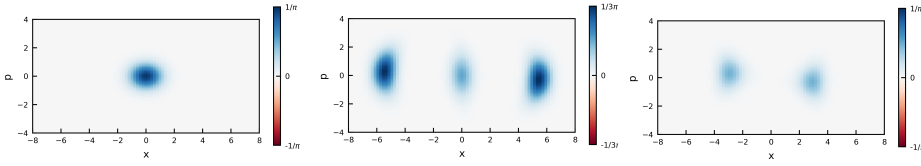


Figure 3.4: Wigner functions of the steady state of a two-photon driven Kerr (Duffing) oscillator when in the various stability regimes. When considering a Kerr oscillator, the left panel is the zero-amplitude state for $\delta = 0.02$, and the center panel is for the tristable state $\delta = -0.01$. The right panel is the bistable state for an oscillator with an explicit Duffing nonlinear term.

3

3.1.2. QUACAT

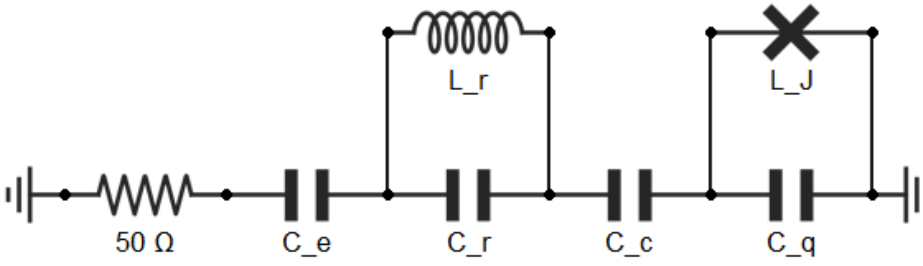


Figure 3.5: A lumped element circuit generated with QuCAT of a transmon qubit capacitively coupled to a resonator with a $Z_0 = 50\Omega$ feedline.

If we proceed with the resonator-transmon system as an example, the next step in designing a device is to translate the frequencies and couplings into capacitances and inductances. To this end, we can use the Quantum Circuit Analyzer Tool (QuCAT), which is a high-level Python library with which a user can draw RLC circuits, input values, and extract their expected frequencies, loss rates, couplings, and nonlinearities [225]. We can start by drawing a lumped element circuit representation of a $\frac{\lambda}{2}$ CPW resonator capacitively coupled to a transmon qubit and a $Z_0 = 50\Omega$ transmission line, as shown in Fig. 3.5.

Once this circuit has been drawn, the user can input capacitance and inductance values to calculate the eigenfrequencies and nonlinearities of each normal mode of the circuit. Each of these circuit parameters can be iterated over, allowing the user to sweep over variables of interest to see how the circuit is changed. For example, when sweeping the Josephson inductance of a transmon qubit (as one may do by varying the magnetic flux through a transmon's SQUID loop), the qubit frequency can be swept through the resonator frequency which gives rise to an avoided crossing related to the linear coupling between the resonator and transmon. We can also plot the self-Kerr nonlinearities of the resonator and transmon, as well as the cross-Kerr coupling, as a function of swept Josephson inductance and note that when the modes strongly hybridize the resonator inherits nonlinearity from the transmon, as was discussed in Sec. 2.2.1.

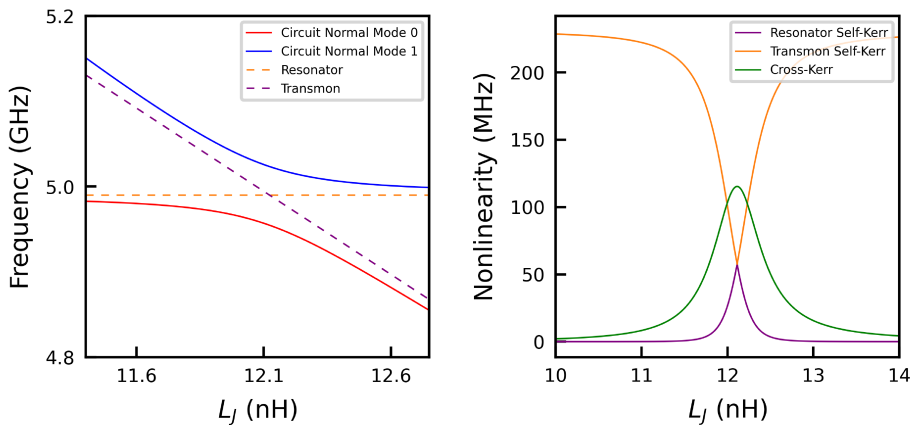


Figure 3.6: The calculated frequencies and nonlinearities of the circuit in Fig. 3.5 for a range of junction inductance values L_j with other circuit parameters fixed.

3.1.3. QISKIT METAL AND ANSYS HFSS

Once we know our desired capacitances and inductances, the last step is to "physicalize" our circuit by actually constructing waveguides and electrodes. From our discussions on transmission lines, we have some inclination as to what the waveguide capacitance and inductance per unit length will be given the widths of the center conductor and gaps as well as the properties of selected materials given Eq. 2.63 - 2.69, but so far we do not have any intuition as to how a transmon should be physically represented on a chip. While we know that we need an electrode (or two) and capacitances to ground and to our CPW, we don't yet have any understanding of how the representation of the resonator-transmon system relates to its existence in physical space. Thus, we require a way to construct the geometries which we wish to later pattern on a chip in a file format that will be understandable by the nanofabrication machines we will use to do so, as well as a simulation software capable of telling us whether our chip layout matches to what we would like to make after our conclusions from theoretical equations and QuTiP and QuCAT simulations.

Luckily, there exists a Python library developed by IBM Quantum named Qiskit Metal, which can be used to construct such chip layouts in the form of `.gds` files, with the added bonus of being able to easily interface with the multiphysics simulation software Ansys HFSS [226, 227]. After programmatically drawing a circuit with Qiskit Metal, we can use HFSS to determine the eigenfrequencies of the normal modes of the system after defining the properties of the intended materials, such as relative permittivity and surface inductance. We can also determine the capacitance matrix of any set of elements being simulated by *lumped oscillator model* (LOM) calculations, as well as use the results of the eigenmode simulation with the Python library `pyEPR` to determine the self- and cross-Kerr nonlinearities as well as the capacitive and inductive participation ratios [228].

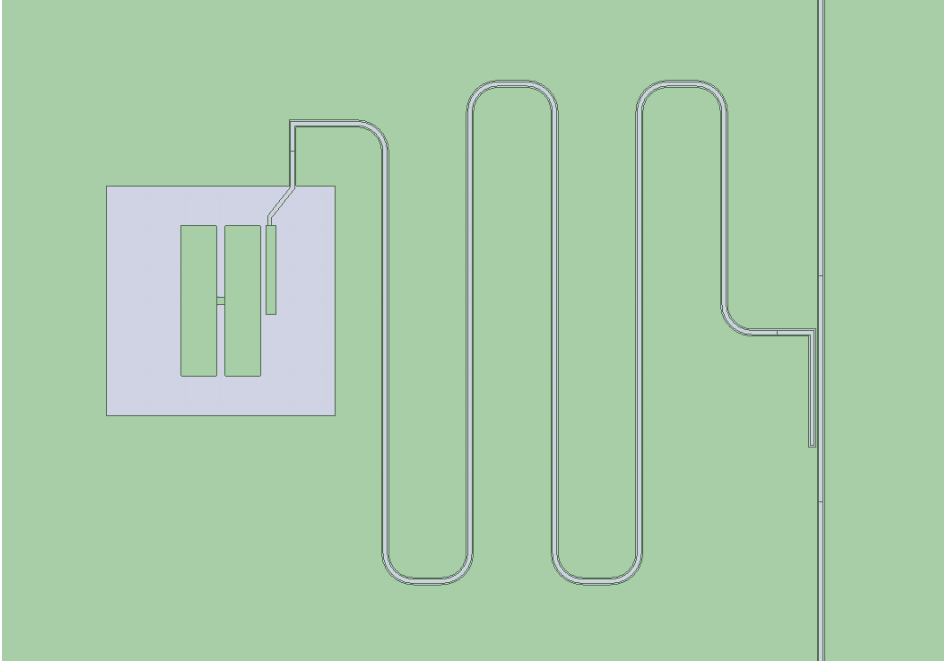


Figure 3.7: A resonator-transmon system programmatically defined in Qiskit Metal and rendered in Ansys HFSS.

As an example, we may follow the process of designing a resonator-transmon system using Qiskit Metal and HFSS. After defining the geometry of $Z_0 = 50\Omega$ transmission lines following the equations in Sec. 2.2.1 taking into account an expected surface inductance of $L_s = 0.98$ pH for a 100nm thick NbTiN film (quoted by SRON, the organization which supplied the wafers used for fabricating various devices in our research group), we can set the approximate resonance frequency of the CPW resonator by its length [229]. We may then run simulations iterating over the length and distance of the "hanger" section parallel to the feedline to obtain a desired external coupling κ_e and turn our attention towards the transmon. The transmon frequency, nonlinearity, and coupling to the resonator are set by the Josephson inductance, the size of the qubit electrodes, the gap between the electrodes and the ground plane, as well as the capacitance to the coupling pad of the resonator. For this analysis, we have set $L_J = 5$ nH and $C_J = 1$ fF.

After performing an eigenmode analysis, the magnitude of the electric field of each mode can be plotted as shown in Fig. 3.8, illustrating that our CPW is indeed $\lambda/2$, and showing that for our transmon, the majority of the electric field is concentrated around the junction and the edges of the electrodes. In general, transmon designs that yield a lower concentration of the electric field in certain regions are desirable so as not to excite two-level systems on materials surfaces and interfaces which act as loss channels for the transmon mode [230–236]. Neglecting factors of 2π for convenience, the eigenmode analysis yields frequencies $\omega_q = 8.38$ GHz and $\omega_r = 6.46$ GHz as well as $Q_{e,q} = 3.3e5$ and $Q_{e,r} = 4.5e3$ which are the Purcell-limited quality factor of the transmon and the external quality factor of the resonator respectively.

After performing a pyEPR analysis of the eigenmode solution, the expected qubit frequency slightly changes to $\omega_q = 8.12$ GHz while the resonator is unchanged at $\omega_r = 6.46$ GHz. We also obtain an inductive participation ratio for the qubit of 0.965, with $K_q = -129.5$ MHz, $K_r = -2.4$ kHz, and $V_{q,r} = 2.23$ MHz for the self-Kerr nonlinearities and the cross-Kerr. Then, we perform a LOM analysis of the circuit, which simulates only the immediate region around the transmon electrodes, including the ground plane and coupling pad of the resonator. After inputting the expected resonator frequency from the eigenmode and pyEPR analyses, the expected transmon frequency again changes to $\omega_q = 8.54$ GHz and the self-Kerr to $K_q = -163.5$ MHz. We also obtain the coupling $g = 156$ MHz, dispersive shift $\chi = 4.40$ MHz, and charge dispersion 2.41 Hz indicating that our ratio of E_J/E_C is indeed sufficiently large (here, about a factor of 100) [111]. Our obtained capacitance matrix also indicates that $C_C = 24$ fF and each electrode has a capacitance to ground of $C_{g,1} = 39$ fF, $C_{g,2} = 47$ fF, with total qubit capacitance $C_q = 65$ fF.

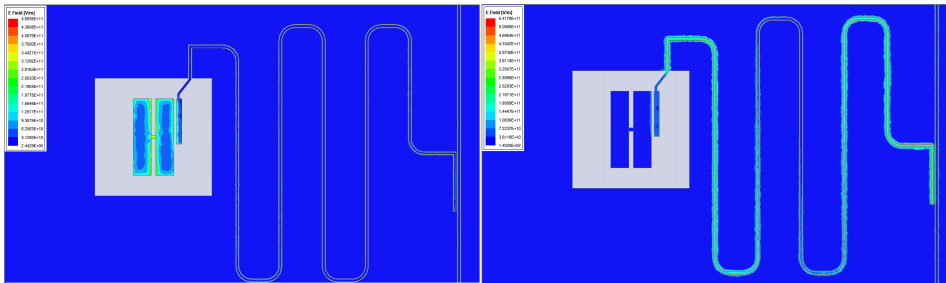


Figure 3.8: The magnitude of the electric field for each normal mode plotted in Ansys HFSS. The results are found after running an eigenmode simulation.

Inputting these capacitances back into QuCAT, we can obtain estimated self- and cross-Kerr nonlinearities of $K_q = -147$ MHz, $K_r = -2.12$ kHz, and $V_{q,r} = 2.23$ MHz, with frequencies $\omega_r = 6.46$ GHz and $\omega_q = 8.81$ GHz, which are similar to the values obtained through HFSS, LOM, and pyEPR analyses. Given that the QuCAT simulation uses the lumped element representation of the circuit and does not include kinetic inductance, we take the pyEPR analysis of the eigenmode solutions to be authoritative in the designing of our circuits.

3.2. FABRICATION

3.2.1. SUBSTRATES AND SUPERCONDUCTING THIN FILMS

In order to create superconducting quantum devices, we must first determine the materials with which we wish to construct our circuits. As the devices will contain coplanar waveguides, we will require a semiconductor substrate and a superconducting film on top of it, which we can use to define our structures. The devices measured in this thesis were fabricated at the Kavli Nanolab Delft facility at the TU Delft [237].

For our substrate and superconductor, we use Si and NbTiN, respectively. For the chips fabricated during the course of this research, we used wafers supplied by the Netherlands Institute for Space Research (SRON), which were Si with NbTiN deposited on top [229]. The Si was 525 μm thick, and the NbTiN was either 100 nm or 200 nm thick. The choice of materials strongly influences the processing and handling of devices, as well as the final frequencies, nonlinearities,

and couplings of the constructed quantum circuits. For example, certain materials grow undesired oxide layers at different rates, some lead to interfaces with higher loss tangents which reduce our device quality factors, and some materials simply do not have well-established processes for creating superconducting qubits with [231, 235, 238–251]. Substrates commonly used for superconducting qubits are Si and Al₂O₃ (sapphire), while superconducting metals are often Al, Nb, TiN, NbTiN, and Ta [235, 252–255]. Our usage of Si and NbTiN is thus partially due to the availability of wafers through an arrangement with SRON, the existence of established treatment processes, and their well-understood characteristics in the context of fabricating quantum circuits. For example, whichever superconductor we choose will have kinetic inductance which contributes along with the geometric inductance of the defined structures to yield a total linear inductance. The kinetic inductance can also contribute to device loss rates, given that the fraction of kinetic to total inductance affects the responsivity of oscillators to quasiparticles [256, 257]. The kinetic inductance per unit length of a CPW is

$$L_k = gL_s = g\mu_0\lambda_L \coth\left(\frac{t}{\lambda_L}\right) \quad (3.7)$$

where L_s is the surface inductance, t is the thickness of the superconductor, μ_0 is the magnetic permeability of vacuum, λ_L is the London penetration depth

$$\lambda_L = \sqrt{\frac{\hbar\rho}{\pi\mu_0\Delta_s}} \quad (3.8)$$

and g is a geometric factor written as

$$g = \frac{\pi + \ln\left(\frac{4\pi s}{t}\right) - k \ln\left(\frac{1+k}{1-k}\right)}{4s(1-k^2)K^2(k)} + \frac{k[\pi + \ln\left(\frac{4\pi(s+2w)}{t}\right) - \frac{1}{k} \ln\left(\frac{1+k}{1-k}\right)]}{4s(1-k^2)K^2(k)} \quad (3.9)$$

where ρ is the resistivity of the film, $\Delta_s \approx 1.764k_B T_c$ is the theoretical superconducting gap at zero temperature, the critical temperature is $T_c \approx 14.4\text{K}$ for our NbTiN film, and $K(k)$, k , s , w are as defined in Sec. 2.2.1 [229, 258–260].

Uniformity of NbTiN deposition across the entire wafer can be difficult to achieve, leading to variations in L_k as a function of position. This means that there will be some variation in L_k for any given chip diced from the wafer, with the greatest uniformity in thickness towards the center of the wafer for typical deposition processes [229]. Thus, while one may fabricate a CPW resonator on a chip from the center of a wafer, measure its frequency, and calibrate their simulation parameters accordingly to account for the kinetic inductance, there will likely be variation again upon fabrication and measurement of an identical resonator on a chip taken from the edge of a wafer. Luckily, for the wafers provided to us by SRON, the expected variation in thickness (and thus frequency) is only on the order of a few percent. For our 100 nm and 200 nm films, we expect $L_s = 0.98\text{ pH}$ and $L_s = 0.53\text{ pH}$ respectively, which can be converted to the kinetic inductance per unit length via the geometric factor g for any CPW geometry. For transmon qubits, the kinetic inductance of the qubit electrodes is typically negligible, and in any case, the junction inductance is engineered to dominate over the total linear inductance.

3.2.2. LITHOGRAPHY

After preparing the wafers, we must then define the structures which comprise the circuit, in this case, by lithographically defining them into a resist, developing the resist, and then etching away regions of metal to form our CPW traces and qubit electrodes. In this thesis, we have mostly used electron beam resist with electron beam (*e-beam*) lithography, however the use of photoresist with UV photolithography is also possible, albeit with larger spatial resolution compared to the electron beam. A resist is an organic compound sensitive to light (and electrons) that undergoes a change in its chemical structure upon exposure. A resist is defined as positive or negative by whether the written area is weakened or strengthened upon exposure to light or electrons, after which the written or unwritten area may then be developed away in a solvent respectively.

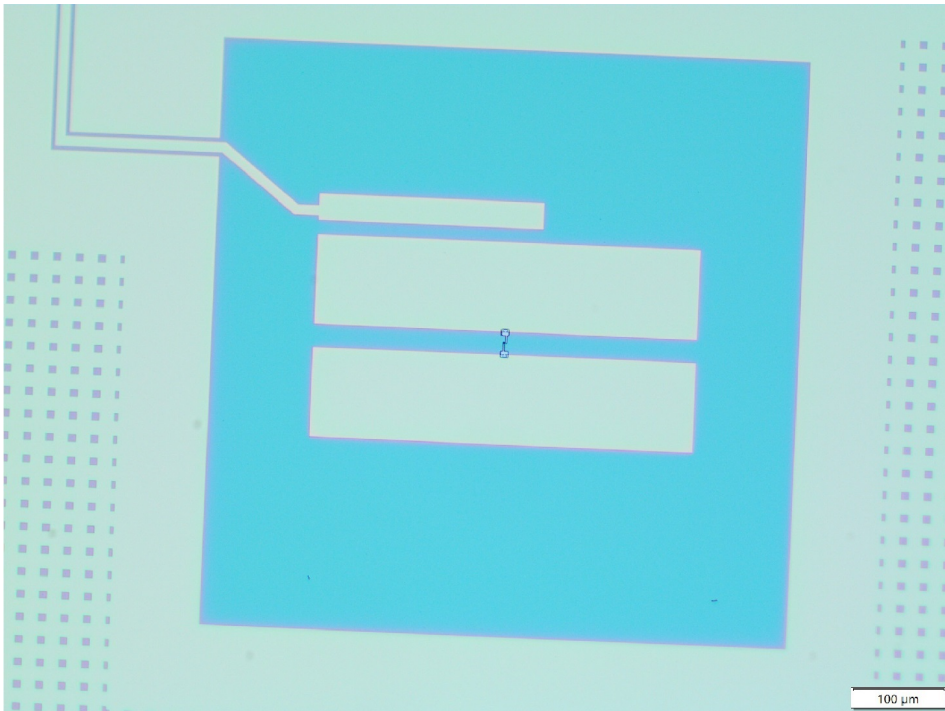


Figure 3.9: A double-island transmon qubit capacitively coupled to a readout resonator. The main structures have already been written, developed, and etched. A secondary lithography step has been performed which defined the Josephson junction connecting the two qubit electrodes. The written resist has been developed and the sample is ready to proceed towards junction evaporation.

When a resist is written, the e-beam gun delivers electrons to the sample, depositing their energy into the resist and scattering into the surrounding area. For positive resists, this decomposes the resist by breaking bonds which have been delivered energy larger than the bond-dissociation energy. The regions of the resist which have been exposed are thus made weaker and are then dissolved in the appropriate developer.

When preparing a sample for lithography, we first clean the surface of the chip with acetone and isopropyl alcohol (IPA). We then spincoat the chip with a resist and bake the chip to harden the resist. The spincoating of any given resist leads to a final thickness dependent on the spincoating speed and the resist properties. We then pattern the resist with an e-beam writer (Raith EBPG-5000+), with e-beam gun parameters dependent on the resist used and circuit feature sizes [261]. For example, when defining the relatively large bulk structures of transmission lines and electrodes, we use the resist AR-P 6200.18 (CSAR62) spun to 800 nm thickness and deliver a dose of $350\text{ }\mu\text{C}/\text{cm}^2$ at a spot size of 62 nm, current of 192 nA, and acceleration voltage of 100 kV [262]. However, when defining the comparatively small junctions, we use a bi-layer resist stack of PMMA A6 950k spun to 500 nm on top of MAA 8.5% EL6 at 180 nm written with $1850\text{ }\mu\text{C}/\text{cm}^2$, 21 nm, 1344 pA, and 100 kV [263].

The written sample then has the resist developed in a solvent, which for AR-P 6200.18 was pentyl acetate, and for the MAA/PMMA stack was a mixture of cold H_2O and IPA in a 1:3 ratio. After developing the unwanted resist and etching the exposed metal away, the resist was then stripped with either dimethylformamide (DMF) or N-Methyl-2-pyrrolidone (NMP) and cleaned with acetone and IPA. As we used positive resists, the areas which were written were developed and etched away, in which case our written patterns were defining the spaces where the substrate would be exposed to air, such as the gaps of our CPW traces.

3.2.3. REACTIVE ION ETCHING

After the pattern has been written and the sample has been developed, the exposed metal areas must then be etched away to produce the trenches separating transmission line center traces and transmon electrodes from the ground plane, which defines our feedlines, resonators, and qubits. This is done by reactive ion etching (RIE), in which the chip is placed into a reactor under vacuum and is bombarded by ions produced by a plasma generated by passing a gas through a strong electromagnetic field [264]. This field is generated by parallel plates on the top and bottom of the reactor across which a voltage is applied, which, when made sufficiently strong will ionize the gas. As a negative charge builds on the sample, the positive gas ions bombard the surface of the chip following the vertical direction of the electric field, reacting both with the exposed metal and the leftover resist. The hardened resist is etched at a much lower rate than the NbTiN for the RIE compounds used (in our case, O_2 , SF_6 , and CF_4), leading to an anisotropic etch of the exposed metal areas which reveal the underlying substrate and leave vertical walls [265].

The anisotropy of the etch and smoothness of the exposed substrate is strongly determined by the sample materials, the etchant used, and the etching conditions, such as reactor pressure, plate bias power, and rate of flow of the etchant. If these conditions are sub-optimal, there can be various deleterious effects. For instance, etched material may be redeposited onto other areas of the chip, and we may also have unintended chemical reactions between the products of the gas ionization and our sample, leading to the creation of fluorocarbon residues [266–271]. In the case of CF_4 , example products such as CF_3^+ , CF_3^- , CF_3 , F^+ , and F^- , may all be present in the reactor chamber along with our sample. Along with achieving the goal of etching the NbTiN and briefly over-etching the exposed Si, these products may also recombine, interact with etched and/or exposed material, and form unwanted compounds that negatively affect the quality of the device. The most common unwanted products are fluorocarbon polymers, which can form when there is an insufficiently large ratio of fluorine to carbon for a given electric

field strength in the chamber. If polymers form on the surfaces of the chip, these dielectrics and other lossy compounds formed can drastically reduce the internal quality factors of final devices, especially if they exist near areas with large electric field concentrations such as junctions.

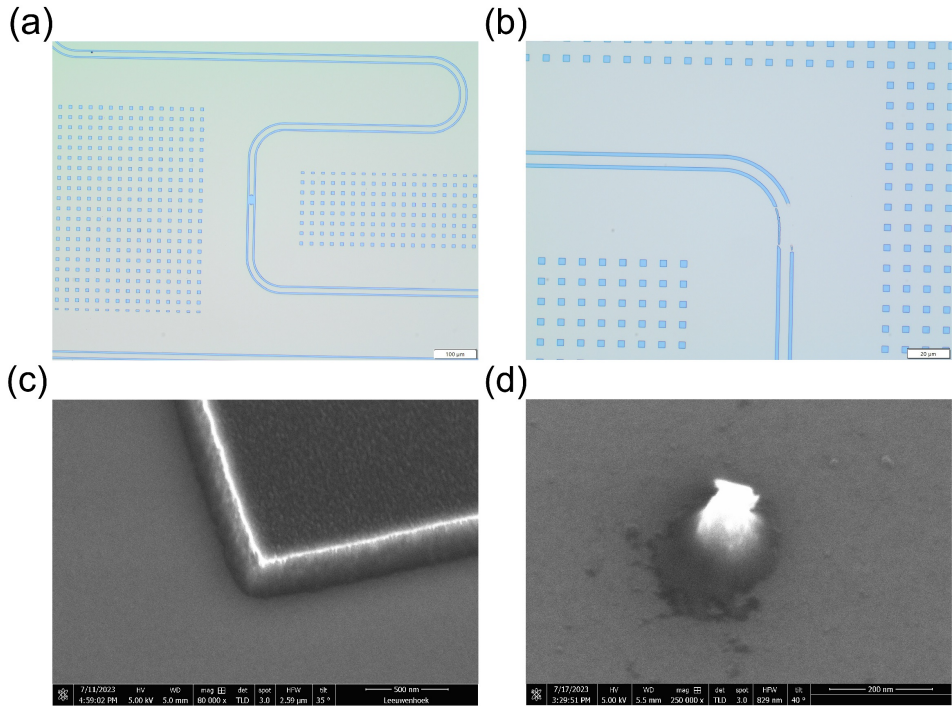


Figure 3.10: Images showing the structures resulting after a reactive ion etch. a) A CPW with space in the center for the evaporation of a Josephson junction. b) A shorted measurement feedline due to insufficient etching of the waveguide trenches. This may be due to an improper development of the resist in this region of the sample or failure due to an insufficiently clean surface. c) A scanning electron microscope (SEM) image of the corner of an etched NbTiN structure on top of a Si substrate. d) Un-etched material left on the substrate due to improper etching conditions.

3.2.4. EVAPORATION AND LIFTOFF

After the bulk structures of the device have been defined, another round of lithography and development will expose the areas of the sample on which we wish to construct Josephson junctions. As we use Al/AlO_x/Al junctions in this thesis, we will be evaporating Al onto the entire surface of the chip, which will deposit and remain only on the exposed areas and, in other regions, will be removed along with the resist during the *liftoff* process. During liftoff, the sample is left in a solvent which strips the resist from the chip along with the Al adhered to it while leaving behind the Al which was evaporated onto the exposed metal and substrate.

Aside from contributions to loss in the substrate and superconducting film, a significant source of loss can be found within the junction itself. Charged two-level systems (TLSs) can form in

dielectrics due to material defects or impurities, which then couple to our relevant device modes, leading to energy exchange with the TLS and critical current noise causing dephasing [233, 252, 272, 273]. Some TLSs can exist in the AlO_x layer of the junction, as well as in the nearby oxide layers of the substrate and superconducting film. In addition to TLSs, non-equilibrium quasiparticles (broken Cooper pairs caused by high energy photons) can directly contribute to a decrease in relaxation times in quantum circuits with Josephson junctions [111, 274–282]. In recent years, methods to combat the negative effects of quasiparticles have included improved qubit designs, substrate phonon injection, phonon trapping, phase biasing, extensive device shielding, dynamical decoupling by pulsed driving, and the use of alternative materials [283–290].

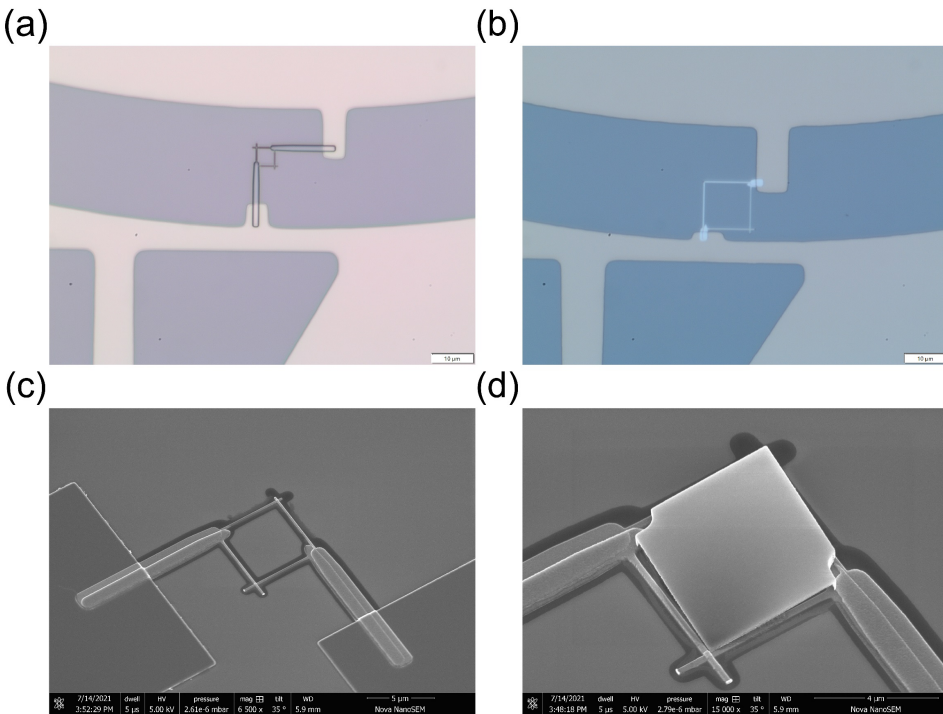


Figure 3.11: Optical microscope and SEM images showing before and after completion of the junction fabrication process. a) The geometry of a SQUID loop is defined by e-beam lithography and the resist is developed away. b) After evaporation and liftoff, the junctions are fabricated. The SQUID bridges the ground plane to the electrode of a single-island transmon qubit. c) A SEM image of a test SQUID with two probing pads. d) The result of a failed liftoff process. An insufficient amount of time and physical agitation in the resist stripping solvent caused a portion of the aluminum inside the SQUID loop to not fully detach.

In contrast to the standard Dolan-bridge, we formed junctions via double angle shadow evaporation [291–295]. We use a relatively tall resist stack in conjunction with a high angle of evaporation along two directions, which allows for evaporation of Al directly along the "streets" defined by our resist, while the "shadow" cast by the resist prevents deposition along or-

thogonal directions. A sufficient height for a given angle of evaporation and junction width can be determined, allowing for the formation of junctions by deposition of the bottom layer, followed by oxidation, and lastly an orthogonal deposition of the top layer. This method allows for a high degree of reproducibility in overlapping junction areas, which in turn leads to reliable junction inductance values for a given overlap area, provided the evaporation and oxidation conditions among other factors are unchanged across fabrication runs.

Special care is taken with this step, as it is the most critical for the construction of nonlinear quantum oscillators. While parameter targeting is especially affected by the adherence of the fabricated junction geometry to design and the oxidation conditions (which largely determine junction inductance), we must also take steps to ensure that the junctions are formed on top of clean surfaces free of lossy materials. Thus, after developing the resist and before evaporating Al, we first clean the chip with an exposure to oxygen plasma as a *descum* step to remove any leftover unwanted resist in the vicinity of the junctions, which may not have fully developed away [296].

We then perform a dip in hydrofluoric acid (HF) which removes any oxides on the surface of our chip. However, once the chip is in ambient conditions again, typically used materials begin to reoxidize with few-nm thick layers growing on the order of minutes, meaning that transporting the sample from the HF dip into the Al evaporator and bringing the chamber to vacuum as soon as possible is also important [245, 297–300]. Another method for preparing the sample surfaces for Al evaporation is by ion milling, such as with Ar. Ion milling the exposed metal can be effective in cleaning the surface to prepare for the deposition of Al, but can also cause damage to the Si substrate surface and may also be detrimental for some metals [301–304]. In order to selectively mill the metal without damaging the substrate, one may apply the ion mill at a high angle, with a rotation of 45 degrees relative to the junction directions, with the angle dependent on the width of the junctions and height of the resist [294].

The junction characteristics are largely determined by the area of overlap of the junction electrodes and the deposition and oxidation conditions of junction formation [305–315]. Once a junction has been formed, the normal state resistance can be probed at room temperature. The critical current, Josephson inductance, and Josephson energy can be estimated via the Ambegaokar-Baratoff relation, given an expected value for the superconducting gap of thin-film Al, which can be related to the critical temperature of Al [316–318]. Estimating a critical temperature of $T_C = 1.174\text{--}1.405$ K as T_C increases for thinner films, the superconducting gap in frequency units can be taken as $2\Delta/h \approx 84$ GHz given junction film thicknesses on the order of tens of nanometers [317, 319, 320]. Then, we have

$$E_J = \frac{h\Delta}{8e^2 R_N} = \frac{\pi\Delta Z_0}{R_N} \quad (3.10)$$

where R_N is the normal state resistance and $Z_0 = \hbar/(2e)^2$ is the reduced impedance quantum. Then, we can directly relate the Josephson inductance to the normal state resistance with a conversion factor as

$$L_J = R_N \left(\frac{\Phi_0}{2\pi} \right)^2 \left(\frac{1}{\pi Z_0 \Delta} \right) = R_N \left(\frac{0.3183\hbar}{\Delta} \right) \approx R_N \times \left(1.2 \frac{nH}{k\Omega} \right). \quad (3.11)$$

In Fig. 3.12, the relationship between the junction overlap area and the normal state resistance and conductance is shown. It is often useful to plot the inverse of the junction resistance (the

normal state conductance, $G_N = 1/R_N$) against the area of overlap, given that there is a linear relationship between conductance and area. For a given instance of junction evaporation and oxidation, the standard deviation in normal state resistance for width values from 100 - 300 nm was generally found to be small, with a relative error of less than 5%. Across different instances of performed lithography, development, evaporation, oxidation, and liftoff steps used, fits of the conductance for separate fabrication runs show a relative deviation of less than 20% for single junctions and 25% for SQUIDs.

This increased variation over different fabrication runs can be due to a variety of factors, including changes in the lithographically defined area versus the designed area, changes in oxidation conditions during the formation of the junction, and human error leading to unconscious deviations from the established recipe. To account for lithographic deviations, the junction area can be checked by measuring the fabricated junction with a scanning electron microscope (SEM) and comparing the normal state characteristics to fabricated rather than designed areas. Junction resistances can also be tuned post-fabrication by the use of laser annealing, to bring the device parameters closer to designed values [321].

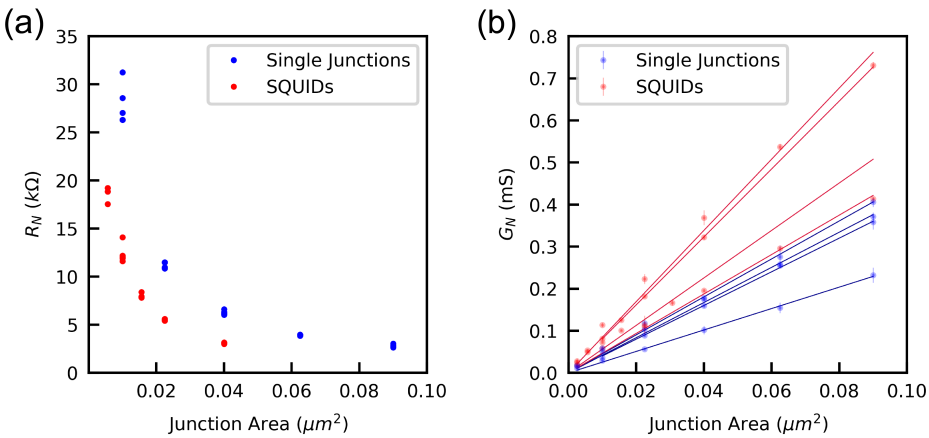


Figure 3.12: Junction parameters determined from room temperature probe measurements versus designed junction areas. a) The measured normal state resistance from two point probe measurements of junctions of varying overlap area. The top and bottom junction electrodes were designed to be of equal length and width in the region of overlap. As the junction area increases, the resistance decreases for both single junctions and SQUIDs. b) Estimated normal state conductance across several independent fabrication runs totaling 152 probe measurements. Plotted points with error bars are the mean and standard deviation of the junction characteristics of each instance of fabrication. Lines are linear fits to the characteristics determined for each fabrication run. $R^2 \geq 0.995$ for all except two SQUID dataset fits, which were $R^2 \approx 0.989$ and $R^2 \approx 0.918$.

The mean and standard deviation of the slopes in Fig. 3.12 b) for single junction fits indicate a conductance of $3.81 \pm 0.752 \text{ mS}/\mu m^2$ and for SQUIDs $6.72 \pm 1.60 \text{ mS}/\mu m^2$. Given Eq. 2.30 - 2.33, 3.10, 3.11 we should expect for symmetric junctions that the SQUID conductance is twice that of the single junction, which is within the bounds set by the standard deviations of the datasets. The dynamic oxidation steps which formed the junctions were set to 11 minutes at

1.3 mbar, and for each junction, the bottom layer of aluminium was 35 nm thick, and the top layer was 75 nm thick. The oxidation step was repeated as the final step to terminally cap the junctions.

After the junctions have been probed, the sample bondpads are wirebonded to a printed circuit board (PCB) and the device is installed inside of a gold-plated copper enclosure. Prior to wirebonding, the coaxial cable connection ports are soldered to the PCB. The entire package is then installed into a cryogenic refrigerator, and the measurement equipment is connected to the device via coaxial cables. The engineering of the microwave packaging is also of importance to ensure that the device is well thermally anchored to the mixing chamber plate of the dilution refrigerator, to reduce signal crosstalk, and to suppress the negative effects of package modes [322].

4

FLUX MODULATED TUNABLE COUPLINGS OF TWO NONLINEAR OSCILLATORS

Try to make things that can become better in other people's minds than they were in yours.

Brian Eno

Access to a wide variety of couplings between oscillators on a single device is highly desirable in order to effectively simulate a host of quantum systems. A superconducting circuit containing two transmon qubits connected both capacitively and inductively by a flux-tunable coupler has shown promise for accessing disparate coupling regimes, such as those in which the single-photon hopping interaction dominates over the cross-Kerr coupling, and vice versa. While such controllability is useful for quantum information processors, it also enables the analog simulation of various physical phenomena including arbitrary spin-spin interactions. Wide tunability also facilitates the study of driven-dissipative oscillator dynamics in previously unexplored parameter regimes. In this work, we demonstrate the ability to selectively enter into regimes in which the system dynamics are dominated by either photon-hopping, two-mode squeezing, or cross-Kerr interactions with the use of parametric modulation. In doing so, we observe level repulsion and attraction in two strongly Kerr-nonlinear oscillators in regimes where the couplings and nonlinearities exceed the decay rates of the system.

J. D. Koenig, G. Barbieri, F. Fani Sani, M. Kounalakis, C.A. Potts and G.A. Steele, *Flux Modulated Tunable Couplings of Two Nonlinear Oscillators*, in preparation (2024).

4.1. INTRODUCTION

Quantum information processors based on superconducting circuits have long relied on the transmon qubit as a robust, reliable, and high-coherence building block in the journey toward large-scale digital quantum computation [111, 323, 324]. Circuit quantum electrodynamical (cQED) devices are also of great interest to the development of analog quantum simulators - devices which are custom-built to emulate the behaviour of distinct systems which are otherwise typically challenging to control or probe directly [325, 326]. Such devices would enable the probing of physics in otherwise inaccessible parameter regimes due to the high degree of engineerability in superconducting circuits afforded by modern nanofabrication techniques and materials science [327–329].

These transmon-based cQED systems may be described as collections of coupled Kerr-nonlinear oscillators, which in recent years have been imbued with in-situ tunable resonance frequencies, couplings, and nonlinearities achievable by external control [330–336]. While such developments have greatly contributed to progress in digital gate-based architectures, there is still unexplored territory in using such platforms to emulate other physical systems such as extended Bose-Hubbard and spin- $\frac{1}{2}$ models [337–343].

Tunable couplers have been successfully used to implement high-fidelity two-qubit gates and are useful elements for mitigating undesirable interactions in designs for scalable quantum computing architectures [344–354]. They have also been of great interest to the field of analog quantum simulations, in which systems of nonlinear oscillators able to enter into and exit out of distinct coupling regimes would be capable of emulating physics from fractional Bloch oscillations to gauge-invariant synthetic magnetic fields and lattice gauge theories [333, 337, 339, 340, 343, 355, 356].

For instance, Kerr-nonlinear oscillators (KNOs) with purely longitudinal coupling exhibit the same dynamics as antiferromagnetically coupled Ising spins, while control over all $\sigma_X\sigma_X$, $\sigma_Y\sigma_Y$, and $\sigma_Z\sigma_Z$ couplings individually would allow for analog simulation of arbitrary XYZ spin-model Hamiltonians [343, 357, 358]. Devices with couplers containing more highly nonlinear elements may also be used to enter into regimes where strictly nonlinear couplings such as correlated photon hopping and photon-pair tunnelling terms dominate, allowing for the simulation of more exotic physics [195].

The dual phenomena of level repulsion and level attraction have been previously investigated in a broad array of platforms ranging from Bose-Einstein condensates to magnonic and nano-optomechanical systems operating in various parameter regimes characterized by the resonance frequencies, coupling strengths and decay rates of the constituent oscillators [193, 194, 359–375]. These interactions have been used to great effect in other contexts to enable (quantum-limited) nondegenerate parametric amplification and perform two-qubit gate operations [193, 194, 346].

Beyond their applicability for quantum information processing tasks, the wide selectivity of system parameters in tunably coupled nonlinear oscillators is of particular interest due to the ability to investigate the formation of instability regimes, their application to parametric amplification, the generation of entanglement, and the non-Hermiticity of generable Hamiltonians [326, 376, 377]. Exquisite control over these couplings would enable direct investigation of the coherence-dissipation competition in coupled nonlinear oscillators and bring predicted

applications in topological energy transfer, quantum sensing, and nonreciprocal photon transmission closer to experimental realization [366, 368, 378, 379].

Here, we present measurements of a superconducting circuit containing two flux-tunable transmon qubits connected by both a fixed capacitive coupling and a tunable nonlinear inductive coupling provided by a highly symmetric superconducting quantum interference device (SQUID). By parametrically modulating the external flux threading the SQUID loop of the coupler, we operated the device in regimes where the longitudinal (cross-Kerr, or ZZ) coupling was dominant over a two-mode squeezing interaction, and in which the single-photon exchange interaction (beam-splitter) and cross-Kerr strengths were comparable.

We observed two-mode squeezing effects through the use of parametric modulation, which, together with the single-photon hopping interaction, are characterized by level attraction and repulsion between the oscillators, respectively. In contrast to previous studies where such effects were explored in linear systems, our measurements represent spectroscopic observation of level attraction between two strongly Kerr-nonlinear oscillators [365, 369, 372]. Our results further illustrate the utility of platforms based on nonlinear oscillators containing tunable couplers to act as analog quantum simulators, which can be driven to explore more highly nonlinear effects and exotic parameter regimes in future studies.

4.2. DEVICE AND FLUX MODULATION

The system consists of two transmon qubits coupled both capacitively and inductively by a SQUID, realizing a tunable coupler as seen in Fig. 4.1 (a), (b). The coupling between the two oscillators is solely characterized by the charging and Josephson energies of the constituent circuit elements, with linear and non-linear interactions tunable via the total DC flux threading the coupler SQUID loop. The Josephson energy of the coupler is written as

$$E_J^C(\Phi_{DC}) = E_{J_{\max}}^C \left| \cos \left(\pi \frac{\Phi_{DC}}{\Phi_0} \right) \right| \sqrt{1 + d_c^2 \tan^2 \left(\pi \frac{\Phi_{DC}}{\Phi_0} \right)} \quad (4.1)$$

where $E_{J_{\max}}^C$ is determined by the inductance of the unbiased SQUID loop, d_c is a measure of the asymmetry of the junction inductances comprising the SQUID, and Φ_{DC} is the DC flux threading the loop [332]. Each of the two transmons is capacitively coupled to its own coplanar waveguide resonator, which are in turn coupled to a common feedline through which the device is driven and probed. The Josephson energies of the two qubits are related to their own flux biases Φ_A and Φ_B in the same form as Eq. 4.1. In the coupled system, the ground to excited state transition frequency for transmon i is given in units where $\hbar = 1$ as

$$\omega_i \approx \sqrt{8\tilde{E}_J^i E_C^i} - E_C^i \quad (4.2)$$

with $\tilde{E}_J^i = E_J^i + E_J^C/4$ the modified Josephson energy due to the coupler and E_C^i the charging energy of transmon i .

We obtain a Hamiltonian following the procedure outlined in Sec. 4.6.2 and Ref. [333] in which we quantize the circuit shown in Fig. 4.1 (a) and retain terms in the expansions of the energy

potentials of the SQUIDS to fourth-order. We can obtain a simplified Hamiltonian given by

$$H = \omega_A \hat{a}^\dagger \hat{a} + \frac{\alpha_A}{2} \hat{a}^\dagger \hat{a}^\dagger \hat{a} \hat{a} + \omega_B \hat{b}^\dagger \hat{b} + \frac{\alpha_B}{2} \hat{b}^\dagger \hat{b}^\dagger \hat{b} \hat{b} + J_1(\hat{a}^\dagger \hat{b} + \hat{a} \hat{b}^\dagger) + J_2(\hat{a}^\dagger \hat{b}^\dagger + \hat{a} \hat{b}) + V \hat{a}^\dagger \hat{a} \hat{b}^\dagger \hat{b} \quad (4.3)$$

where we have defined:

$$J_{1,2} := \pm \left(\frac{\tilde{E}_J^A \tilde{E}_J^B E_C^A E_C^B}{4} \right)^{1/4} \left(\frac{E_C^C}{\sqrt{E_C^A E_C^B}} \mp \frac{E_C^C}{2\sqrt{\tilde{E}_J^A \tilde{E}_J^B}} \right) \quad (4.4)$$

and

$$V := -\frac{E_C^C}{8} \sqrt{\frac{E_C^A E_C^B}{\tilde{E}_J^A \tilde{E}_J^B}} \quad (4.5)$$

where J_1 is the strength of the hopping interaction, J_2 the squeezing, V the cross-Kerr, $\alpha_i \approx -E_C^i$ the anharmonicity, and we have neglected higher order terms which are far off-resonant from the relevant dynamics of the measurements performed.

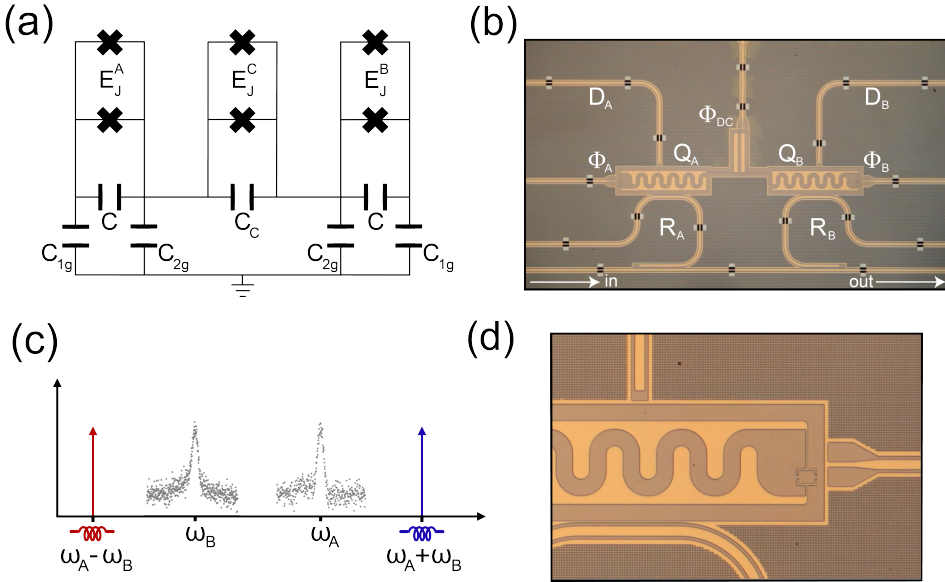


Figure 4.1: Device and measurement scheme. (a) Circuit diagram for the device. On the left and right sides are two flux-tunable transmon qubits consisting of asymmetric SQUIDS with gate capacitances to the ground. The tunable coupler in the center consists of a coupling capacitor and symmetric SQUID. (b) Optical microscope image of the device, including transmission line, readout resonators (R_i), drive lines (D_i), flux lines (Φ_i), two transmons (Q_i), and the tunable coupler. (c) Schematic of the experiment. The flux incident on the coupler SQUID loop is modulated at either the difference or sum frequency of the two transmons. (d) Optical microscope image of Qubit B.

Under the Rotating Wave Approximation (RWA) and when the two transmons are brought into resonance, the single-photon hopping and cross-Kerr effects are observable with strengths J_1 and V , while the two-mode squeezing interaction is far off-resonant. In previous measurements on this device, the single-photon hopping and cross-Kerr interactions were shown to be highly tunable dependent on the choice of static coupler flux bias point with deep access to the regime $J_1 > V$ [333]. Unfortunately, the region $J_1 < V$ was not clearly accessible due to hybridization with a tertiary circuit mode (see Sec. 4.6.2) at the particular bias points at which it was theoretically expected to be accessible. However, by parametrically modulating the flux threading the SQUID loop of the coupler, we can access parameter regimes in which either the photon hopping or two-mode squeezing terms can be selectively activated, as well as access the region where $J_{1,2} < V$.

We consider the case in which the magnetic flux threading the coupler contains a static DC component as well as a periodic AC component, where the total flux is given by

$$\Phi_C(t) = \Phi_{DC} + \Phi_{AC} \cos(\omega_m t) \quad (4.6)$$

and ω_m is the frequency of the modulation. Provided that the strength of modulation is small relative to the bias point ($\sin(\Phi_{DC}) \gg \sin(\Phi_{AC})$), we can insert Eq. 4.6 into Eq. 4.1 and obtain a new expression for the Josephson energy of the coupler as

$$\begin{aligned} E_J^C(\Phi_C(t)) &\approx E_{J_{\max}}^C \left| \cos\left(\pi \frac{\Phi_{DC}}{\Phi_0}\right) \right. \\ &\quad \left. - \pi \frac{\Phi_{AC}}{\Phi_0} \sin\left(\pi \frac{\Phi_{DC}}{\Phi_0}\right) \cos(\omega_m t) \right| \sqrt{1 + d_c^2 \tan^2\left(\pi \frac{\Phi_{DC}}{\Phi_0}\right)} \\ &= E_{J,DC}^C + E_{J,AC}^C(t) \end{aligned} \quad (4.7)$$

which is now comprised of a static term $E_{J,DC}^C$ and a time-dependent term $E_{J,AC}^C(t)$ due to the modulation.

After re-deriving the expressions for the hopping and two-mode squeezing interactions, it can be shown that by modulating the coupler at the difference or sum frequency $\omega_m = |\omega_A \pm \omega_B|$, either interaction can be selectively activated for non-resonant oscillators as the coupling strengths under modulation are modified to

$$J_1 \rightarrow [J_{1,DC} + J_{AC}(e^{i\omega_m t} + e^{-i\omega_m t})](\hat{a}^\dagger \hat{b} e^{i(\omega_A - \omega_B)t} + \hat{a} \hat{b}^\dagger e^{-i(\omega_A - \omega_B)t}) \quad (4.8)$$

$$J_2 \rightarrow [J_{2,DC} + J_{AC}(e^{i\omega_m t} + e^{-i\omega_m t})](\hat{a}^\dagger \hat{b}^\dagger e^{i(\omega_A + \omega_B)t} + \hat{a} \hat{b} e^{-i(\omega_A + \omega_B)t}) \quad (4.9)$$

where $J_{1,DC}$, $J_{2,DC}$ are as in Eq. 4.4 and the strength of the modulated interaction may be approximated as

$$J_{AC} \approx \frac{\pi \Phi_{AC}}{4\sqrt{2}\Phi_0} \sin\left(\pi \frac{\Phi_{DC}}{\Phi_0}\right) E_{J_{\max}}^C \left(\frac{E_C^A E_C^B}{\bar{E}_J^A \bar{E}_J^B}\right)^{1/4}. \quad (4.10)$$

After applying the RWA, we may choose to activate either interaction with strength J_{AC} depending on the frequency of modulation, while other terms not commensurate with the modulation become fast-rotating and play a negligible role in the system dynamics. The full form of Eq. 4.10 and the contributions from higher order interactions are shown in Sec. 4.6.2.

4.3. OBSERVATION OF PARAMETRICALLY ACTIVATED COUPLINGS

In order to measure the strength of the couplings under time-periodic pumping, we modulated the DC current supplied to the tunable coupler at a frequency ω_m . From the full Hamiltonian, the static component of the system under modulation can be written as

$$H_{DC} = \omega_A a^\dagger a + \frac{\alpha_A}{2} a^\dagger a^\dagger a a + \omega_B b^\dagger b + \frac{\alpha_B}{2} b^\dagger b^\dagger b b + V a^\dagger a b^\dagger b \quad (4.11)$$

with additional terms present depending on the frequency at which the coupler flux is modulated. When modulating at the red sideband (RSB), we have

$$H_{RSB} = H_{DC} + H_\Delta \quad (4.12)$$

$$H_\Delta = J_{AC}(a^\dagger b + a b^\dagger) \quad (4.13)$$

and when modulating at the blue sideband (BSB), we similarly obtain

$$H_{BSB} = H_{DC} + H_\Sigma \quad (4.14)$$

$$H_\Sigma = J_{AC}(a^\dagger b^\dagger + a b). \quad (4.15)$$

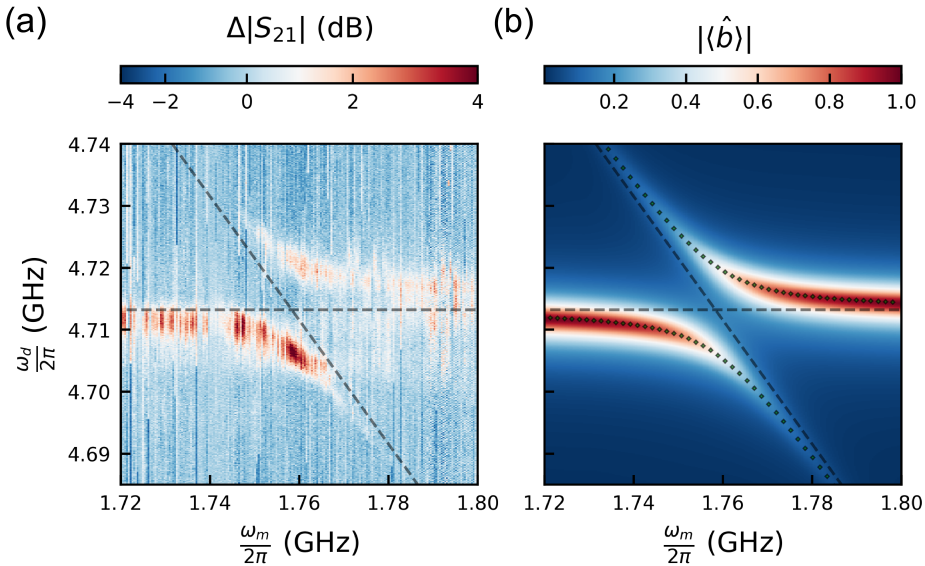


Figure 4.2: Single-photon hopping interaction induced by red sideband flux modulation of the coupler. (a) Change in normalized transmission amplitude while driving transmon B and sweeping the modulation frequency of the DC signal incident on the tunable coupler through the red sideband of the two oscillators. The black dashed lines are guides for the eye. The horizontal dashed line is the first transition frequency of transmon B, and the diagonal dashed line is $(\omega_A - \omega_m)/2\pi$. (b) Eigenfrequencies obtained from fitting to the level repulsion model (green markers) and the normalized expectation value of \hat{b} obtained from a numerical simulation of a quantum master equation for the system [218].

In Fig. 4.2 we set $\omega_A/2\pi = 6.471$ GHz, $\omega_B/2\pi = 4.713$ GHz, $\Phi_{DC} = 0.342\Phi_0$ and performed two-tone spectroscopy on transmon B while sweeping $\omega_m/2\pi$ through $(\omega_A - \omega_B)/2\pi$. As the modulation frequency approached the red sideband of the oscillators, we observed an avoided crossing from which we extracted a single-photon hopping interaction strength of $J_{AC}/2\pi = 7.09$ MHz and a cross-Kerr strength of $V/2\pi = -6.79$ MHz by finding $\vec{\Phi} = [\Phi_A, \Phi_B, \Phi_{DC}, \Phi_{AC}]$. Extracted parameters were determined by an analytical level repulsion model given observed oscillator frequencies and interaction strengths, as well as by numerically simulating the system Hamiltonian as outlined in Sec. 4.6.3. The magnitude of the observed splitting reflects the strength of the exchange interaction between the two oscillators at the resonance condition met under parametric modulation. The values of all parameters which comprise Eq. 4.12 were calculated from $\vec{\Phi}$ and are displayed in Table 4.1 shown in Sec. 4.6.3.

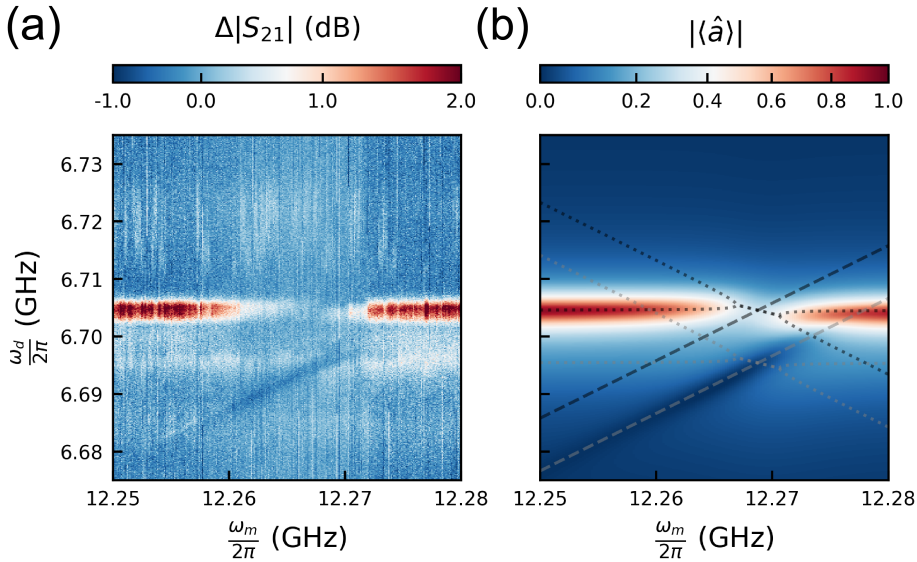


Figure 4.3: Two-mode squeezing interaction induced by blue sideband flux modulation of the coupler. (a) Transmission amplitude while driving transmon A and sweeping the modulation frequency of the DC bias incident on the tunable coupler through the blue sideband of the two oscillators. (b) The dashed lines are the sum frequency resonance condition $(\omega_m - \omega_B)/2\pi$ and the same shifted by $V/2\pi$. The dotted lines are the eigenfrequencies of the system determined from fits to the data to the analytical level attraction model outlined in the main text. The underlying spectrum is the normalized expectation value of \hat{a} obtained from a numerical simulation of a quantum master equation for the system [218].

Similarly, in Fig. 4.3 we set $\omega_A/2\pi = 6.705$ GHz, $\omega_B/2\pi = 5.573$ GHz and $\Phi_{DC} = 0.214\Phi_0$ and performed two-tone spectroscopy on transmon A while sweeping $\omega_m/2\pi$ through $(\omega_A + \omega_B)/2\pi$. As the pump frequency crossed the blue sideband, we observed features associated with the phenomenon of level attraction occurring between the two oscillators. Following an analytical model outlined in Sec. 4.6.3, we extracted a two-mode squeezing strength of $J_{AC}/2\pi = 1.852$ MHz and a cross-Kerr strength of $V/2\pi = -9.161$ MHz with the cross-Kerr shifted transition additionally visible below the frequency of the primary oscillator response.

In the level attraction region where frequency degeneracy of the eigenmodes is theoretically predicted, we observed the primary resonance feature disappear. In this same region, we observed the emergence of a dark dash in the transmission spectrum related to a loss of excited state population in transmon A. This dash is shifted from the primary resonance feature by $V/2\pi$ and is associated with the swept microwave drive bringing the oscillator to its ground state from the $|11\rangle$ state populated by the parametric modulation. In Sec. 4.6.3, we discuss this feature in more detail and provide additional numerical simulations of the change in system state under simultaneous parametric modulation and microwave driving.

4.4. COUPLING REGIMES AND ANALOG QUANTUM SIMULATIONS

Through the use of parametric modulation, we were able to observe interactions between two nonlinear oscillators in coupling regimes which were previously inaccessible with this device when changing the static flux bias point alone [333]. When modulating the flux through the coupler, the strength of the single-photon hopping and two-mode squeezing interactions are to first order linearly dependent on the amplitude of the modulation signal and thus can be tuned to far lower or higher interaction strengths relative to the cross-Kerr for a wide range of static biases. The dependence of the interaction strengths on bias point and modulation amplitude is shown in Fig. 4.4, where the green region indicates the range of possible cross-Kerr values depending on the flux bias points of the transmons and coupler. In contrast, the grey region shows the values of $J_{AC}/2\pi$ for a range of modulation strengths.

While we demonstrated the ability to enter into this coupling regime, we were also able to observe two-mode squeezing interactions, which are typically far off-resonant and fast-rotating in the frame of the oscillators. This interaction generates entangled signal and idler photon pairs between the two systems and has been used to perform two-qubit gate (bSWAP) operations in the truncated qubit subspace [346, 380, 381]. The ability to activate this term enables the tuning of XX-YY interactions between the oscillators, broadening the array of systems that such devices can effectively simulate. The modulated strength is tunable over a wide range, enabling the possibility for simulation of arbitrary XYZ spin-model Hamiltonians when coupled with the controllability demonstrated by the XX+YY and ZZ interactions [343].

Prospects for bichromatic flux pumps are also promising, where phase differences between simultaneously applied red and blue sideband pumps would allow for pure XX or YY interactions. Such driven coupler schemes have been previously investigated in the context of Floquet engineering, in which tunable and selectively activatable interactions are integral to the proposed analog quantum simulation of Kitaev honeycomb models [343]. The nonstoquastic terms which a parametrically modulated tunable coupler can contribute to the system are also of great interest with respect to the study of possible quantum advantage over classical approaches in annealing protocols [337, 382, 383].

In addition to the utility that transmon-based devices containing tunable couplers contribute to the development of analog quantum simulators, the parametric interactions that we activate provide insight into the dual phenomena of level repulsion and attraction. The red and blue sideband measurements illustrate the ability to transition between coherent (real) coupling and dissipative (imaginary) coupling without the use of coherence-dissipation engineering but rather with an applied modulation pump. Such couplings have long been the focus of study in magnonic, Bose-Einstein condensate, and optomechanical systems, typically

operating in regimes where the nonlinearities of the oscillators are small [359, 360, 362–366, 368–370, 372, 379].

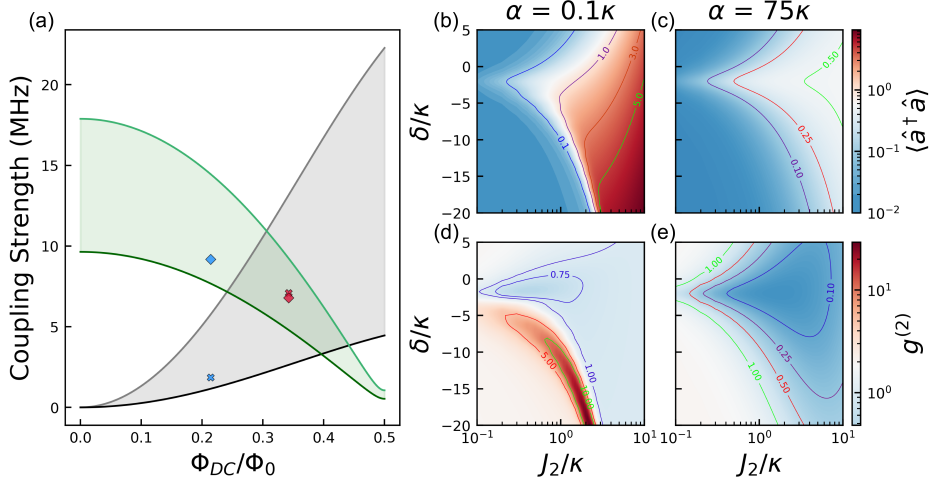


Figure 4.4: Interaction strengths and distinct response parameter regimes. (a) The calculated interaction strengths as the DC flux bias point of the coupler is changed. The gradient of curves in green shows the possible values of the cross-Kerr interaction for the range of $\Phi_{A,B} \in [0.0, 0.5\Phi_0]$ at each value of Φ_{DC} . The gradient of curves in gray shows the values of single-photon hopping or two-mode squeezing interactions for a range of modulation strengths between $\Phi_{AC} = \Phi_{DC}/50$ and $\Phi_{AC} = \Phi_{DC}/10$. The diamond ($V/2\pi$) and cross ($J_{AC}/2\pi$) markers indicate the extracted interaction strengths from Fig. 4.2 (red) and Fig. 4.3 (blue). (b), (c) The photon number expectation value for one mode of a system of two coupled Kerr-nonlinear oscillators subject to a drive-induced two-mode squeezing interaction where the strength of the interaction J_2 , detuning of the drive from the sum frequency resonance condition δ , and nonlinearity α are varied relative to the loss rates of the oscillators κ . (d), (e) The second-order correlation function of one of the oscillators as in (b), (c).

In the case of level attraction, a system of coupled linear oscillators exhibits a region of parametric instability with two exceptional points indicating the transition of the system to one with complex eigenfrequencies with opposite-sign imaginary components. In this situation, one eigenmode grows exponentially and becomes unstable while the other decays exponentially. Such a situation arises only when the dissipation rates of the two oscillator modes are commensurate and the coupling exceeds the oscillator decay rates [365]. For our two oscillators, the linewidths are each on the order of a few MHz for the flux points investigated, and the coupling strength can be tuned to less than or greater than the dissipation rates for typical transmon coherence times given the choice of modulation amplitude.

The same interaction was also previously observed between two coupled weakly nonlinear modes of a SQUID-terminated coplanar waveguide resonator subject to flux modulation [384]. Nondegenerate parametric oscillations were observed when the system was driven beyond the parametric instability threshold for a range of sufficient detunings and modulation strengths. In this system, the self-Kerr and cross-Kerr couplings of the modes were much smaller than

the decay rates, while the parametric response diagram for each mode is similar to those of parametrically driven (single-mode squeezed) Kerr and Duffing nonlinear oscillators [384–387]. Upon the application of an additional drive, such phase-degenerate oscillators can also become injection-locked to the drive [384, 388, 389].

The main distinctions between the behaviour outlined above and what is shown in Fig. 4.3 are that the oscillators measured are strongly nonlinear and that we do not observe a region of parametric instability due to the low strength of the two-mode squeezing interaction relative to the decay rates and self-Kerr nonlinearities of the oscillators. Further, our oscillators are additionally cross-Kerr coupled which yields a frequency shift of the spectroscopic features. In order to investigate these distinctions and better understand the contributions of the self-Kerr and cross-Kerr terms to the phenomenon of level attraction between strongly nonlinear oscillators, we numerically simulated both weakly and strongly nonlinear oscillators.

In Fig. 4.4(b-e), we show for one mode the photon number expectation values $\langle a^\dagger a \rangle$ and second-order correlation function $g^{(2)} = \langle \hat{a}^{\dagger 2} \hat{a}^2 \rangle / \langle \hat{a}^\dagger \hat{a} \rangle^2$ in a system of two Kerr-nonlinear oscillators as in Eq. 4.14 where the correlated squeezing terms are set to zero, determined from quantum master equation simulations [218]. We set $V = -2\kappa$ and vary the strength of the two-mode squeezing term J_2 and detuning of the modulation frequency from the sum frequency resonance condition δ for the case of weakly nonlinear oscillators $\alpha = 0.1\kappa$ and strongly nonlinear oscillators $\alpha = 75\kappa$. For the weakly nonlinear system, as the strength of the two-mode squeezing interaction increases, the parametric response region, which provides an increased photon number, shifts to large, negative detunings. Additionally, a sudden peak in $g^{(2)}$ bounds the parametric response region from below, which is a known marker of a phase transition in Kerr-nonlinear oscillators [390, 391].

In contrast, for the strongly nonlinear oscillators (*i.e.* transmon qubits), for $J_2 < E_C$ and in a region centered about the cross-Kerr shifted sum frequency resonance condition, the photon number expectation and second-order correlation function remain below one. In this case, the two-mode squeezing interaction acts effectively on the qubit subspace alone, generating an XX-YY interaction. The large self-Kerr nonlinearities of the oscillators prevents the system from reaching a parametric instability as in the case of the linear and weakly nonlinear two-mode squeezed systems, instead generating a low photon number entangled state.

In Sec. 4.6.3, we also display the relative change in the occupation of the first two oscillator energy levels with the self-Kerr and cross-Kerr terms included in the system Hamiltonian. We find that the negative cross-Kerr nonlinearity shifts down the energy of the $|11\rangle$ state, leading to the appearance of a “ghost” level attraction window corresponding to the population being driven out of the jointly excited state by the qubit drive, which the parametric modulation populates.

4.5. CONCLUSION

We have demonstrated the operation of a transmon-based circuit containing a flux tunable coupler in a way that allowed for access into different coupling regimes, including where the cross-Kerr effect is the dominant interaction between two nonlinear oscillators. By parametrically modulating the inductance of the coupler SQUID loop with an applied time-dependent magnetic field, we were able to selectively activate either a single-photon hopping interac-

tion or two-mode squeezing between two transmon qubits with strength tunable by choice of DC flux bias point and the amplitude of modulation. In combination with previously reported values of strong single-photon hopping interactions, this enables access to parameter regions where $J_{1,2} > V$, $J_{1,2} \approx V$, and $J_{1,2} < V$ [333].

This tunability allows for the simulation of various systems, including Ising ZZ, Bose-Hubbard, and Heisenberg XXZ models, as in the qubit subspace these regimes are equivalent to $(\sigma_X \sigma_X \pm \sigma_Y \sigma_Y) > \sigma_Z \sigma_Z$, $(\sigma_X \sigma_X \pm \sigma_Y \sigma_Y) \approx \sigma_Z \sigma_Z$, and $(\sigma_X \sigma_X \pm \sigma_Y \sigma_Y) < \sigma_Z \sigma_Z$ [325, 326, 338, 343, 392, 393]. The ability to tune into and out of these regimes is of particular interest to the field of analog quantum simulations, where such superconducting devices can be made to emulate a variety of physical systems with solely in-situ control and a broad range of coupling strengths achievable. Our model predicts that further measurements in which such couplers are modulated to satisfy other resonance conditions should also activate more highly nonlinear effects such as photon-pair tunnelling, correlated photon hopping, and photon-pressure interactions. The exchange of SQUIDs for asymmetric nonlinear elements such as SNAILs would also enable the simulation of more exotic interactions and enable tunability of several device parameters, such as the self-Kerr, which can be tuned from negative to positive values [195, 394–396].

In addition, we observed level attraction in a system of coupled strongly nonlinear oscillators under tunable blue sideband modulation. The behaviour of the system differs from previously established theoretical descriptions and experimental observations of linear systems exhibiting level attraction [365, 369, 372]. Using an extension of existing methods and numerical simulations, we were able to determine that the cross-Kerr coupling yields an additional shifted spectroscopic feature of level attraction. Under bichromatic $2\omega_A$ and $2\omega_B$ pumps, such a system would also be useful for investigating stabilized dissipation in driven Bose-Hubbard systems containing entangled modes [397]. Further, the independently tunable strengths of the photon hopping and two-mode squeezing interactions should allow for investigation into novel parametric interaction regimes such as those studied in optomechanical systems [376, 398].

4.5.1. CONTRIBUTIONS

Author names are as given in the List of Publications. J.D.K., G.B., and M.K. carried out the theoretical analysis. M.K. designed and fabricated the device in the group of Leo DiCarlo. J.D.K., F.F.S, and M.K. conducted the measurements. J.D.K and G.B. performed the simulations. C.A.P. and G.A.S. supervised the project. J.D.K. wrote the chapter with input from the authors. The authors acknowledge financial support by the EU program H2020-FETOPEN project 828826 Quro-morphic. This contribution statement is tentative and may be changed prior to publication of these results.

4.6. SUPPLEMENTARY INFORMATION

4.6.1. EXPERIMENTAL SETUP

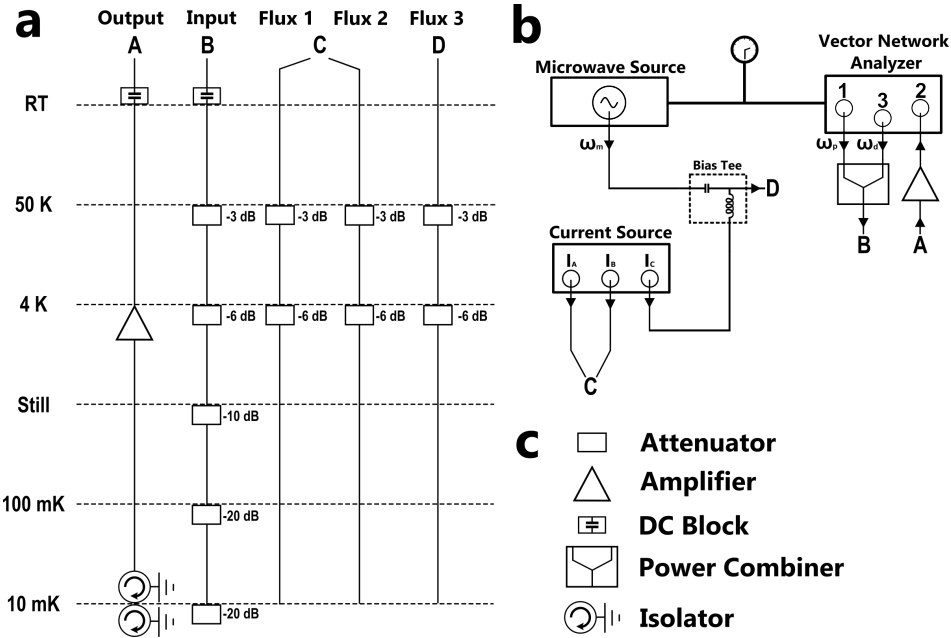


Figure 4.5: Measurement setup for the experiment. (a) Wiring configuration from the top of the dilution refrigerator to the device. The input and flux lines are attenuated before reaching the device, while the outgoing signal passes through two isolators and is amplified before returning to the network analyzer. (b) Wiring configuration at the instrument rack. The device probe and drive signals are sent from ports 1 and 3 of the vector network analyzer (VNA), while the returning signal is further amplified before arriving at port 2. The DC signals sent to the flux lines are produced at a current source, with the coupler current modulated by a signal from an additional microwave source. The microwave source and VNA share a common reference clock signal. (c) Legend for microwave components.

The device in Fig. 4.1 (b) of the main text contains a transmission line with input and output for probing and driving of the qubits, two coplanar waveguide readout resonators, two transmon qubits with dedicated flux lines and (unused) drive lines, and the tunable coupler with a dedicated flux line. The device is the same as in Ref. [333], with elements defined on a NbTiN film deposited on a Si substrate, with the chip wirebonded to a printed circuit board mounted inside of a copper box, and the entire unit housed in a mu-metal shield for protection against external magnetic fields.

The measurement setup shown in Fig. 4.5 consists of a Keysight PNA N5222A network analyzer connected to the device transmission line for spectroscopy measurements as well as a Keysight E8257D signal generator connected to a bias tee to supply the modulation signal to the coupler flux line. The input and output lines had DC blocks installed at room temperature. The DC currents were supplied by a QuTech SPI Rack S4g current source module to the three flux lines. For amplification of the signal returning from the circuit, we used the Low Noise

Factory cryogenic amplifier LNF-LNC4_8C and a room temperature Narda-MITEQ amplifier in the 4-8 GHz range. The drive powers quoted in the main text are those at the output of the measurement instruments.

4.6.2. CIRCUIT QUANTIZATION

We begin by treating the circuit in the harmonic limit by neglecting the nonlinear contributions of the inductors. We can construct a Lagrangian for our circuit by defining the node basis as $\Phi^T = [\Phi_1, \Phi_2, \Phi_3, \Phi_4]$ with

$$\mathcal{L} = \mathcal{E}_C - \mathcal{E}_L = \frac{1}{2} \dot{\Phi}^T [\mathbf{C}] \dot{\Phi} - \frac{1}{2} \Phi^T [\mathbf{L}^{-1}] \Phi \quad (4.16)$$

where the capacitance and inductance matrices are written as

$$[\mathbf{C}] = \begin{pmatrix} C + C_{1g} & -C & 0 & 0 \\ -C & C + C_{2g} + C_c & -C_c & 0 \\ 0 & -C_c & C + C_{2g} + C_c & -C \\ 0 & 0 & -C & C + C_{1g} \end{pmatrix} \quad (4.17)$$

$$[\mathbf{L}^{-1}] = \begin{pmatrix} 1/L_1 & -1/L_1 & 0 & 0 \\ -1/L_1 & 1/L_1 + 1/L_c & -1/L_c & 0 \\ 0 & -1/L_c & 1/L_2 + 1/L_c & -1/L_2 \\ 0 & 0 & -1/L_2 & 1/L_2 \end{pmatrix}. \quad (4.18)$$

We perform a change of basis to express the first two normal modes of the circuit as what will become the transmon modes, $\Psi_A \equiv \Phi_1 - \Phi_2$ and $\Psi_B \equiv \Phi_3 - \Phi_4$. There exists a third normal mode associated with the coupler, as charge oscillations “slosh” across the circuit. We define this mode as $\Psi_S \equiv \frac{1}{2}(\Phi_1 + \Phi_2 - \Phi_3 - \Phi_4)$. There also exists a final zero-frequency “rigid” mode associated with the charging of all capacitors in unison, defined as $\Psi_R \equiv \frac{1}{2}(\Phi_1 + \Phi_2 + \Phi_3 + \Phi_4)$. The change of basis from Φ^T to $\Psi^T = [\Psi_A, \Psi_B, \Psi_S, \Psi_R]$ leads to the redefinition of the capacitance matrix as

$$[\mathbf{C}'] = \begin{pmatrix} \frac{C_{1g} + C_{2g}}{8} & 0 & \frac{C_{1g} - C_{2g}}{8} & \frac{C_{1g} - C_{2g}}{8} \\ 0 & \frac{C_{1g} + C_{2g} + 2C_c}{8} & \frac{-C_{1g} + C_{2g} + 2C_c}{8} & \frac{C_{1g} - C_{2g} - 2C_c}{8} \\ \frac{C_{1g} - C_{2g}}{8} & \frac{-C_{1g} + C_{2g} + 2C_c}{8} & C + \frac{C_{1g} + C_{2g} + 2C_c}{4} & \frac{-C_c}{4} \\ \frac{C_{1g} - C_{2g}}{8} & \frac{C_{1g} - C_{2g} - 2C_c}{8} & \frac{-C_c}{4} & C + \frac{C_{1g} + C_{2g} + 2C_c}{4} \end{pmatrix}. \quad (4.19)$$

We now treat the inductors as nonlinear elements with energy in reduced units of flux quanta, $\psi_i = \frac{2\pi}{\Phi_0} \Psi_i$. After defining the conjugate momenta as $Q_i = \frac{\partial \mathcal{L}}{\partial \dot{\Psi}_i}$, we perform a Legendre transformation and obtain

$$H = \frac{Q_A^2}{2\tilde{C}} + \frac{Q_B^2}{2\tilde{C}} + \frac{Q_S^2}{2\tilde{C}_S} + \frac{Q_R^2}{2\tilde{C}_R} + \frac{C_c C_{1g}^2}{4 \text{Det}[\mathbf{C}']} Q_A Q_B + \frac{1}{\tilde{C}_{ABS}} Q_S (Q_A - Q_B) \\ + \frac{1}{\tilde{C}_{ABR}} Q_R (Q_A + Q_B) - E_J^A \cos(\psi_A) - E_J^B \cos(\psi_B) - E_J^C \cos\left(\frac{\psi_A - \psi_B}{2} - \psi_S\right) \quad (4.20)$$

where

$$\tilde{C} = 4\text{Det}[\mathbf{C}'] [C_{1g} C_{2g} (C_{1g} + C_{2g}) + C_{1g} C_c (C_{1g} + 2C_{2g}) + C(C_{1g} + C_{2g})(C_{1g} + C_{2g} + 2C_c)]^{-1} \quad (4.21)$$

$$\tilde{C}_S = 2 \frac{C_{1g}(C_{2g} + 2C_c) + C(C_{1g} + C_{2g} + 2C_c)}{4C + C_{1g} + C_{2g} + 2C_c} \quad (4.22)$$

$$\tilde{C}_R = 2 \frac{C_{1g} C_{2g} + C(C_{1g} + C_{2g})}{4C + C_{1g} + C_{2g}} \quad (4.23)$$

$$\tilde{C}_{ABS} = 2 \frac{C_{1g}(C_{2g} + 2C_c) + C(C_{1g} + C_{2g} + 2C_c)}{C_{2g} - C_{1g} + 2C_c} \quad (4.24)$$

$$\tilde{C}_{ABR} = 2 \frac{C_{1g} C_{2g} + C(C_{1g} + C_{2g})}{C_{2g} - C_{1g}} \quad (4.25)$$

$$\text{Det}[\mathbf{C}'] = \frac{C_{1g} C_{2g} + C(C_{1g} + C_{2g})}{4(C_{1g}(C_{2g} + 2C_c) + C(C_{1g} + C_{2g} + 2C_c))}. \quad (4.26)$$

We can neglect the rigid mode entirely by shifting the charging energies of the transmons and coupler, account for the addition of inductive energy from the coupler to each transmon by taking $E_j^i \rightarrow E_j^i + E_j^C/4$ from here on, and express the Hamiltonian in the number basis as $N = \frac{1}{2e}Q$. We expand the cosine terms above and retain terms to fourth order, obtaining $H = H_T + H_S$ where

$$\begin{aligned} H_T = & 4E_C N_A^2 + \frac{E_J^A}{2} \psi_A^2 - U_A \psi_A^4 + 4E_C N_B^2 + \frac{E_J^B}{2} \psi_B^2 - U_B \psi_B^4 + E_C^C N_A N_B \\ & + \frac{4e^2}{\tilde{C}_{ABS}} N_S (N_A - N_B) - \frac{E_J^C}{4} \psi_A \psi_B - \frac{E_J^C}{2} (\psi_A - \psi_B) \psi_S \\ & - \frac{E_J^C}{64} \psi_A^2 \psi_B^2 + \frac{E_J^C}{96} (\psi_A^3 \psi_B + \psi_A \psi_B^3) - \frac{E_J^C}{16} (\psi_A - \psi_B)^2 \psi_S^2 + \frac{E_J^C}{12} (\psi_A - \psi_B) \psi_S^3 \end{aligned} \quad (4.27)$$

$$H_S = 4E_C^S N_S^2 + \frac{E_J^C}{2} \psi_S^2 - \frac{E_J^C}{24} \psi_S^4 \quad (4.28)$$

where H_T is the transmon Hamiltonian, H_S is the "sloshing" mode Hamiltonian, e is the electron charge, $E_C = \frac{e^2}{2} \left(\frac{1}{C} - \frac{C_R}{C_{ABR}^2} \right)$, $E_C^C = e^2 \left(\frac{C_c C_{1g}^2}{4\text{Det}[\mathbf{C}']} - \frac{C_R}{C_{ABR}^2} \right)$, $E_C^S = \frac{e^2}{2C_S}$, and $U_i = E_j^i/24 + E_j^C/384$.

We can now move to the harmonic oscillator basis by defining

$$\psi_A = \left(2 \frac{E_C}{E_J^A} \right)^{1/4} (\hat{a}^\dagger + \hat{a}) \quad (4.29)$$

$$\psi_B = \left(2 \frac{E_C}{E_J^B} \right)^{1/4} (\hat{b}^\dagger + \hat{b}) \quad (4.30)$$

$$\psi_S = \left(2 \frac{E_C^S}{E_J^S}\right)^{1/4} (\hat{s}^\dagger + \hat{s}) \quad (4.31)$$

$$N_A = i \left(\frac{E_J^A}{32E_C}\right)^{1/4} (\hat{a}^\dagger - \hat{a}) \quad (4.32)$$

$$N_B = i \left(\frac{E_J^B}{32E_C}\right)^{1/4} (\hat{b}^\dagger - \hat{b}) \quad (4.33)$$

$$N_S = i \left(\frac{E_J^C}{32E_C^S}\right)^{1/4} (\hat{s}^\dagger - \hat{s}) \quad (4.34)$$

for the two transmons A and B, and the sloshing mode given by S. The terms proportional to N^2 , ψ^2 , and ψ^4 describe uncoupled Duffing oscillators. The interaction terms solely between the transmons may be expressed in this basis as

$$E_C^C N_A N_B = \left(\frac{E_J^A E_J^B}{32E_C^2}\right)^{1/4} [(a^\dagger b + ab^\dagger) - (a^\dagger b^\dagger + ab)] \quad (4.35)$$

$$\begin{aligned} \frac{E_J^C}{64} \psi_A^2 \psi_B^2 = & \frac{E_J^C E_C}{8\sqrt{E_J^A E_J^B}} [a^\dagger a b^\dagger b + \frac{1}{2}(a^\dagger a + b^\dagger b) + \frac{1}{4}(a^{\dagger 2} b^2 + a^2 b^{\dagger 2})] \\ & + \frac{1}{4}(a^{\dagger 2} b^{\dagger 2} + a^2 b^2) + \frac{1}{4} a^\dagger a (b^{\dagger 2} + b^2) + \frac{1}{4} b^\dagger b (a^{\dagger 2} + a^2) \end{aligned} \quad (4.36)$$

$$\begin{aligned} \frac{E_J^C}{96} \psi_A^3 \psi_B = & \frac{E_J^C E_C}{48((E_J^A)^3 E_J^B)^{1/4}} [(a^\dagger b + ab^\dagger) + (a^\dagger b^\dagger + ab) + 2(a^\dagger + a)a^\dagger a(b^\dagger + b) \\ & + (a^{\dagger 3} b + a^3 b^\dagger) + (a^{\dagger 3} b^\dagger + a^3 b)] \end{aligned} \quad (4.37)$$

$$\begin{aligned} \frac{E_J^C}{96} \psi_A \psi_B^3 = & \frac{E_J^C E_C}{48(E_J^A (E_J^B)^3)^{1/4}} [(a^\dagger b + ab^\dagger) + (a^\dagger b^\dagger + ab) + 2(a^\dagger + a)b^\dagger b(b^\dagger + b) \\ & + (a^\dagger b^3 + ab^{\dagger 3}) + (a^\dagger b^{\dagger 3} + ab^3)] \end{aligned} \quad (4.38)$$

while those also involving the sloshing mode are written as

$$\begin{aligned} N_S(N_A - N_B) = & \frac{4e^2}{\tilde{C}_{ABS}} \left[\left(\frac{E_J^C E_J^A}{32E_C^S E_C}\right)^{1/4} ((a^\dagger s + as^\dagger) - (a^\dagger s^\dagger + as)) \right. \\ & \left. - \left(\frac{E_J^C E_J^B}{32E_C^S E_C}\right)^{1/4} ((b^\dagger s + bs^\dagger) - (b^\dagger s^\dagger + bs)) \right] \end{aligned} \quad (4.39)$$

$$\begin{aligned} \frac{E_J^C}{12} (\psi_A - \psi_B) \psi_S^3 = & \frac{1}{6} (E_J^C E_C (E_C^S)^3)^{1/4} \left[\frac{1}{(E_J^A)^{1/4}} (a^\dagger s^3 + as^{\dagger 3}) + \frac{1}{(E_J^B)^{1/4}} (b^\dagger s^3 s + bs^{\dagger 3}) \right] \end{aligned} \quad (4.40)$$

$$\frac{E_J^C}{16} \psi_A^2 \psi_S^2 = \frac{1}{4} \sqrt{\frac{E_J^C E_C E_C^S}{E_J^A}} (a^\dagger a + s^\dagger s + 2a^\dagger a s^\dagger s) \quad (4.41)$$

$$\frac{E_J^C}{16} \psi_B^2 \psi_S^2 = \frac{1}{4} \sqrt{\frac{E_J^C E_C E_C^S}{E_J^B}} (b^\dagger b + s^\dagger s + 2b^\dagger b s^\dagger s) \quad (4.42)$$

$$\frac{E_J^C}{8} \psi_A \psi_B \psi_S^2 = \frac{1}{2} \sqrt{\frac{E_J^C E_C E_C^S}{(E_J^A E_J^B)^{1/4}}} (s^\dagger s + \frac{1}{2}) [(a^\dagger b + a b^\dagger) + (a^\dagger b^\dagger + a b)] \quad (4.43)$$

Notably, the sloshing mode contributes small corrections to the transmon frequencies and hopping/squeezing interactions, as well as cross-Kerr effects between the transmons and the sloshing mode. Most transitions of the sloshing mode are far off-resonant from the transmon transition frequencies. However, the 0-3 transition of the sloshing mode is near-resonant for $\Phi_{DC} \approx 0.3\Phi_0$.

In the context of Eq. 4.12 and Eq. 4.14 from the main text, we then have for $i \in \{A, B\}$:

$$\omega_i = \sqrt{8E_J^i E_C} + \alpha_i - \frac{1}{4} \sqrt{\frac{E_J^C E_C E_C^S}{E_J^i}} \quad (4.44)$$

$$\alpha_i = -E_C \left[1 - \frac{E_J^C}{16} \left(\frac{1}{E_J^i} - \frac{1}{\sqrt{E_J^A E_J^B}} \right) \right] \quad (4.45)$$

$$\omega_S = \sqrt{8E_J^C E_C^S} + \alpha_S - \frac{1}{4} \sqrt{E_J^C E_C E_C^S} \left(\frac{1}{\sqrt{E_J^A}} + \frac{1}{\sqrt{E_J^B}} \right) \quad (4.46)$$

$$\alpha_S = -E_C^S \quad (4.47)$$

$$V = -\frac{E_J^C E_C}{8\sqrt{E_J^A E_J^B}} \quad (4.48)$$

$$J_{AC} = \frac{\pi\Phi_{AC}}{8\Phi_0} E_C^{J_{max}} \sin\left(\frac{\pi\Phi_{DC}}{\Phi_0}\right) \left[\left(\frac{4E_C^2}{E_J^A E_J^B} \right)^{1/4} - \frac{E_C}{12} \left(\frac{1}{((E_J^A)^3 E_J^B)^{1/4}} + \frac{1}{(E_J^A (E_J^B)^3)^{1/4}} \right) - \left(\frac{E_C^2 (E_C^S)^2}{E_J^{C^2} E_J^A E_J^B} \right)^{1/4} \right] \quad (4.49)$$

$$J_{n_A} = \frac{\pi\Phi_{AC}}{24\Phi_0} E_C^{J_{max}} \sin\left(\frac{\pi\Phi_{DC}}{\Phi_0}\right) E_C \left(\frac{1}{(E_J^A)^3 E_J^B} \right)^{1/4} \quad (4.50)$$

$$J_{n_B} = \frac{\pi\Phi_{AC}}{24\Phi_0} E_C^{J_{max}} \sin\left(\frac{\pi\Phi_{DC}}{\Phi_0}\right) E_C \left(\frac{1}{E_J^A (E_J^B)^3} \right)^{1/4} \quad (4.51)$$

$$J_{n_S} = \frac{\pi\Phi_{AC}}{2\Phi_0} E_{J_{max}}^C \sin\left(\frac{\pi\Phi_{DC}}{\Phi_0}\right) \left(\frac{E_C^2 (E_C^S)^2}{(E_J^C)^2 E_J^A E_J^B}\right)^{1/4} \quad (4.52)$$

$$V_{iS} = -\frac{1}{2} \sqrt{E_C E_C^S \frac{E_J^C}{E_J^i}} \quad (4.53)$$

where all E_J^i for the transmons and coupler are dependent on their static flux biases. For simulations of the system, we use $E_J^A/h = 21.97\text{GHz}$, $E_J^B/h = 21.02\text{GHz}$, $E_J^C/h = 7.75\text{GHz}$, $d_c = 0.051$, $C_1 = 39\text{fF}$, $C_2 = 39\text{fF}$, $C_{1g} = 61\text{fF}$, $C_{2g} = 87\text{fF}$, and $C_c = 20\text{fF}$ where E_J^i are the values at the zero flux points [333]. For $E_J^i \gg E_C^i$ as is the case for this device, Eq. 4.49 may be approximated as Eq. 4.10 given the small contributions to the coupling of the second and third terms. When simulating the system, the full expressions were used.

4.6.3. EXTRACTION OF COUPLINGS

We begin with the full system Hamiltonian given in Sec. 4.6.2. Most terms are fast-rotating in the frame of the drives, but the choice of modulation frequency can selectively activate certain interactions. Whether modulating at the sum or difference frequency $\omega_m = \omega_A \pm \omega_B$, we retain the static terms which account for the frequencies, self-Kerr, and cross-Kerr coupling of the two transmons. Neglecting higher-order interactions with negligible effect and the small contributions of the sloshing mode, we are left with two Kerr-nonlinear oscillators

$$H_{DC} = \omega_A a^\dagger a + \frac{\alpha_A}{2} a^\dagger a^\dagger a a + \omega_B b^\dagger b + \frac{\alpha_B}{2} b^\dagger b^\dagger b b + V a^\dagger a b^\dagger b. \quad (4.54)$$

When modulating at the difference and sum frequencies, we have in addition, the couplings given by

$$H_\Delta = (J_{AC} + J_{n_A} a^\dagger a + J_{n_B} b^\dagger b + J_{n_S} s^\dagger s)(a^\dagger b + a b^\dagger) \quad (4.55)$$

$$H_\Sigma = (J_{AC} + J_{n_A} a^\dagger a + J_{n_B} b^\dagger b + J_{n_S} s^\dagger s)(a^\dagger b^\dagger + a b) \quad (4.56)$$

which includes the occupation-dependent modifications of the single-photon hopping and two-mode squeezing interactions. In determining the total interaction strength under red and blue sideband modulation, we consider $\tilde{J}_{AC} = J_{AC} + J_{n_A} n_A + J_{n_B} n_B + J_{n_S} n_S$ where n_i are the photon number expectation values of each mode, simply fitting to the total strength of the observed interaction.

The presence of crosstalk between the flux ports could allow for the modulation of each of the two transmon SQUIDs, which would produce contributions to the interactions generated by the coupler alone [399, 400]. Thus, \tilde{J}_{AC} is the total strength of the hopping and squeezing interactions which we observe upon modulation of the flux signal incident on the coupler SQUID, however the magnitude of the observed interaction is likely not entirely due to the coupler alone. In previous measurements on this device reported in Ref. [333], the DC flux crosstalk was found to be approximately 10% between the flux ports of the coupler and those of each transmon.

We first compare our measurements to an analytical equation following the method of Ref. [365]. For the case of red sideband modulation, we use the real component of the level repulsion equation, which yields the system eigenfrequencies

$$\omega_\Delta = \frac{\omega_A + \omega_B}{2} \pm \sqrt{\left(\frac{\omega_A - \omega_B}{2}\right)^2 + \tilde{J}_{AC}^2} \quad (4.57)$$

Table 4.1: Parameters determined from comparison of spectroscopy measurements to level repulsion and level attraction models, as well as numerical simulations for the data shown in Fig. 4.2 and Fig. 4.3.

Extracted Parameters			
Name	Variable	RSB Value	BSB Value
Frequency of Transmon A	$\omega_A/2\pi$	6.471 GHz	6.705 GHz
Frequency of Transmon B	$\omega_B/2\pi$	4.713 GHz	5.573 GHz
Anharmonicity of Transmon A	$\alpha_A/2\pi$	-244.053 MHz	-241.252 MHz
Anharmonicity of Transmon B	$\alpha_B/2\pi$	-237.811 MHz	-236.367 MHz
Linewidth of Measured Transmon	$\kappa/2\pi$	2.439 MHz	1.299 MHz
Flux Bias of Transmon A	Φ_A/Φ_0	0.113	0.016
Flux Bias of Transmon B	Φ_B/Φ_0	0.479	0.320
Flux Bias of Coupler	Φ_{DC}/Φ_0	0.342	0.214
AC Modulation Strength	Φ_{AC}	$\Phi_{DC}/18.002$	$\Phi_{DC}/29.100$
Hopping / Squeezing	$\tilde{J}_{AC}/2\pi$	7.090 MHz	1.852 MHz
Cross-Kerr	$V/2\pi$	-6.787 MHz	-9.161 MHz

and under blue sideband modulation, the eigenfrequencies for level attraction are given by

$$\omega_\Sigma = \frac{\omega_A + \omega_B}{2} \pm \sqrt{\left(\frac{\omega_A - \omega_B}{2}\right)^2 - \tilde{J}_{AC}^2}. \quad (4.58)$$

Following Ref. [365], we can expand on Eq. 4.58 by including the self-Kerr and cross-Kerr terms to the system Hamiltonian. For oscillator A, these simply shift the frequency $\omega_A \rightarrow \omega_A + \alpha_A n_A + V n_B$ and vice-versa for oscillator B. Then, when the two-mode squeezing interaction is applied at the appropriate frequencies, we expect to observe regions of level attraction at frequencies ω_Σ shifted by the self-Kerr and cross-Kerr nonlinearities dependent on the oscillator states. The secondary set of eigenfrequencies shown in Fig. 4.3 reflects this shifted feature. Then, using Eq. 4.57 and 4.58, we obtain the coupling strengths shown in Table 4.1.

When performing the numerical simulations with QuTiP, we obtain the expectation value of the photon annihilation operator for either mode as well as the state occupation probabilities for the system subject to a drive $H_d = \epsilon_d(a^\dagger e^{-i\omega_d t} + a e^{i\omega_d t})$ when measuring qubit A and similarly $H_d = \epsilon_d(b^\dagger e^{-i\omega_d t} + b e^{i\omega_d t})$ for qubit B. The time evolution of the system is calculated under driving while sweeping the modulation frequency through either the red or blue sideband. The data for the full time evolution is then used to calculate the relevant expectation values once the system has reached a steady state, which is compared with the results of the analytical equations in Fig. 4.2 and Fig. 4.3.

Below are the results of numerical simulations performed with QuTiP, which show the relative change in the population of each state spanned by the ground and first excited states of the two oscillators as functions of drive and modulation frequency for red and blue sideband modulation [218]. The relative change is shown in arbitrary units, given that the change in population is dependent on the choice of qubit drive power in the simulation, which has not been fitted to the experimental data. The purpose of the qubit drive in these simulations is to reveal in a probative manner the effects of the couplings activated by parametric modulation, which were determined and shown in the main text of the chapter.

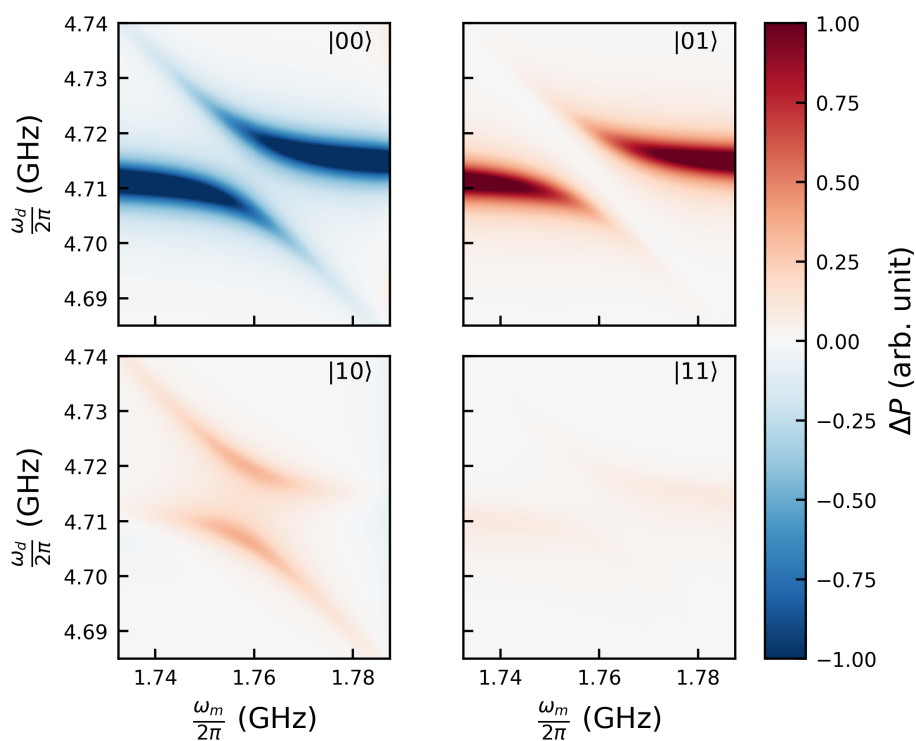


Figure 4.6: The relative change in population for each of the joint two-qubit states as predicted by QuTiP, given the parameters in Fig. 4.2 and with a small thermal occupation of each oscillator. Around the region of the avoided crossing, there is a relative increase in the $|01\rangle$ state as expected, correlated with a relative decrease in $|01\rangle$ populated by the drive away from the RSB modulation resonance condition.

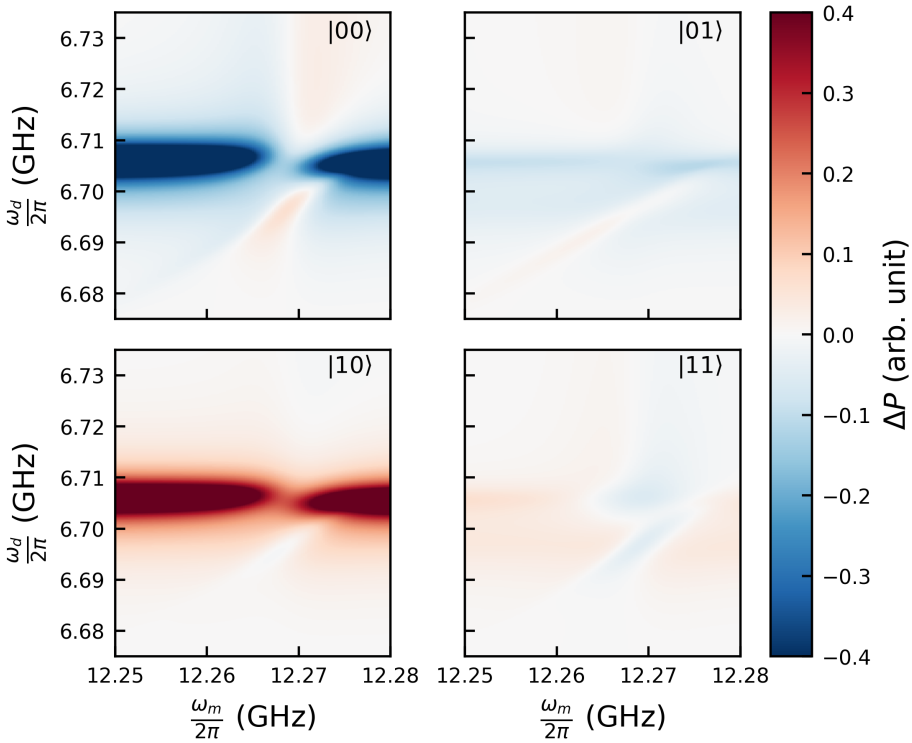


Figure 4.7: The relative change in population for each of the joint two-qubit states as predicted by QuTiP, given the parameters in Fig. 4.3 and with a small thermal occupation of each oscillator. Around the BSB modulation frequency, which activates the two-mode squeezing interaction, there is a relative increase in the $|00\rangle$ and $|01\rangle$ populations and an associated decrease in the $|10\rangle$ and $|11\rangle$ populations at the cross-Kerr shifted resonance condition. When the system is modulated on the BSB, driving at the cross-Kerr shifted frequency induces a relative population transfer down from the higher-level state occupied by the modulation.

5

SPECTROSCOPIC OBSERVATION OF A FEW-PHOTON PARAMETRIC STATE IN A KERR NONLINEAR OSCILLATOR

*If you want to be a different fish,
you've got to jump out of the school.*

Captain Beefheart

Driven-dissipative nonlinear oscillators have been utilized for a variety of important applications ranging from parametric amplification for quantum-limited signal detection to analog quantum simulations and digital quantum computation. The nonlinear oscillators frequently employed in Josephson junction-based quantum circuits continue to be the focus of physical inquiry beyond their practical applicability. Here, we present the response of a Kerr nonlinear oscillator to an all-microwave bichromatic two-photon drive and the associated dynamical phase transition. We analyze our results with a theoretical model derived from the classical parametrically driven Duffing oscillator and perform quantum master equation simulations, finding discrepancies between our results and those predicted by semiclassical methods.

J. D. Koenig, O. Ameye, S. Lécuyer-Seguineau, G. C. Arends, C. A. Potts, O. Zilberberg and G.A. Steele, *Spectroscopic Observation of a Few-Photon Parametric State in a Kerr Nonlinear Oscillator*, in preparation (2024).

5.1. INTRODUCTION

Driven-dissipative Duffing and Kerr nonlinear oscillators have a long history of physical study across a wide variety of fields, including nanomechanics, optics, electronics, and magnonics. [401–413]. These nonlinear oscillators are also ubiquitous in superconducting quantum circuits, from readout resonators to parametric amplifiers and transmon qubits. The vast disparity in exhibited behaviour and platforms with which these oscillators are realizable, along with their highly engineerable characteristics, couplings to other systems, and implementable driving and tomography schemes has sustained decades-long research interest in terms of both practical applications, quantum information processing, and inquiries into fundamental nonlinear and quantum physics [111, 116, 118, 414–421].

One defining parametrization of Kerr oscillators is the ratio of nonlinearity K to damping κ , with transmon qubits often used for superconducting quantum computation having high nonlinearity and low damping. In contrast, the opposite is true for the Josephson parametric amplifier (JPA) used for quantum noise-limited amplification and detection of weak signals [415, 416, 422, 423]. While devices operating in these two extremes have enjoyed a high degree of utility, the intermediate regime of nonlinearity and damping which includes the single-photon Kerr regime is also of physical interest given the ability to induce photon blockade, generate Schrödinger cat states, and serve as an alternative platform for quantum information processing and analog quantum simulation [191, 358, 424–429].

Driven-dissipative Duffing and Kerr nonlinear oscillators, especially those parametrically pumped, have been previously studied in contexts ranging from the generation of long-lived metastable states, observations of dissipative phase transitions, symmetry breaking and chaotic behaviour, as well as have provided insight into the nature of classical versus quantum transitions [385, 387, 429–442]. In particular, the parametrically driven Kerr oscillator is known to exhibit rich physics both near and above the parametric threshold, with proposals to use such systems to prepare superpositions of quasienergy states, implement Ising models, and enable dissipation-induced dynamical phase transitions [358, 443–445].

In this work, we observe a parametrically pumped Kerr nonlinear oscillator as it is driven into a parametric state. In this regime, the oscillator response is strongly modified about the frequency of the parametric tone, and we observe exceptional-point-like behaviour as the pump is swept in frequency. This provides evidence of the occurrence of a dynamical phase transition characterized by an exchange of the signal and idler modes about the parametric tone before and after the system is driven into a parametric state [445, 446]. We find agreement between this system and a rescaled effective model derived from the classical parametrically driven nonlinear oscillator which determines the response of the system under a variety of parametric drive strengths and detunings.

5.2. DEVICE AND BICHROMATIC DRIVING

Our device is a nonlinear microwave circuit consisting of a superconducting coplanar waveguide resonator with an embedded Josephson junction. A false-color micrograph of the device is shown in Fig. 5.1 (c) with a zoom-in of the Josephson junction in Fig. 5.1 (d). We can model the device, keeping terms up to fourth order, as a quantum Duffing oscillator with the Hamiltonian

$$\hat{H}_D/\hbar = \omega_0 \hat{a}^\dagger \hat{a} + \beta (\hat{a}^\dagger + \hat{a})^4 \quad (5.1)$$

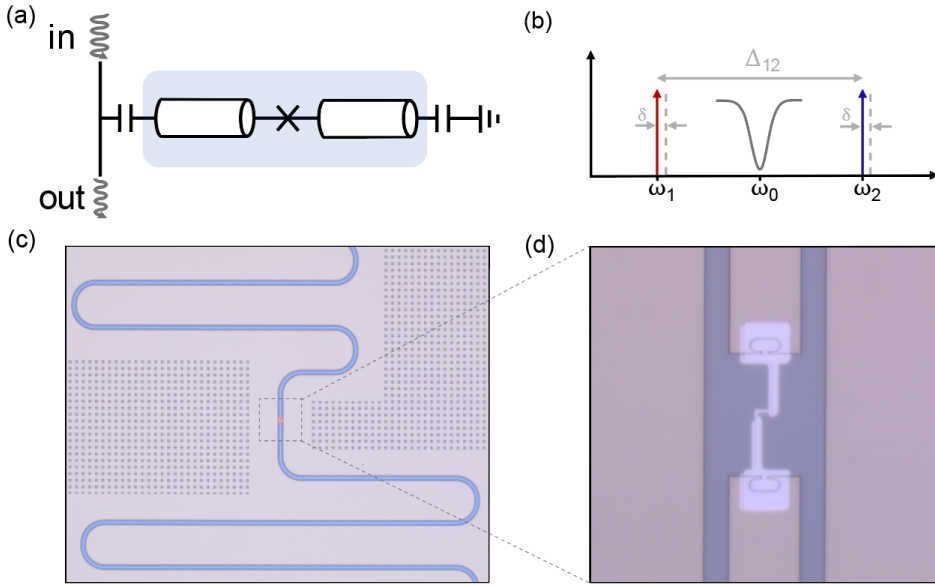


Figure 5.1: System and schematic of the experiment. (a) The oscillator is realized by a superconducting coplanar waveguide cavity with an embedded Josephson junction. (b) Two coherent microwave drives are applied to the device, with frequency spacing Δ_{12} and detuning of the midpoint of the drives from the oscillator resonance by δ . (c) A false color optical micrograph of the coplanar waveguide (blue) and Josephson junction (red). (d) The Josephson junction connects the two segments of the waveguide.

where ω_0 is the resonance frequency of the oscillator and β is the Duffing nonlinearity [215]. In this work, we focus on the third eigenmode of this resonator, which was engineered to have a nonlinearity slightly larger than its damping κ . We neglect the couplings of this mode to the other resonator normal modes, given that they are far detuned from the drives we apply in the experiment. Thus, their contributions to the system dynamics average out in a frame rotating at the oscillator frequency under the rotating wave approximation (RWA).

As depicted in Fig. 5.1, the nonlinear cavity is capacitively coupled on one side to a transmission line in a side-coupled geometry through which we drive and probe the system and monitor its output field. When measuring the transmission coefficient under a weak probe tone of frequency ω_{pr} , the theoretically expected response is a dip in transmission with a Lorentzian lineshape centered at ω_0 given by

$$S_{21} = 1 - \frac{\kappa_e}{\kappa + 2i(\omega_{pr} - \omega_0)} \quad (5.2)$$

where the linewidth is set by the total damping or decay rate $\kappa = \kappa_i + \kappa_e = 2\pi \times 322$ kHz, where $\kappa_e = 2\pi \times 275$ kHz and κ_i, κ_e are the internal and external decay rates, respectively. In this experiment, we apply two microwave drives of frequencies ω_1 and ω_2 to the system, with the drives separated by a spacing $\Delta_{12} = \omega_2 - \omega_1$. It has been previously shown that such a bichromatic scheme can be used to generate a parametric drive on the oscillator [215, 217]. In this scheme, illustrated in Fig. 5.1 (b), we parameterize our driven system in terms of

the detuning δ of the midpoint of the drives ω_p from the oscillator, where $\delta = \omega_p - \omega_o = \frac{(\omega_1 + \omega_2)}{2} - \omega_o$. Given the nonlinearity of the Josephson junction, the effect of these drives is to modulate the inductance of the junction near twice the resonance frequency of the oscillator, which realizes an effective two-photon pump or parametric drive of strength λ in a frame rotating at the parametric drive frequency ω_p .

At low bichromatic drive powers, the strength of the two-photon pump is insufficient to generate any parametric response in the oscillator. However, the oscillator response to each individual drive may be observed, as shown in Fig. 5.2 (a). As the two drives are swept in frequency at equal fixed powers, the cavity frequency shifts due to its nonlinearity as the intracavity photon number $n = \langle \hat{a}^\dagger \hat{a} \rangle$ increases as a result of the nearby drives. Such an effect is well understood in the Kerr nonlinear oscillator (KNO), to which the Duffing oscillator in Eq. 5.1 may be well approximated for $|\beta| \ll \omega_o$. The Hamiltonian of the KNO is given by

$$\hat{\mathcal{H}}_K/\hbar = \tilde{\omega}_o \hat{a}^\dagger \hat{a} + K \hat{a}^\dagger \hat{a}^\dagger \hat{a} \hat{a} \quad (5.3)$$

where $\tilde{\omega}_o = \omega_o - 2K = 2\pi \times 6.5477$ GHz and $K = 6\beta \approx 2\pi \times -523$ kHz is the self-Kerr nonlinearity. The oscillator frequency is then shifted by nK from its intrinsic undriven value. A second spectroscopic feature (the *idler*) appears as a peak in $|S_{21}|$, which can be seen in Fig. 5.2 (a), (b) on the opposite side of each drive with respect to the shifted oscillator frequency. Due to the interaction of the probe tone and drive with the KNO, two sidebands are generated at the shifted signal frequency and symmetrically spaced idler frequency, which are generated via a four-wave mixing process [374, 447].

5.3. SPECTROSCOPY OF A PARAMETRIC PHASE STATE

As the powers of the drives are increased, the frequency shift of the oscillator due to each nearby drive becomes more pronounced, and a new feature appears at the midpoint of the drives visible in Fig. 5.2 (b). Under the RWA and in a frame rotating at ω_p , we can rewrite the above Hamiltonian as the *Cassian* or Kerr parametric oscillator (KPO) Hamiltonian given by

$$\hat{\mathcal{H}}_{\text{KPO}}/\hbar = -\Delta_{\text{eff}} \hat{a}^\dagger \hat{a} + K \hat{a}^\dagger \hat{a}^\dagger \hat{a} \hat{a} + \frac{\lambda}{2} \hat{a}^{\dagger 2} + \frac{\lambda^*}{2} \hat{a}^2 \quad (5.4)$$

where Δ_{eff} is the effective detuning of the oscillator due to the drives and we have a parametric drive frequency detuning $\tilde{\delta} = \tilde{\omega}_o - \omega_p$ from the undriven oscillator frequency. Given that the oscillator experiences a frequency shift due to the two drives, the full expression of Eq. 5.4 is given in Sec. 5.6.2.

From the KPO Hamiltonian, we can calculate the eigenvalues of the dynamical matrix describing the excitation spectrum of the system, which determines the fluctuations around extremal points of the quasipotential defined by the above Hamiltonian [445]. These complex eigenvalues can be written as

$$\omega_{\text{KPO},0} = \pm \frac{1}{2} \sqrt{\Delta_{\text{eff}}^2 - \lambda^2} \quad (5.5)$$

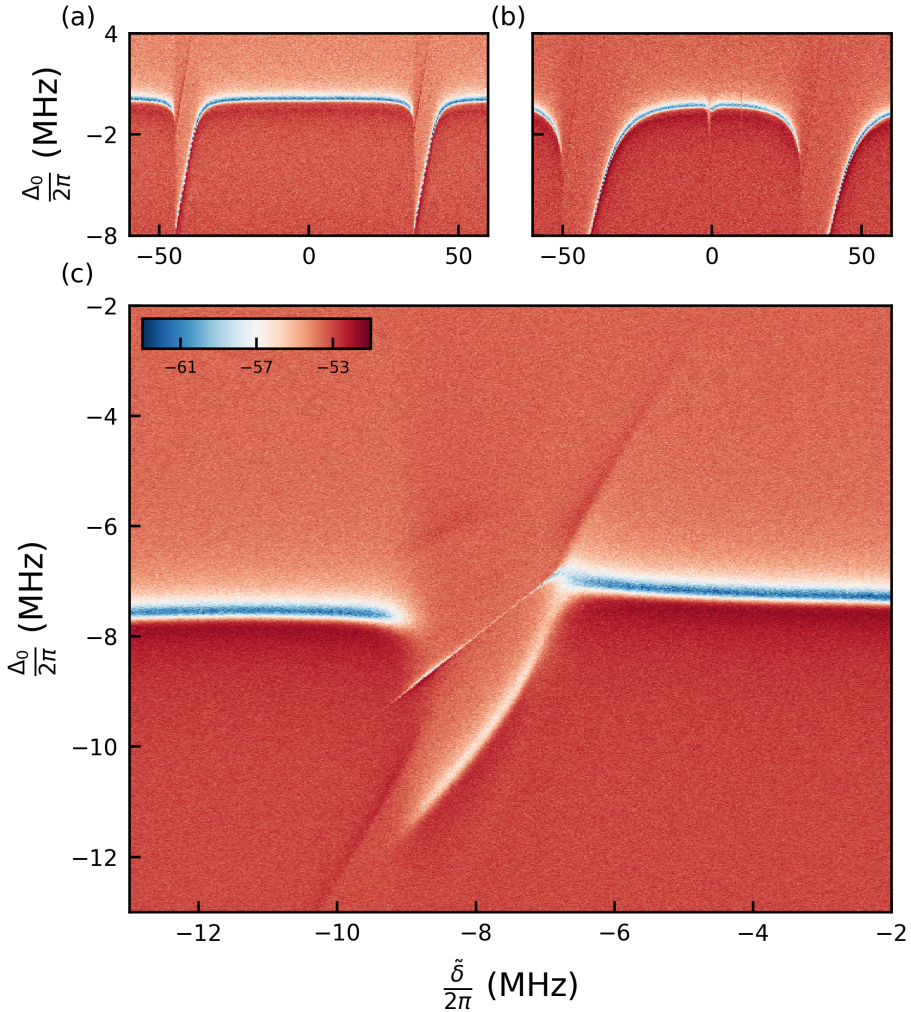


Figure 5.2: Observation of parametric oscillations in a bichromatically driven KNO. (a) The oscillator is probed by a weak signal at frequency ω_{pr} detuned from the undriven oscillator resonance frequency by $\Delta_0 = \omega_{pr} - \tilde{\omega}_0$ and bichromatically driven with a swept detuning of the center of the drives $\tilde{\delta}$, with power at the output of the generator $P_{out} = -20$ dBm and drive spacing $\Delta/2\pi = 80$ MHz. When each component of the bichromatic drive is far detuned, the linear response of the oscillator to the weak probe is a dip in the transmission magnitude $|S_{21}|$. However, as either drive approaches resonance, the oscillator bifurcates, and its frequency shifts with increasing intracavity photon number. In addition to the frequency-shifted signal mode, a second idler mode emerges symmetrically about the nearby drive as a peak in $|S_{21}|$, resulting from a four-wave mixing process between the probe tone and drive tone with the two sidebands generated by the cavity nonlinearity. (b) As the strengths of the two drives increase to $P_{out} = -8$ dBm, a modification of the oscillator response is observed near the midpoint of the drives. (c) At stronger drive powers $P_{out} = 12$ dBm, as the frequency of the midpoint of the drives is swept through the oscillator resonance, the response sharply narrows at the frequency of the parametric drive ω_p where each component of the bichromatic drive is positioned at $\omega_p \pm \Delta_{12}/2$ with $\Delta_{12}/2\pi = 200$ MHz yielding $\lambda/2\pi = 686$ kHz. The detunings $\tilde{\delta}$ where the modified oscillator response is observed are in good agreement with the drive parameters for which our rescaled effective model predicts a parametric response, as discussed in Sec. 5.6.2.

for the zero-amplitude (non-parametric) state and

$$\omega_{\text{KPO,par}} = \pm 2\sqrt{\lambda(\Delta_{\text{eff}} + \lambda)} \quad (5.6)$$

for the parametric (bistable) state. These eigenvalues provide insight into the stability of the system as well as the frequencies of the signal and idler modes under parametric driving. These eigenvalues fully determine which parametric drive detunings and strengths will produce a parametric response from the oscillator, with the zero-amplitude state dynamically unstable for $|\lambda| > |\Delta_{\text{eff}}|$ which yields exceptional points in the spectrum of the oscillator. The non-equilibrium stationary states which can be determined by this eigenvalue analysis have also been found to be quantum metastable states in certain parameter regimes [438, 448].

Upon closer inspection of this feature at the midpoint of the bichromatic drives in Fig. 5.2 (c), we observe the effect of the parametric driving on the oscillator. As ω_p nears the parametric resonance condition, the signal and idler modes appear to converge to a sharp dip in transmission, and we observe a narrow response feature at the frequency of the parametric drive. Symmetrically spaced about the excitation at ω_p , a dip and barely-visible peak in the transmission are additionally observed. As ω_p is further detuned, the signal and idler modes reappear swapped to opposite sides of the parametric drive frequency, following a small window of detunings where all five spectroscopic features are visible concurrently.

A similar effect has been previously observed in coupled KPOs subject to sum frequency driving, which induced a two-mode squeezing interaction (nondegenerate parametric oscillation) between the oscillators. It was shown that upon the application of an additional near-resonant drive, either mode became injection locked to the frequency of the secondary drive within a narrow window, while with a difference frequency drive, parametric locking was observed [384, 389]. In our system, we instead observe the formation of a distinct parametric state in which the response of a single KPO appears to converge to synchronize in frequency with the pump at ω_p , while in reality, it is driven into a parametric state with eigenfrequencies spaced about the midpoint of the bichromatic drives [445].

5.4. OCCURRENCE OF A DYNAMICAL PHASE TRANSITION

A theoretical analysis of the system for the applied parametric drive detunings and strength in Fig. 5.2 (c) shows that the signal and idler sidebands at positive and negative frequencies relative to ω_p correspond to the nondegenerate imaginary parts of the KPO Hamiltonian eigenvalues [445]. In contrast, the degenerate real parts relate to the decay rates of each sideband mode. When a KPO is driven into a squeezed state, the imaginary parts become degenerate and zero-valued, while the real parts diverge and become nondegenerate. This nondegeneracy of the decay rates of the two modes is indicative of phase-dependent gain of the KPO as the steady-state fluctuations become overdamped in this parametric locking regime [445].

For low dissipation, the KPO would ordinarily acquire at least one positive real eigenvalue, which causes the fluctuations to diverge and leads to instability as the system is driven beyond the parametric threshold into a region of the parameter space often referred to as an Arnold tongue or parametric lobe. When the KPO is driven above the threshold, it can instead acquire two stable steady-state solutions with equal amplitude and opposite phase, called *phase states*, while the previous zero-amplitude steady-state becomes unstable. Such a transition is known as a *pitchfork bifurcation* or *critical slowing down*, where the bifurcation is

supercritical as we enter the lobe and *subcritical* as we exit the lobe [216]. Depending on the drive parameters (in particular the detuning), the system may maintain the zero-amplitude state as a stationary state along with the phase states, in which case the system is said to be *tristable* [385, 387]. In this region, the system has nondegenerate imaginary components (frequency) and degenerate real components (decay rates) [445].

The effect of dissipation in the KPO is to push the parametric threshold to stronger drive powers, unveiling a region of the parameter space where the system can be parametrically driven below threshold to produce phase-dependent gain. The stability brought to the system by dissipative processes such as single-photon loss has led to the region to be called *dissipation stabilized* and transitions through this region to be called *dissipation-induced phase transitions* (DIPT) [445]. Within this region, which only exists in the presence of damping, the motion of the oscillator under these squeezed fluctuations is locked to the parametric drive at ω_p as the detuning is swept. In contrast, on either side of the region, the signal and idler mode frequencies are exchanged relative to ω_p .

This exchange of the signal and idler modes is evidence that a dynamical phase transition has occurred and is related to the fact that the monostable zero-amplitude states of the system on either side of the dissipation-stabilized and parametric regimes are dynamically different. For weak parametric drive strengths and large detunings, the KPO Hamiltonian potential resembles a single well, with the stationary state the zero-amplitude monostable state of the system. After the parametric drive is swept in frequency through the dissipation-stabilized regime, the KPO Hamiltonian potential changes to an inverted well. Thus, after the transition has occurred, the steady-state is the state which would be - in the absence of dissipation - the excited state of the KPO driven into tristability [445].

For the response shown in Fig. 5.2 (c), the oscillator transitions through each of the regimes discussed above. Initially, the system is monostable, but as the parametric drive is swept in frequency, it briefly becomes squeezed, followed by an extended window where it is bistable between approximately $\tilde{\delta}/2\pi = -7$ MHz and -9 MHz. This bistability is resolved spectrally by the appearance of sidebands on either side of the response at ω_p , with the sideband corresponding to a dip in transmission more visible. For a small range of detunings near $\tilde{\delta}/2\pi = -9$ MHz, the signatures of the inverted monostable state coexist with the bistable state, indicating that the system becomes tristable. After this, the system is in the inverted monostable state, evidenced by the exchange in signal and idler frequencies relative to ω_p .

The exchange of frequencies and corresponding inversion of the steady-state potential after undergoing such a dynamical phase transition can be seen as a sign inversion of the symplectic norm of the excitation spectrum eigenvalues [216, 445]. This inversion can also be seen as an excitation changing from particle-like to hole-like in nature or the transition from a positive-mass particle in a well to a negative-mass particle in an inverted well [445]. A similar phenomenon was recently observed in a strongly driven, weakly nonlinear optomechanical system, where an inversion was observed as a change from a positive mass to an effective negative mass oscillator [449].

In order to fully determine the dynamics of this system under bichromatic driving, we derive an effective model from the semiclassical equations of a Duffing oscillator subject to two drives with a fixed spacing Δ_{12} . We may then solve for the steady-state response of the sys-

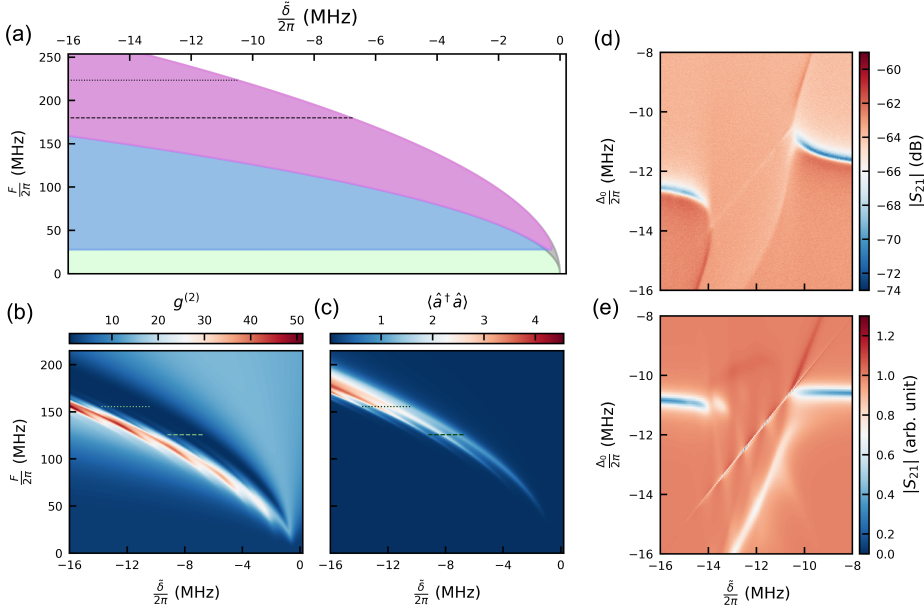


Figure 5.3: Expected response of the system based on an effective model Hamiltonian (a) The semi-classical stability diagram of the system given the device parameters and analytical steady-state solutions of the mean-field equations shown in Sec. 5.6.2. The grey region indicates the dissipation-stabilized regime, purple indicates bistability, blue indicates tristability, white indicates zero-amplitude monostability, and green indicates inverted monostability. (b), (c) The second-order correlation function $g^{(2)} = \langle \hat{a}^{\dagger 2} \hat{a}^2 \rangle / \langle \hat{a}^\dagger \hat{a} \rangle^2$ and photon number expectation value $\langle \hat{a}^\dagger \hat{a} \rangle$ determined from a numerical simulation of the rescaled effective model Hamiltonian as discussed in Sec. 5.6.2. The dashed and dotted lines indicate the approximate parametric drive strengths corresponding to the range of detunings which provided a parametric response in the datasets shown in Fig. 5.2 (c) and in (d) of this figure, respectively. (d) Spectroscopic response of the device with $P_{Out} = 16$ dBm and $\Delta_{12}/2\pi = 200$ MHz yielding $\lambda/2\pi = 993$ kHz. (e) QuTiP spectroscopy simulation of the oscillator at the parametric drive settings indicated by the green dotted lines in (b), (c).

tem as a function of drive parameters. From this model outlined in Sec. 5.6.2, we can obtain the predicted parametric drive strength and drive-induced frequency shift of the oscillator in terms of the nonlinearity and coherent fields of the two drives.

From this model, we can determine the number of stable and unstable solutions of the oscillator under bichromatic driving for any set of drive frequencies and strengths, as shown in Fig. 5.3 (a). The white region marks the region with the monostable zero-amplitude steady-state solution, the grey marks the region of dissipation-induced stability and squeezing, the purple indicates the region of bistability in which the stationary states of the KPO are \mathbb{Z}_2 symmetric phase states, blue marks the region of tristability, and green marks the region with the inverted monostable state [445].

The black dashed and dotted lines in Fig. 5.3 (a) indicate the predicted range of detunings for which a parametric response is produced in a measurement starting with ω_p at positive de-

tuning swept toward negative frequencies. We mark the beginning of the parametric response as occurring at the force for which we observe a modification of the oscillator response spectroscopically, which is the point where the signal and idler modes converge. The semiclassical effective model predicts that the device will continue to produce a parametric response to large negative detunings, a result which is in disagreement with experimental observations. Given that the width of the region of parametric response is 4λ per Eq. 5.6, we determined that the value of λ predicted by the effective model was too large for the observed detunings at which a parametric response was produced and the observed frequency shifts of the oscillator from the bare, undriven frequency. Thus, for quantitative analysis, we applied a rescaling factor to the two-photon pump strength, as discussed in Sec. 5.6.2.

In Fig. 5.3 (b), (c) we plot the second-order correlation function $g^{(2)}$ and photon number expectation value $\langle \hat{a}^\dagger \hat{a} \rangle$ numerically calculated with QuTiP [218] as a function of effective bichromatic drive force and parametric detuning with the rescaled expression for the two-photon pump strength. The dashed and dotted lines indicate the detunings of modified response for the spectroscopy measurements in Fig. 5.2 (c) and Fig. 5.3 (d), respectively, for the forces which provided the closest agreement between simulation and data. In Fig. 5.3 (b), (c), we observe peaks occurring at spacings of $2K$ corresponding to multi-photon resonances as expected theoretically [390].

Abrupt changes in $g^{(2)}$ and $\langle \hat{a}^\dagger \hat{a} \rangle$ are known to be markers of dissipative phase transitions, while values of $g^{(2)} < 1$ indicate sub-Poissonian statistics which coincide with the regions of multistability [390]. A peak in $g^{(2)}$ was previously used to identify the occurrence of a first-order dissipative phase transition in a similar system [438]. In Fig. 5.3 (d), we show the results of a spectroscopy simulation performed with QuTiP for a sweep of $\tilde{\delta}/2\pi$ at $F/2\pi$ corresponding to the value at the dotted green line. We find that the range of detunings which provide a parametric response matches with experimental observations, albeit with deviations in the frequency shifts of the signal and idler modes. We ascribe the source of these discrepancies to the same effects outlined in Sec. 5.6.2 and note that an improved effective model is currently being developed in order to obtain closer agreement.

In Fig. 5.4 (a), (b), we display the measured output field power spectral density (PSD) for the drive detunings and powers corresponding to where the parametric response in Fig. 5.2 (c) was observed. Within the parametric response region, we observe a Lorentzian gain peak in the PSD and an oblong distribution in the 2D histogram of the output field quadratures, shown in Fig. 5.4 (b), (f) respectively. From the numerical simulations of the rescaled effective model in Fig. 5.3 (c), we expect the photon number of the state generated by the parametric drive to only be on the order of a few photons. In general, we expect small photon number states to be produced given that the device is operated in the *mesoscopic* nonlinear regime, where for $K/\kappa = 1.62$ and $\tilde{\delta}/2\pi = -8$ MHz it can be estimated that the device can support bistable states of size between $n = 2.55$ photons and $n = 7.65$ photons [428].

In Fig. 5.4 (c), (d) we plot the numerically simulated Wigner quasiprobability distribution for the zero-amplitude and small bistable states predicted by the rescaled effective model to correspond to the drive parameters which were used to obtain the measurements in Fig. 5.4 (e), (f) [223, 450]. Given the size of the small photon number signal relative to the added noise of the 1.5 K noise temperature cryogenic amplifiers in our measurement chain, such a bistable state is not expected to be resolvable without the use of a noise-limited parametric amplifier

at the output of the device or by following a more complex detection and analysis protocol [416, 417, 451, 452].

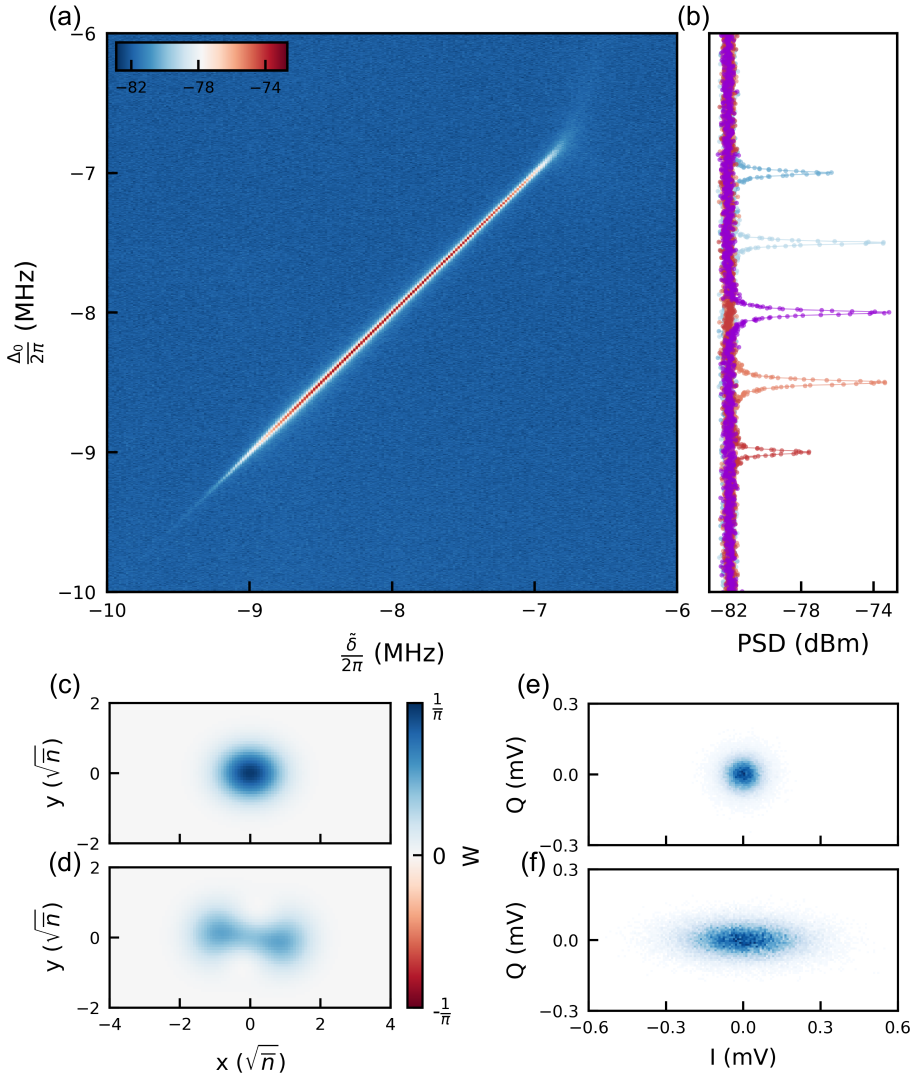


Figure 5.4: Output field spectrum, quadratures, and simulated Wigner functions while transiting the parametric regime (a) The output field power spectral density (PSD) as δ is swept through the region observed in Fig. 5.2 (c). (b) Linecuts from (a) at detunings $\delta/2\pi = -7$ MHz, -7.5 MHz, -8 MHz, -8.5 MHz, and -9 MHz from top to bottom. (c), (d) Wigner functions simulated for $\delta/2\pi = -5$ MHz and $\delta/2\pi = -8$ MHz for the system parameters determined from the rescaled effective model. (e), (f) Output field quadrature 2D histograms for $\delta/2\pi = -5$ MHz and $\delta/2\pi = -8$ MHz respectively.

5.5. CONCLUSION

In this chapter, we have presented spectroscopic and output field measurements, which show the effects of the application of a parametric pump generated by an all-microwave bichromatic driving scheme to a few-photon Kerr nonlinear oscillator. Spectroscopically, we observed a modification of the oscillator response at the midpoint of red-detuned bichromatic drives for sufficiently strong drive powers. These effects were observable in the shift of the oscillator from its bare frequency and the exchange of the signal and idler modes relative to the midpoint of the pump as the parametric response region was crossed indicating that a dynamical phase transition had occurred. Additionally, the appearance of modes on either side of the midpoint of the drives in the parametric response region was observed, as expected for a KPO driven into a bistable state. We also observed the coexistence of signatures of the monostable and bistable states spectroscopically, indicating that the system was driven into tristability.

We performed semiclassical analysis to derive an effective model of the system under bichromatic driving to determine the expected frequency shift of the oscillator and parametric drive strengths given the device and bichromatic driving parameters. We found discrepancies between the semiclassical approach and our observations, which indicated either deficiencies in the form of the equations of motion used, quantum mechanical effects not captured by the semiclassical techniques, or both. We applied a rescaling factor to the parametric drive strength predicted by the semiclassical approach and found agreement with the measurements with respect to the spectral positions of the observed modifications of the oscillator response due to parametric effects. Additional research is being done to further investigate these discrepancies.

Dissipative phase transitions have previously been investigated and experimentally observed in similar systems, where a sharp change in the expectation values of the driven mode is indicative of the occurrence of a phase transition and the transient dynamics of the bistable state were investigated [390, 391, 438, 439, 453–456]. Similarly, comparisons with semiclassical methods as well as the generalized Jaynes-Cummings model were used to analyze the response of a qubit-resonator system, where the nonlinear resonator operated in the $K < \kappa$ regime [391]. In contrast, we have investigated the steady-state response of the system spectroscopically as the parameters of bichromatic driving are swept, in the $K > \kappa$ regime. Previous measurements performed in the $K > \kappa$ regime showed that quantum fluctuations were significant in the system, leading to the identification of the out-of-equilibrium stationary states as quantum metastable states [438].

The reconstruction of the Wigner function of the few-photon parametric state is a natural next step to enable direct comparison of the system state with results determined from quantum master equation simulations. For example, it was recently demonstrated that the Wigner function of few-photon KPO states could be reconstructed from their output field spectra [452]. Recent theoretical work has also shown that the Wigner function can be determined from spectroscopic measurements following a scheme involving the application of a time-dependent drive field [457]. Such techniques would allow for further investigations into the relative contributions of classical and quantum effects to the dynamics of few-photon KPOs.

5.5.1. CONTRIBUTIONS

Author names are as given in the List of Publications. O.A. carried out the semiclassical theoretical analysis with the supervision of O.Z. J.D.K. designed and fabricated the device. J.D.K., S.L-S., and G.C.A. conducted the measurements with the supervision of C.A.P. and G.A.S. J.D.K performed the QuTiP simulations and O.A. performed the harmonic balance simulations. O.Z. and G.A.S. supervised the project. J.D.K. wrote the main text of the chapter and O.A. wrote the theoretical sections of the supplementary information, each with input from the authors. The NbTiN-coated Si wafer was provided by the Dutch Institute for Space Research (SRON). The authors acknowledge financial support by the EU program H2020-FETOPEN project 828826 Quromorphic. This contribution statement is tentative and may be changed prior to publication of these results.

5.6. SUPPLEMENTARY INFORMATION

5.6.1. EXPERIMENTAL SETUP

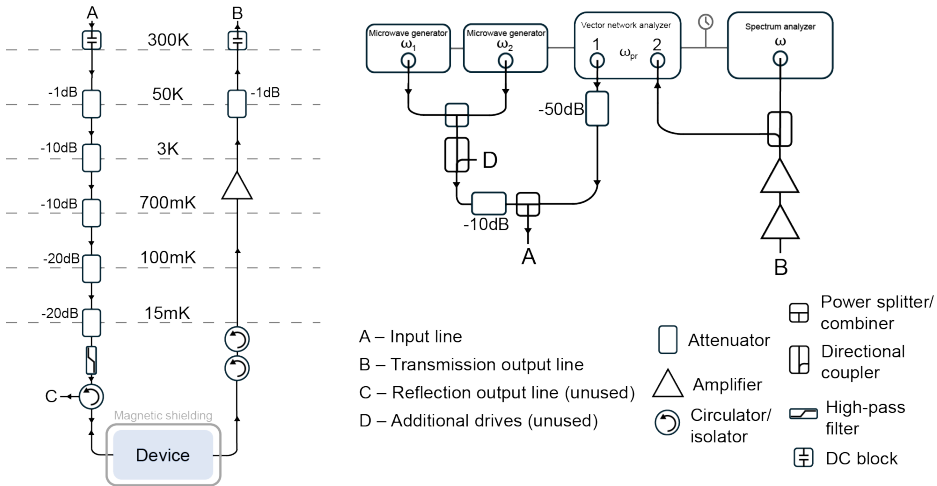


Figure 5.5: Experimental setup. (a) The device is mounted to the mixing chamber plate of a Bluefors dilution refrigerator and connected to our measurement instruments via coaxial cables. On the microwave input line, the signals are attenuated at each stage to varying degrees, with stronger attenuation at lower stages. The input signal then passes through a filter (Mini-Circuits VHF-3500+) and a circulator (Pasternack PE8402). The gold-plated copper box which houses the printed circuit board to which the device chip is connected is contained within a mu-metal magnetic shielding can. The box is also thermally anchored to the mixing chamber plate. On the output line, two terminated circulators (Pasternack PE8402) are placed between the device and the high electron mobility transistor (HEMT) amplifier (Low Noise Factory LNF-LNC4_8F) to reduce the thermal occupation of the device due to the thermal noise of the HEMT. DC blocks (BLKD-183-S+) are placed at room temperature on the input (A) and output (B) lines. (b) The bichromatic drives and probe tone are sent from two microwave generators (Rohde & Schwarz SGS100A) and a vector network analyzer (VNA) (Keysight N5221A PNA) through power combiners (Mini-Circuits ZFSC-2-10G+) into the input line of the fridge. An unused directional coupler (SM Electronics MC2045-10) is present in the drive line. The returning signal from the output line of the fridge is further amplified at room temperature (AT Microwave AT-LNA-0408-2501X) and passed through a directional coupler (Pasternack PE2CP1104) to the VNA and spectrum analyzer (Keysight N9010B EXA).

In Fig. 5.5, we show the experimental setup for the measurements performed on the device outlined in this chapter. The drive powers at the output of the measurement instruments corresponding to Fig. 5.2 (c) and Fig. 5.3 (d) are 12 dBm and 16 dBm respectively. For the drives, when accounting for the attenuators and insertion loss of components (approximately -80 dB), and attenuation of the cables used both at room temperature and cryogenic temperatures (approximately -20dB), we can compare the expected power at the device to the forces of the bichromatic drives predicted from the theoretical model.

Considering the detuning at which we first observe the emergence of a parametric response spectroscopically for each drive power configuration, we expect the two measurements to correspond to drive forces of $F/2\pi = 125.7$ MHz and 155.6 MHz for the $P_{out} = 12$ dBm and 16

dBm datasets respectively. We can calculate the expected drive strength at the device by $F = \sqrt{\frac{\kappa_e P_{dev}}{\hbar\omega}}$ where κ_e is the external linewidth of the oscillator, P_{dev} is the power at the device considering the total attenuation in the line, and ω is the frequency of the drive. From this, we can estimate values of $F/2\pi \approx 124.6$ MHz and 127.4 MHz for the higher frequency and lower frequency component respectively given $P_{out} = 12$ dBm, and values of $F/2\pi \approx 198.9$ MHz and 202.0 MHz given $P_{out} = 16$ dBm. While the expected forcing given the lower drive power dataset with $P_{out} = 12$ dBm agrees well with our rescaled theoretical model, there is a discrepancy of approximately 46.4 MHz (2.5 dBm) for the $P_{out} = 16$ dBm dataset.

We ascribe this discrepancy to the neglect of higher order effects of bichromatic driving in determining the effective parametric drive force and detuning with the semiclassical theoretical model, in particular those effects due to nonlinear mixing of the drives. In determining the effective model parameters, the responses at the two bichromatic drive frequencies are treated linearly, and back-action of the generated response at the midpoint of the drives to the drives themselves are not accounted for. Additionally, we apply a simple scalar factor to the effective parametric drive strength rather than a factor with parameter dependence (see Sec. 5.6.2). When comparing the agreement of the $P_{out} = 12$ dBm and $P_{out} = 16$ dBm drive powers to the model, it appears that this scaling factor becomes insufficient for increasing powers. When comparing to the detunings at which a parametric state first emerges in Fig. 5.2 (c) and Fig. 5.3 (d), the unscaled model predicts forces of $F/2\pi \approx 180$ MHz and 223 MHz (a difference of 1 to 3 dBm) respectively. However, the unscaled model predicts that the region of parametric response is sustained for far larger, negative detunings than what was observed experimentally.

5.6.2. EFFECTIVE MODEL

MEAN-FIELD EQUATIONS OF MOTION

In the following, units $\hbar = m = 1$ are taken. We consider the quantized phase space coordinates \hat{x} and \hat{p} . The Hamiltonian of our system is

$$H(\mathbf{x}, t) = \frac{\hat{p}^2}{2} + \frac{\omega_0^2}{2} \hat{x}^2 + \frac{\alpha}{4} \hat{x}^4 - F_c(\cos(\omega_1 t) + \cos(\omega_2 t))\hat{x} \quad (5.7)$$

where $\omega_1 = \omega_0 + \delta - \Delta/2$ and $\omega_2 = \omega_0 + \delta + \Delta/2$. In the main text above, Δ is written Δ_{12} . Our system is a nonlinear oscillator subject to two drives of equal force F_c separated by a frequency spacing Δ . The goal is to compute an effective time-independent Hamiltonian, which describes the parametric response at the midpoint of the pumps, at frequency $\omega_3 = \frac{\omega_1 + \omega_2}{2}$. For this, we employ a Floquet expansion as in Ref. [458, 459]. We begin by utilizing harmonic balance methods to analyze the system at the frequencies

$$\omega_1 = \omega_0 + \delta - \Delta/2, \quad \omega_2 = \omega_0 + \delta + \Delta/2 \quad \text{and} \quad \omega_3 = \omega_0 + \delta \quad (5.8)$$

The expansion can be understood as the result of measuring the system at three different frequencies with a lock-in amplifier [460].

The resulting mean-field equation of motion are

$$\begin{aligned} i\dot{\alpha}_1 &= (\Delta_1 - 2K_1)\alpha_1 + K_1|\alpha_1|^2\alpha_1 + 4K_1(|\alpha_2|^2 + |\alpha_3|^2)\alpha_1 + 2K_1\alpha_2^*\alpha_3^2 + F_1 \\ i\dot{\alpha}_2 &= (\Delta_2 - 2K_2)\alpha_2 + K_2|\alpha_2|^2\alpha_2 + 4K_2(|\alpha_1|^2 + |\alpha_3|^2)\alpha_2 + 2K_2\alpha_1^*\alpha_3^2 + F_2 \\ i\dot{\alpha}_3 &= (\Delta_3 - 2K_3)\alpha_3 + K_3|\alpha_3|^2\alpha_3 + 4K_3(|\alpha_1|^2 + |\alpha_2|^2)\alpha_3 + 4K_3\alpha_1\alpha_2\alpha_3^* \end{aligned} \quad (5.9)$$

where $\Delta_j = \frac{\omega_j^2 - \omega_0^2}{2\omega_j}$, $K_j = \frac{3\hbar\alpha}{8\omega_j^2}$ and $F_j = \frac{F_c}{2\sqrt{2\omega_j\hbar}}$ are the frequency rescaled detunings, nonlinearities, and forces. The steady-state solutions of the above system of equations can be calculated and are displayed as the boundaries between the parametric response regions in the main text of the chapter, Fig. 5.3 (a). These boundaries are also in agreement with the results of harmonic balance analysis performed with the HarmonicBalance.jl suite [461].

DERIVING AN EFFECTIVE HAMILTONIAN

By analyzing the equation for the coherent field at the midpoint of the pumps α_3 , we can see that it contributes an effective squeezing term

$$G_{\text{eff}} = 4K_3\alpha_1\alpha_2 \quad (5.10)$$

and frequency shift on the oscillator

$$\Delta_{\text{eff}} = 4K_3(|\alpha_1|^2 + |\alpha_2|^2). \quad (5.11)$$

Hence, we may consider the response of the system at ω_3 to be an effective Kerr parametric oscillator (KPO) with the Hamiltonian

$$H_{\text{eff}} = -(\Delta_{\text{eff}} - 2K_3)\hat{b}^\dagger\hat{b} + K_3\hat{b}^\dagger\hat{b}^\dagger\hat{b}\hat{b} + \frac{G_{\text{eff}}}{2}\hat{b}^\dagger\hat{b}^\dagger + \frac{G_{\text{eff}}^*}{2}\hat{b}\hat{b}. \quad (5.12)$$

However, to have a more complete effective model we require the contributions from the solutions of the coherent fields α_1 and α_2 which also depend on α_3 . This effective system is the same as can be found in Ref. [215]. The expression for G_{eff} and Δ_{eff} in terms of the parameters of the device can be derived using secular perturbation theory, however the following also yields the same result [462]. The bichromatically driven KNO Hamiltonian can be written as

$$H_{\text{Kerr}} = \tilde{\omega}_0\hat{b}^\dagger\hat{b} + K\hat{b}^\dagger\hat{b}^\dagger\hat{b}\hat{b} + F(e^{i\omega_1 t}\hat{b} + e^{i\omega_2 t}\hat{b} + h.c.) \quad (5.13)$$

where $\tilde{\omega}_0 = \omega_0 - 2K$ and $F_1 = F_2 = F$. Given that we want to determine the effective response of the Kerr oscillator at ω_3 , we perform a frame rotation following the transformation $\hat{b} \rightarrow \hat{b}_3 e^{-i\omega_3 t}$. In addition to integrating out the drives, we also apply a displacement transformation

$$\hat{b}_3 \rightarrow \hat{b}_3 + \alpha_1 e^{-i\omega_1 t} + \alpha_2 e^{-i\omega_2 t}. \quad (5.14)$$

Here α_j is the classical zeroth-order response for either drive with $\alpha_j \approx \frac{F_j}{\Delta_{3j}}$ with $\Delta_{3j} = \frac{\omega_3^2 - \omega_j^2}{2\omega_3}$ the rescaled detuning. Applying these transformations and averaging at ω_3 results in the following effective model

$$H_{\text{eff}} = -\tilde{\Delta}_{\text{eff}}\hat{b}^\dagger\hat{b} + \frac{\omega_0^2 K_0}{\omega_3^2}\hat{b}^\dagger\hat{b}^\dagger\hat{b}\hat{b} + \frac{G_{\text{eff}}}{2}\hat{b}^\dagger\hat{b}^\dagger + \frac{G_{\text{eff}}^*}{2}\hat{b}\hat{b} \quad (5.15)$$

where

$$G_{\text{eff}} = \frac{256F_3^2 K_3 \omega_3^2}{\Delta^4 - 16\Delta^2 \omega_3^2} = \frac{256F_0^2 K_0 \omega_0^3}{\omega_3 (\Delta^4 - 16\Delta^2 \omega_3^2)} \quad (5.16)$$

$$\tilde{\Delta}_{\text{eff}} = \tilde{\Delta}_{30} + \frac{512F_3^2 K_3 \omega_3^2 (\Delta^2 + 16\omega_3^2)}{(\Delta^3 - 16\Delta\omega_3^2)^2} = \frac{\omega_3^2 - \omega_0^2}{2\omega_3} - \frac{2K_0\omega_0^2}{\omega_3^2} + \frac{512F_0^2 K_0 \omega_0^3 (\Delta^2 + 16\omega_3^2)}{\omega_3 (\Delta^3 - 16\Delta\omega_3^2)^2} \quad (5.17)$$

with $F_o = F_3 \sqrt{\omega_3/\omega_o} = (\frac{3}{8} \sqrt{\frac{\omega_o^3}{3K_o}}) (\frac{\sqrt{\alpha} F_3 \varepsilon}{\omega_o^3})$ the effective force on the oscillator due to the two drives denoted F in the main text and $K_o = K_3 \omega_3^2/\omega_o^2$ the renormalized nonlinearity [460]. For the measurements performed in the main text of this chapter, all variables of this Hamiltonian are known with the exception of the force F_o , which uniquely determines the parametric drive strength G_{eff} (written λ in the main text) and the frequency shift of the oscillator $\tilde{\Delta}_{\text{eff}}$.

During the comparison of the theoretical predictions with experimental data, we observed that the boundaries between stability regions found from Eq. 5.9, the regions of parametric response indicated by Eq. 5.16, 5.17, and a numerical harmonic balance stability analysis of the system following Eq. 5.7 indicated regions of parametric response which were sustained for a wide range of parametric drive detunings $\tilde{\delta}$, which was not supported by the experimental data [461]. Numerical simulations performed with QuTiP following the effective Hamiltonian in Eq. 5.15 also produced these wide regions of parametric response at fixed values of F_o , which did not agree with experimental observations. However, a simple rescaling of Eq. 5.16 by a factor of ≈ 0.2 brought the regions of parametric response calculated by QuTiP close to agreement with the data shown in the main text of this chapter. The source of this discrepancy is the current focus of our theoretical studies, and we endeavor to resolve this disagreement prior to publication of these results. Given that the discrepancy exists also in the numerical harmonic balance stability analysis, we suspect that the source is in the omission of higher order effects, and due to the fact that our device satisfies $K > \kappa$ which in general is known to make semiclassical analysis techniques insufficient where quantum effects must be considered [390, 428, 438].

WIGNER FUNCTIONS AND STATE POPULATIONS UNDER PARAMETRIC DRIVING

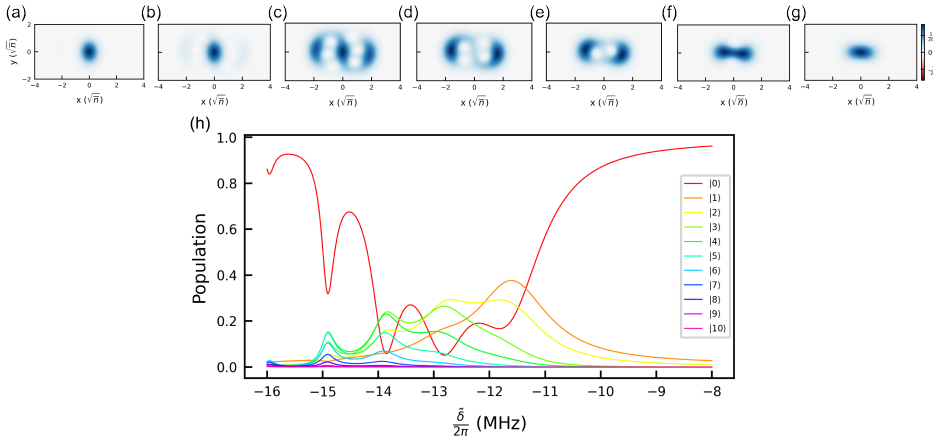


Figure 5.6: System state while traversing the parametric regime. (a), (b), (c), (d), (e), (f), (g) Wigner function of the system, given the effective Hamiltonian in Eq. 5.15, for drive detunings of $\tilde{\delta}/2\pi = -16$ MHz, -15 MHz, -14 MHz, -13 MHz, -12 MHz, -11 MHz, and -10 MHz respectively, for $F/2\pi = 155.6$ MHz. (h) The Fock state populations of the first ten energy levels of the system as the parametric drive frequency is swept.

Using the effective model, we can numerically simulate the Wigner function and Fock state population distribution for a variety of drive detunings and powers. In Fig. 5.6 we show a

subset of Wigner functions corresponding to the drive parameters displayed in Fig. 5.4 (d), where $F/2\pi = 155.6$ MHz, along with the expected Fock state populations. As the drive is swept towards larger negative detunings, the system state evolves from a squeezed monostable state to bistable, tristable, and lastly to a squeezed inverted monostable state.

6

BIASED SWITCHING DYNAMICS IN A PARAMETRICALLY DRIVEN KERR NONLINEAR OSCILLATOR

*And you may ask yourself,
"Well, how did I get here?"*

David Byrne

In recent years, the parametrically driven Kerr nonlinear oscillator (KNO) has been investigated for its relevance to various quantum information processing tasks. Quantum Kerr parametric oscillators (KPOs) have been studied as devices to be utilized for computation based on coherent and cat states, quantum annealing, and analog quantum simulations. The KPO has also been the focus of intense theoretical study, in particular with regards to the relative contributions of classical and quantum effects to the dynamics of non-equilibrium stationary states. Here, we show a KPO driven into bistability by the application of an all-microwave bichromatic two-photon drive. As the system stochastically switches between two phase states, we measure the change in switching time as a function of drive power and discuss the contributions of classical and quantum effects. In addition, we demonstrate control over the phase of the state upon the application of a symmetry-breaking weak resonant microwave drive.

J. D. Koenig, O. Ameye, L. R. van Everdingen, C. A. Potts, O. Zilberberg and G.A. Steele, *Biased Switching Dynamics in a Parametrically Driven Kerr Nonlinear Oscillator*, in preparation (2024).

6.1. INTRODUCTION

Nonlinearity is a highly desirable characteristic of engineerable classical and quantum oscillators, in large part due to the exploitable effects which are enabled by such oscillators upon the application of parametric driving. Nonlinear parametric oscillators have been used to great effect in the amplification of small signals with minimal added noise, the generation of squeezed states of light, and as integral components of quantum information processors [84, 194, 415, 416, 422, 423, 426, 463–465]. Parametric oscillators with Duffing or Kerr-type nonlinearities are well-known to have multistable stationary states when driven above the parametric threshold, where the strength of parametric driving exceeds the dissipation rates of the system. Such multistable states have been predicted and experimentally observed in nonlinear oscillators realized on a variety of platforms, ranging from microwave to optical, nanomechanical, magnonic, and optomechanical systems [398, 405, 406, 409, 432, 446, 466–488]

Systems driven into large-photon number multistable states have been the focus of great interest in recent decades, in particular with respect to their applications in quantum information processing [120, 358, 425, 426, 443, 457, 489–494]. The KPO Hamiltonian has so far been utilized to achieve these purposes in superconducting systems by introducing nonlinear junction elements (SNAILS) and by engineered dissipation [490, 495, 496]. In such systems, information has been encoded in the space spanned by linear combinations of bistable states, which can realize error-protected and noise-biased qubits with lengthy coherence times.

Prior to these recent works, the KPO had also been investigated for its unique physical properties, which dictate the system's dynamics. In particular, the processes by which the oscillator switches between multistable states have been found to have both classical and quantum mechanical contributions, from thermally-induced hopping as well as quantum activation via diffusion over quasienergy level states in each well and tunnelling through the barrier [434]. These contributions to the system dynamics from classical and quantum processes have been recently explored, finding that in devices with larger ratios of nonlinearity to dissipation semiclassical methods for predicting the switching rate fail, necessitating modelling with a full quantum master equation including stochastic noise processes [428].

6.2. DEVICE, BICHROMATIC DRIVING, AND BISTABILITY

Our device consists of two arrays of SQUIDs connected via a large capacitor, with one end shorted to ground and the other galvanically connected to a reflection measurement port, as shown in Fig. 6.1 (a), (b). Additionally, there is a separate drive line independent of the reflection port through which we apply drives via capacitive coupling to the junction array. This device is known as a Dimer Josephson Junction Array Amplifier (DJJAA), which may be operated as a parametric amplifier and hosts a series of amplification bands at the N normal modes of the circuit determined by the number of junctions in each array [193].

Provided that we do not drive at frequencies which induce interactions between our mode of interest and the off-resonant modes of the system, we can reasonably well describe the mode as a single Duffing oscillator, which may be approximated as a Kerr oscillator after neglecting fast-rotating terms with the Hamiltonian written as

$$\mathcal{H}/\hbar = \omega_0 \hat{a}^\dagger \hat{a} + K \hat{a}^\dagger \hat{a}^\dagger \hat{a} \hat{a} \quad (6.1)$$

where $\omega_0/2\pi = 4.604$ GHz is the bare oscillator frequency, with $K/2\pi \approx -10.571$ kHz, total

linewidth $\kappa/2\pi = 15.825$ MHz and external linewidth $\kappa_e/2\pi = 6.043$ MHz [193]. The linear response of the system to a weak probe tone is a dip in $|S_{11}|$ as shown in Fig. 6.1 (c). This dimer is the second normal mode of the device and the lower frequency component of the dimer is spaced approximately 560 MHz away. Additional information regarding the device is given in Sec. 6.6.1.

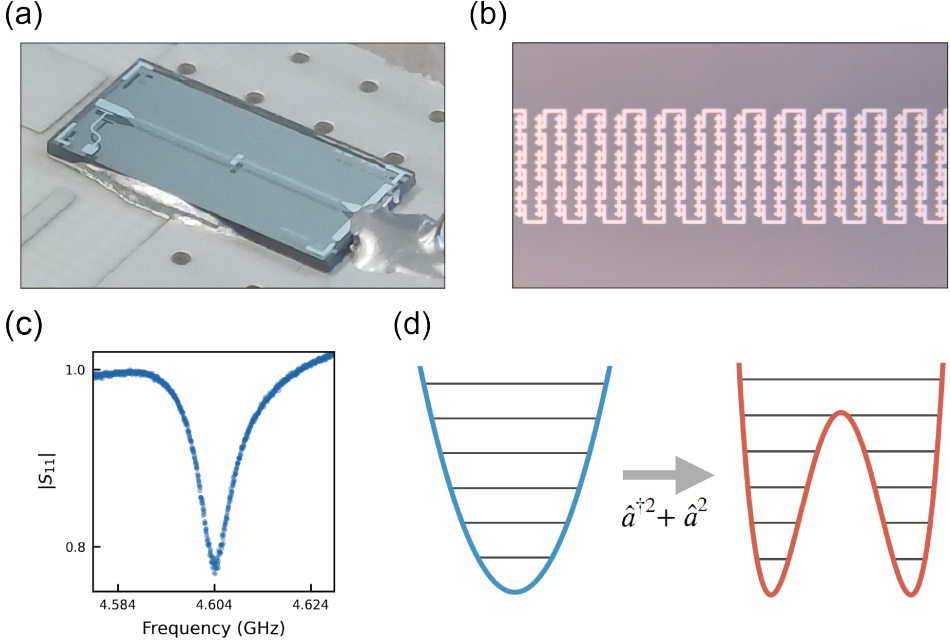


Figure 6.1: Device and system. (a) The device is a Josephson junction array amplifier with a reflection port and drive line wirebonded to a printed circuit board, with a thermal connection to the board via silver epoxy. The photograph was taken before wirebonding. (b) A zoom-in of a section of the aluminium Josephson junction array. (c) A characteristic reflection measurement at low probe power exhibits a Lorentzian response centered at the natural frequency of a mode of the device. (d) A diagram illustrating the change in Hamiltonian function from a harmonic potential to the double-well KPO potential upon the application of a parametric drive which realizes a two-photon pump.

We consider the effect of two pumps at frequencies ω_1 and ω_2 , where $\Delta_{12} = \omega_2 - \omega_1$ and $\delta = \frac{(\omega_1 + \omega_2)}{2} - \omega_0$ are the inter-pump detuning and parametric drive detuning respectively. In a frame rotating at the frequency of the midpoint of the pumps, we may rewrite our effective Hamiltonian under the effects of bichromatic driving as

$$\mathcal{H}'/\hbar \approx -\Delta_{eff} \hat{a}^\dagger \hat{a} + \frac{\epsilon_p}{2} \hat{a}^{\dagger 2} + \frac{\epsilon_p^*}{2} \hat{a}^2 + K \hat{a}^\dagger \hat{a}^\dagger \hat{a} \hat{a} \quad (6.2)$$

where ϵ_p is the two-photon pump strength, the oscillator frequency is shifted by the field amplitudes of each pump to Δ_{eff} , and additional terms fast-rotating at frequency Δ_{12} may be neglected under the RWA for $\Delta_{12} \gg \epsilon_p$ [215].

The effect of applying two detuned pumps with their center frequency held near the oscillator is to induce a frequency shift proportional to pump strength and self-Kerr nonlinearity, as well as to generate a two-photon pump interaction. When the midpoint of the pumps aligns with the shifted oscillator frequency, we are left with the Cassinian or Kerr Parametric Oscillator (KPO) Hamiltonian given by

$$\mathcal{H}_c/\hbar = \frac{\epsilon_p}{2} \hat{a}^{\dagger 2} + \frac{\epsilon_p^*}{2} \hat{a}^2 + K \hat{a}^\dagger \hat{a}^\dagger \hat{a} \hat{a}. \quad (6.3)$$

The Hamiltonian function $V(x, y)$ of this system in the absence of dissipation, illustrated along one axis in Fig. 6.1 (d), takes the shape of a double-well with two valleys of equal depth at $(x, y) = (\pm\alpha_0, 0)$ where $\alpha_0 = \sqrt{\epsilon_p/2K}$ is the size of the coherent state with photon number $n = |\alpha_0|^2$. Their equal depths indicate that these two stationary states $|\pm\alpha_0\rangle$ where $\nabla V = 0$ are degenerate ground states of the Hamiltonian. Thus, our two-photon pumped Kerr-nonlinear oscillator can be driven into a parameter regime in which the two stable solutions of the system are states of equal amplitude and opposite phase, also known as the bistable KPO.

For weak nonlinearities relative to damping $\kappa \gg K$, the KPO can be well described by the classical equations of motion for a parametrically driven Duffing oscillator. In Sec. 6.6.2, we provide a theoretical description of the system from a classical perspective and identify the bichromatic drive parameter regimes in which the steady-states of the driven-dissipative system are single-valued and multistable. However, the intra- and inter-well dynamics have classical and quantum contributing factors, as will be discussed below [434, 497]. For example, while the parametric drive strengths and detunings that yield a bistable state of a given size can be well described by classical equations, in certain oscillator parameter regimes (i.e. $K \approx \kappa$ and $K > \kappa$), quantum mechanical effects must also be accounted for to fully capture the system dynamics as the steady-state photon numbers above the parametric threshold are low [390, 428, 452].

6.3. OUTPUT FIELD MEASUREMENTS OF A PARAMETRIC PHASE STATE

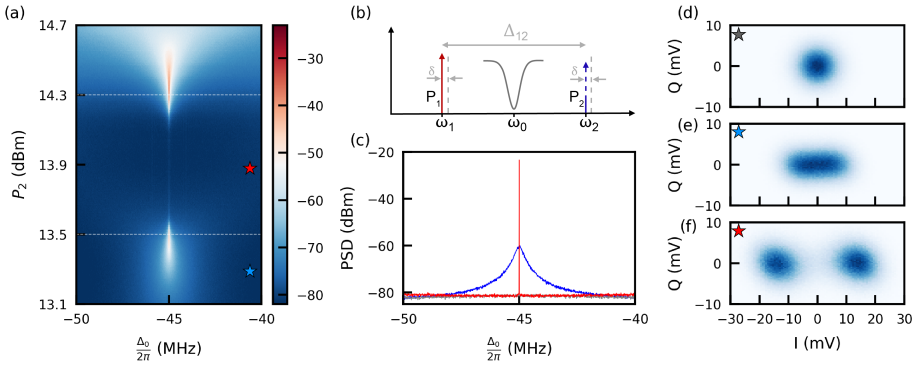


Figure 6.2: Transition from gain to bistability after crossing the parametric threshold. (a) As the effective parametric pump strength $\epsilon_p/2\pi$ increases with P_2 , the power spectral density (PSD) displays an increasing amount of gain in the output field of the device. In the region of parametric instability (approximately indicated by dashed lines), the output field spectrum is a narrow, high-amplitude peak. The frequency response is shown as a function of detuning $\Delta_0/2\pi$ from the undriven oscillator frequency. (b) The oscillator is bichromatically driven with two microwave tones, which realizes an effective parametric pump on the system. (c) Linecuts of the plot in (a) are representative of the PSD for a zero-amplitude state (grey), squeezed state (blue), and bistable state (red). (d) A histogram of the IQ quadratures of the device output field under low parametric drive strengths (zero-amplitude state), (e) under strong parametric driving below the instability threshold (squeezed state), and (f) upon crossing the parametric threshold (bistable state). Beyond the threshold, the output field changes from a squeezed state as it enters a bistable regime in which the oscillator stochastically switches between two coherent states of equal amplitude and opposite phase.

In order to bring the device into bistability, we first apply a bichromatic drive as shown in Fig. 6.2 (b) with the lower frequency (red-detuned) component of the pair with a fixed, high strength of $P_1 = 20$ dBm and sweep the higher frequency (blue-detuned) drive power P_2 . The inter-drive spacing is set to $\Delta_{12}/2\pi = 40$ MHz, and the center of the pumps is fixed to a value of $\delta/2\pi = -45$ MHz, which anticipates the negative frequency shift of the oscillator with increasing drive power. As the strength of the blue-detuned drive P_2 is increased, the effective parametric drive strength $\epsilon_p/2\pi$ grows, and the frequency of the primary oscillator response shifts into resonance with $\delta/2\pi$.

At this point, we observe gain in the PSD and squeezing of the output field IQ quadratures of the device as shown in Fig. 6.2, with the phase-dependent gain increasing with drive power. This is consistent with the frequency components of the dynamical eigenvalues (imaginary parts) of the system Hamiltonian becoming degenerate as the oscillator frequency synchronizes with the parametric pump tone at $\delta/2\pi$ [445]. This response occurs for a range of bichromatic drive strengths and detunings which coincide with the region where the same oscillator would be driven into multistability if it were a closed, undamped system. In this so-called *dissipation-stabilized* region, the presence of a large decay rate $\kappa/2\pi$ allows for a wide variety of parametric driving conditions which produce phase-dependent gain such as that seen

in Fig. 6.2 [445].

As the effective parametric drive strength increases, we continue to observe larger amounts of gain until the parametric threshold is reached, at which point the system is pushed into bistability. Beyond this threshold, we observe a narrow high-amplitude peak in the PSD and the formation of two distinctly separate phase states of equal and opposite amplitude in the IQ quadrature histograms, as shown in Fig. 6.2 (f). The linewidth of this narrow peak in the bistable regime is known to relate to the lifetime of the phase states sustained between stochastic switching events [467, 468, 498].

As the drive strength is further increased, we observe a return to phase-dependent gain as the system transits through the region of bistability. The parametric response phase space for this system shown in Sec. 6.6.2 is highly complicated. For some parametric drive parameters $\delta/2\pi$, $\Delta_{12}/2\pi$, and P_1 , the system would next return from a squeezed state to the zero-amplitude state with further increasing P_2 . For other values (generally for large drive powers and negative detunings of $\delta/2\pi$), the system may also exhibit chaotic behaviour as explored in Chapter 7.

6.4. STOCHASTIC SWITCHING AND PHASE CONTROL

An analysis of the switching rates in Fig. 6.3 within the bistability region shows a several order of magnitude increase in the time between switching events, from microseconds to seconds. At the optimal pump power for this value of $\delta/2\pi$, we observe an average amount of time spent in either bistable state of 3.25 seconds. The rate of increase and decrease of switching time with respect to drive strength is exponential, with a slower decrease from the maximal value compared to the increase from the onset of bistability. This qualitative dependence on P_2 is best understood through the relationship of switching time on the effective two-photon pump strength $\epsilon_p/2\pi$ in this region of the corresponding parametric response diagram, which predicts a bistable response. As discussed in Sec. 5.6.2, Sec. 6.6.2, and Chapter 7, this behaviour is strongly dependent on the choice of $\delta/2\pi$ and each of the drive strengths P_1 and P_2 which contribute to $\epsilon_p/2\pi$. Sweeping only the detuning or effective parametric drive strength alone does not allow one to continually evolve the system inside the region of bistable response with increasingly large photon numbers, but rather to transit through the bistable region.

While the boundary between the dissipation-stabilized region defined by phase-dependent gain and the bistable regime defined by the emergence of distinct phase states and stochastic switching is clear theoretically, we observe experimentally a continuous transition in the time-resolved output field IQ data. For example, in Fig. 6.3 (a), the fluctuations in voltage for each phase state are a significant portion of the amplitude of each phase state. It is only at higher parametric drive powers that the fluctuations become much smaller than the phase state amplitudes. Thus, for very small phase states, the output field quadratures that we measure may be obscured under the added noise of our measurement chain, in particular by the HEMT amplifier placed after the device output. When the signal of the small-photon number phase state is much smaller than the added noise of the HEMT amplifier, the bistable state only appears to be squeezed as the magnitude of fluctuations causes the states to seem to overlap in amplitude.

We may consider the contributions to this stochastic switching to be due to three effects: thermal hopping, quantum activation, and quantum tunnelling [499–502]. Switching due to

quantum tunnelling is expected to be rare except for extremely low oscillator damping rates, which is not the case for our device [500, 502]. Thermally activated switching events due to escape from metastable states are well understood to have an exponential form dependent on the system potential, given by Kramers [503, 504]. However, in KPOs cooled to $\hbar\omega \gg k_B T$, such thermal effects are expected to be negligible, and other factors should primarily cause switching events to occur.

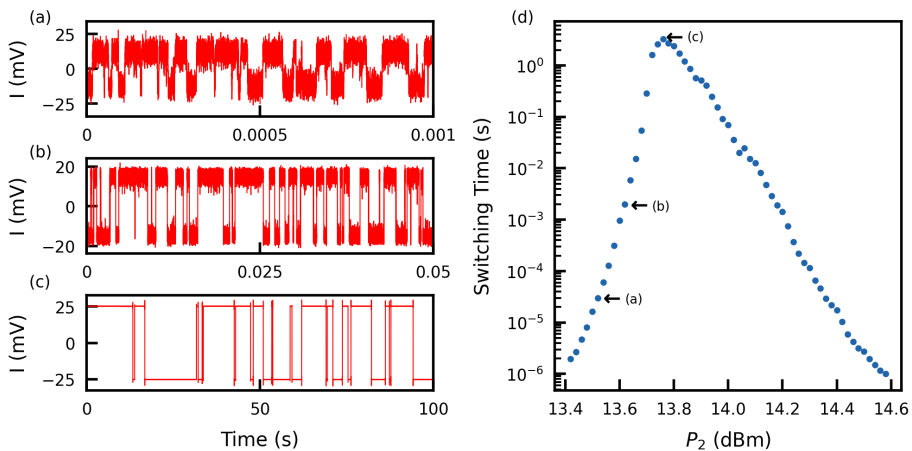


Figure 6.3: Exponential increase in the stochastic switching time of the oscillator bistable state with increased drive power. (a) After crossing the instability threshold, the system rapidly switches between two low-amplitude coherent states, where $P_2 = 13.52$ dBm. (b) As the parametric drive strength becomes greater, the switching time and amplitude of the phase states increases, where $P_2 = 13.62$ dBm. (c) At the optimal drive strength, the oscillator switches between phase states on the timescale of seconds, where $P_2 = 13.76$ dBm. (d) The switching time exponentially increases to a maximal value of 3.25 seconds between switches, after which it decreases as the parametric drive parameters become incongruous with the bistability lobe.

For low thermal occupations, *quantum heating*, which gives rise to the phenomenon of quantum activation, has been predicted to be a key contributor to switching dynamics in the KPO [434, 497]. In the non-rotating frame, the state of the system is a linear combination of Fock states for which an excited state relaxes over time to the ground state $|0\rangle$. However, in the parametrically driven rotating frame, which defines our KPO Hamiltonian, the system state is best described by quasienergy levels existing in each well defined by linear combinations of Fock states [434].

While relaxation mechanisms in Fock space lead to the occupation of the ground state, these same mechanisms (for example, single-photon loss) lead to larger occupations of lower levels, but also quantum heating up to higher quasienergy levels due to quantum noise [434, 505, 506]. This *diffusion* across levels leads to nonzero occupation of higher quasienergy states, which then switch stochastically to the corresponding quasienergy level of the opposite well and remain in that well until a diffusion-induced switching event again occurs. As the geometry of the potential depends on the parametric driving, the upward transition rates through

quasienergy levels are greater for weak driving, which leads to more switching events and lower for strong driving, at which a greater switching time is reached and switching events are rare, corresponding to further separation between the wells in phase space [434].

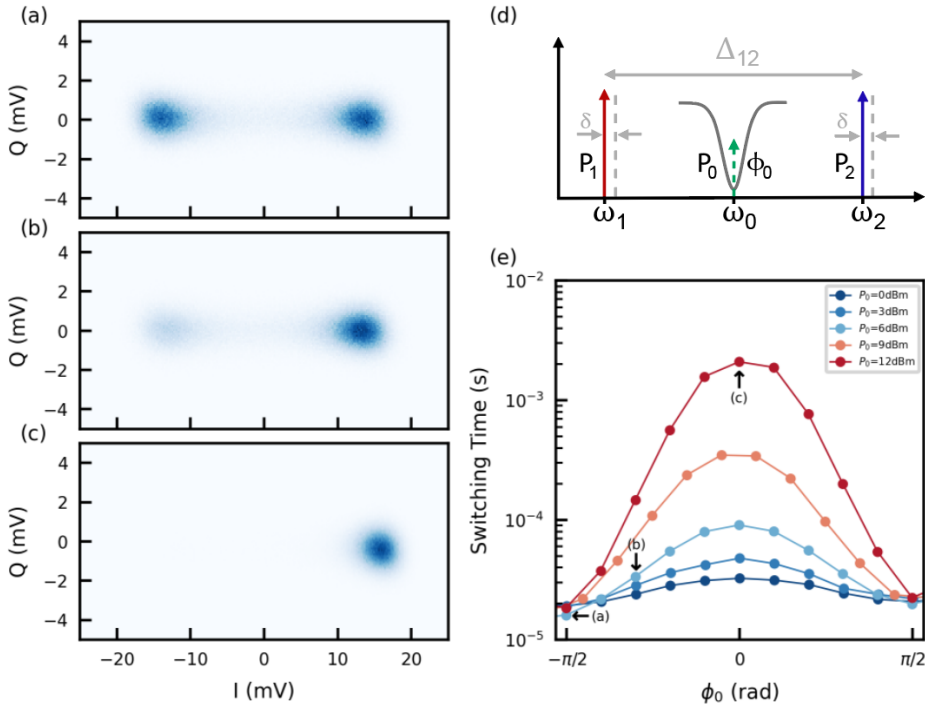


Figure 6.4: Observation of spontaneous Z_2 symmetry breaking under a weak, phase-biased resonant drive. (a) A histogram of the IQ quadratures of the device output field under a weak resonant drive, orthogonal to the axis of bistability. (b) As the strength of the drive is increased and brought close to phase-alignment with one of the states, the switching time increases and more counts are observed in the phase-aligned state rather than the state of the opposite phase. (c) At strong drive power and when driven in phase with one of the states, the switching time further increases, and the system is heavily biased into one of the two states. (d) In addition to the bichromatic drives, a weak, resonant microwave drive is applied to the bistable oscillator. (e) As the strength and phase of the drive are varied, the system can be phase-biased into either state. For strong phase-aligned drives, the switching time is increased by orders of magnitude. The bichromatic drive powers are fixed at $P_1 = 20\text{dBm}$ and $P_2 = 13.5\text{ dBm}$.

The expected switching rate for a parametrically driven nonlinear oscillator can be calculated given the device parameters and conditions of parametric driving. Further, the individual contributions to the switching rate from each of the mechanisms discussed above can be predicted [434, 502, 507, 508]. It is the focus of current theoretical work to calculate the contributions of each to the observed switching rates given the driving parameters in Fig. 6.3 (d). Once the expected switching rates due to thermal hopping, quantum activation, and quantum tunnelling are calculated, we intend to compare our results to the theoretically predicted values and determine the relative contributions of each effect. We expect this and other analyses

will enable us to determine the role of classical and quantum effects on the system as the oscillator evolves from a few-photon to a large photon number bistable state.

Once a bistable state has been prepared, one can lift the two-fold ground state degeneracy of the KPO with the application of a resonant drive with the form $\epsilon_o e^{i\phi_o} \hat{x}$. This biases the system preferentially into the $|\pm\alpha_o\rangle$ state for $\phi_o = \{0, \pi\}$ with resultant energy splitting between the ground states related to the strength of the drive and size of the phase states, causing one well to be lower in energy compared to the other [358, 429]. This biasing of the double-well potential creates an asymmetry in the switching rates, leading to an exponential increase in lifetime for the biased state due to the first-order $\sin(\phi_o)$ dependence of the upward transition rates over the well quasienergy levels [441].

In Fig. 6.4 (b), we illustrate the aforementioned bichromatic driving scheme with the addition of a weak resonant drive, which is varied in power P_o and phase ϕ_o . As the strength of this bias is increased with vector components aligned along the phase axis of the bistable states, the oscillator is biased into that particular phase-aligned state as the system potential is deformed. As one well becomes deeper and further nondegenerate with the other, the stationary state of the system approaches that of a single displaced coherent state as the probability of switching events is suppressed. In Fig. 6.4 (a) - (c), this effect is observed as the system is more strongly biased into the positive amplitude state with few observed counts in the IQ quadrature histograms at the negative amplitude position. Shown in Fig. 6.4 (e) is the phase-dependence of the switching time for various bias drive strengths, with more pronounced biasing observed for stronger drives.

6.5. CONCLUSION

We have parametrically driven a Kerr nonlinear oscillator into bistability and observed the device output field PSD and quadratures for a range of red-detuned bichromatic drive strengths. As the strength of the upper-frequency bichromatic drive was increased, we observed an exponential increase and decay in the time between stochastic switching events in the KPO phase states. The parameter regime in which a change in switching time occurs can be understood from a stability analysis of the parametrically driven Duffing oscillator, as shown in Sec. 6.6.2. The oscillator state is bistable for only a subset of possible bichromatic drive parameters. Depending on the detuning of the bichromatic drives and strength of the fixed lower frequency component, after performing a sweep of the upper-frequency drive power, the system may return to a monostable zero-amplitude state, or it may instead evolve into a multistable state with more than two stable solutions. This topic is explored further in Chapter 7.

Further, we showed control over the phase of the bistable state upon the application of an additional resonant drive. The modification of switching time with the application of a phase-biasing drive demonstrates a controllable deformation of the KPO Hamiltonian double-well potential. Such control enables one to stabilize the phase of the parametric state and mitigate noise, which could be used to enhance sensitive detection schemes based on phase-locked parametric oscillators (PPOs) [429, 473, 509, 510]. The application of a resonant drive breaks the time-translation symmetry between the parametric phase states, enabling the further investigation of new dynamical phases in parametrically driven quantum many-body systems [441, 511, 512].

In networks of coupled KPOs, such bias drives have been proposed to be used to investigate Boltzmann sampling in Ising machines enabled by quantum heating [513]. Additionally, the effects of bias drives on quasienergy states prepared by Landau-Zener-type transitions could be the topic of future study [443]. The KPO is an essential component for the implementation of a variety of proposed quantum information processing tasks, to which end a deeper understanding of its classical and quantum behaviour when subject to bichromatic and flux modulated parametric drives is a compelling topic of further study [358, 428, 429, 431, 433–436, 438, 446, 491, 492, 494, 514–516].

6.5.1. CONTRIBUTIONS

Author names are as given in the List of Publications. O.A. carried out the semiclassical theoretical analysis with the supervision of O.Z. L.R.vE. designed and fabricated the device. J.D.K. conducted the measurements with the supervision of C.A.P. and G.A.S. J.D.K. performed the QuTiP and harmonic balance simulations. O.Z. and G.A.S. supervised the project. J.D.K. wrote the chapter with input from the authors. The original design for the DJJAA was provided by the group of Ioan M. Pop at the Karlsruhe Institute of Technology. The authors acknowledge financial support by the EU program H2020-FETOPEN project 828826 Quomorphic. This contribution statement is tentative and may be changed prior to publication of these results.

6.6. SUPPLEMENTARY INFORMATION

6.6.1. EXPERIMENTAL SETUP

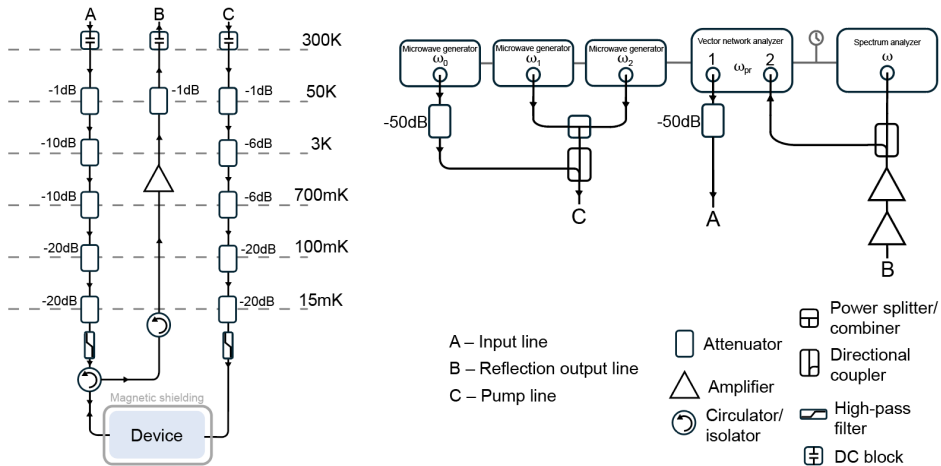


Figure 6.5: Experimental setup (a) The device is mounted to the mixing chamber plate of a Bluefors dilution refrigerator and connected to our measurement instruments via coaxial cables. On the microwave input line, the signal is attenuated at each stage to varying degrees, with stronger attenuation at lower stages. The input signal then passes through a filter (Mini-Circuits VHF-3500+) and a circulator (Paster-nack PE8402). The box which houses the printed circuit board to which the device chip is connected is contained within a mu-metal magnetic shielding can. A superconducting coil is attached directly to the bottom of the device packaging inside of the shielding and connected via a loom to room-temperature electronics for flux biasing of the device with a current source (Stanford RS CS580). The reflected signal returns to the circulator, then passes through an additional isolator (LNF-ISC4_8A) placed between the circulator and the high electron mobility transistor (HEMT) amplifier (Low Noise Factory LNF-LNC4_8F) to reduce the thermal occupation of the device due to the thermal noise of the HEMT. An additional pump line with reduced attenuation is connected to the dedicated drive port of the device, filtered (ZLSS-11G-S+) below the mixing chamber plate. DC blocks (BLKD-183-S+) are placed at room temperature on the input (A), output (B), and pump (C) lines. (b) The bichromatic drives are sent from microwave generators (Rohde & Schwarz SGS100A) and combined (Mini-Circuits ZFSC-2-10G+), which then pass through a directional coupler (SM Electronics MC2045-10) to which the resonant bias drive supplied from a third generator (Anapico APUASYN20) is coupled, and all drives are sent to the pump line. The probe tone is sent by a vector network analyzer (VNA) (Keysight N5221A PNA) through power combiners and into the input line of the fridge. The returning signal from the output line of the fridge is further amplified at room temperature (AT Microwave AT-LNA-0408-2501X) and passed through a directional coupler (Paster-nack PE2CP1104) to the VNA and spectrum analyzer (Keysight N9010B EXA).

In Fig. 6.5 we show the experimental setup for the measurements performed on the device in this chapter. The actual temperature of the mode measured depends on how well thermalized the sample is to the ≈ 20 mK mixing chamber stage. In addition to fits of stochastic switching rates to thermal effects in the bistable regime, additional measurements can be performed to determine the effective temperature of the mode under investigation in the future [322, 517–523].

The drive powers quoted in the main text are those at the output of the measurement instruments. When accounting for the attenuators and insertion loss of components (approximately -58.5 dB for the bichromatic drives and -114 dB for the bias drive), and attenuation of the cables used both at room temperature and cryogenic temperatures (approximately -20 dB), we can use the expected power at the device to obtain the bichromatic drive strengths predicted from the theoretical model. For the bias drive powers shown in Fig. 6.4, this corresponds to a sweep of estimated drive strength in frequency units from $F_0/2\pi = 3.54$ MHz to 14.10 MHz. For the bichromatic drive powers shown in Fig. 6.2, the values of P_1 and P_2 correspond to $F_1/2\pi = 21.25$ GHz and $F_2/2\pi$ from 9.56 GHz to 11.50 GHz. For the bichromatic drive powers of $P_1 = 20$ dBm and $P_2 = 13.5$ dBm used in Fig. 6.4, we estimate the parametric drive strength from Eq. 6.7 and obtain $\epsilon_p/2\pi = 23.17$ GHz. We note that this value is found without the application of a scaling factor as was done in Chapter 5, and that the effective parametric drive strength is likely much lower in reality for these bichromatic drive powers.

We can estimate the photon number in the bistable state with these drive parameters for an unbiased dissipative KPO following Ref. [496] using $n = \frac{1}{2K} \sqrt{(2\epsilon_p)^2 - \kappa^2}$ and find $n \approx 2.18 \times 10^6$ photons for the bichromatic drive powers used in Fig. 6.4 and $n \approx 2.25 \times 10^6$ photons for the bichromatic drive powers used in Fig. 6.3 (c). This corresponds to an exponential increase in switching time by a factor of $\times 4.88$ per photon, a scaling larger than the $\times 1.4$ per photon found in Ref. [496]. We can also estimate the bounds for generable photon numbers in the bistable state following Ref. [428], where $n_{\pm} = -\frac{\Delta_{\text{eff}}}{K} [1 \mp \sqrt{1 - \frac{3}{4}(1 + \frac{\kappa^2}{4\Delta_{\text{eff}}^2})}]$ which yields photon numbers between 1.90×10^6 and 5.76×10^6 photons for P_2 between 13.5 dBm and 13.76 dBm.

These values are estimates, given that we previously observed the need for corrections to account for higher order effects which necessitated the application of a scaling factor in Chapter 5. Here, the bichromatic drive powers used are much stronger than in Chapter 5, where effective parametric drive strengths were of order 1 MHz. Given this, we expect that the true values of $\epsilon_p/2\pi$ used in the experiment are lower than what we have calculated above. Further, harmonic balance analysis of this device indicates that one would achieve parametric responses for lower values of F_1 and F_2 , on the order of a few GHz, rather than 10-20 GHz. Additional unaccounted for attenuation is required for our applied drive powers to reconcile with the results of the harmonic balance analysis. However, another potentiality is that the forces and detunings for which our unscaled effective model and harmonic balance simulations predict parametric effects become unreliable for extreme drive conditions of large forces and detunings. This is expected, as HarmonicBalance.jl makes an RWA-like approximation that the drive forces are less than the frequency of the oscillator, which is not the case for such large powers as used in the experiment (provided there was not additional unknown attenuation). Nonetheless, the response of the system under extreme parametric driving to first order can be used to qualitatively determine whether it can in general be driven into states with large numbers of solutions using harmonic balance analysis, albeit for inaccurate drive forces and detunings. We endeavour to complete analysis of the system with an improved model accounting for higher order effects prior to publication of these results.

DJJA PARAMETERS

The DJJA was fabricated on a sapphire wafer of thickness $330 \mu\text{m}$ with a ground plane formed on the underside of the chip by a 150 nm platinum coating and 5 nm titanium layer. The end of the DJJA shorted to ground was galvanically connected to the ground plane by silver

epoxy. The junctions were formed by optical lithography to define each layer followed by two aluminium evaporation and liftoff processes. The first layer of aluminium was 30 nm thick and the second was 40 nm thick. Before deposition of the top layer, the first aluminium layer was cleaned by Ar ion milling prior to oxidation and deposition. The oxidation was performed at pressures of 30 mbar for 3 minutes and 15 seconds. The DJJAA consists of two sections of 800 SQUIDs capacitively coupled to each other by a large capacitor C_c . Each junction had a designed overlap area of $4 \mu\text{m} \times 4 \mu\text{m}$. DJJAAs fabricated at wafer scale varied from $R_N = 42.5\text{k}\Omega$ to $148.2\text{k}\Omega$ per half of the arrays.

The designs of the DJJAAs and thicknesses of the sapphire wafer and deposited aluminium were identical to those of Ref. [193] and have been reported on in Ref. [524]. However, the potential for small variations in realized feature sizes exists due to mismatches between fabricated and originally designed geometries. We take the same parameters as for Ref. [193] "Sample II" as a starting point and compare calculations of device mode frequencies to the frequencies of the measured modes of the DJJAA. The obtained values written in Fig. 6.6 imply smaller than designed overlap areas for this device, within the typical variation of $\approx 1\text{-}2 \mu\text{m}$ for our optical lithography processes.

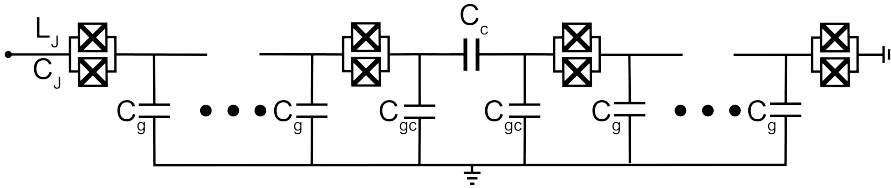


Figure 6.6: Circuit diagram of the DJJAA. We find good agreement with observed mode frequencies for $L_J = 103.25 \text{ pH}$, $L_s = 19.67 \text{ pH}$, $\gamma_L = 0.84$, $R_N^{in} = 77.40 \text{ k}\Omega$, $R_N^{out} = 78.55 \text{ k}\Omega$, $C_{gc} = 25 \text{ fF}$, $C_g = 0.26 \text{ fF}$, $C_c = 40 \text{ fF}$, and $C_J = 700 \text{ fF}$, where R_N^{in} and R_N^{out} are the resistances from the input port to the coupling capacitor and from the coupling capacitor to ground respectively, L_s is the stray inductance, and γ_L is the inductance participation ratio $\gamma_L = L_J / (L_J + L_s)$.

6.6.2. EFFECTIVE MODEL AND STABILITY ANALYSIS

In the following, units $\hbar = m = 1$ are taken. We consider the quantized phase space coordinates \hat{x} and \hat{p} . The Hamiltonian of the system is

$$H(\mathbf{x}, t) = \frac{\hat{p}^2}{2} + \frac{\omega_0^2}{2} \hat{x}^2 + \frac{\alpha}{4} \hat{x}^4 - (F_{1,c} \cos(\omega_1 t) + F_{2,c} \cos(\omega_2 t)) \hat{x} \quad (6.4)$$

where $\omega_1 = \omega_0 + \delta - \Delta/2$ and $\omega_2 = \omega_0 + \delta + \Delta/2$. In the main text above, Δ is written Δ_{12} . Our system is a nonlinear oscillator subject to two drives of unequal force $F_{1,c}$ and $F_{2,c}$ separated by a frequency spacing Δ . The goal is to compute an effective time-independent Hamiltonian, which describes the parametric response at the midpoint of the pumps, at frequency $\omega_3 = \frac{\omega_1 + \omega_2}{2}$. For this, we employ a Floquet expansion as in Ref. [458, 459]. We can utilize harmonic balance methods to analyze the system at the frequencies

$$\omega_1 = \omega_0 + \delta - \Delta/2, \quad \omega_2 = \omega_0 + \delta + \Delta/2 \quad \text{and} \quad \omega_3 = \omega_0 + \delta. \quad (6.5)$$

The expansion can be understood as the result of measuring the system at three different frequencies with a lock-in amplifier [460]. We analyze the response of the system at these three frequencies using the HarmonicBalance.jl suite [461].

We can derive an effective parametric drive strength and detuning as in Sec. 5.6.2 for unbalanced pumps and find the Hamiltonian

$$H_{\text{eff}} = -\tilde{\Delta}_{\text{eff}} \hat{b}^\dagger \hat{b} + \frac{\omega_0^2 K_0}{\omega_3^2} \hat{b}^\dagger \hat{b}^\dagger \hat{b} \hat{b} + \frac{G_{\text{eff}}}{2} \hat{b}^\dagger \hat{b}^\dagger + \frac{G_{\text{eff}}^*}{2} \hat{b} \hat{b} \quad (6.6)$$

where

$$G_{\text{eff}} = \frac{256 F_1 F_2 K_0 \omega_0^3}{\omega_3 (\Delta^4 - 16 \Delta^2 \omega_3^2)} \quad (6.7)$$

$$\tilde{\Delta}_{\text{eff}} = \frac{\omega_3^2 - \omega_0^2}{2\omega_3} - \frac{2K_0\omega_0^2}{\omega_3^2} + \frac{256K_0\omega_0^3 (F_1^2(\Delta + 4\omega_3)^2 + F_2^2(\Delta - 4\omega_3)^2)}{\omega_3 (\Delta^3 - 16\Delta\omega_3^2)^2} \quad (6.8)$$

with $F_i = \frac{F_{i,c}}{2\sqrt{2}\omega_i \hbar}$, $K_i = \frac{3\hbar\alpha}{8\omega_i^2}$, and K_0 written as K in the main text.

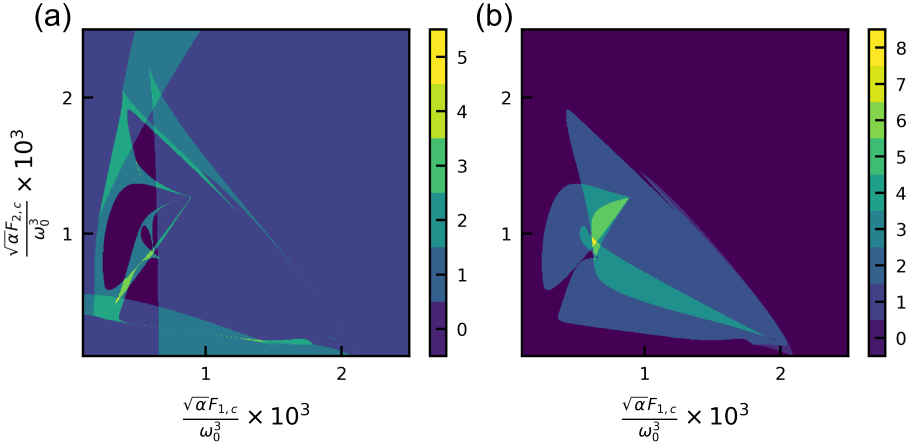


Figure 6.7: Stability diagrams determined by numerical harmonic balance analysis for $\delta/2\pi = -45$ MHz and $\Delta_{12}/2\pi = 40$ MHz as in the main text. Colorbars show the number of solutions. (a) Stability diagram indicating regions of the bichromatic driving force parameter space yielding varying numbers of stable solutions for the system. (b) The same as in (a), but showing numbers of Hopf solutions.

We perform a sweep of the normalized dimensionless forces determined by $F_{1,c}$ and $F_{2,c}$ and obtain a set of parameters for which the response of the system is stable (the eigenvalues of the Jacobian matrix of the system have negative real parts) and for which the solutions are Hopf-like (there are two eigenvalues with positive real parts which are complex conjugates of each other) [461]. In Fig. 6.7 (a), we can see that there are large regions of the stability diagram where there are only one, two, three, or four stable solutions. In the harmonic balance analysis, these are regions in which the system may be in a zero-amplitude monostable state,

a squeezed state, a bistable phase state, or a tristable state. In this chapter, we only examine the behaviour of the oscillator driven into bistable states, while in Chapter 7 we explore in more detail the system which is driven to admit larger numbers of solutions.

Interestingly, there appear to be regions where more solutions than those corresponding to bistable or tristable states are accessible, as well as regions with no stable solutions. Further, in Fig. 6.7 (b), where we show the Hopf-like solutions, there is a large region of parameter space in which the driving forces can produce zero, one, two, four, six, or eight solutions which are Hopf-like. The above numerical simulation produced no regions where three, five, or seven Hopf solutions were found, but this may change upon analysis with finer resolution.

Of particular interest are the interfaces of regions with many stable and Hopf solutions, as beyond the density of solutions which can indicate chaotic behaviour, they may also indicate that a Hopf bifurcation has occurred (where a stable solution changes to a Hopf solution) [216]. When Hopf bifurcations occur, stable solutions change into periodic solutions such as limit cycles. Beyond the drive powers used in Fig. 6.2, Fig. 6.3 in the main text of this chapter and for different parametric drive detunings, we observe responses indicative of chaotic behaviour. These topics are discussed further in Chapter 7.

7

CHAOTIC BEHAVIOUR OF A STRONGLY PARAMETRICALLY DRIVEN DUFFING OSCILLATOR

Why should things be easy to understand?

Thomas Pynchon

Parametrically driven damped Duffing oscillators are nonlinear systems that can be operated to produce phase-dependent gain and can be driven into multistability, chaos, and limit cycles. In this chapter, we operate superconducting circuits at cryogenic temperatures, which are engineered to have the properties of Duffing oscillators. We apply an all-microwave bichromatic drive, which realizes an effective parametric pump on the oscillator and causes the system to exhibit a variety of parametric responses. We perform numerical harmonic balance simulations of the classical system which provides insight into the measured responses.

J. D. Koenig, O. Ameye, M. Hylkema, L. R. van Everdingen, C. A. Potts, O. Zilberberg and G.A. Steele, *Chaotic Behaviour of a Strongly Parametrically Driven Duffing Oscillator*, in preparation (2024).

7.1. INTRODUCTION

Chaotic behaviour has long been understood to be a property of nonlinear oscillators, especially so in strongly driven Duffing oscillators [213, 216, 402, 525–532]. When operating driven Duffing and Kerr nonlinear oscillators as degenerate parametric amplifiers, they are intentionally operated at low enough driving powers that they produce only conventionally useful effects from an engineering perspective such as phase-dependent gain [415, 416, 464, 533–537]. When these systems are driven strongly, they exceed the parametric response threshold and generate multiple stationary states [387]. When pushed even further, the strongly driven Duffing oscillator is well known to undergo Hopf bifurcations, exhibit chaotic behaviour, and can be driven into limit cycles [216, 526, 527, 537–548]. Despite the widespread employment of Duffing and Kerr nonlinear oscillators in quantum information processors in the form of parametric amplifiers and superconducting qubits, the out-of-equilibrium dynamics of such nonlinear quantum circuits in exotic driving regimes have been the focus of limited experimental investigation [411, 549–551].

The emergence of chaotic behaviour in parametrically driven nonlinear oscillators was previously shown to be a universal characteristic of nonlinear systems, with a few key spectral markers of and common routes to chaos [527, 552–556]. Such systems may follow the *period-doubling* route to chaos, where a cascade of period-doubling bifurcations produces turbulent, aperiodic dynamics [526, 527, 557–561]. These successive bifurcations produce a spectrum of peaks with universally determinable Fourier components [527]. After several period-doubling bifurcations have occurred, chaotic behaviour can emerge with the associated appearance of *noise rise* [539, 541, 543, 545, 551, 562–567]. The physical origin of noise rise associated with period-doubling bifurcations has been previously attributed to an increase in device noise temperature due to the effects of telegraph noise-induced switching between the two steady states of a period-doubled oscillator [543]. The ratio of noise gain to signal gain of the oscillator near a period-doubling bifurcation depends on the detuning and strength of the drive, with many regions of the parameter space allowing for a significant amount of noise gain versus signal gain [543].

7

The time-domain output field quadratures of chaotic nonlinear circuits display aperiodic behaviour, which, when displayed as a two-dimensional histogram, leads to the appearance of diffuse points broadly distributed in phase space [564, 568–573]. The phase space representation of the output field quadratures can provide insight into the trajectories of the oscillator integrated over a period of time. In particular, for the bistable Duffing oscillator, chaotic behaviour can be observed around the two fixed-amplitude phase states of the system where intra-well and inter-well dynamics are dictated by chaos in some regions of parameter space [569, 573–576]. The aperiodic dynamics are then localized around either bistable phase state in between switching events (intra-well dynamics) and distributed between the phase states during switching events (inter-well dynamics), causing a characteristic diffuse phase space portrait to form.

7.2. DEVICES AND CHAOTIC BEHAVIOUR IN DUFFING OSCILLATORS

The system and driving scheme are the same as in Chapter 6, for which the details are repeated here. The data displayed in this chapter and Appendix B.2 were obtained from measurements on modes of two separate devices with the similar circuit designs, denoted "Device A" and

"Device B." Each device consists of two arrays of 800 SQUIDs connected via a large capacitor, with one end shorted to ground and the other galvanically connected to a reflection measurement port, as shown in Fig. 7.1 (a), (b) and previously discussed in Sec. 6.6.1. Additionally, there is a separate drive line independent of the reflection port through which we apply drives via capacitive coupling to the junction array. This device is known as a Dimer Josephson Junction Array Amplifier (DJJAA), which may be operated as a parametric amplifier and hosts a series of amplification bands at the N normal modes of the circuit determined by the number of junctions in each array [193].

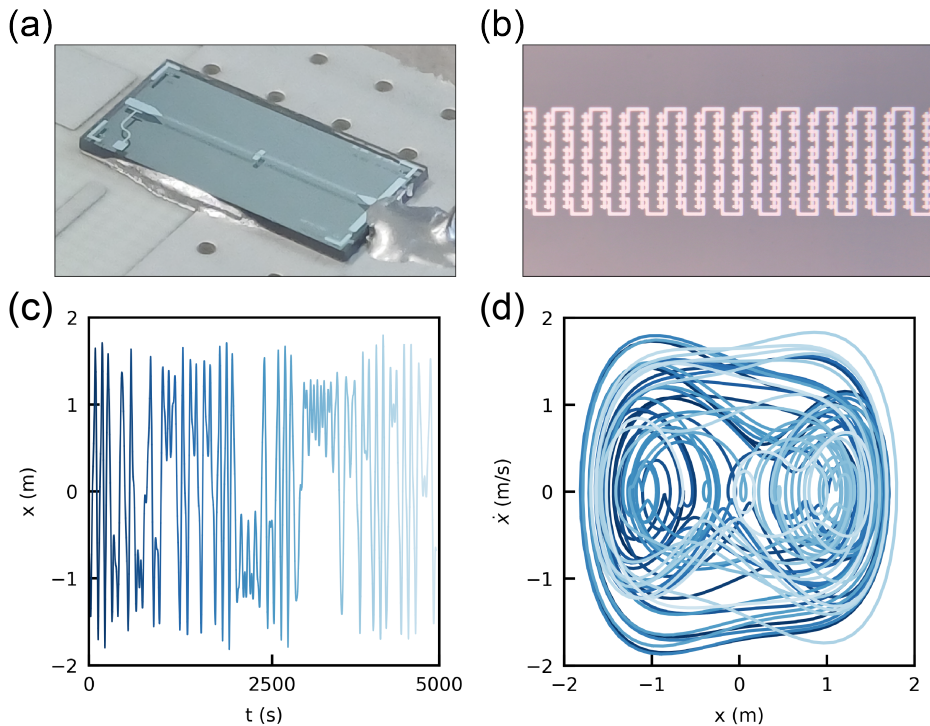


Figure 7.1: Device and system. (a) Each device is a Josephson junction array amplifier with a reflection port and drive line wirebonded to a printed circuit board, with thermal connection to the board via silver epoxy. The photograph was taken prior to wirebonding. (b) A zoom-in of a section of the aluminium Josephson junction array. (c), (d) Simulated characteristic quadrature response of a classical bistable Duffing oscillator driven to exhibit chaotic behaviour [577]. In (c) aperiodic behaviour in the position of the oscillator is shown distributed about two fixed displacements corresponding to the stationary states of the bistable oscillator. In (d), the phase portrait of the system is shown as the oscillator quadratures evolve over time. Darker colours correspond to earlier times, while lighter colours correspond to later times.

Provided that we do not drive at frequencies which induce interactions between our mode of interest and the off-resonant modes of the system, we can reasonably well describe the mode as a single Duffing oscillator after retaining terms in the expansion of the inductive potential

of the circuit to fourth order to obtain the Hamiltonian

$$\mathcal{H}/\hbar = \omega_0 \hat{a}^\dagger \hat{a} + \frac{K}{6} (\hat{a}^\dagger + \hat{a})^4 \quad (7.1)$$

where for Device A we have $\omega_0/2\pi = 5.405$ GHz as the bare oscillator frequency, with $K/2\pi \approx -27.737$ kHz, total linewidth $\kappa/2\pi = 23.465$ MHz, and external linewidth $\kappa_e/2\pi = 14.562$ MHz. For Device B we have $\omega_0/2\pi = 4.604$ GHz as the bare oscillator frequency, with $K/2\pi \approx -10.571$ kHz, total linewidth $\kappa/2\pi = 15.825$ MHz and external linewidth $\kappa_e/2\pi = 6.043$ MHz. In Sec. 7.6.1 we discuss the experimental setups for each device, and note that Device A is not expected to have satisfied the relation $\hbar\omega > k_B T$. Thus, to the degree that there exist any quantum mechanical contributions to the observed behaviour outlined in this chapter, they would be found in measurements of Device B and are left undetermined in this work.

We consider the effect of two pumps at frequencies ω_1 and ω_2 , where $\Delta_{12} = \omega_2 - \omega_1$ and $\delta = \frac{(\omega_1 + \omega_2)}{2} - \omega_0$ are the inter-pump spacing and parametric drive detuning respectively. In a frame rotating at the frequency of the parametric drive, we may rewrite our effective Hamiltonian under the effects of bichromatic driving under the Kerr approximation of the Duffing oscillator as

$$\mathcal{H}'/\hbar \approx -\Delta_{eff} \hat{a}^\dagger \hat{a} + \frac{\epsilon_p}{2} \hat{a}^{\dagger 2} + \frac{\epsilon_p^*}{2} \hat{a}^2 + K \hat{a}^\dagger \hat{a}^\dagger \hat{a} \hat{a} \quad (7.2)$$

where ϵ_p is the two-photon pump strength, the oscillator frequency is shifted by the field amplitudes of each pump $|\alpha_1|^2, |\alpha_2|^2$ to Δ_{eff} , and additional terms fast-rotating at frequency Δ_{12} may be neglected under the RWA for $\Delta_{12} \gg \epsilon_p$. When the parametric drive is resonant with the frequency-shifted oscillator, the RWA breakdown condition becomes $\Delta_{12} \gg \kappa$ where κ is the total linewidth of the oscillator [215].

The effect of applying two detuned pumps with their center frequency held near the oscillator is to induce a frequency shift proportional to pump strength and self-Kerr nonlinearity, as well as to generate a two-photon pump interaction. When the midpoint of the pumps aligns with the shifted oscillator frequency, we are left with the Cassinian or Kerr Parametric Oscillator (KPO) Hamiltonian given by

$$\mathcal{H}_c/\hbar = \frac{\epsilon_p}{2} \hat{a}^{\dagger 2} + \frac{\epsilon_p^*}{2} \hat{a}^2 + K \hat{a}^\dagger \hat{a}^\dagger \hat{a} \hat{a}. \quad (7.3)$$

The Hamiltonian function $V(x, y)$ of this system in the absence of dissipation takes the shape of a double-well with two valleys of equal depth at $(x, y) = (\pm\alpha_0, 0)$ where $\alpha_0 = \sqrt{\epsilon_p/2K}$ is the size of the coherent state with photon number $n = |\alpha_0|^2$. Their equal depths indicate that these two stable states $|\pm\alpha_0\rangle$ where $\nabla V = 0$ are degenerate ground states of the Hamiltonian. Thus, our two-photon pumped Duffing oscillator can be driven into a parameter regime in which the two steady states of the system are equal amplitude phase states. For weak nonlinearities relative to damping $\kappa \gg K$, the KPO can be well described by the classical equations of motion for a parametrically driven Duffing oscillator. In the rotating frame, the steady states of the KPO (or, *parametron*) are known as out-of-equilibrium or *non-equilibrium stationary states* (NESS), given that stable solutions of the system are located at the extrema of the quasipotential [481, 487, 578–581].

As discussed in Sec. 6.6.2, we can determine the number of stable, unstable, and Hopf solutions for the classical parametrically driven Duffing oscillator by numerical harmonic balance

analysis [461, 582, 583]. In the case where stable solutions become Hopf solutions, limit cycles (a kind of periodic orbit) are known to form [216]. Given that chaotic behaviour is known to occur in regions of parameter space with dense periodic solutions, the region of overlap between Hopf and stable solutions is of particular interest. In Fig. 7.2, we plot the number of stable and Hopf solutions as a function of the normalized dimensionless forcing $\sqrt{\alpha}F_i/\omega_0^3$ where F_i is the classical force of either bichromatic drive and α is the nonlinearity (see Sec. 6.6.2). In this parametrization, changes in the frequency and nonlinearity of the oscillator serve only to shift the forces at which we predict parametric responses. The device parameters used are the same as for the experimental data displayed in Fig. 7.3.

We focused our analysis on the ranges of F_i for which Hopf solutions were found and observed an overlap in parameter space with regions of bistability. Here, one real solution corresponds to monostability, two corresponds to photon-dependent frequency shifts, bifurcation, and squeezing, and three corresponds to bistability. The numerical harmonic balance analysis can provide insight into regions where chaotic behaviour may be observed through the large number of coexisting solutions but cannot provide information on the effects of chaos in these regimes. This is due to the harmonic balance analysis requiring the frequencies of response to be specified initially, while in chaotic regions, responses at new frequencies are created, which are not captured. There are additionally higher order effects which are not captured by harmonic balance analysis, as discussed in Sec. 6.6.1.

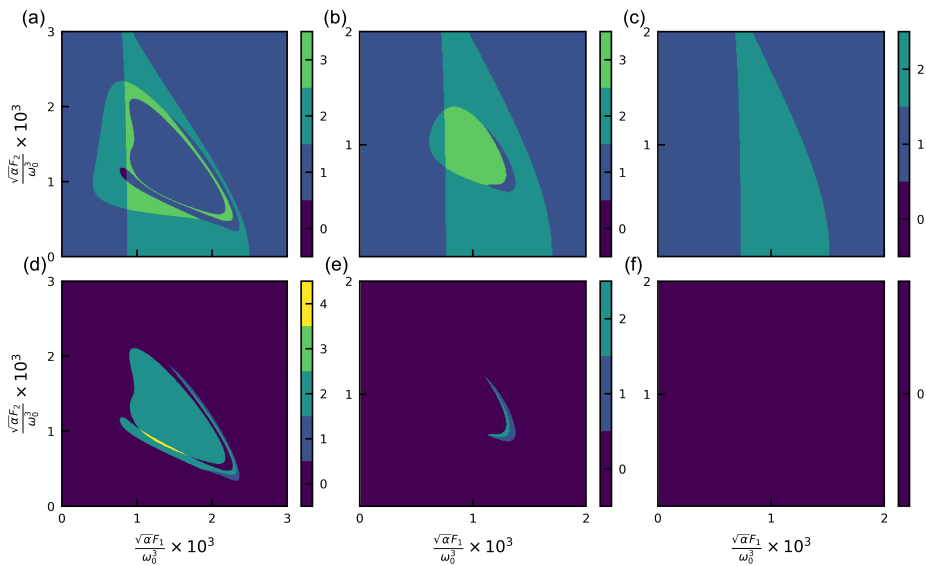


Figure 7.2: Stability phase diagram of the parametrically driven Duffing oscillator determined by numerical harmonic balance analysis. (a), (b), (c) The number of stable solutions for Device A are plotted for $\Delta_{12}/2\pi = 80$ MHz and $\delta/2\pi = -45$ MHz, -25 MHz, and -20 MHz respectively for swept values of bichromatic drive forces. (d), (e), (f) The number of Hopf solutions for the parameters in (a), (b), and (c) respectively. The analysis predicts a small region of parameter space in which Hopf solutions exist and stable solutions do not, which appears for the furthest detuned parametric drive shown at $\delta/2\pi = -45$ MHz.

7.3. EMERGENCE OF CHAOTIC SIGNATURES

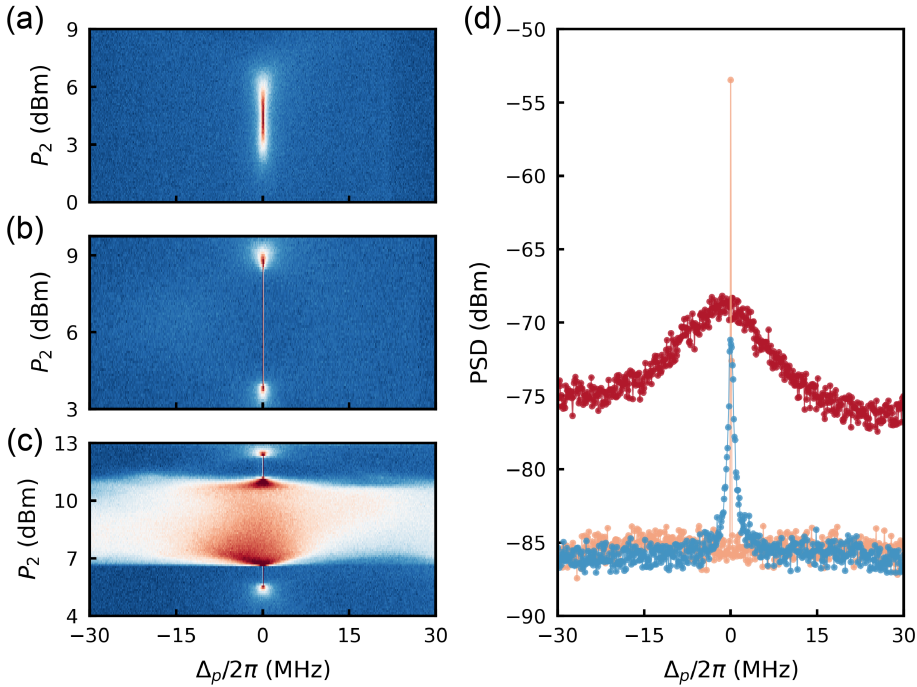


Figure 7.3: Emergence of chaotic behavior under detuned bichromatic driving. (a) The device (Device A) PSD is shown for increasing parametric drive strength at a fixed detuning of $\delta/2\pi = -20$ MHz and bichromatic drive spacing $\Delta_{12}/2\pi = 80$ MHz. As the drive strength is increased, output field phase-dependent gain (squeezing) is observed for a narrow region of powers before the oscillator returns to a zero-amplitude state. (b) For a further detuned parametric drive with detuning $\delta/2\pi = -25$ MHz gain is briefly observed before the system is driven into bistability, evidenced by a narrow peak in the PSD. As the drive power is further increased, the system again exhibits output field gain before returning to a zero-amplitude state. (c) At a large detuning of $\delta/2\pi = -45$ MHz, the oscillator state transitions from squeezed to bistable before entering into a chaotic regime in which wide-band noise rise is observed in the PSD. As the pump strength is further increased, we again observe a transition into bistability, followed by squeezing, before the system returns to a zero-amplitude state. (d) Representative linecuts in the gain (squeezing), bistable, and chaotic regimes at parametric pump detunings $\delta/2\pi = -20$ MHz, -25 MHz, and -45 MHz, and $P_2 = 3.2$ dBm, 7.2 dBm, and 8.5 dBm marked by data shown in blue, peach, and red respectively.

In Fig. 7.3, we show the output field power spectral density (PSD) of Device A for a set of parametric drive detunings. We sweep the power of the upper-frequency bichromatic drive while holding the lower-frequency drive fixed at $P_1 = 13$ dBm. This effectively increases the parametric drive strength, allowing us to probe the state of the oscillator at different detunings for which we expect to transit distinct regions of the parametric response phase space of the system depicted in Fig. 7.2.

At a relatively small detuning of $\delta/2\pi = -20$ MHz, we simply observe phase-dependent gain (squeezing) for a range of drive powers, consistent with the oscillator transiting the dissipation-stabilized region below the parametric instability threshold. As we further detune the parametric drive to $\delta/2\pi = -25$ MHz and sweep the power, we briefly observe gain before the oscillator crosses the instability threshold and becomes bistable indicated by a narrow peak in the PSD. In this region, the oscillator stochastically switches between two equal amplitude phase states before returning to a squeezed state as the power is further increased. This behaviour is consistent with transiting the dissipation-stabilized and bistable regions. In general, the parametric phase states are directly identifiable via the device output spectra by both the narrow, high amplitude feature at the frequency of parametric driving and the appearance of two broad peaks of lesser amplitude symmetrically spaced on either side of the narrow peak [445, 446]. In Appendix B.2, several datasets displaying these side peaks are shown, where the frequency and linewidth of the peaks can be determined from the eigenvalues of the dynamical matrix of the Hamiltonian [445, 446]. For power spectra, the relative amplitudes of the two peaks are generally asymmetric and their positions are a function of parametric drive strength and the geometry of the Hamiltonian function of the system [445, 584]

With even further detuned parametric driving at $\delta/2\pi = -45$ MHz, after the oscillator state again transitioned from squeezed to bistable, we observed a significant increase in the noise floor of the spectrum by ≈ 10 dBm over a wide frequency range as well as a broad, asymmetric peak and the disappearance of the narrow signature in PSD indicative of bistability. This behaviour persisted for a wide range of powers until finally, the system returned to bistability, followed again by squeezing and return to a zero-amplitude state. This increase in output field noise (noise-rise) is well-known to occur in nonlinear oscillators as they are parametrically driven into chaos [539, 541, 543, 545, 551, 562, 564, 566, 567].

7.4. CONFLUENCE OF PERIOD-HALVING AND DOUBLING BIFURCATION CASCADES

Along with noise rise, another signature of chaos in parametrically driven nonlinear oscillators is subharmonic generation, in which the output field of a periodically modulated oscillator displays an increasingly dense spectrum of peaks around the frequency of parametric driving [526, 527, 557–559]. These peaks increase in number as the system undergoes successive period-doubling bifurcations, until the system eventually becomes chaotic. In Fig. 7.4 Device B under strong and far-detuned bichromatic driving displays uniformly spaced peaks bounded between the two microwave drives as well as noise rise as the drive strength is increased. Rather than immediately undergoing successive period-doublings, the oscillator suddenly transitions to a chaotic state characterized by multiple peaks. As we increase the pump strength we observe period-halving bifurcations until approximately the midpoint of the region, after which point the system then undergoes a cascade of period-doubling bifurcations. The sudden transitions into and out of a chaotic state are reminiscent of an oscillator following the *crisis* route to chaos [569, 585, 586].

Interestingly, the period-doubling bifurcation cascade appears to bring the system into a zero-amplitude state and out of the region of noise rise, while the successive period-halving bifurcations bring the system into the center of the region. In general, period-halving bifurcations enable the suppression and control of chaotic behaviour in nonlinear systems as period-

doubling is reversed [587–590]. As the period-halving and period-doubling bifurcations meet at the center of this region, we observe an absence of sharp peaks. Given that this occurs where the successive period-doublings begin and the period-halvings end, this is indicative of a region of suppressed chaotic effects.

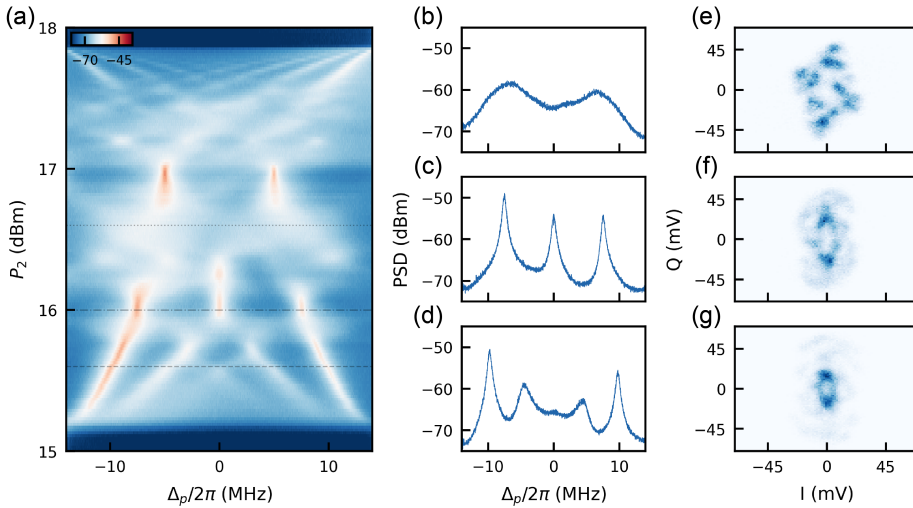


Figure 7.4: Observation of structured spectral features in the output field of a Duffing oscillator parametrically driven into chaos. (a) The oscillator (Device B) output field PSD is shown for increasing parametric drive strength at a detuning of $\delta/2\pi = -50$ MHz, $P_1 = 20$ dBm, and bichromatic drive spacing $\Delta_{12}/2\pi = 30$ MHz. As the drive power is increased, the oscillator transitions directly from a zero-amplitude state into a region where wide-band noise rises. As the system transits this region, evenly spaced peaks appear and uniformly converge, followed by splitting and diverging into an array of peaks before the system exits the chaotic region. (b) Linecut of the output field PSD at the power $P_2 = 15.6$ dBm, indicated by the dotted line in (a). (c) The same is true for the power indicated by the dot-dashed line at $P_2 = 16$ dBm, (d). The same is true for the power indicated by the dashed line at $P_2 = 16.6$ dBm. (e), (f), (g) Output field quadrature histograms of the device at the indicated drive powers as in (b), (c), and (d) respectively.

7

It has been long established that the nonlinear systems and periodically driven Duffing oscillator have solutions which allow for the formation of stable “bubbles” in which period-halving and period-doubling bifurcations meet [587–590]. Such a situation is similar to the results of the measurements in Fig. 7.4 (e), in which we observe the most structure in the output field quadrature histogram for the center of the chaotic region. An alternative explanation is that the system is driven into period- k orbits, which can be sustained from suppressed chaotic behaviour in doubly-forced Duffing oscillators with unbalanced drives and in systems with deformed double well potentials [591–594]. Here, the quadrature voltage counts are less diffuse than at the edges of the region, as the majority of the oscillator dynamics appear to be concentrated around a handful of points. This occurs far away from the edges of the noise-rise region, where multiple period-doubling bifurcations have taken place and we expect the most chaotic behaviour. As the drive power is increased, the escape of the oscillator from the chaotic region is as sudden as the transition into chaotic behaviour from the zero-amplitude

state.

In Fig. 7.5, we show the stable and Hopf solutions for Device B subject to the drive parameters of Fig. 7.4. In comparison with the measurements on Device A, our analysis predicts a greater number of both stable and Hopf solutions. Given the large number of solutions and overlap between regions of stable and Hopf solutions, further measurements and analysis in this parameter regime may reveal the presence of Hopf bifurcations and limit cycles [216]. The boundaries of the region indicated to have no stable solutions, but several Hopf solutions are of particular interest. The stability diagrams in this chapter and Appendix B.2 indicate that larger numbers of solutions are found for smaller bichromatic drive spacings Δ_{12} and larger parametric detunings δ while the use of unbalanced pump strengths is required to fully explore the system parameter space.

We found that regions with odd numbers of Hopf solutions were, in general, far less common than regions with even numbers, where in the case of Fig. 7.5 no region was found containing seven solutions for the forces analyzed and in Fig. 7.2 (d) no region with three solutions was found. Additional analyses with finer resolution may produce regions with these numbers of solutions, but for the simulations shown in this thesis, points in the parameter space with odd numbers of Hopf solutions were found far less often than for even numbers.

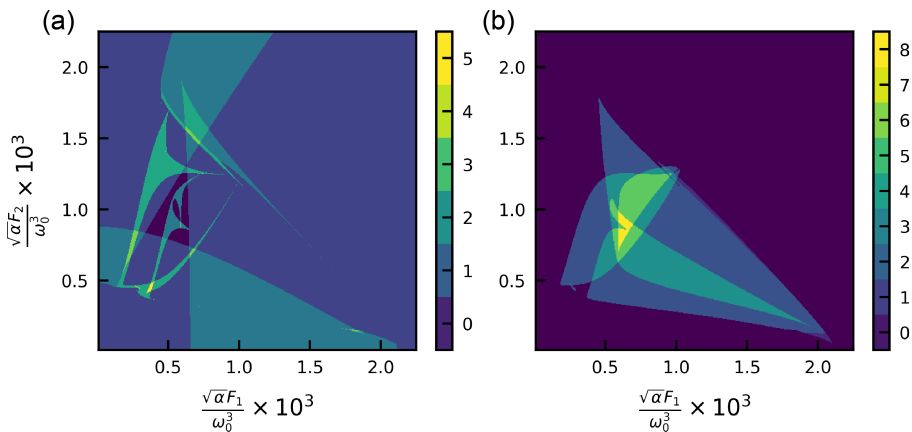


Figure 7.5: Large solution number stability phase diagram of the parametrically driven Duffing oscillator determined by numerical harmonic balance analysis. (a) The number of stable solutions for Device B is plotted for $\Delta_{12}/2\pi = 30$ MHz and $\delta/2\pi = -50$ MHz for swept values of bichromatic drive forces. (b) The number of Hopf solutions for the same parameters. For both stable and Hopf solutions, a larger number is found relative to the parameters used in Fig. 7.2.

The doubly-forced or quasiperiodically forced Duffing oscillator (in our language, bichromatically driven), in particular, has been previously investigated and was found to exhibit chaotic behaviour under certain driving conditions, while unbalanced drives can be used to suppress chaotic behaviour [593, 595–597]. Such driving schemes can result in quasiperiodic orbits, in which the oscillator dynamical evolution is defined by orbits which never return to their same point each cycle [597]. The oscillator behaviour shown in Fig. 7.3 and Fig. 7.4 represents only a

small subspace of the parametric response phase diagram of the system. In Appendix B.2, we show several more measurements displaying the response of strongly bichromatically driven Duffing oscillators at various δ , Δ_{12} , P_1 , and P_2 . While dense spectra of peaks around the frequency of driving and noise rise are consistent features, we observed a broad array of behaviours in the output field quadrature histograms which we attribute to chaotic intra-well and inter-well dynamics in multistationary states [213, 575, 576]. We also provide PSD datasets along the δ and Δ_{12} axes for P_2 sweeps with fixed P_1 at each Δ_{12} . From this, we can infer the general structure of a region of the parametric response phase diagrams of the devices, by observing for which ranges of powers and detunings markers of phase-dependent gain, bistability, and chaos are visible in the device output field.

7.5. CONCLUSION

We have performed a series of measurements on parametrically driven Duffing oscillators realized in superconducting quantum circuits. The system was driven at a variety of parametric detunings and for various drive strengths for which we observed the transition from phase-dependent gain, to bistability, and into regimes where signatures of chaotic behaviour were present in the output field of the device. We compared our results to the theoretically expected behaviour of strongly parametrically driven Duffing oscillators in chaotic regimes and identified similarities in the experimental data.

We performed numerical harmonic balance analysis of the classical Duffing oscillator for the bichromatic drive frequencies utilized experimentally. We produced parameter sweeps to identify stability diagrams which illustrate the response of the classical Duffing oscillator at the parametric drive frequency for various classical driving forces. We found a region of the dual-force parameter space in which Hopf solutions exist, in the vicinity of regions where two stable solutions exist (the bistable state). Given that our observations of other signatures associated with chaos (noise-rise, period-doubling bifurcations) occurred in the vicinity of parameter space which produced bistable states, we focused our analysis on regions where large numbers of stable and Hopf solutions were predicted by harmonic balance.

Strongly driven superconducting quantum circuits in the Duffing regime are highly engineerable and controllable systems which can be used for the study of non-equilibrium and chaotic behaviour at cryogenic temperatures. Given the high degree of control over system parameters, possibility of dissipation engineering, and the ability to linearly and nonlinearly couple to other systems, superconducting circuits are a promising platform for experimentally investigating and utilizing chaotic behaviour in nonlinear oscillators. The use of an additional resonant phase biasing drive to controllably deform the potential of the system could be used in such chaotic regimes to further explore the range of accessible system responses. The intersection of classical and quantum effects in chaotic regimes, among other nonlinear dynamics topics, could be further explored with such devices [436, 437, 566, 586, 598–622].

7.5.1. CONTRIBUTIONS

Author names are as given in the List of Publications. O.A. carried out the semiclassical theoretical analysis with the supervision of O.Z. L.R.vE. designed and fabricated the device. J.D.K. conducted the measurements with the supervision of C.A.P. and G.A.S. M.H. contributed to the experimental setup. J.D.K. performed the harmonic balance simulations. O.Z. and G.A.S. super-

vised the project. J.D.K. wrote the chapter with input from the authors. The original designs for the DJJAAs were provided by the group of Ioan M. Pop at the Karlsruhe Institute of Technology. The authors acknowledge financial support by the EU program H2020-FETOPEN project 828826 Quromorphic. This contribution statement is tentative and may be changed prior to publication of these results.

7.6. SUPPLEMENTARY INFORMATION

7.6.1. EXPERIMENTAL SETUP

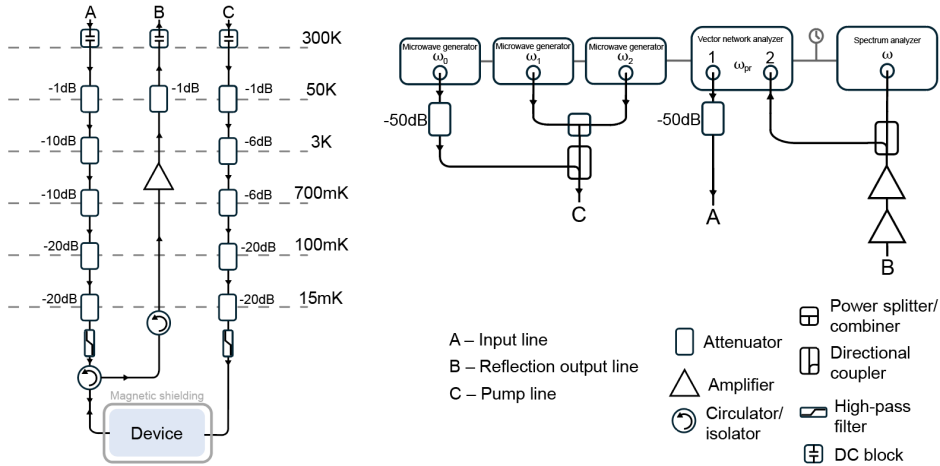


Figure 7.6: Experimental setup.(a) The device (Device B) is mounted to the mixing chamber plate of a Bluefors dilution refrigerator and connected to our measurement instruments via coaxial cables. On the microwave input line, the signal is attenuated at each stage to varying degrees, with the stronger attenuation at lower stages. The input signal then passes through a filter (Mini-Circuits VHF-3500+) and a circulator (Pasternack PE84o2). The box which houses the printed circuit board to which the device chip is connected is contained within a mu-metal magnetic shielding can. A superconducting coil is attached directly to the bottom of the device packaging inside of the shielding and connected via a loom to room temperature electronics for flux biasing of the device with a current source (Stanford RS CS58o). The reflected signal returns to the circulator, then passes through an additional isolator (LNF-ISC4_8A) placed between the circulator and the high electron mobility transistor (HEMT) amplifier (Low Noise Factory LNF-LNC4_8F) to reduce the thermal occupation of the device due to the thermal noise of the HEMT. An additional pump line with reduced attenuation is connected to the dedicated drive port of the device, filtered (ZLSS-11G-S+) below the mixing chamber plate. DC blocks (BLKD-183-S+) are placed at room temperature on the input (A), output (B), and pump (C) lines. (b) The bichromatic drives are sent from microwave generators (Rohde & Schwarz SGS100A) and combined (Mini-Circuits ZFSC-2-10G+), which then pass through a directional coupler (SM Electronics MC2o45-1o) to which the resonant bias drive supplied from a third generator (Anapico APUASYN2o) is coupled, and all drives are sent to the pump line. The probe tone is sent by a vector network analyzer (VNA) (Keysight N5221A PNA) through power combiners and into the input line of the fridge. The returning signal from the output line of the fridge is further amplified at room temperature (AT Microwave AT-LNA-o4o8-25o1X) and passed through a directional coupler (Pasternack PE2CP11o4) to the VNA and spectrum analyzer (Keysight N9o1oB EXA).

Shown in Fig. 7.6 is the experimental setup for the measurements performed on Device B. The drive powers quoted in the main text are those at the output of the measurement instruments. The experimental setup for Device B is the same as in Chapter 6. The drive powers quoted in the main text are those at the output of the measurement instruments.

The room temperature measurement setup for Device A was similar; however, with zero attenuation at the output of the vector network analyzer (VNA). Device A was measured at the

300 mK stage of an Entropy Cryogenics cryostat with -10 dB attenuation at each of the 70 K and 4 K stages and -20 dB at the 1 K stage for both the input and pump lines. The input line had an additional -6 dB of attenuation at the 300 mK stage. We can thus estimate a total attenuation including cables to be approximately -64 dB. The output line contained an isolator at the 300 mK stage and a HEMT at the 4 K stage. Devices A and B were wirebonded to a PCB, thermalized to the PCB with silver epoxy, and the PCB was then mounted into a copper package with SMA connectors. The closed package was then mounted with a superconducting coil and placed inside of magnetic shielding. Each device contained junction arrays with 2×800 SQUIDs and the details of Device B are given in Sec. 6.6.1. Differences in the parameters of Device A compared to Device B are likely a consequence of variation under wafer-scale fabrication processes causing inhomogeneity in realized junction overlap areas, as indicated by the large variation in measured normal state resistances of the arrays across numerous samples.

We expect that the contributions of thermal effects to the out-of-equilibrium dynamics of Device A were much larger than those of Device B, given the difference in temperature of the lowest stages of the dilution refrigerators each were measured in (≈ 300 mK and ≈ 20 mK respectively) and the frequencies of the modes. Indeed, Device A does not satisfy $\hbar\omega > k_B T$. The actual temperatures of the modes measured also depend on how well thermalized the samples are to the mK stages. In addition to fits of stochastic switching rates to thermal effects in the bistable regime, additional measurements can be performed to determine the effective temperatures of the modes under investigation in the future [322, 517–523].

As discussed in Sec. 6.6.1, for the extreme drive parameters which we apply to our devices in Chapters 6, 7, the quantitative predictions of effective parametric drive strengths and detunings which produce large numbers of solutions for the parametrically driven system are expected to be inaccurate. Another analysis one can perform is to estimate the total circulating current in the device relative to the critical currents of the SQUIDs composing the DJJAA. Given the mode inductance and frequency, one can calculate the circulating current upon resonant driving of the mode by $I = \sqrt{\frac{2E}{L}} = \sqrt{\frac{2n\hbar\omega}{L}}$. Given for Device B a per-SQUID Josephson inductance of $L_J = 103.25$ pH and stray inductance $L_s = 12.67$ pH found in Sec. 6.6.1 with 800 SQUIDs per half of the array, we can calculate the circulating current in the mode to be $I = 7.877$ nA $\times \sqrt{n}$ for n photons.

For the drive parameters used in Fig. 7.4 (d), (g), we can determine $n = \frac{\kappa_e}{(\Delta_{12}/2)^2 + (\kappa/2)^2} \frac{P}{\hbar\omega}$ from Ref. [222] to obtain 5.05×10^6 and 1.59×10^6 photons from each drive individually and can calculate the mean-field estimate of the corresponding photon number of the parametric state following Ref. [496] by using $n = \frac{1}{2K} \sqrt{(2\epsilon_p)^2 - \kappa^2}$, which yields 5.58×10^6 photons. We thus find that the circulating current is $I = 18.61$ μ A, which can be compared to the per-SQUID critical current of $I_c = 3.19$ μ A. While the parametric drive strength value from our unscaled model likely overestimates the strength and thus the number of photons, the photons from each of the two bichromatic drives are comparable to this value and are determined only from the line attenuation. We note that in Ref. [563], it was found that a relationship between regions of chaos and finite voltage in the parameter space of driven Josephson parametric amplifiers exists. As our estimates indicate that we are driving the system beyond the critical currents of the constituent SQUIDs of the array, we find this to be another indication that what we observe is chaotic behaviour and that the system is likely driven into a finite-voltage state.

8

CONCLUSION

*"It began as toil for bread and butter
and ended in a love of science".*

Wild Strawberries, Ingmar Bergman

8.1. FINDINGS

In this thesis we presented experimental observations on parametrically driven superconducting quantum circuits containing systems ranging from strongly nonlinear in the transmon qubit limit, to moderately nonlinear in the Kerr regime, and lastly to weakly nonlinear in the Duffing oscillator limit. We explored the quantum interactions between two tunably coupled transmon qubits, the dynamics of a few-photon Kerr oscillator at the interface of the quantum and classical regimes, and of the large amplitude parametric responses of strongly driven Duffing oscillators.

In Chapter 4 we applied a parametrically modulated flux to a SQUID loop which inductively coupled two transmon qubits. Together with the contributions of a fixed capacitive coupling, the tunable contributions of the inductive energy of the SQUID to the linear and cross-Kerr couplings can be controlled by the application of static DC biases. When the two oscillators were flux tuned to be far off-resonant from each other, we applied red sideband and blue sideband amplitude modulations to the DC bias of the coupler SQUID, with modulation frequency equal to the difference and sum frequencies of the transmons respectively. When modulating on the red sideband, we observed spectroscopic signatures of level repulsion and extracted the strength of the single-photon hopping interaction between the oscillators from numerical simulations and an analytical model. When modulating on the blue sideband, we observed level attraction between the two transmons, with a cross-Kerr shifted signature visible spectroscopically below the primary resonance feature. Similarly, we determined the strength of the corresponding two-mode squeezing interaction between the oscillators from numerical simulations and an analytical model.

In Chapter 5 we reported observations of a moderately Kerr-nonlinear oscillator (KNO) subject to a parametric pump realized by an all-microwave bichromatic driving scheme. When the center frequency of the two drives was applied red-detuned from the bare oscillator frequency, we observed a modification of the oscillator response at the midpoint of the drives. For strong bichromatic drives swept in frequency through the shifted oscillator response we observed signatures of a few-photon parametric phase state generated in the KNO characterized by a strongly modified response at the midpoint of the pumps and the appearance of two modes on either side of the frequency of the parametric tone. This behaviour is well known to occur in the Kerr parametric oscillator (KPO) when the system is driven above the parametric threshold determined by its damping. When driven into a parametric state, the KPO gains two bistable solutions with mode frequencies determined by the eigenvalues of the dynamical matrix of the system. As the parametric drives were further detuned, the oscillator returned to a zero-amplitude state, however with an exchange of the signal and idler mode frequencies relative to the midpoint of the drives. This exchange in signal and idler modes has been previously identified as evidence of a dynamical phase transition in which the third stationary state of the tristable KPO becomes the steady state of the system in the presence of dissipation. We measured the output field of the device subject to parametric driving and observed gain in the region of detuning for which the parametric response was observed spectroscopically. We compared our observations with a semiclassical effective model and used a modified version to perform numerical simulations of the quantum master equation to estimate the photon number and second-order correlation function of the system subject to bichromatic drives. We observed deviations from the semiclassical model consistent with previous reports noting the necessity of accounting for quantum effects in such systems and due to higher order

effects of the bichromatic driving scheme not accounted for in the model.

In Chapter 6 we applied the same all-microwave bichromatic driving scheme to a weakly nonlinear oscillator realized by a superconducting quantum circuit. For strong bichromatic drives red-detuned from the bare oscillator frequency, we observed in the output field PSD of the device the formation of an extremely narrow and high amplitude peak at the frequency of the midpoint of the drives. The output field quadrature histograms for swept drive powers at this frequency revealed the formation of parametric phase states consistent with the behaviour expected of weakly nonlinear KPOs driven above the parametric threshold. The combination of low nonlinearity and strong damping enabled the generation of large photon number phase states with correspondingly long stochastic switching times between the bistable stationary states of the system. We measured the time-dependent output field quadratures as the drive strength was increased and found an exponential increase in the stochastic switching time to a maximal value followed by a decay in switching times until the system was no longer bistable. We discussed this behaviour in the context of the stability diagram of the parametrically driven Duffing oscillator, where regions of parameter space for which bistability is possible are finite. Before entering and after exiting bistability, the system may be in zero-amplitude monostable, tristable, or other out-of-equilibrium stationary states. The decrease in switching time with increasing power from a maximal value is consistent with the oscillator exiting the bistable regime due to nonlinear effects. Lastly, we applied a weak resonant microwave drive at the midpoint of the pumps while the oscillator was bistable and demonstrated control over the phase biasing and switching time as a function of drive power and phase relative to the bistable states. We discussed these observations in the context of known quantum and classical contributions to the stochastic switching rates in the KPO and expect to quantify the relative contributions of these effects upon the further development of our theoretical model.

In Chapter 7 we applied bichromatic drives to a weakly nonlinear Duffing oscillator realized in a superconducting quantum circuit. We discussed the expected behaviour of such systems when strongly parametrically driven, which include the exhibiting of chaotic behaviour following period-doubling bifurcation cascades and the associated noise-rise of the device output field. We drove two Duffing oscillators beyond bistability for a variety of bichromatic drive detunings and strengths and observed noise-rise and the formation of dense spectra between the drives in the output field PSD, as well as fluctuations in the output field quadratures which presented as diffuse points about islands of larger occupation in the 2D histograms. We performed numerical harmonic balance analysis on the system and identified regions of the bichromatic driving parameter space which permit large numbers of stable, unstable, and Hopf solutions, albeit with deficiencies due to the neglect of higher order effects.

8.2. OUTLOOK

While tunable couplings will likely continue to find great applicability in digital quantum information processors, their utility in enabling the emulation of physics from entirely different platforms and to perform analog quantum simulations is also exciting. In particular, combinations of parametric drives of different frequencies applied to SQUID couplers with phase control would enable the simulation of arbitrary XYZ, Ising ZZ, Bose-Hubbard, and Heisenberg XXZ models [325, 326, 338, 343, 392]. The use of asymmetric nonlinear inductive elements

such as SNAILs to tunably couple transmons or KNOs would enable a variety of interactions to be selectively activated when the coupler is parametrically driven, including the linear and quadratic optomechanical photon pressure interactions and photon-pair tunnelling in systems where the self-Kerr nonlinearities of the coupled oscillators may be tuned from negative to positive values [195, 394, 395]. The phenomenon of level attraction in parametrically driven strongly nonlinear oscillators is also of interest, in particular in the context of understanding more deeply the relationship between coherent and dissipative couplings, and the equivalence of level repulsion and attraction subject to an exchange of frequency and dissipation rates [365, 369, 372].

The few-photon KPO has been the focus of a number of theoretical studies and experiments in recent years and the platform is expected to continue to be a topic of interest into the future. KPOs in this parameter regime are ideal systems for investigating the intersection of quantum and classical effects, with several theoretical proposals that can be experimentally implemented. When considering KPOs with larger photon numbers as well as weakly nonlinear Duffing oscillators, the breadth of topics of future study grows to include information processing and quantum simulation, noise mitigation and sensitive detection schemes, as well as the investigation of dynamical phase transitions and symmetry breaking operations in many-body systems [358, 425–429, 433, 435, 441, 443, 452, 457, 473, 510–513, 515].

The strongly parametrically driven Duffing nonlinear oscillator is a system known to exhibit chaotic behaviour. Given that within the field of circuit quantum electrodynamics the ability to fabricate superconducting quantum circuits which are well described as Duffing oscillators with engineerable frequencies, nonlinearities, couplings, and dissipations exists, there is great potential in using Josephson junction-based devices at cryogenic temperatures to investigate chaotic behaviour in systems that exhibit both classical and quantum dynamics. Such studies can be extended to systems of linearly and nonlinearly coupled oscillators, in a variety of parameter regimes, and subject to resonant and parametric drives. Given that superconducting circuits are able to emulate the physics of various other systems (i.e. optomechanical) and couple to other platforms (i.e. magnonic, phononic) in hybrid quantum systems, it may be interesting to investigate these strongly driven Duffing oscillators in such situations. A natural extension is to combine the techniques used in the experiments performed on the tunable coupler to enable the emulation of exotic interactions with the use of asymmetric inductive coupling elements and apply strong parametric drives to the constituent nonlinear oscillators of the system [195, 196, 436, 437, 566, 586, 598–604, 606, 607, 609–621, 623].

APPENDICES

A.1. SOLUTIONS TO THE PARAMETRICALLY DRIVEN DUFFING OSCILLATOR

For the below equations the variables are the dimensionless parameters given in Sec. 2.3, where here we omit the tildes. The analytical solutions are those of Eq. 2.122, 2.123 where $|X| = \sqrt{u^2 + v^2}$ and they account for the monostable, bistable, and tristable states. The solutions were determined by using the symbolic mathematics Python library, *SymPy* [624].

$$|X_0|^2 = 0 \quad (1)$$

$$\begin{aligned}
 |X_1|^2 = & \frac{-4\Omega^6\eta^3\gamma + 24\Omega^6\eta^2 - 2\Omega^4\eta^3\gamma\lambda + 4\Omega^4\eta^3\gamma - 12\Omega^4\eta^2\gamma^2 + 6\Omega^4\eta^2\lambda}{W} \\
 & + \frac{-12\Omega^4\eta^2\sqrt{Z} - 48\Omega^4\eta^2 + 108\Omega^4\eta\gamma - 3\Omega^2\eta^2\lambda^2 - 6\Omega^2\eta^2\lambda\sqrt{Z} - 6\Omega^2\eta^2\lambda}{W} \\
 & + \frac{12\Omega^2\eta^2\sqrt{Z} + 24\Omega^2\eta^2 - 18\Omega^2\eta\gamma\lambda - 72\Omega^2\eta\gamma\sqrt{Z} - 108\Omega^2\eta\gamma + 108\Omega^2\gamma^2}{W} \\
 & + \frac{54\Omega^2\lambda + 108\Omega^2\sqrt{Z} - 27\lambda^2 - 54\lambda\sqrt{Z} - 54\lambda - 108\sqrt{Z}}{W} + \frac{\left(-\frac{1}{2}\lambda + \sqrt{Z}\right)^2}{G} \\
 & \times \left(-4\Omega^6\eta^3\gamma + 24\Omega^6\eta^2 - 2\Omega^4\eta^3\gamma\lambda + 4\Omega^4\eta^3\gamma - 12\Omega^4\eta^2\gamma^2 + 6\Omega^4\eta^2\lambda - 12\Omega^4\eta^2\sqrt{Z}\right) \\
 & \times \left(-48\Omega^4\eta^2 + 108\Omega^4\eta\gamma - 3\Omega^2\eta^2\lambda^2 - 6\Omega^2\eta^2\lambda\sqrt{Z}\right) \\
 & \times \left(-6\Omega^2\eta^2\lambda + 12\Omega^2\eta^2\sqrt{Z} + 24\Omega^2\eta^2 - 18\Omega^2\eta\gamma\lambda - 72\Omega^2\eta\gamma\sqrt{Z}\right) \\
 & \times \left(-108\Omega^2\eta\gamma + 108\Omega^2\gamma^2 + 54\Omega^2\lambda + 108\Omega^2\sqrt{Z} - 27\lambda^2 - 54\lambda\sqrt{Z} - 54\lambda - 108\sqrt{Z}\right)
 \end{aligned} \quad (2)$$

$$\begin{aligned}
|X_2|^2 &= \frac{-4\Omega^6\eta^3\gamma + 24\Omega^6\eta^2 - 2\Omega^4\eta^3\gamma\lambda + 4\Omega^4\eta^3\gamma - 12\Omega^4\eta^2\gamma^2 + 6\Omega^4\eta^2\lambda}{W} \\
&+ \frac{-12\Omega^4\eta^2\sqrt{Z} - 48\Omega^4\eta^2 + 108\Omega^4\eta\gamma - 3\Omega^2\eta^2\lambda^2 - 6\Omega^2\eta^2\lambda\sqrt{Z} - 6\Omega^2\eta^2\lambda}{W} \\
&+ \frac{12\Omega^2\eta^2\sqrt{Z} + 24\Omega^2\eta^2 - 18\Omega^2\eta\gamma\lambda - 72\Omega^2\eta\gamma\sqrt{Z} - 108\Omega^2\eta\gamma + 108\Omega^2\gamma^2}{W} \\
&+ \frac{54\Omega^2\lambda + 108\Omega^2\sqrt{Z} - 27\lambda^2 - 54\lambda\sqrt{Z} - 54\lambda - 108\sqrt{Z}}{W} + \frac{\left(\frac{1}{2}\lambda - \sqrt{Z}\right)^2}{G} \\
&\times \left(-4\Omega^6\eta^3\gamma + 24\Omega^6\eta^2 - 2\Omega^4\eta^3\gamma\lambda + 4\Omega^4\eta^3\gamma - 12\Omega^4\eta^2\gamma^2 + 6\Omega^4\eta^2\lambda - 12\Omega^4\eta^2\sqrt{Z}\right) \\
&\times \left(-48\Omega^4\eta^2 + 108\Omega^4\eta\gamma - 3\Omega^2\eta^2\lambda^2 - 6\Omega^2\eta^2\lambda\sqrt{Z}\right) \\
&\times \left(-6\Omega^2\eta^2\lambda + 12\Omega^2\eta^2\sqrt{Z} + 24\Omega^2\eta^2 - 18\Omega^2\eta\gamma\lambda - 72\Omega^2\eta\gamma\sqrt{Z}\right) \\
&\times \left(-108\Omega^2\eta\gamma + 108\Omega^2\gamma^2 + 54\Omega^2\lambda + 108\Omega^2\sqrt{Z} - 27\lambda^2 - 54\lambda\sqrt{Z} - 54\lambda - 108\sqrt{Z}\right)
\end{aligned} \tag{3}$$

$$\begin{aligned}
|X_3|^2 &= \frac{-4\Omega^6\eta^3\gamma + 24\Omega^6\eta^2 - 2\Omega^4\eta^3\gamma\lambda + 4\Omega^4\eta^3\gamma - 12\Omega^4\eta^2\gamma^2 + 6\Omega^4\eta^2\lambda}{W} \\
&+ \frac{12\Omega^4\eta^2\sqrt{Z} - 48\Omega^4\eta^2 + 108\Omega^4\eta\gamma - 3\Omega^2\eta^2\lambda^2 + 6\Omega^2\eta^2\lambda\sqrt{Z} - 6\Omega^2\eta^2\lambda}{W} \\
&+ \frac{-12\Omega^2\eta^2\sqrt{Z} + 24\Omega^2\eta^2 - 18\Omega^2\eta\gamma\lambda + 72\Omega^2\eta\gamma\sqrt{Z} - 108\Omega^2\eta\gamma + 108\Omega^2\gamma^2}{W} \\
&+ \frac{54\Omega^2\lambda - 108\Omega^2\sqrt{Z} - 27\lambda^2 + 54\lambda\sqrt{Z} - 54\lambda + 108\sqrt{Z}}{W} + \frac{\left(-\frac{1}{2}\lambda - \sqrt{Z}\right)^2}{G} \\
&\times \left(-4\Omega^6\eta^3\gamma + 24\Omega^6\eta^2 - 2\Omega^4\eta^3\gamma\lambda + 4\Omega^4\eta^3\gamma - 12\Omega^4\eta^2\gamma^2 + 6\Omega^4\eta^2\lambda + 12\Omega^4\eta^2\sqrt{Z}\right) \\
&\times \left(-48\Omega^4\eta^2 + 108\Omega^4\eta\gamma - 3\Omega^2\eta^2\lambda^2 + 6\Omega^2\eta^2\lambda\sqrt{Z}\right) \\
&\times \left(-6\Omega^2\eta^2\lambda - 12\Omega^2\eta^2\sqrt{Z} + 24\Omega^2\eta^2 - 18\Omega^2\eta\gamma\lambda + 72\Omega^2\eta\gamma\sqrt{Z}\right) \\
&\times \left(-108\Omega^2\eta\gamma + 108\Omega^2\gamma^2 + 54\Omega^2\lambda - 108\Omega^2\sqrt{Z} - 27\lambda^2 + 54\lambda\sqrt{Z} - 54\lambda + 108\sqrt{Z}\right)
\end{aligned} \tag{4}$$

$$\begin{aligned}
|X_4|^2 = & \frac{-4\Omega^6\eta^3\gamma + 24\Omega^6\eta^2 - 2\Omega^4\eta^3\gamma\lambda + 4\Omega^4\eta^3\gamma - 12\Omega^4\eta^2\gamma^2 + 6\Omega^4\eta^2\lambda}{W} \\
& + \frac{12\Omega^4\eta^2\sqrt{Z} - 48\Omega^4\eta^2 + 108\Omega^4\eta\gamma - 3\Omega^2\eta^2\lambda^2 + 6\Omega^2\eta^2\lambda\sqrt{Z} - 6\Omega^2\eta^2\lambda}{W} \\
& + \frac{-12\Omega^2\eta^2\sqrt{Z} + 24\Omega^2\eta^2 - 18\Omega^2\eta\gamma\lambda + 72\Omega^2\eta\gamma\sqrt{Z} - 108\Omega^2\eta\gamma + 108\Omega^2\gamma^2}{W} \\
& + \frac{54\Omega^2\lambda - 108\Omega^2\sqrt{Z} - 27\lambda^2 + 54\lambda\sqrt{Z} - 54\lambda + 108\sqrt{Z}}{W} + \frac{\left(\frac{1}{2}\lambda + \sqrt{Z}\right)^2}{G} \\
& \times \left(-4\Omega^6\eta^3\gamma + 24\Omega^6\eta^2 - 2\Omega^4\eta^3\gamma\lambda + 4\Omega^4\eta^3\gamma - 12\Omega^4\eta^2\gamma^2 + 6\Omega^4\eta^2\lambda + 12\Omega^4\eta^2\sqrt{Z}\right) \\
& \times \left(-48\Omega^4\eta^2 + 108\Omega^4\eta\gamma - 3\Omega^2\eta^2\lambda^2 + 6\Omega^2\eta^2\lambda\sqrt{Z}\right) \\
& \times \left(-6\Omega^2\eta^2\lambda - 12\Omega^2\eta^2\sqrt{Z} + 24\Omega^2\eta^2 - 18\Omega^2\eta\gamma\lambda + 72\Omega^2\eta\gamma\sqrt{Z}\right) \\
& \times \left(-108\Omega^2\eta\gamma + 108\Omega^2\gamma^2 + 54\Omega^2\lambda - 108\Omega^2\sqrt{Z} - 27\lambda^2 + 54\lambda\sqrt{Z} - 54\lambda + 108\sqrt{Z}\right)
\end{aligned} \tag{5}$$

where

$$G = \Omega^2\lambda (\Omega^4\eta^4 + 18\Omega^2\eta^2 + 81) \left(\frac{1}{3}\Omega^2\eta + \frac{1}{6}\eta\lambda - \frac{1}{3}\eta + \gamma\right)^2 \tag{6}$$

$$W = \Omega^4\eta^4\lambda + 18\Omega^2\eta^2\lambda + 81\lambda \tag{7}$$

$$Z = -\frac{1}{9}\Omega^6\eta^2 + \frac{2}{9}\Omega^4\eta^2 - \frac{2}{3}\Omega^4\eta\gamma + \frac{1}{36}\Omega^2\eta^2\lambda^2 - \frac{1}{9}\Omega^2\eta^2 + \frac{2}{3}\Omega^2\eta\gamma - \Omega^2\gamma^2 + \frac{1}{4}\lambda^2 \tag{8}$$

B.2. ADDITIONAL DATASETS OF PARAMETRICALLY DRIVEN DUFFING NON-LINEAR OSCILLATORS

B.2.1. STABILITY DIAGRAMS

Below we show additional stability diagrams obtained by numerical harmonic balance analysis of Device A and Device B which, together with the diagrams in Chapters 6 and 7, illustrate the structure of the parametric response phase space for many of the bichromatic drive power sweeps shown in this section.

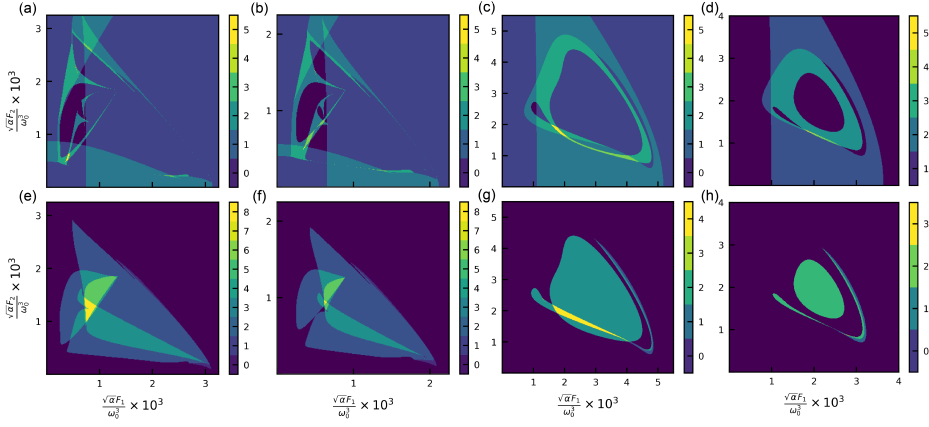


Figure 1: Stability diagrams for Device A. (a) The forces of the bichromatic drives are swept for $\delta/2\pi = -60$ MHz and $\Delta_{12}/2\pi = 50$ MHz are the numbers of stable solutions are shown. (b) The same with $\delta/2\pi = -45$ MHz and $\Delta_{12}/2\pi = 40$ MHz. (c) The same with $\delta/2\pi = -60$ MHz and $\Delta_{12}/2\pi = 160$ MHz. (d) The same with $\delta/2\pi = -40$ MHz and $\Delta_{12}/2\pi = 140$ MHz. (e), (f), (g), (h) The number of Hopf solutions for the drive parameters in (a), (b), (c), and (d) respectively.

Below we show a force-detuning sweep for the parameters of Device A for equal bichromatic drive forces F_c and $\Delta_{12}/2\pi = 80$ MHz.

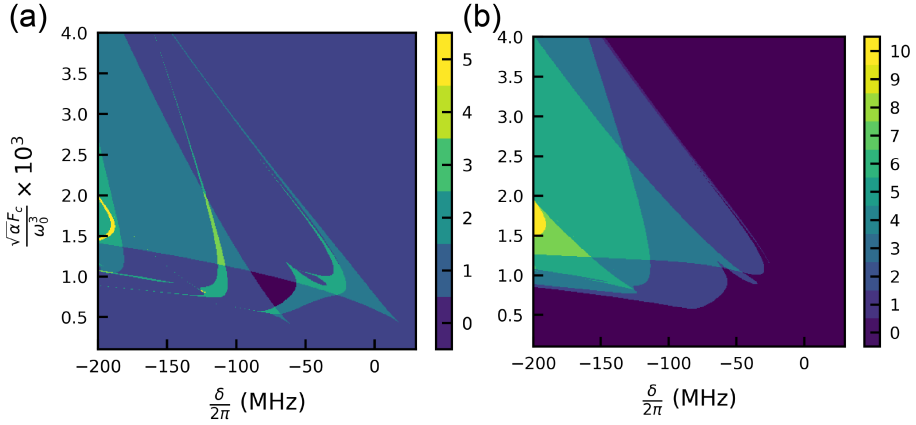


Figure 2: Force-detuning stability diagram for Device A. (a) The force of the bichromatic drives F_c and the detuning $\delta/2\pi$ are swept for $\Delta_{12}/2\pi = 80$ MHz, with the numbers of stable solutions shown. (b) The same as in (a), but with the numbers of Hopf solutions shown.

B.2.2. SHARED SPECTROSCOPIC FEATURES OF PARAMETRIC STATES FOR DETUNING AND POWER SWEEPS OF DUFFING AND KERR OSCILLATORS

On the next page we show again data from Chapter 5 (top row) to compare with additional data from the first device discussed in Chapter 7 (bottom row). The dataset in the top row shows the output field PSD and $|S_{21}|$ for a parametric pump detuning sweep on a $K \gtrsim \kappa$ Kerr oscillator, while the bottom row shows the same for a parametric pump power sweep on a $K \ll \kappa$ Duffing oscillator. In each case, the oscillators are driven above the parametric threshold, but in the case of the Kerr oscillator the excitations at the frequencies symmetric about the pump are below the measurement chain noise floor due to a modest G_{eff} and the small size of the few-photon parametric state generated. In contrast, for the Duffing oscillator gain at the frequencies symmetric about the pump are clearly visible due to the greater G_{eff} and larger photon number parametric states generated.

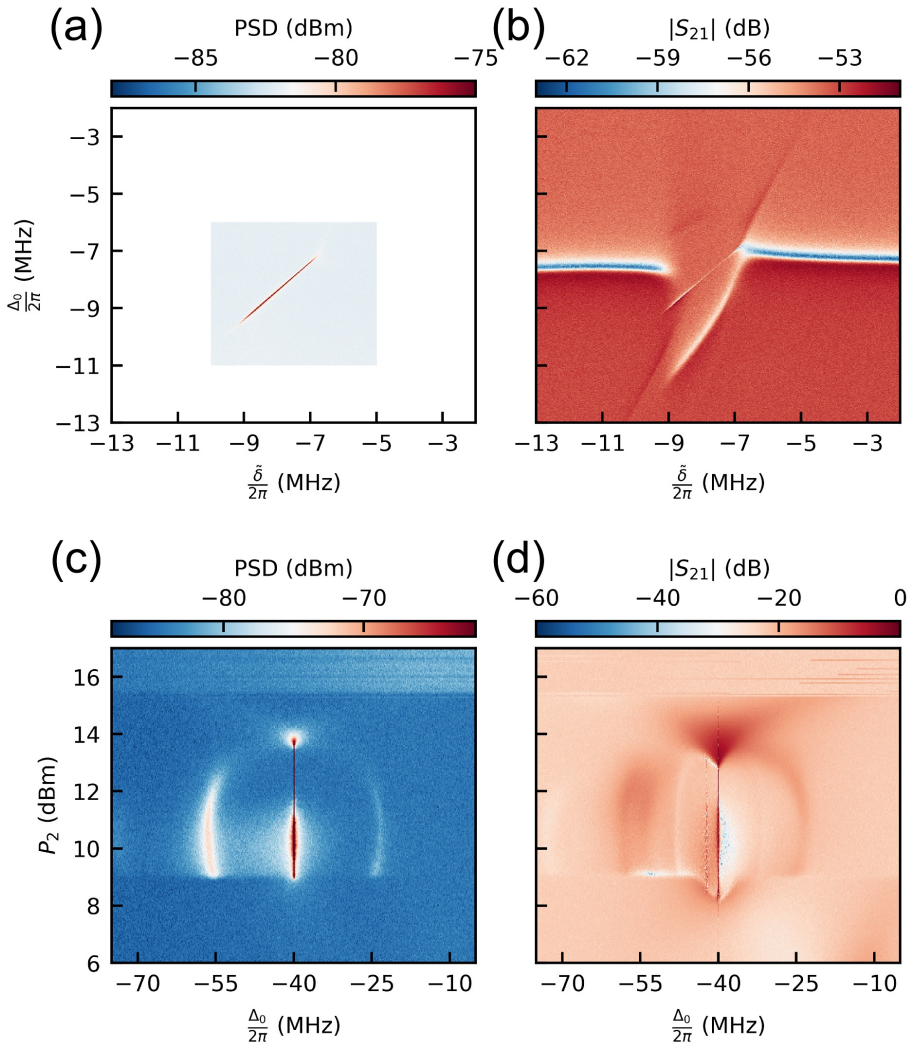
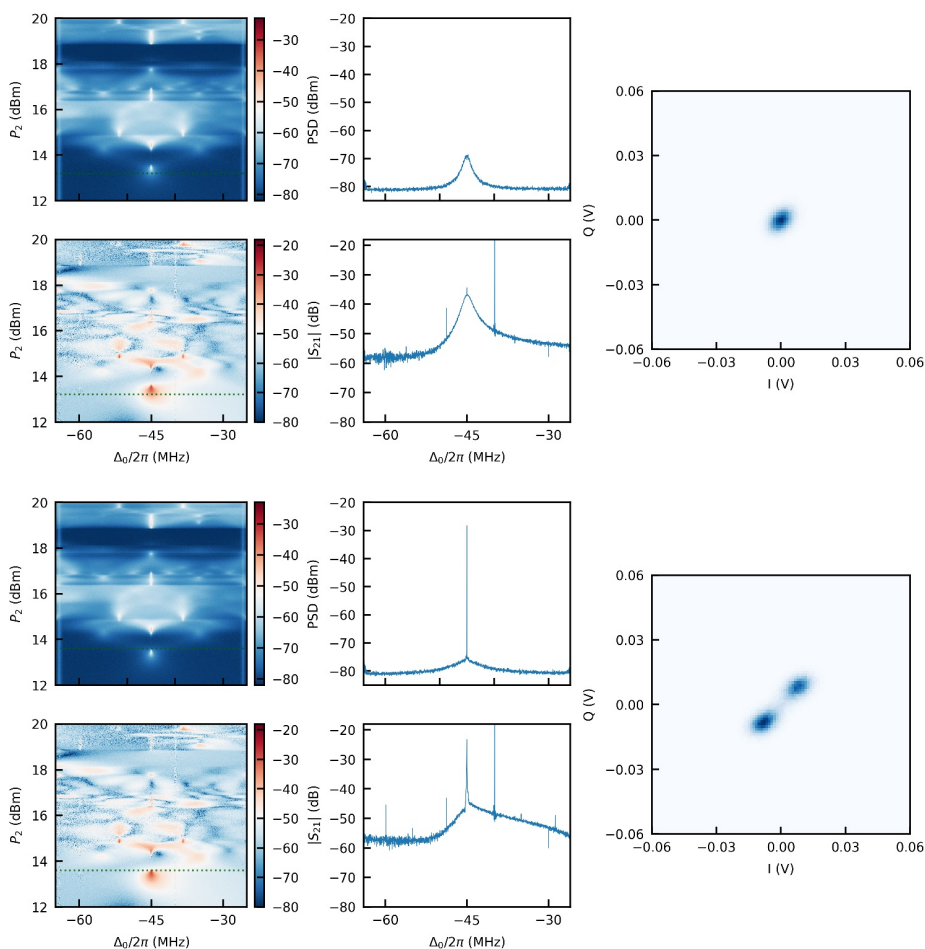
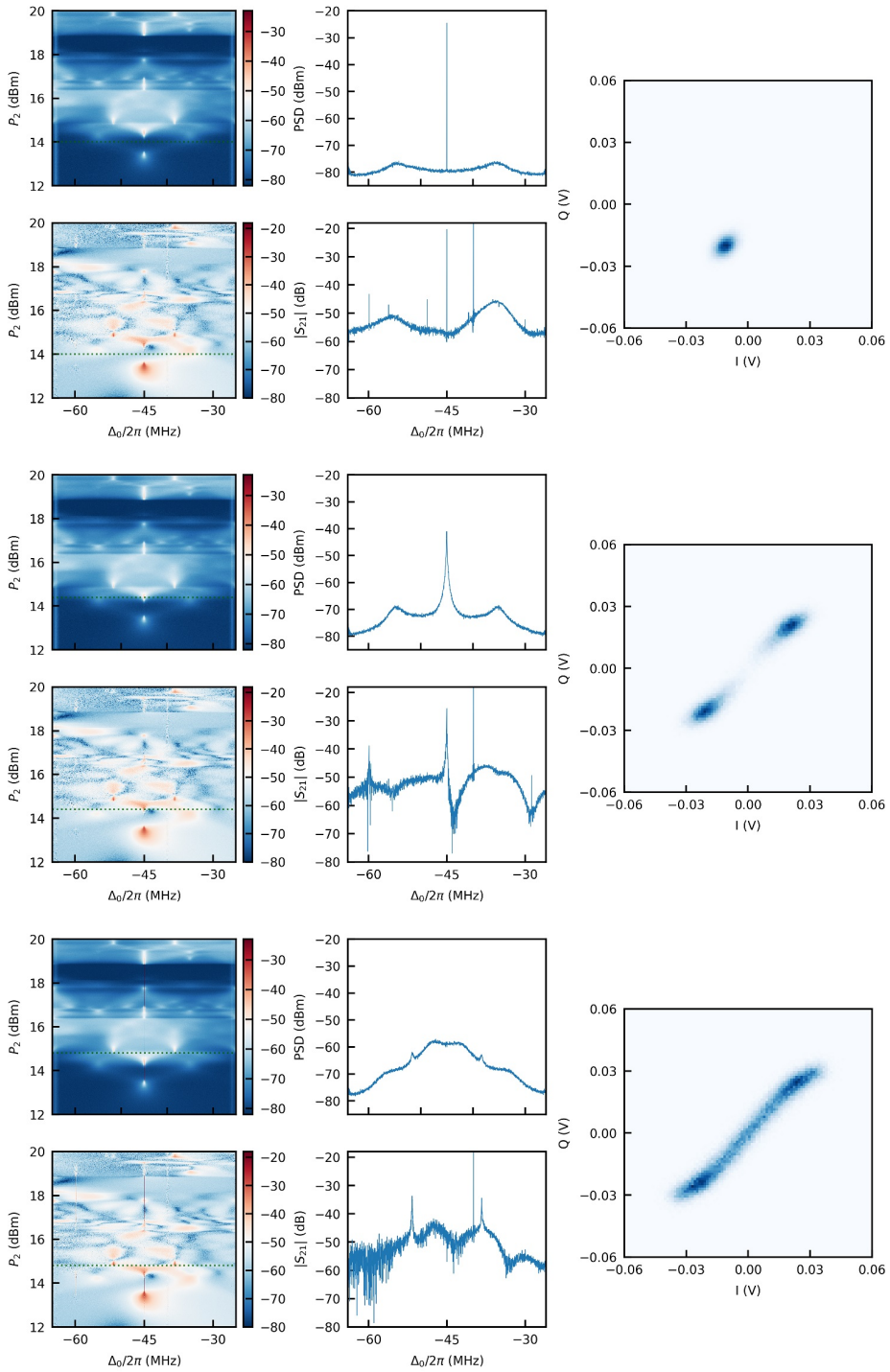


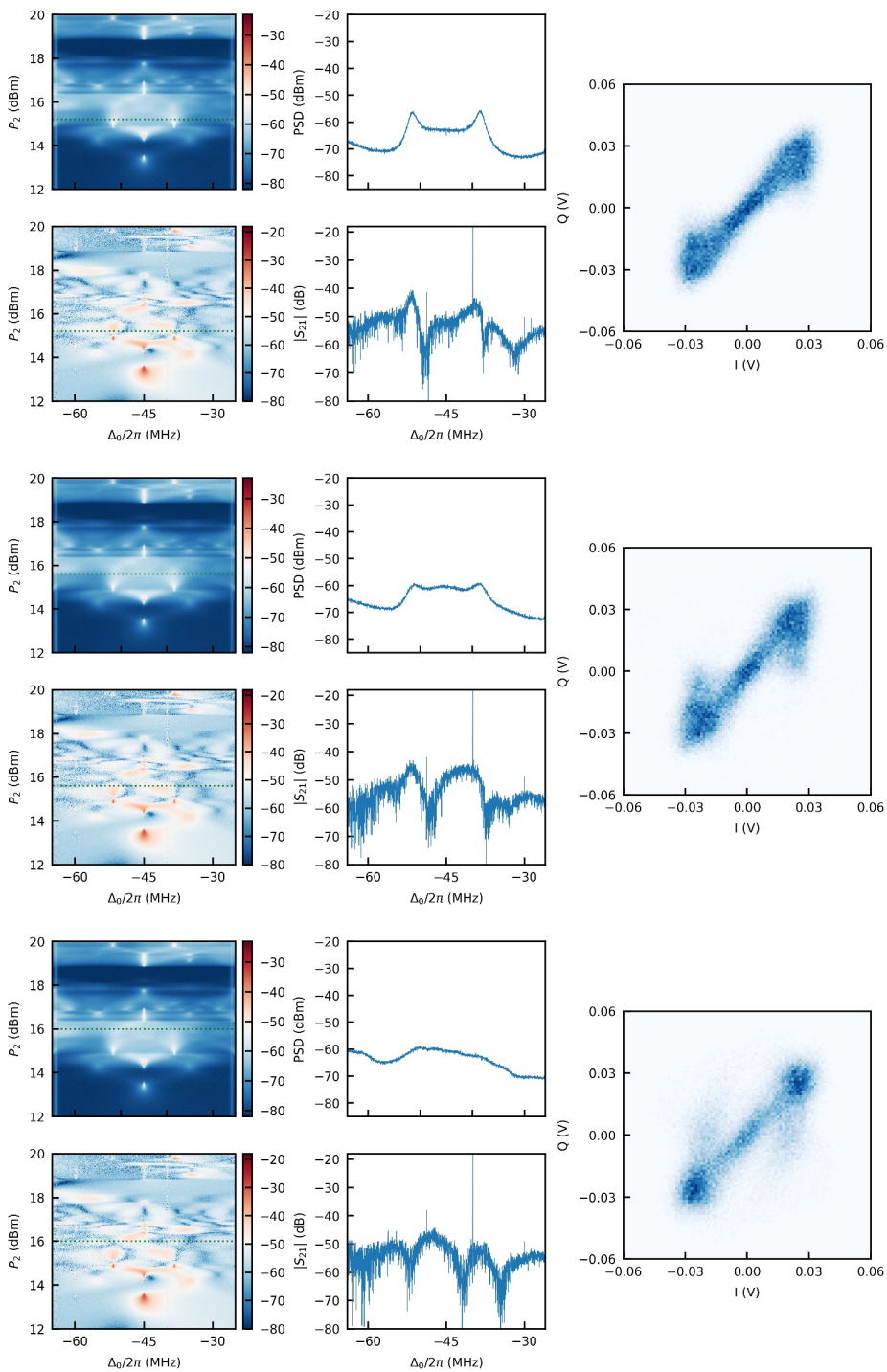
Figure 3: Output field PSD and $|S_{21}|$ for two oscillators in different parameter regimes. a), b) The response of the moderately nonlinear Kerr oscillator (the device from Chapter 5) to a parametric pump detuning sweep. Here, $P_1 = P_2 = 12\text{dBm}$ and $\Delta_{12}/2\pi = 200$ MHz. c), d) The response of the weakly nonlinear Duffing oscillator ("Device A" from Chapter 7) to a parametric drive power sweep. Here, $P_1 = 19\text{dBm}$, $\Delta_{12}/2\pi = 140$ MHz and $\delta/2\pi = -40$ MHz at the analysis (c) and probe (d) frequency difference from the bare resonance $\Delta_0/2\pi$.

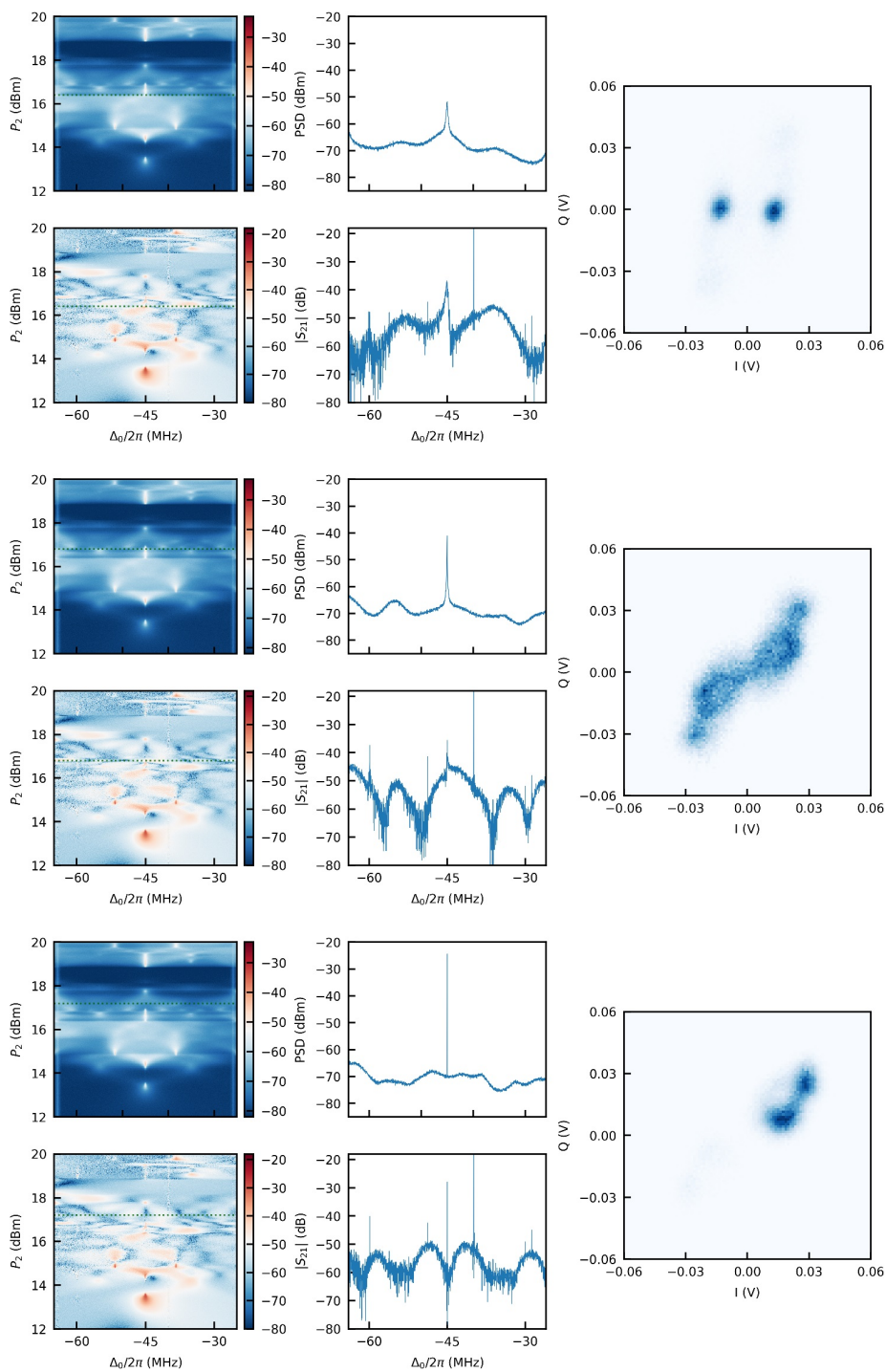
B.2.3. RESPONSE SNAPSHOTS OF A PARAMETRICALLY DRIVEN DUFFING OSCILLATOR FOR VARIOUS DRIVE PARAMETERS

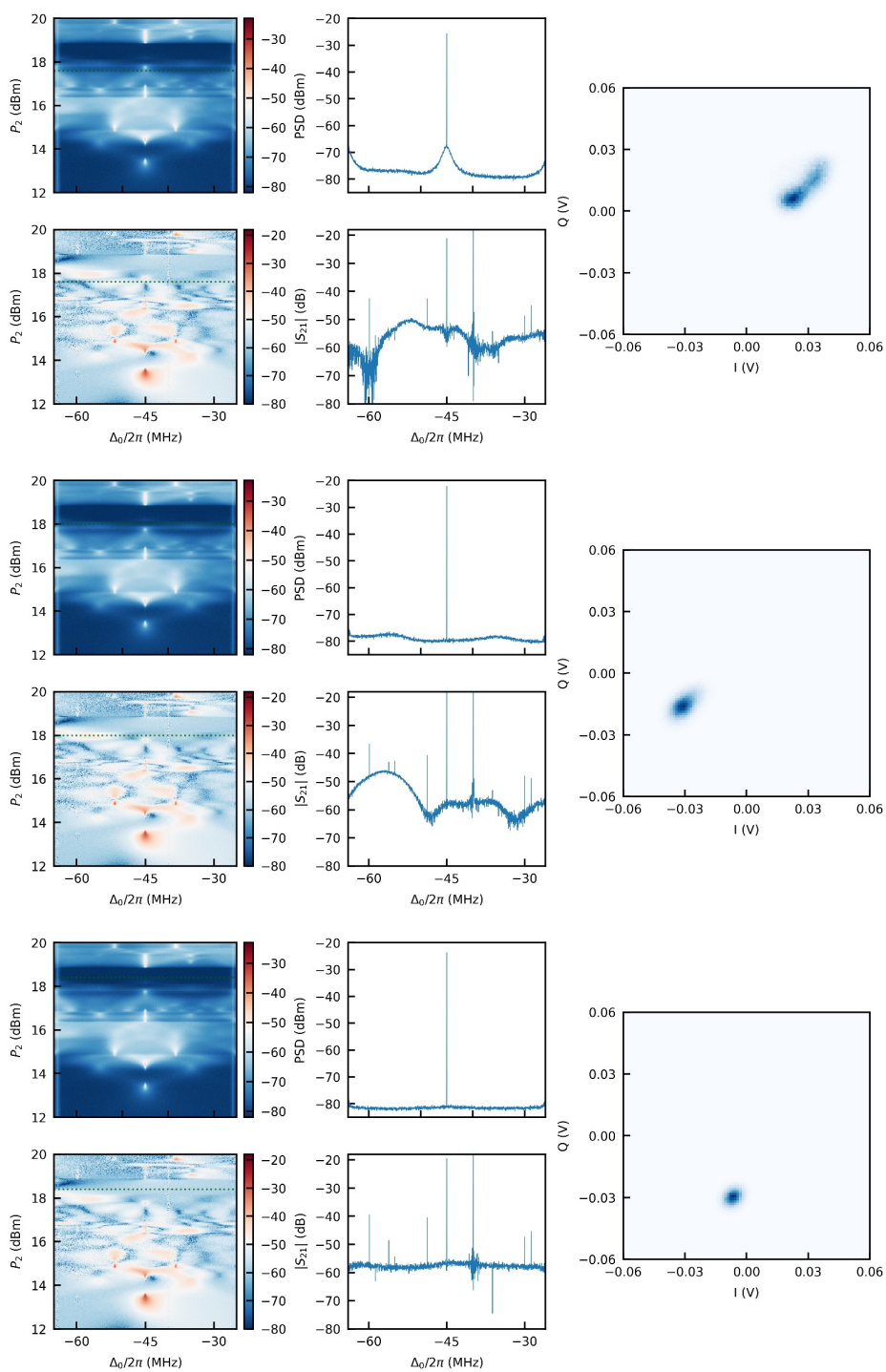
Below we plot additional data measured from the device discussed in Chapters 6 - 7, "Device B". In the left-hand column are displayed the output field PSD and $|S_{21}|$ of the device as a function of swept upper frequency bichromatic drive power P_2 (with the lower frequency drive fixed at $P_1 = 20$ dBm), $\delta/2\pi = -45$ MHz, and $\Delta_{12}/2\pi = 40$ MHz where $\Delta_0/2\pi$ is the frequency response detuning relative to $\omega_0/2\pi$. In the center column, the PSD and $|S_{21}|$ as a function of frequency are shown at the powers indicated by the green dotted lines in the leftmost column plots. In the rightmost column is the output field quadrature 2D histogram for the powers indicated by the green dotted lines, measured with an analysis bandwidth of 25 MHz.

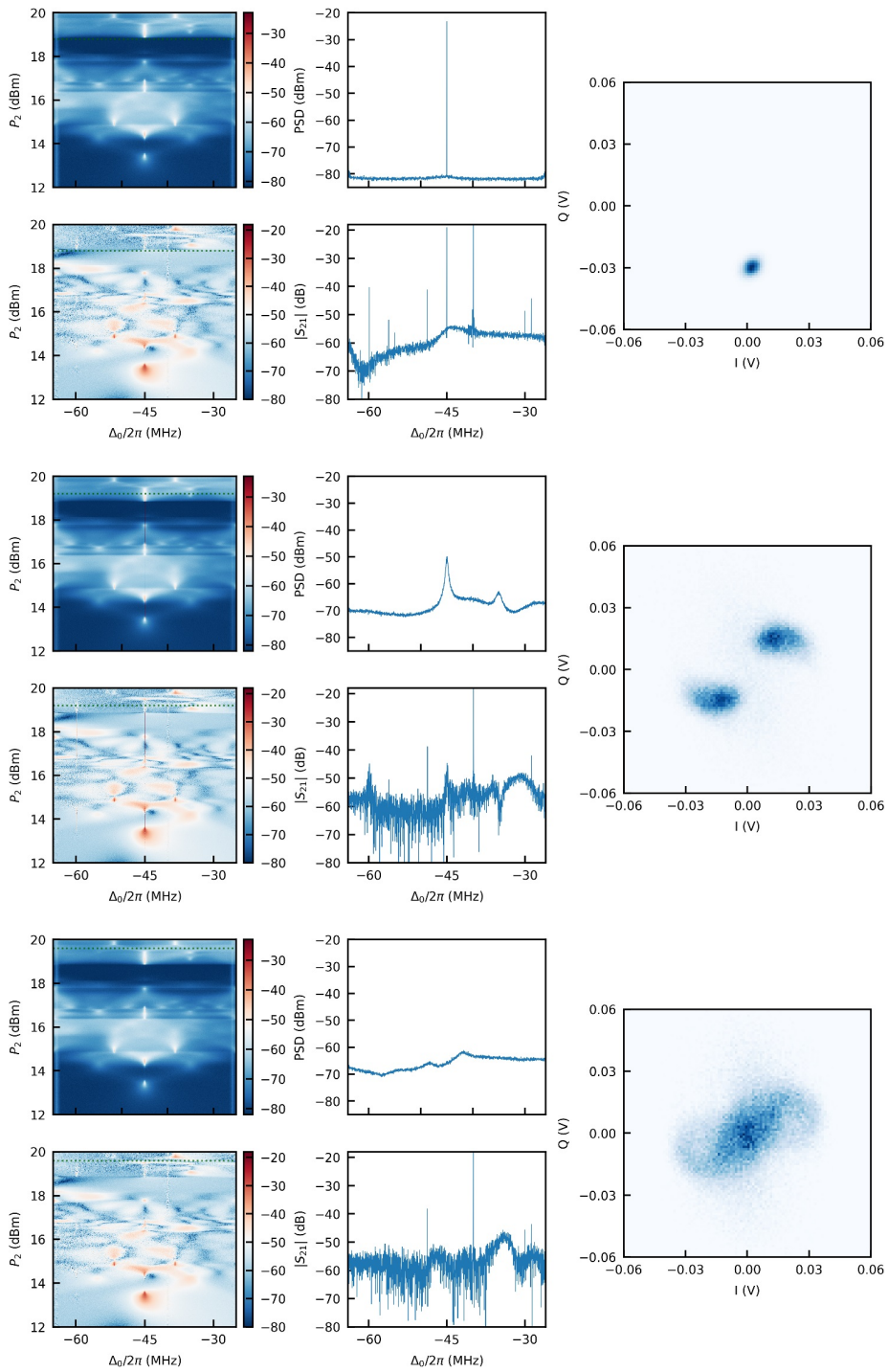




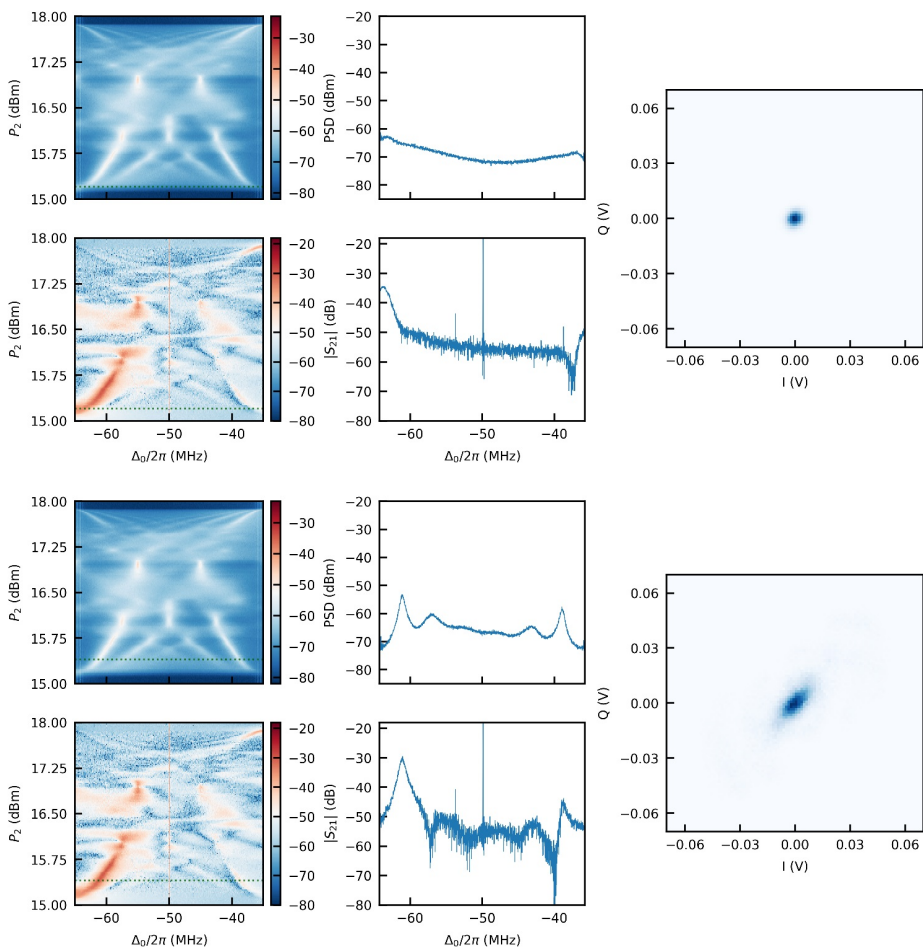


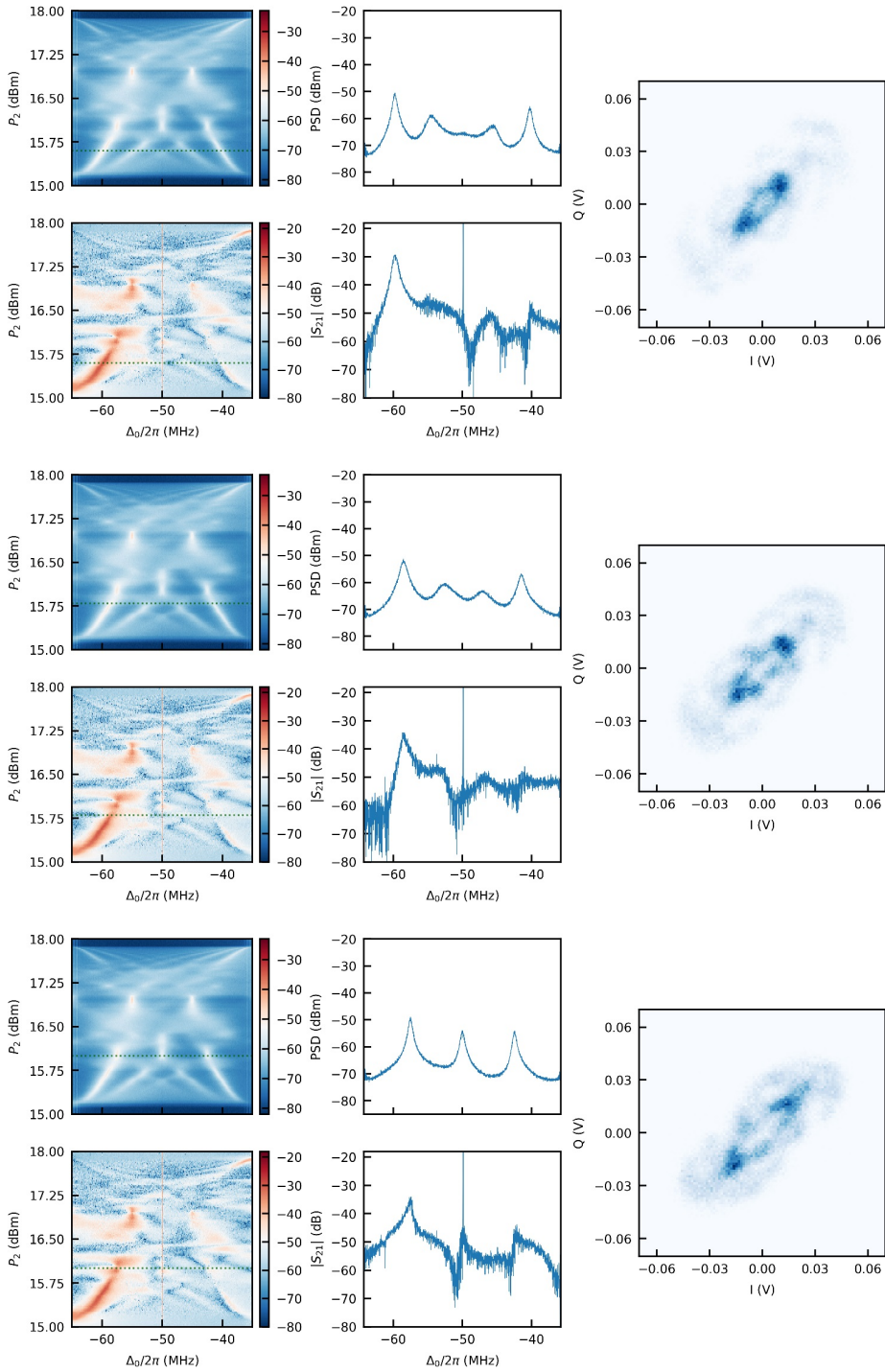


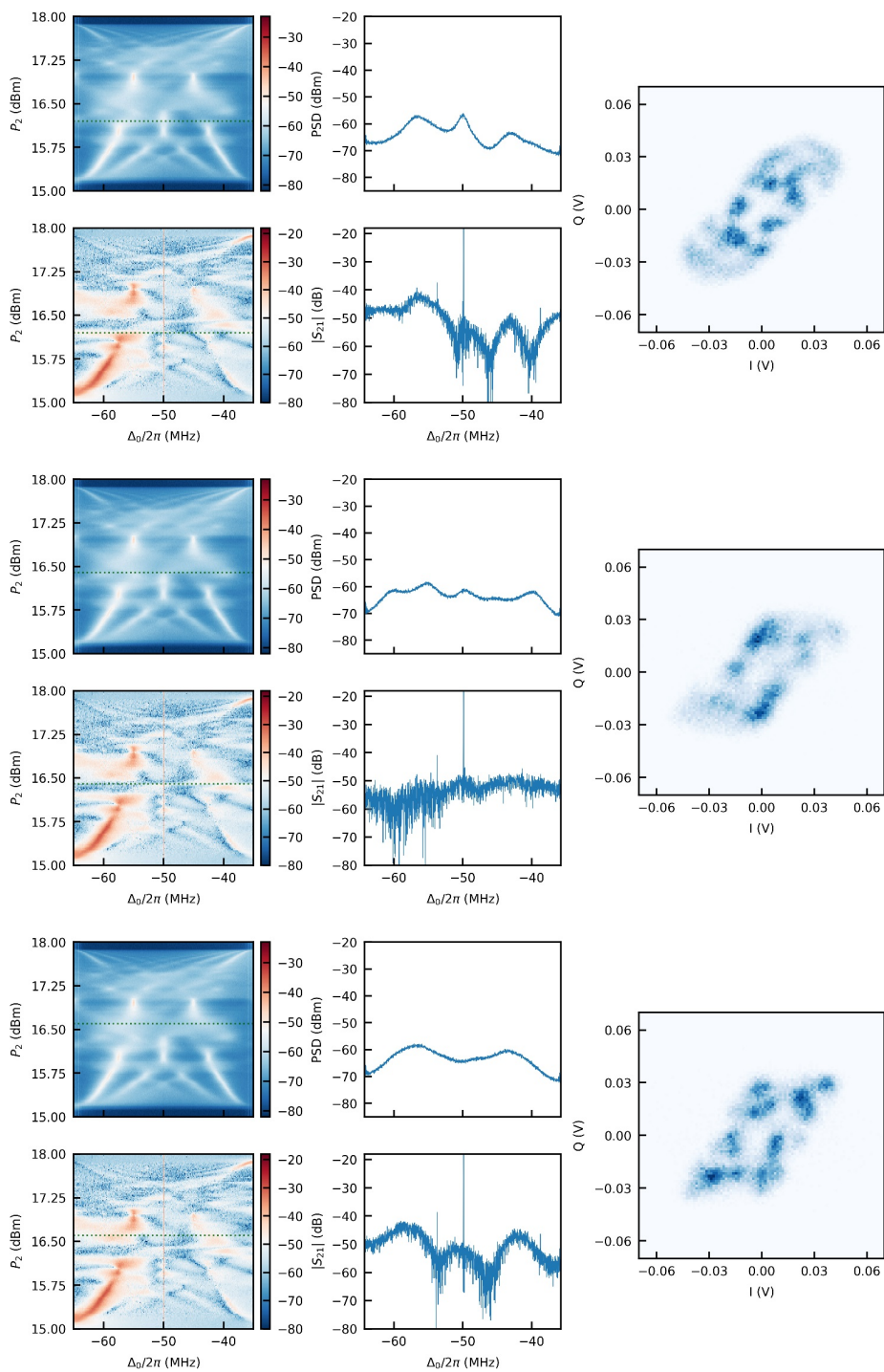


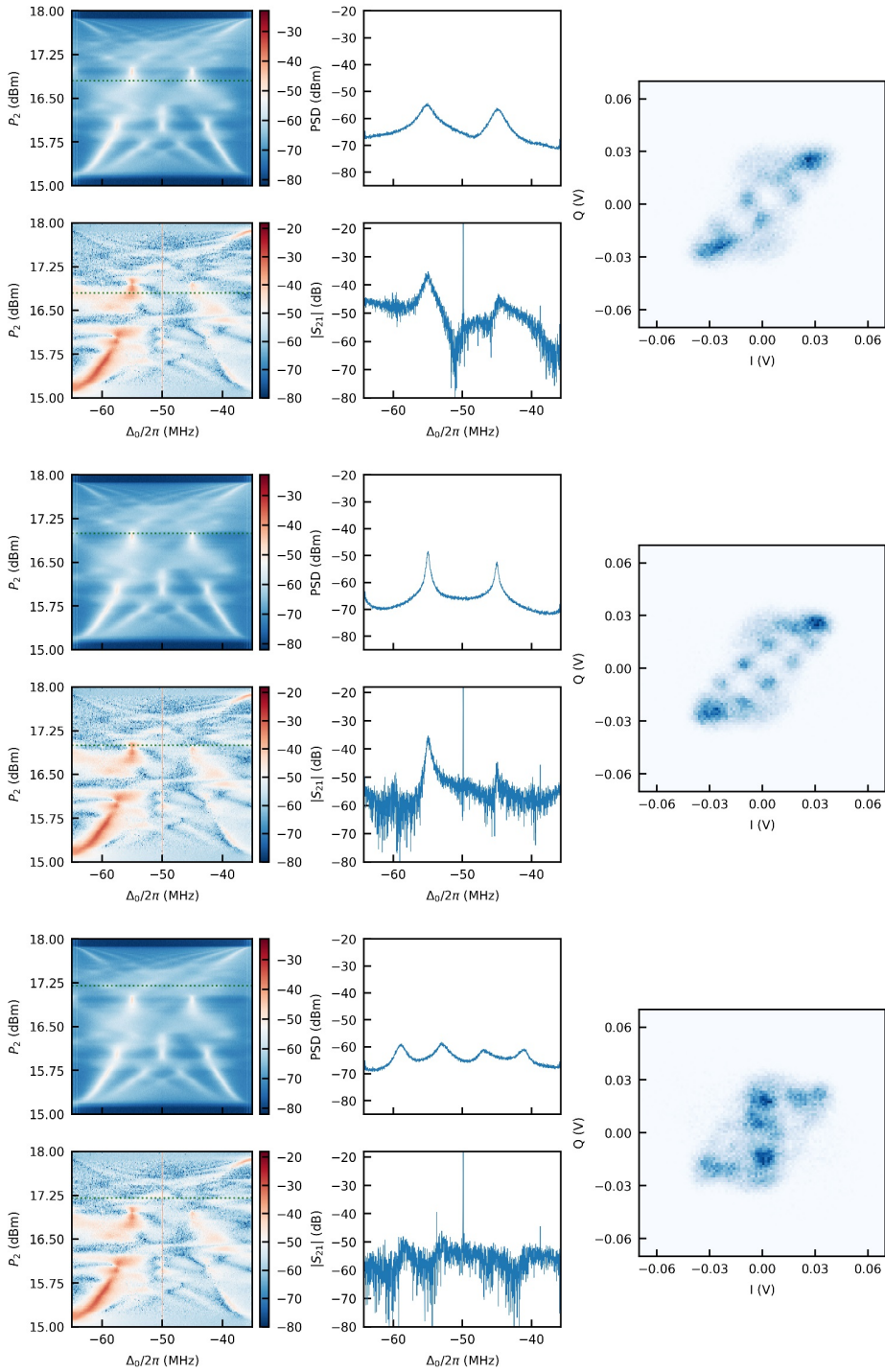


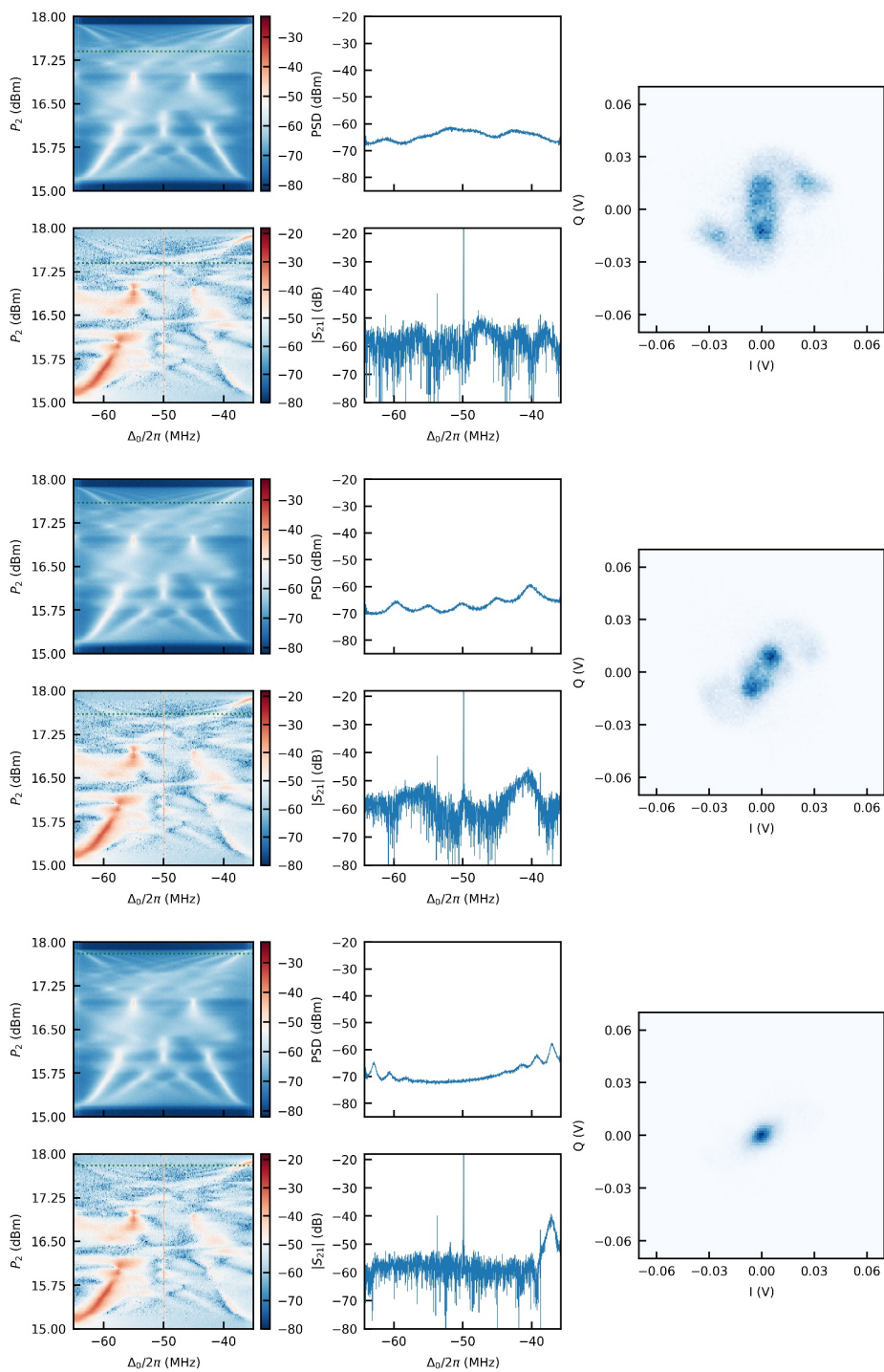
Below we show in the same format the Device B response for fixed $P_1 = 20\text{dBm}$, $\delta/2\pi = -50$ MHz, and $\Delta_{12}/2\pi = 30$ MHz, with the quadratures measured with an analysis bandwidth of 20 MHz.



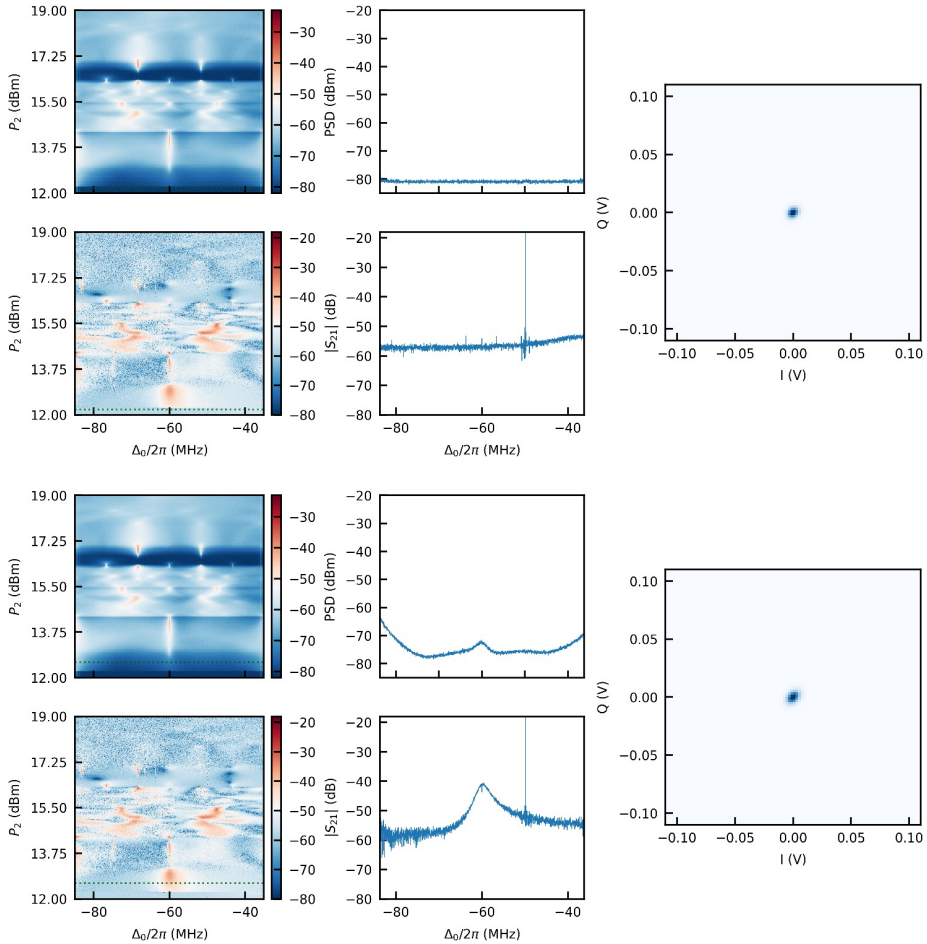


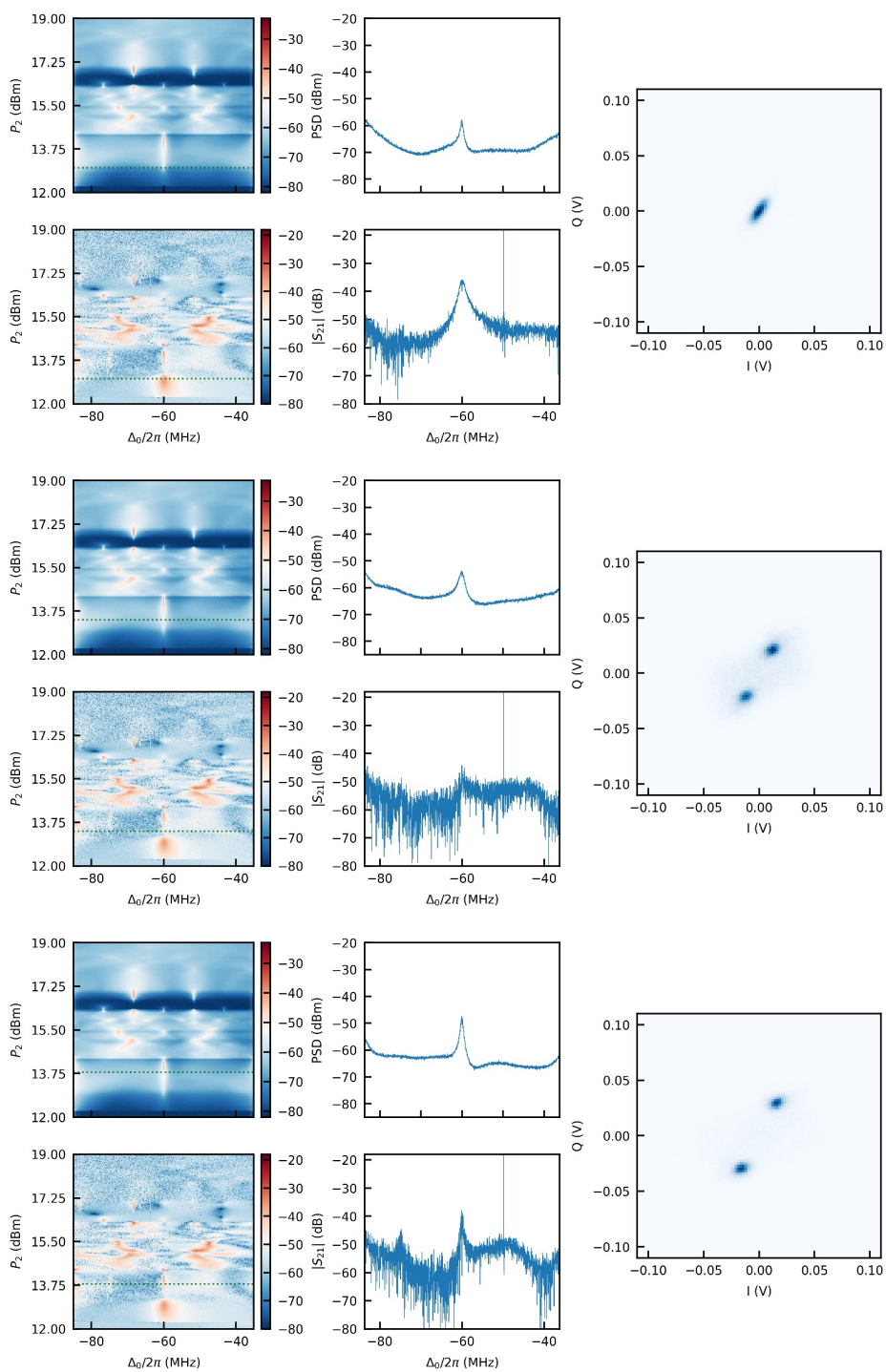


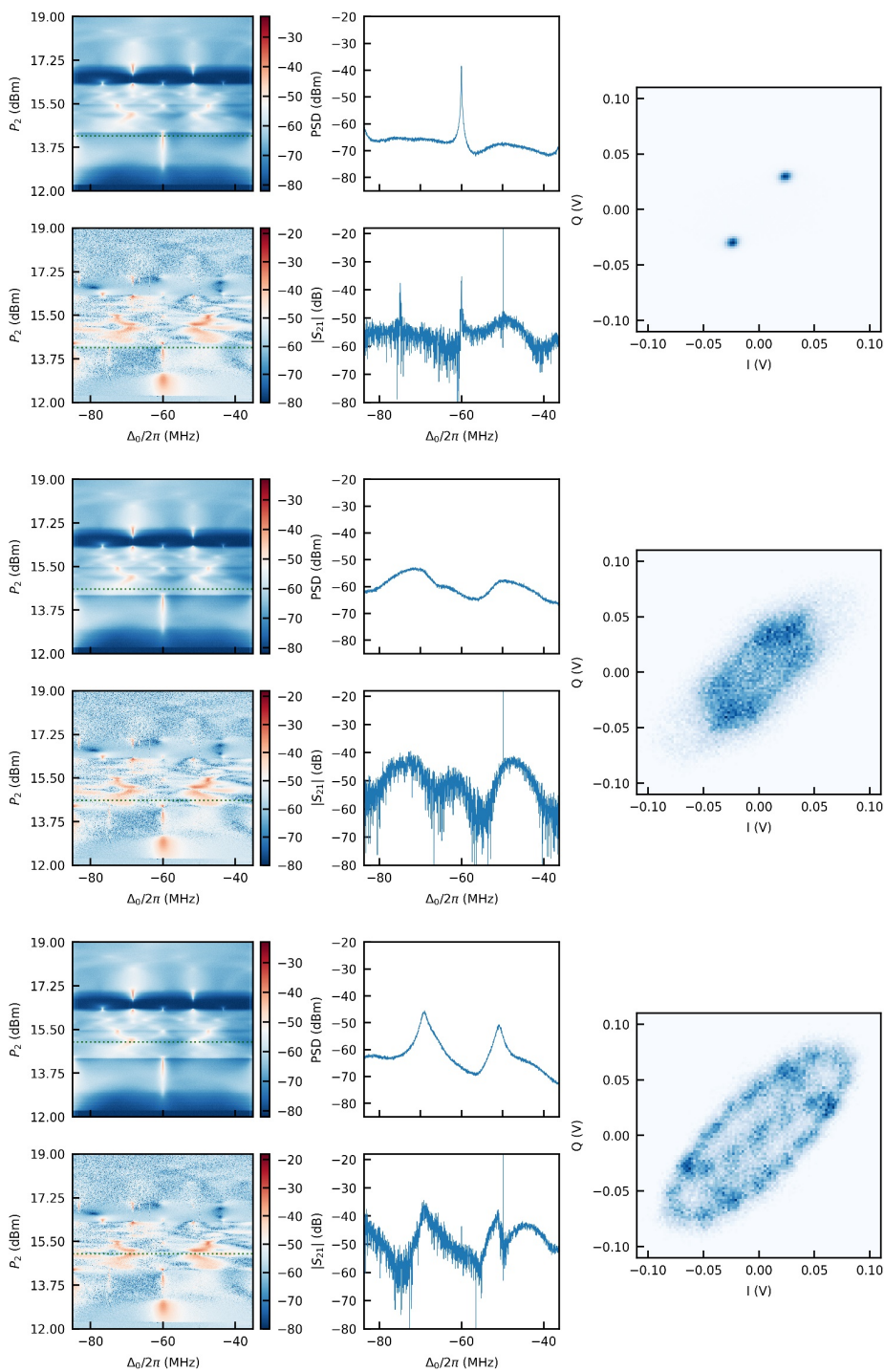


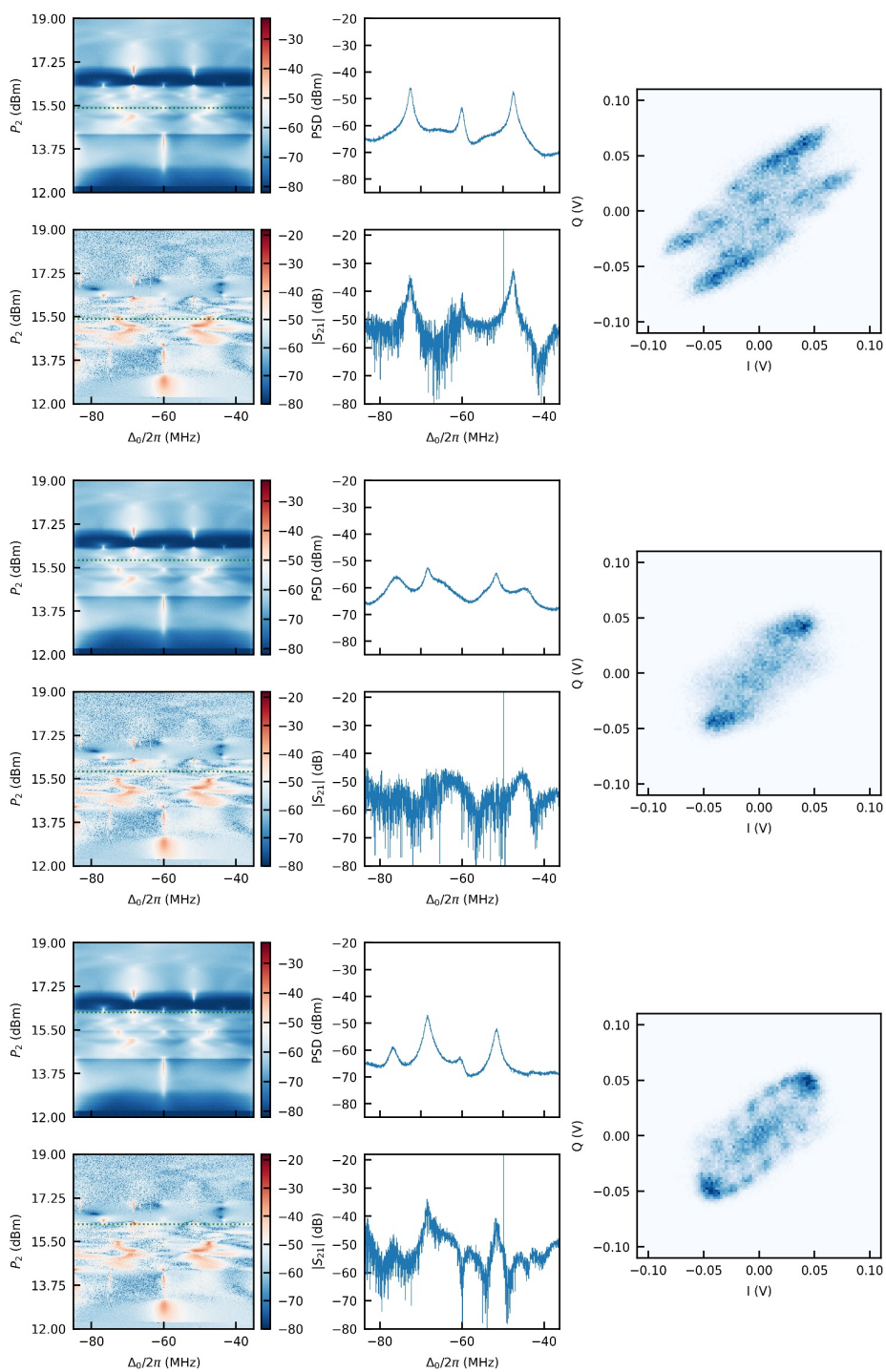


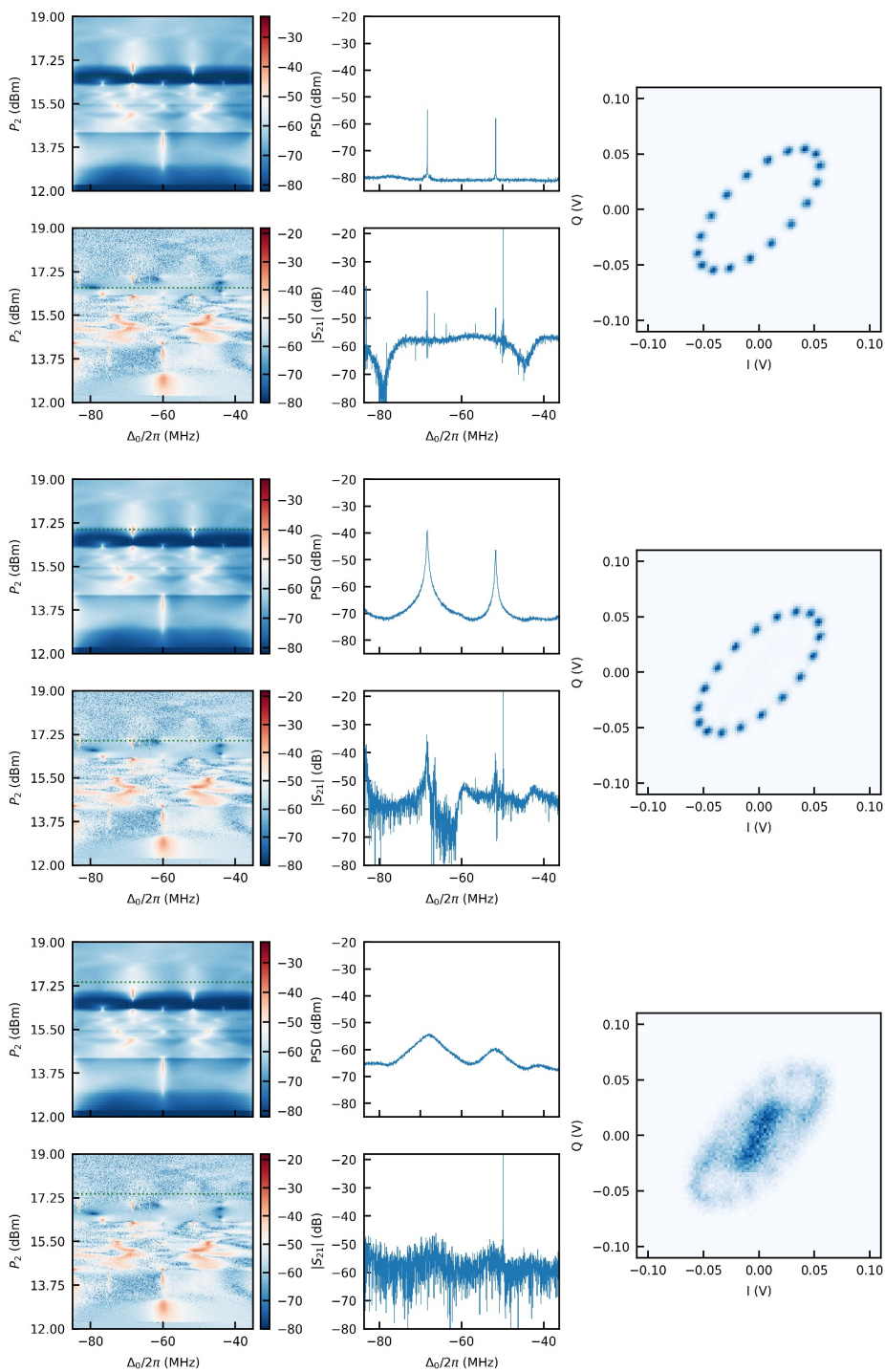
Below we show in the same format the Device B response for fixed $P_1 = 20\text{dBm}$, $\delta/2\pi = -60\text{ MHz}$, and $\Delta_{12}/2\pi = 50\text{ MHz}$, with the quadratures measured with an analysis bandwidth of 24 MHz.

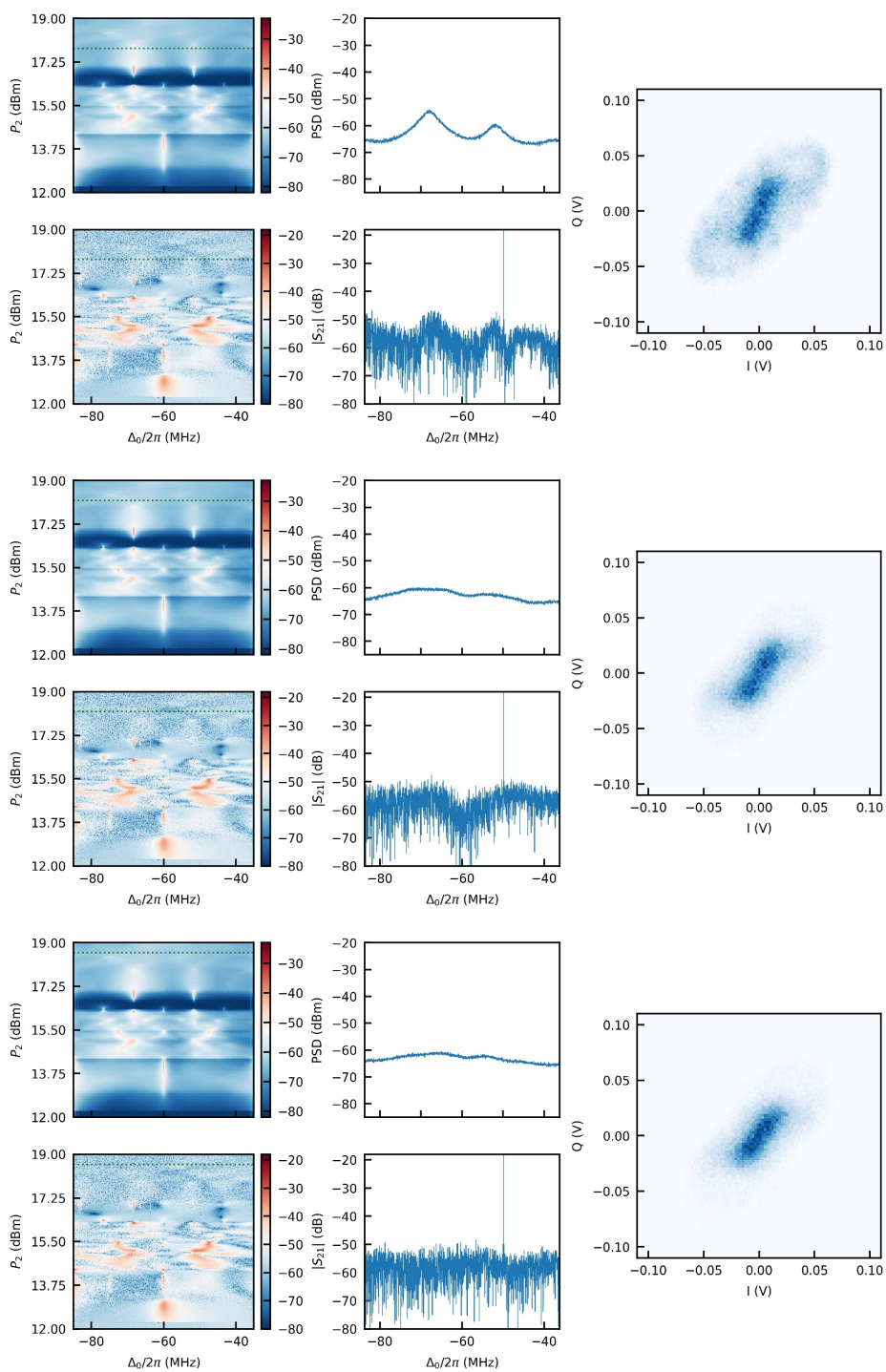






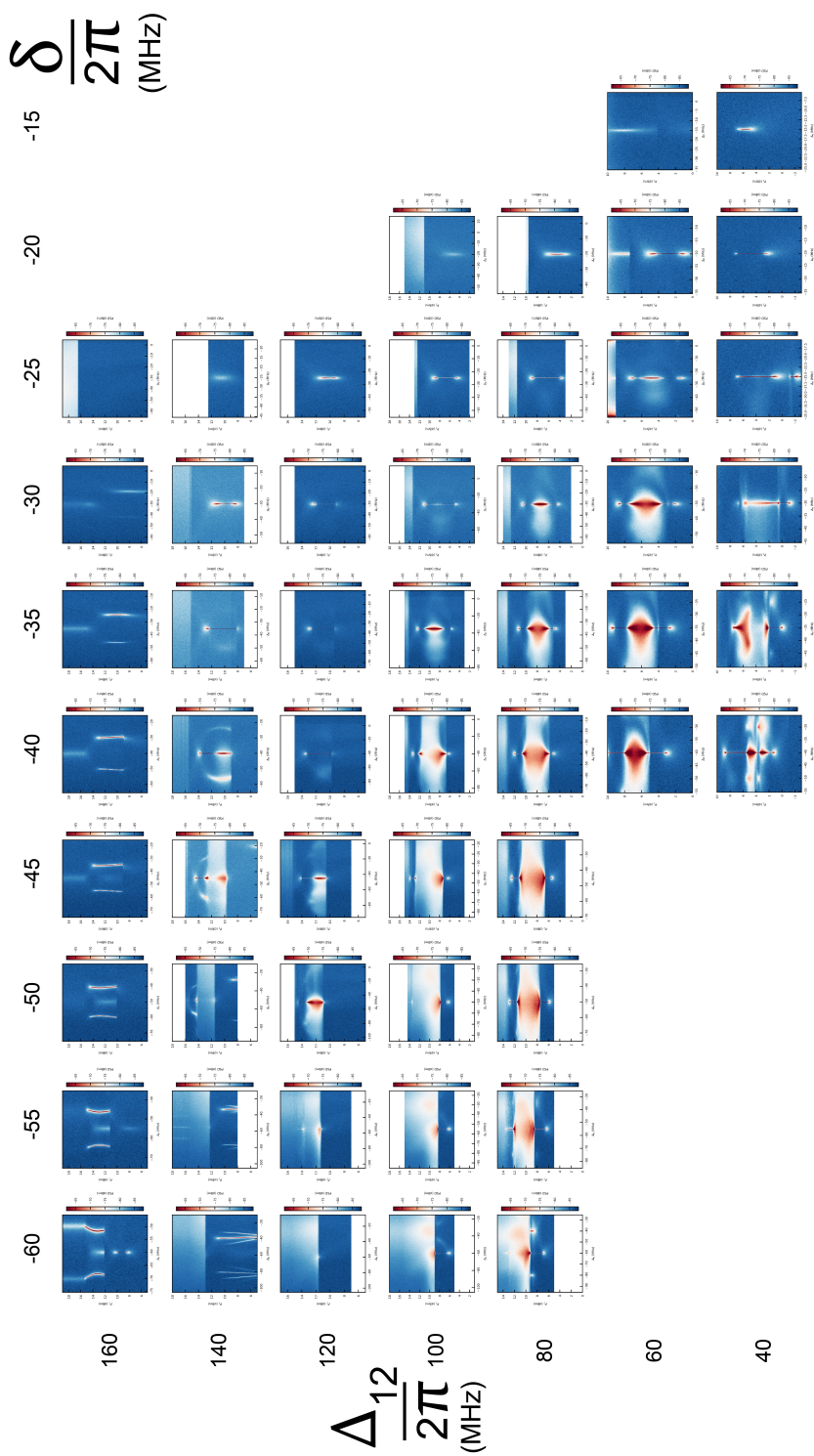






B.2.4. RESPONSE MAP OF A PARAMETRICALLY DRIVEN DUFFING OSCILLATOR FOR VARIOUS DRIVE PARAMETERS

On the next page we show a response map for the Device A discussed in Chapter 7 where each column is the PSD for a fixed bichromatic pump detuning δ with varied Δ_{12} , P_1 , and across each row there is a fixed Δ_{12} , P_1 and varied δ . For each PSD, the response as a function of P_2 is shown. From top to bottom, the values of P_1 in each row are [19, 19, 16, 16, 13, 10, 8] dBm. For each plot, the y-axis is P_2 (dBm) and the x-axis is $\Delta_0/2\pi$ (MHz).



On the next pages we show in more detail a subset of PSD plots from the previous response map (Device A) along with their corresponding $|S_{21}|$ measurements. In each panel a separate parametric drive detuning δ is fixed and the power of the upper frequency bichromatic drive P_2 is swept.

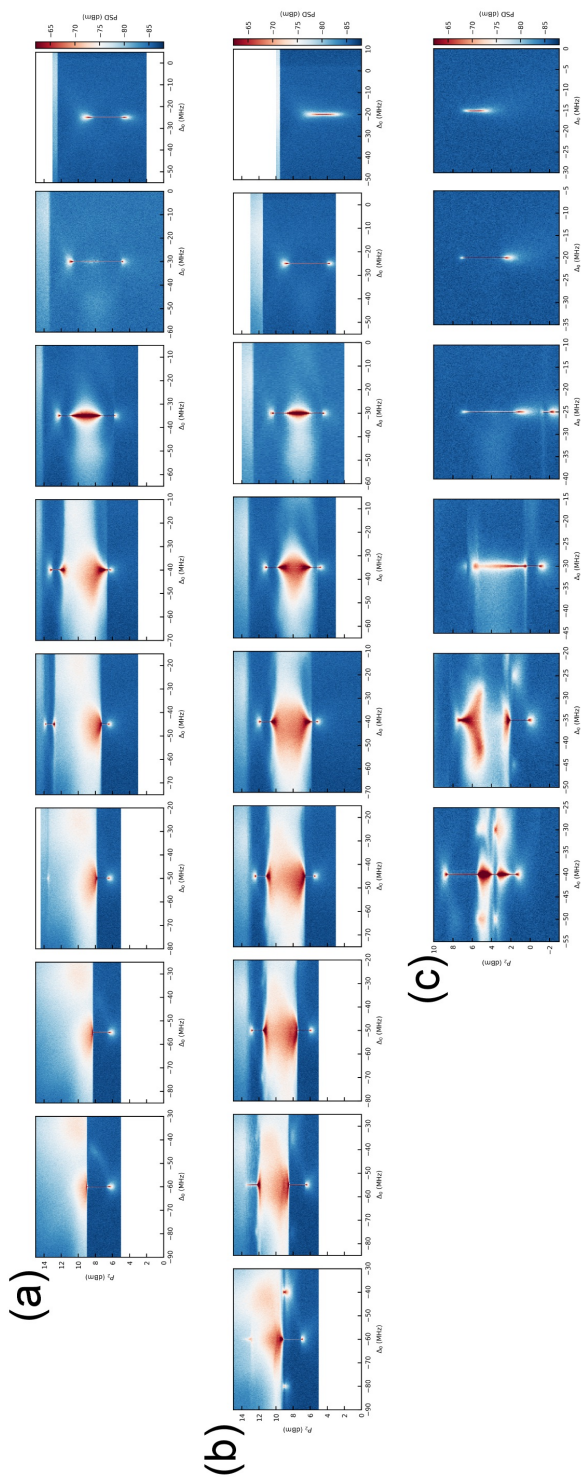


Figure 4: Output field PSD under parametric driving. a) Datasets for $P_1 = 16\text{dBm}$, $\Delta_{12}/2\pi = 100\text{ MHz}$, Δ_{12} varied from -60 MHz to -25 MHz in steps of 5 MHz . b) Datasets for $P_1 = 13\text{dBm}$, $\Delta_{12}/2\pi = 80\text{ MHz}$ and $\delta/2\pi$ varied from -60 MHz to -20 MHz in steps of 5 MHz . c) Datasets for $P_1 = 8\text{dBm}$, $\Delta_{12}/2\pi = 40\text{ MHz}$ and $\delta/2\pi$ varied from -40 MHz to -15 MHz in steps of 5 MHz .

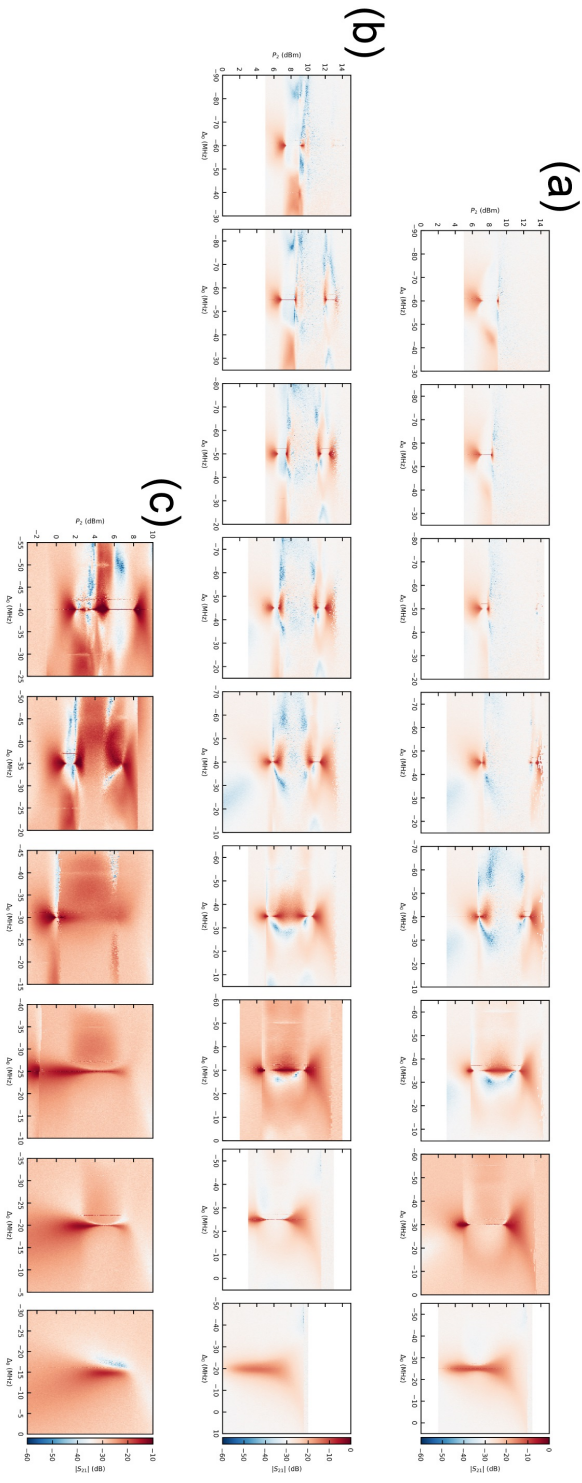


Figure 5: $|S_{21}|$ under parametric driving. a) Datasets for $P_1 = 16$ dBm, $\Delta L_2/2\pi = 100$ MHz and $\delta/2\pi$ varied from -60 MHz to -25 MHz in steps of 5 MHz. b) Datasets for $P_1 = 13$ dBm, $\Delta L_2/2\pi = 80$ MHz and $\delta/2\pi$ varied from -60 MHz to -20 MHz in steps of 5 MHz. c) Datasets for $P_1 = 8$ dBm, $\Delta L_2/2\pi = 40$ MHz and $\delta/2\pi$ varied from -40 MHz to -15 MHz in steps of 5 MHz.

Below we show over a wider frequency range the dependence of the PSD on the fixed power P_1 of the lower frequency component of the bichromatic drive for Device A. For $\Delta_{12}/2\pi = 160$ MHz, $\delta/2\pi = -60$ MHz, we set P_1 in each plot from left to right as [19, 18, 17] dBm.

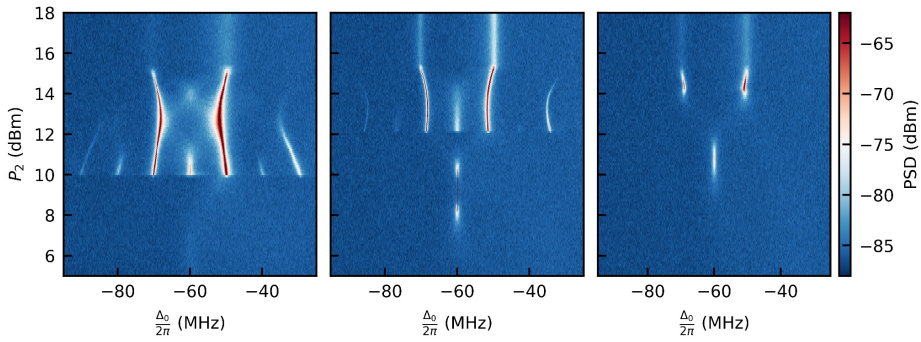


Figure 6: From right to left as P_1 is increased from 17 dBm to 19 dBm, additional evenly-spaced gain peaks appear in the PSD, indicating that a chaotic response is accessible nearby these bichromatic drive parameter settings.

ACKNOWLEDGEMENTS

I would not have been able to arrive at the end of my PhD journey without the valuable support of numerous individuals. Both within the TU and outside of it, there are many that I would like to thank.

Gary, your passion for physics has always been the ultimate motivator for myself and everyone else who has worked for you. You are always brewing up new ideas for experiments to perform, diagnosing sources of issues as they appear, and handing out information that can take anywhere from minutes to years for your students to process. Whenever things are tough - samples aren't working as we expect, the project's direction is unclear, or problems seem intractable - you always know when the right time is to give breathing room, to provide guidance, and when to direct. I think that your role is an incredibly difficult one, in that the core missions are to craft continual generations of young researchers into independently capable scientists and facilitate the unraveling of the physical unknown all at once. It can't be easy to manage the different personalities, ambitions, intuitions, inclinations, and interests of those who spend time in your group. I've learned that being a good mentor is hard, and that I'm fortunate to have had one as great as you.

Clinton, your contributions to both my research and overall enjoyment of my PhD has been immense. You have always been available to bounce ideas off of and have always made it easy to feel comfortable asking stupid questions to. You have always provided the guidance I needed when I got stuck on something and provided insight into areas that I had never thought deeply about before. The final stretch of my PhD would have been incredibly more difficult without you in the group - thank you for everything!

Jasper, you were the first person I met when I joined SteeleLab! You always brought a great atmosphere to the lab and had lots of ideas to make work more fun. I will always remember that one of my first introductions to Dutch cuisine was the frikandel speciaal! Even when you were very busy with your project, you always lightened up the mood and offered helpful advice to others with their research. We made a lot of great memories during our overlapping time in the group, and I'm happy to now join you in the post-PhD life!

Jean-Paul, even though for most of our time in the group we didn't have much overlap in terms of research topics, I always found myself talking to you a lot about physics! I've always appreciated the humour, eccentricity, and levity that you bring to the group, and I knew who to go to when I needed a good laugh. The PhD life can be a slog, and you've always been there to put a smile on everyone's faces to help them through rough patches. I will always remember

searching for the engineering lab with you while carrying a very leaky döner wrap. Good luck with wrapping up your thesis!

Ines, you were one of the first people from SteeleLab that I met, and I think the person that I've collaborated with for the longest! You helped me to learn everything I know about cavity optomechanics, and while those topics didn't end up in my thesis, everything that I learned from working together with you will always remain firmly embedded in my head. I really enjoyed our overlapping time together in the group and I'm so happy for you, JP, and Emily!

Sercan, whether I was supervising you as a student or whether you were my coworker as a PhD in the group, I've always greatly enjoyed talking with you about physics and everything else! I was really lucky to have you as my first student, because your insightful questions always forced me to think through my answers as deeply as I could. I truly learned a lot from you, and I'm really glad to see how well you've been doing in your PhD. I'm sure that your thesis will be great, and I'm looking forward to reading it!

Robin, you've really excelled as a PhD and are making tons of great chips in the cleanroom! You've brought a lot of advancements to the group in a short time - bringing up coherence times and overhauling our setups in particular! Good luck with the rest of your PhD, I am sure you will do a great job!

Mario, Marios, Adrián, Sarwan, Byoung-moo, and Fatemeh, as I was in the beginning of my PhD, you were all nearing the end of your time in the SteeleLab. It was great having you all around to lend your experience and knowledge to the group, and my research benefited a lot from conversations with each of you!

Orjan, I've had a really great time collaborating with you! We've learned a lot together, and I think it's wonderful that we've been able to bring our research directions together. Every time we talk, I learn physics and math that helps me to both more deeply understand concepts that I'd come across before in different contexts, and to learn entirely new things altogether. Best of luck in your PhD!

To my students **Giulio, Hans, Leon, and Solal**, the supervision of your projects and the contributions you brought to my own research taught me perhaps more than anything else during the course of my PhD. I am sure that you will all be successful in your lives, whether you continue to pursue research or otherwise!

Matteo and Sarah, it may feel that you've only just started your PhD journeys, but it goes by fast! With each of you in the lab, the future of SteeleLab is bright and I know that you both have the abilities to make the best out of your time here. Good luck! And thanks to **Marius**, the next generation is in good hands!

Prior to joining the SteeleLab, I was fortunate to have had the guidance and advice of numerous postdocs, professors, supervisors, and mentors, without whom I would certainly not be writing this thesis. **Thomas, Jeongwan, Yonuk, Taewan, Gwanyeol, Nakamura-sensei, Usami-sensei, Shikano-sensei, Yamazaki-san, Tabuchi-san, Kono-san, Sunada-san, Fujiwara-san, Hisatomi-san, Takahashi-san, Dany, Arnaud, Kun, Cosmic, Arjan, Andreas, Christopher, Johannes, Simon, Tamate-san, and Nakata-san**, thank you for everything!

To my **friends** back in Canada, thank you! Life has gone by fast these past few years I've been away, and our 30's are upon us! The marriages are already happening and I'm sure that babies won't be too far away. **James, Quinn, Ryan, Matt, Martin, and Aris**, you all helped me in your own unique ways, and I'm looking forward to seeing you all soon!

To my **family**, I certainly would not have been able to reach this point without all of your support. The end of my PhD is the end of a long journey in education that started when I was first enrolled in school by my parents. The things I was interested in studying have changed over the years and you all have always supported my choices at every step of the way. Your constant support in encouraging me to try to anything I wanted helped the most. As I'm sure you know, I'm very happy to be at the end of this road, and am looking forward to forcing all of you to start referring to me as Dr. Koenig!

りこちゃん、いつも応援してくれてありがとう。りこちゃんはいつも私がやりたいことは何でもできると信じてくれた。たとえ実現が難しいような夢であっても、りこちゃんがそれを疑ったことは一度もなかった。周囲の人々の日々の励ましとサポートがなければ、博士号を取得することはできませんでした。また、りこちゃんの家族も常にとっても協力的で、私の成功をいつも祈ってくれていました。りこちゃんに出会えて本当に幸せです。りこちゃんのような素晴らしい人に支えていただけるようなことを私が今までの人生でしてきたとは思えません。だからこそ、これからの人生と一緒に過ごせることをとても楽しみにしています。

Delft, The Netherlands

09.04.2025

CURRICULUM VITÆ

Jacob Daniel KOENIG

23-05-1995 Born in Toronto, Canada.

EDUCATION

2009–2013 Secondary School
St. Mary Catholic Secondary School, Pickering, Canada

2013–2018 BSc in Physics and Astronomy
University of Waterloo, Waterloo, Canada

2020–2025 PhD Physics
Technische Universiteit Delft
Thesis: Parametrically Activated Interactions in Circuit
Quantum Electrodynamical Systems
Promotors: Prof. dr. G. A. Steele and Prof. dr. B. M. Terhal

LIST OF PUBLICATIONS

5. **J. D. Koenig**, O. Ameye, M. Hylkema, L. R. van Everdingen, C. A. Potts, O. Zilberberg and G.A. Steele, *Chaotic Behaviour of a Strongly Parametrically Driven Duffing Oscillator*, in preparation (2024).
4. **J. D. Koenig**, O. Ameye, L. R. van Everdingen, C. A. Potts, O. Zilberberg and G.A. Steele, *Biased Switching Dynamics in a Parametrically Driven Kerr Nonlinear Oscillator*, in preparation (2024).
3. **J. D. Koenig**, O. Ameye, S. Lécuyer-Seguineau, G. C. Arends, C. A. Potts, O. Zilberberg and G.A. Steele, *Spectroscopic Observation of a Few-Photon Parametric State in a Kerr Nonlinear Oscillator*, in preparation (2024).
2. **J. D. Koenig**, G. Barbieri, F. Fani Sani, M. Kounalakis, C. A. Potts and G.A. Steele, *Flux Modulated Tunable Couplings of Two Nonlinear Oscillators*, in preparation (2024).
1. S. Masuda, **J. D. Koenig** and G.A. Steele, *Acceleration and deceleration of quantum dynamics based on inter-trajectory travel with fast-forward scaling theory*. [Sci Rep 12, 10744 \(2022\)](#).

The titles and author lists of the above articles in preparation are subject to change prior to publication.

BIBLIOGRAPHY

- [1] C. E. Shannon. "A mathematical theory of communication". In: *The Bell System Technical Journal* 27.3 (1948), pp. 379–423.
- [2] Konrad Zuse. *The computer—my life*. Berlin, Heidelberg: Springer-Verlag, 1993. ISBN: 0387564535.
- [3] A. M. Turing. "On Computable Numbers, with an Application to the Entscheidungsproblem". In: *Proceedings of the London Mathematical Society* s2-42.1 (1937), pp. 230–265. [Link](#).
- [4] D.S. Halacy. *Charles Babbage, Father of the Computer*. Crowell-Collier Press, 1970. [Link](#).
- [5] J. Fuegi and J. Francis. "Lovlace Babbage and the creation of the 1843 'notes'". In: *IEEE Annals of the History of Computing* 25.4 (2003), pp. 16–26.
- [6] Michael A. Nielsen and Isaac L. Chuang. *Quantum Computation and Quantum Information*. Cambridge University Press, 2000. ISBN: 9780521635035. [Link](#).
- [7] W. Heisenberg. "Über eine Abänderung der formalen Regeln der Quantentheorie beim Problem der anomalen Zeemaneffekte". In: *Zeitschrift für Physik* 26.1 (Dec. 1924), pp. 291–307. ISSN: 0044-3328. [Link](#).
- [8] E. Schrödinger. "An Undulatory Theory of the Mechanics of Atoms and Molecules". In: *Phys. Rev.* 28 (6 Dec. 1926), pp. 1049–1070. [Link](#).
- [9] Max Born. "Max Karl Ernst Ludwig Planck, 1858-1947". In: *Obituary Notices of Fellows of the Royal Society* 6.17 (1948), pp. 161–188. [Link](#).
- [10] T. Sauer et al. *David Hilbert's Lectures on the Foundations of Physics 1915-1927: Relativity, Quantum Theory and Epistemology*. Springer Berlin Heidelberg, 2009. ISBN: 9783540206064. [Link](#).
- [11] Paul Benioff. "The computer as a physical system: A microscopic quantum mechanical Hamiltonian model of computers as represented by Turing machines". In: *Journal of Statistical Physics* 22.5 (May 1980), pp. 563–591. ISSN: 1572-9613. [Link](#).
- [12] Richard P. Feynman. "Simulating physics with computers". In: *International Journal of Theoretical Physics* 21.6 (June 1982), pp. 467–488. ISSN: 1572-9575. [Link](#).
- [13] D Deutsch. "Quantum theory, the Church–Turing principle and the universal quantum computer". en. In: *Proc. R. Soc. Lond.* 400.1818 (July 1985), pp. 97–117.
- [14] A. O. Caldeira and A. J. Leggett. "Influence of Dissipation on Quantum Tunneling in Macroscopic Systems". In: *Phys. Rev. Lett.* 46 (4 Jan. 1981), pp. 211–214. [Link](#).
- [15] Richard F. Voss and Richard A. Webb. "Macroscopic Quantum Tunneling in 1- μm Nb Josephson Junctions". In: *Phys. Rev. Lett.* 47 (4 July 1981), pp. 265–268. [Link](#).
- [16] A.O Caldeira and A.J Leggett. "Quantum tunnelling in a dissipative system". In: *Annals of Physics* 149.2 (1983), pp. 374–456. ISSN: 0003-4916. [Link](#).

- [17] W. H. Zurek. "Reversibility and Stability of Information Processing Systems". In: *Phys. Rev. Lett.* 53 (4 July 1984), pp. 391–394. [Link](#).
- [18] Michel H. Devoret, John M. Martinis, and John Clarke. "Measurements of Macroscopic Quantum Tunneling out of the Zero-Voltage State of a Current-Biased Josephson Junction". In: *Phys. Rev. Lett.* 55 (18 Oct. 1985), pp. 1908–1911. [Link](#).
- [19] John M. Martinis, Michel H. Devoret, and John Clarke. "Energy-Level Quantization in the Zero-Voltage State of a Current-Biased Josephson Junction". In: *Phys. Rev. Lett.* 55 (15 Oct. 1985), pp. 1543–1546. [Link](#).
- [20] DV Averin, AB Zorin, and KK Likharev. "Bloch oscillations in small Josephson junctions". In: *Sov. Phys. JETP* 61.2 (1985), pp. 407–413.
- [21] Asher Peres. "Reversible logic and quantum computers". In: *Phys. Rev. A* 32 (6 Dec. 1985), pp. 3266–3276. [Link](#).
- [22] D. B. Schwartz et al. "Quantitative Study of the Effect of the Environment on Macroscopic Quantum Tunneling". In: *Phys. Rev. Lett.* 55 (15 Oct. 1985), pp. 1547–1550. [Link](#).
- [23] Y. Yamamoto and H. A. Haus. "Preparation, measurement and information capacity of optical quantum states". In: *Rev. Mod. Phys.* 58 (4 Oct. 1986), pp. 1001–1020. [Link](#).
- [24] Norman Margolus. "Quantum Computation". In: *Annals of the New York Academy of Sciences* 480.1 (1986), pp. 487–497. [Link](#).
- [25] John M. Martinis, Michel H. Devoret, and John Clarke. "Experimental tests for the quantum behavior of a macroscopic degree of freedom: The phase difference across a Josephson junction". In: *Phys. Rev. B* 35 (10 Apr. 1987), pp. 4682–4698. [Link](#).
- [26] K. Igeta and Y. Yamamoto. "Quantum mechanical computers with single atom and photon fields". In: *International Conference on Quantum Electronics*. Optica Publishing Group, 1988, Tul4. [Link](#).
- [27] John Clarke et al. "Quantum Mechanics of a Macroscopic Variable: The Phase Difference of a Josephson Junction". In: *Science* 239.4843 (1988), pp. 992–997. [Link](#).
- [28] G. J. Milburn. "Quantum optical Fredkin gate". In: *Phys. Rev. Lett.* 62 (18 May 1989), pp. 2124–2127. [Link](#).
- [29] V.Ya. Aleshkini and D.V. Averin. "Resonant tunneling of Cooper pairs in a double Josephson junction system". In: *Physica B: Condensed Matter* 165-166 (1990). LT-19, pp. 949–950. ISSN: 0921-4526. [Link](#).
- [30] Benjamin Schumacher. "Information from quantum measurements". In: *Complexity, Entropy and the Physics of Information* (1990), pp. 29–37.
- [31] M. G. Raizen et al. "Ionic crystals in a linear Paul trap". In: *Phys. Rev. A* 45 (9 May 1992), pp. 6493–6501. [Link](#).
- [32] Ethan Bernstein and Umesh Vazirani. "Quantum complexity theory". In: *Proceedings of the Twenty-Fifth Annual ACM Symposium on Theory of Computing*. STOC '93. San Diego, California, USA: Association for Computing Machinery, 1993, pp. 11–20. ISBN: 0897915917. [Link](#).
- [33] A. Chi-Chih Yao. "Quantum circuit complexity". In: *Proceedings of 1993 IEEE 34th Annual Foundations of Computer Science*. 1993, pp. 352–361.

- [34] D.R. Simon. "On the power of quantum computation". In: *Proceedings 35th Annual Symposium on Foundations of Computer Science*. 1994, pp. 116–123.
- [35] G. Schön and A. D. Zaikin. "Parity Effects on Electron Tunnelling Through Small Superconducting Islands". In: *Europhysics Letters* 26.9 (June 1994), p. 695. [Link](#).
- [36] W. J. Elion et al. "Direct demonstration of Heisenberg's uncertainty principle in a superconductor". In: *Nature* 371.6498 (Oct. 1994), pp. 594–595. ISSN: 1476-4687. [Link](#).
- [37] P.W. Shor. "Algorithms for quantum computation: discrete logarithms and factoring". In: *Proceedings 35th Annual Symposium on Foundations of Computer Science*. 1994, pp. 124–134.
- [38] P. Joyez et al. "Observation of parity-induced suppression of Josephson tunneling in the superconducting single electron transistor". In: *Phys. Rev. Lett.* 72 (15 Apr. 1994), pp. 2458–2461. [Link](#).
- [39] Benjamin Schumacher. "Quantum coding". In: *Phys. Rev. A* 51 (4 Apr. 1995), pp. 2738–2747. [Link](#).
- [40] Charles H. Bennett. "Quantum Information and Computation". In: *Physics Today* 48.10 (Oct. 1995), pp. 24–30. ISSN: 0031-9228. [Link](#).
- [41] Adriano Barenco et al. "Elementary gates for quantum computation". In: *Phys. Rev. A* 52 (5 Nov. 1995), pp. 3457–3467. [Link](#).
- [42] David P. DiVincenzo. "Quantum Computation". In: *Science* 270.5234 (1995), pp. 255–261. [Link](#).
- [43] J. I. Cirac and P. Zoller. "Quantum Computations with Cold Trapped Ions". In: *Phys. Rev. Lett.* 74 (20 May 1995), pp. 4091–4094. [Link](#).
- [44] Isaac L. Chuang and Yoshihisa Yamamoto. "Simple quantum computer". In: *Phys. Rev. A* 52 (5 Nov. 1995), pp. 3489–3496. [Link](#).
- [45] P. Domokos et al. "Simple cavity-QED two-bit universal quantum logic gate: The principle and expected performances". In: *Phys. Rev. A* 52 (5 Nov. 1995), pp. 3554–3559. [Link](#).
- [46] C. Monroe et al. "Demonstration of a Fundamental Quantum Logic Gate". In: *Phys. Rev. Lett.* 75 (25 Dec. 1995), pp. 4714–4717. [Link](#).
- [47] Lov K. Grover. "A fast quantum mechanical algorithm for database search". In: *Proceedings of the Twenty-Eighth Annual ACM Symposium on Theory of Computing*. STOC '96. Philadelphia, Pennsylvania, USA: Association for Computing Machinery, 1996, pp. 212–219. ISBN: 0897917855. [Link](#).
- [48] Raymond Laflamme et al. "Perfect Quantum Error Correcting Code". In: *Phys. Rev. Lett.* 77 (1 July 1996), pp. 198–201. [Link](#).
- [49] Wojciech Hubert Zurek and Raymond Laflamme. "Quantum Logical Operations on Encoded Qubits". In: *Phys. Rev. Lett.* 77 (22 Nov. 1996), pp. 4683–4686. [Link](#).
- [50] Seth Lloyd. "Universal Quantum Simulators". In: *Science* 273.5278 (1996), pp. 1073–1078. [Link](#).
- [51] A. M. Steane. "Error Correcting Codes in Quantum Theory". In: *Phys. Rev. Lett.* 77 (5 July 1996), pp. 793–797. [Link](#).

- [52] P.W. Shor. "Fault-tolerant quantum computation". In: *Proceedings of 37th Conference on Foundations of Computer Science*. 1996, pp. 56–65.
- [53] Charles H. Bennett et al. "Strengths and Weaknesses of Quantum Computing". In: *SIAM Journal on Computing* 26.5 (1997), pp. 1510–1523. [Link](#).
- [54] Y. Nakamura, C. D. Chen, and J. S. Tsai. "Spectroscopy of Energy-Level Splitting between Two Macroscopic Quantum States of Charge Coherently Superposed by Josephson Coupling". In: *Phys. Rev. Lett.* 79 (12 Sept. 1997), pp. 2328–2331. [Link](#).
- [55] Alexander Shnirman, Gerd Schön, and Ziv Hermon. "Quantum Manipulations of Small Josephson Junctions". In: *Phys. Rev. Lett.* 79 (12 Sept. 1997), pp. 2371–2374. [Link](#).
- [56] D Bruss et al. "Quantum computing with controlled-NOT and few qubits". en. In: *Philos. Trans. A Math. Phys. Eng. Sci.* 355.1733 (Dec. 1997), pp. 2259–2266.
- [57] Lov K. Grover. "Quantum Mechanics Helps in Searching for a Needle in a Haystack". In: *Phys. Rev. Lett.* 79 (2 July 1997), pp. 325–328. [Link](#).
- [58] Peter W. Shor. "Polynomial-Time Algorithms for Prime Factorization and Discrete Logarithms on a Quantum Computer". In: *SIAM Journal on Computing* 26.5 (1997), pp. 1484–1509. [Link](#).
- [59] Lu-Ming Duan and Guang-Can Guo. "Preserving Coherence in Quantum Computation by Pairing Quantum Bits". In: *Phys. Rev. Lett.* 79 (10 Sept. 1997), pp. 1953–1956. [Link](#).
- [60] Neil A. Gershenfeld and Isaac L. Chuang. "Bulk Spin-Resonance Quantum Computation". In: *Science* 275.5298 (1997), pp. 350–356. [Link](#).
- [61] David G. Cory, Amr F. Fahmy, and Timothy F. Havel. "Ensemble quantum computing by NMR spectroscopy". In: *Proceedings of the National Academy of Sciences* 94.5 (1997), pp. 1634–1639. [Link](#).
- [62] D.V. Averin. "Adiabatic quantum computation with Cooper pairs". In: *Solid State Communications* 105.10 (1998), pp. 659–664. ISSN: 0038-1098. [Link](#).
- [63] Jonathan A. Jones, Michele Mosca, and Rasmus H. Hansen. "Implementation of a quantum search algorithm on a quantum computer". In: *Nature* 393.6683 (May 1998), pp. 344–346. ISSN: 1476-4687. [Link](#).
- [64] John Preskill. "Quantum computing: pro and con". en. In: *Proc. Math. Phys. Eng. Sci.* 454.1969 (Jan. 1998), pp. 469–486.
- [65] Peter W. Shor. "Quantum computing." eng. In: *Documenta Mathematica* (1998), pp. 305–324. [Link](#).
- [66] David Deutsch and Artur Ekert. "Quantum computation". In: *Physics World* 11.3 (Mar. 1998), p. 47. [Link](#).
- [67] Isaac L. Chuang, Neil Gershenfeld, and Mark Kubinec. "Experimental Implementation of Fast Quantum Searching". In: *Phys. Rev. Lett.* 80 (15 Apr. 1998), pp. 3408–3411. [Link](#).
- [68] Daniel Loss and David P. DiVincenzo. "Quantum computation with quantum dots". In: *Phys. Rev. A* 57 (1 Jan. 1998), pp. 120–126. [Link](#).
- [69] B. E. Kane. "A silicon-based nuclear spin quantum computer". In: *Nature* 393.6681 (May 1998), pp. 133–137. ISSN: 1476-4687. [Link](#).

- [70] Noah Linden, Hervé Barjat, and Ray Freeman. “An implementation of the Deutsch–Jozsa algorithm on a three-qubit NMR quantum computer”. In: *Chemical Physics Letters* 296.1 (1998), pp. 61–67. ISSN: 0009-2614. [Link](#).
- [71] V Bouchiat et al. “Quantum coherence with a single Cooper pair”. In: *Physica Scripta* 1998.T76 (Jan. 1998), p. 165. [Link](#).
- [72] Vlatko Vedral and Martin B. Plenio. “Basics of quantum computation”. In: *Progress in Quantum Electronics* 22.1 (1998), pp. 1–39. ISSN: 0079-6727. [Link](#).
- [73] Daniel Gottesman and Isaac L. Chuang. “Demonstrating the viability of universal quantum computation using teleportation and single-qubit operations”. In: *Nature* 402.6760 (Nov. 1999), pp. 390–393. ISSN: 1476-4687. [Link](#).
- [74] Yuriy Makhlin, Gerd Scöhn, and Alexander Shnirman. “Josephson-junction qubits with controlled couplings”. In: *Nature* 398.6725 (Mar. 1999), pp. 305–307. ISSN: 1476-4687. [Link](#).
- [75] A. Imamoglu et al. “Quantum Information Processing Using Quantum Dot Spins and Cavity QED”. In: *Phys. Rev. Lett.* 83 (20 Nov. 1999), pp. 4204–4207. [Link](#).
- [76] Y. Nakamura, Yu. A. Pashkin, and J. S. Tsai. “Coherent control of macroscopic quantum states in a single-Cooper-pair box”. In: *Nature* 398.6730 (Apr. 1999), pp. 786–788. [Link](#).
- [77] A. Rauschenbeutel et al. “Coherent Operation of a Tunable Quantum Phase Gate in Cavity QED”. In: *Phys. Rev. Lett.* 83 (24 Dec. 1999), pp. 5166–5169. [Link](#).
- [78] Anders Sørensen and Klaus Mølmer. “Quantum Computation with Ions in Thermal Motion”. In: *Phys. Rev. Lett.* 82 (9 Mar. 1999), pp. 1971–1974. [Link](#).
- [79] E. Knill, R. Laflamme, and G. J. Milburn. “A scheme for efficient quantum computation with linear optics”. In: *Nature* 409.6816 (Jan. 2001), pp. 46–52. ISSN: 1476-4687. [Link](#).
- [80] D. Kielpinski, C. Monroe, and D. J. Wineland. “Architecture for a large-scale ion-trap quantum computer”. In: *Nature* 417.6890 (June 2002), pp. 709–711. ISSN: 1476-4687. [Link](#).
- [81] A.Yu. Kitaev. “Fault-tolerant quantum computation by anyons”. In: *Annals of Physics* 303.1 (2003), pp. 2–30. ISSN: 0003-4916. [Link](#).
- [82] John Clarke and Frank K. Wilhelm. “Superconducting quantum bits”. In: *Nature* 453.7198 (June 2008), pp. 1031–1042. ISSN: 1476-4687. [Link](#).
- [83] J. C. Bergquist et al. “Observation of Quantum Jumps in a Single Atom”. In: *Phys. Rev. Lett.* 57 (14 Oct. 1986), pp. 1699–1702. [Link](#).
- [84] R. Vijay, D. H. Slichter, and I. Siddiqi. “Observation of Quantum Jumps in a Superconducting Artificial Atom”. In: *Phys. Rev. Lett.* 106 (11 Mar. 2011), p. 110502. [Link](#).
- [85] B.D. Josephson. “Possible new effects in superconductive tunnelling”. In: *Physics Letters* 1.7 (1962), pp. 251–253. ISSN: 0031-9163. [Link](#).
- [86] B. D. Josephson. “The discovery of tunnelling supercurrents”. In: *Rev. Mod. Phys.* 46 (2 Apr. 1974), pp. 251–254. [Link](#).
- [87] M. Büttiker. “Zero-current persistent potential drop across small-capacitance Josephson junctions”. In: *Phys. Rev. B* 36 (7 Sept. 1987), pp. 3548–3555. [Link](#).
- [88] T. P. Orlando et al. “Superconducting persistent-current qubit”. In: *Phys. Rev. B* 60 (22 Dec. 1999), pp. 15398–15413. [Link](#).

- [89] Y Nakamura, Yu.A Pashkin, and J.S Tsai. "Quantum coherence in a single-Cooper-pair box: experiments in the frequency and time domains". In: *Physica B: Condensed Matter* 280.1 (2000), pp. 405–409. ISSN: 0921-4526. [Link](#).
- [90] Caspar H. van der Wal et al. "Quantum Superposition of Macroscopic Persistent-Current States". In: *Science* 290.5492 (2000), pp. 773–777. [Link](#).
- [91] Jonathan R. Friedman et al. "Quantum superposition of distinct macroscopic states". In: *Nature* 406.6791 (July 2000), pp. 43–46. ISSN: 1476-4687. [Link](#).
- [92] Y. Nakamura, Yu. A. Pashkin, and J. S. Tsai. "Rabi Oscillations in a Josephson-Junction Charge Two-Level System". In: *Phys. Rev. Lett.* 87 (24 Nov. 2001), p. 246601. [Link](#).
- [93] Yuriy Makhlin, Gerd Schön, and Alexander Shnirman. "Quantum-state engineering with Josephson-junction devices". In: *Rev. Mod. Phys.* 73 (2 May 2001), pp. 357–400. [Link](#).
- [94] D. Vion et al. "Manipulating the Quantum State of an Electrical Circuit". In: *Science* 296.5569 (2002), pp. 886–889. [Link](#).
- [95] Yang Yu et al. "Coherent Temporal Oscillations of Macroscopic Quantum States in a Josephson Junction". In: *Science* 296.5569 (2002), pp. 889–892. [Link](#).
- [96] John M. Martinis et al. "Rabi Oscillations in a Large Josephson-Junction Qubit". In: *Phys. Rev. Lett.* 89 (11 Aug. 2002), p. 117901. [Link](#).
- [97] Y. Nakamura et al. "Charge Echo in a Cooper-Pair Box". In: *Phys. Rev. Lett.* 88 (4 Jan. 2002), p. 047901. [Link](#).
- [98] I. Chiorescu et al. "Coherent Quantum Dynamics of a Superconducting Flux Qubit". In: *Science* 299.5614 (2003), pp. 1869–1871. [Link](#).
- [99] K. W. Lehnert et al. "Measurement of the Excited-State Lifetime of a Microelectronic Circuit". In: *Phys. Rev. Lett.* 90 (2 Jan. 2003), p. 027002. [Link](#).
- [100] Yu. A. Pashkin et al. "Quantum oscillations in two coupled charge qubits". In: *Nature* 421.6925 (Feb. 2003), pp. 823–826. ISSN: 1476-4687. [Link](#).
- [101] A. J. Berkley et al. "Entangled Macroscopic Quantum States in Two Superconducting Qubits". In: *Science* 300.5625 (2003), pp. 1548–1550. [Link](#).
- [102] Philip R. Johnson et al. "Spectroscopy of capacitively coupled Josephson-junction qubits". In: *Phys. Rev. B* 67 (2 Jan. 2003), p. 020509. [Link](#).
- [103] T. Duty et al. "Coherent dynamics of a Josephson charge qubit". In: *Phys. Rev. B* 69 (14 Apr. 2004), p. 140503. [Link](#).
- [104] S. Saito et al. "Multiphoton Transitions in a Macroscopic Quantum Two-State System". In: *Phys. Rev. Lett.* 93 (3 July 2004), p. 037001. [Link](#).
- [105] O. Astafiev et al. "Single-shot measurement of the Josephson charge qubit". In: *Phys. Rev. B* 69 (18 May 2004), p. 180507. [Link](#).
- [106] P. Bertet et al. "Dephasing of a Superconducting Qubit Induced by Photon Noise". In: *Phys. Rev. Lett.* 95 (25 Dec. 2005), p. 257002. [Link](#).
- [107] R. McDermott et al. "Simultaneous State Measurement of Coupled Josephson Phase Qubits". In: *Science* 307.5713 (2005), pp. 1299–1302. [Link](#).

- [108] G. Ithier et al. “Decoherence in a superconducting quantum bit circuit”. In: *Phys. Rev. B* 72 (13 Oct. 2005), p. 134519. [Link](#).
- [109] J. B. Majer et al. “Spectroscopy on Two Coupled Superconducting Flux Qubits”. In: *Phys. Rev. Lett.* 94 (9 Mar. 2005), p. 090501. [Link](#).
- [110] I. Siddiqi et al. “Dispersive measurements of superconducting qubit coherence with a fast latching readout”. In: *Phys. Rev. B* 73 (5 Feb. 2006), p. 054510. [Link](#).
- [111] Jens Koch et al. “Charge-insensitive qubit design derived from the Cooper pair box”. In: *Phys. Rev. A* 76 (4 Oct. 2007), p. 042319. [Link](#).
- [112] Alexandre Blais et al. “Cavity quantum electrodynamics for superconducting electrical circuits: An architecture for quantum computation”. In: *Phys. Rev. A* 69 (6 June 2004), p. 062320. [Link](#).
- [113] I. Chiorescu et al. “Coherent dynamics of a flux qubit coupled to a harmonic oscillator”. In: *Nature* 431.7005 (Sept. 2004), pp. 159–162. ISSN: 1476-4687. [Link](#).
- [114] A. Wallraff et al. “Strong coupling of a single photon to a superconducting qubit using circuit quantum electrodynamics”. In: *Nature* 431.7005 (Sept. 2004), pp. 162–167. ISSN: 1476-4687. [Link](#).
- [115] D. I. Schuster et al. “ac Stark Shift and Dephasing of a Superconducting Qubit Strongly Coupled to a Cavity Field”. In: *Phys. Rev. Lett.* 94 (12 Mar. 2005), p. 123602. [Link](#).
- [116] J. Majer et al. “Coupling superconducting qubits via a cavity bus”. In: *Nature* 449.7161 (Sept. 2007), pp. 443–447. ISSN: 1476-4687. [Link](#).
- [117] D. I. Schuster et al. “Resolving photon number states in a superconducting circuit”. In: *Nature* 445.7127 (Feb. 2007), pp. 515–518. ISSN: 1476-4687. [Link](#).
- [118] Alexandre Blais et al. “Circuit quantum electrodynamics”. In: *Rev. Mod. Phys.* 93 (2 May 2021), p. 025005. [Link](#).
- [119] Isaac L. Chuang, Debbie W. Leung, and Yoshihisa Yamamoto. “Bosonic quantum codes for amplitude damping”. In: *Phys. Rev. A* 56 (2 Aug. 1997), pp. 1114–1125. [Link](#).
- [120] P. T. Cochrane, G. J. Milburn, and W. J. Munro. “Macroscopically distinct quantum-superposition states as a bosonic code for amplitude damping”. In: *Phys. Rev. A* 59 (4 Apr. 1999), pp. 2631–2634. [Link](#).
- [121] E. Knill et al. *A Cat-State Benchmark on a Seven Bit Quantum Computer*. 1999. [Link](#).
- [122] Daniel Gottesman, Alexei Kitaev, and John Preskill. “Encoding a qubit in an oscillator”. In: *Phys. Rev. A* 64 (1 June 2001), p. 012310. [Link](#).
- [123] Samuel L. Braunstein and Peter van Loock. “Quantum information with continuous variables”. In: *Rev. Mod. Phys.* 77 (2 June 2005), pp. 513–577. [Link](#).
- [124] Brian Vlastakis et al. “Deterministically Encoding Quantum Information Using 100-Photon Schrödinger Cat States”. In: *Science* 342.6158 (2013), pp. 607–610. [Link](#).
- [125] Mazyar Mirrahimi et al. “Dynamically protected cat-qubits: a new paradigm for universal quantum computation”. In: *New Journal of Physics* 16.4 (Apr. 2014), p. 045014. [Link](#).
- [126] L. Sun et al. “Tracking photon jumps with repeated quantum non-demolition parity measurements”. In: *Nature* 511.7510 (July 2014), pp. 444–448. ISSN: 1476-4687. [Link](#).

- [127] Z. Leghtas et al. “Confining the state of light to a quantum manifold by engineered two-photon loss”. In: *Science* 347.6224 (2015), pp. 853–857. [Link](#).
- [128] Chen Wang et al. “A Schrödinger cat living in two boxes”. In: *Science* 352.6289 (2016), pp. 1087–1091. [Link](#).
- [129] Mazyar Mirrahimi. “Cat-qubits for quantum computation”. In: *Comptes Rendus Physique* 17.7 (2016). Quantum microwaves / Micro-ondes quantiques, pp. 778–787. ISSN: 1631-0705. [Link](#).
- [130] Daniel J. Weigand and Barbara M. Terhal. “Generating grid states from Schrödinger-cat states without postselection”. In: *Phys. Rev. A* 97 (2 Feb. 2018), p. 022341. [Link](#).
- [131] Takahiro Serikawa et al. “Generation of a Cat State in an Optical Sideband”. In: *Phys. Rev. Lett.* 121 (14 Oct. 2018), p. 143602. [Link](#).
- [132] C. Flühmann et al. “Encoding a qubit in a trapped-ion mechanical oscillator”. In: *Nature* 566.7745 (Feb. 2019), pp. 513–517. ISSN: 1476-4687. [Link](#).
- [133] Ofir Milul et al. “Superconducting Cavity Qubit with Tens of Milliseconds Single-Photon Coherence Time”. In: *PRX Quantum* 4 (3 Sept. 2023), p. 030336. [Link](#).
- [134] Peter W. Shor. “Scheme for reducing decoherence in quantum computer memory”. In: *Phys. Rev. A* 52 (4 Oct. 1995), R2493–R2496. [Link](#).
- [135] D. G. Cory et al. “Experimental Quantum Error Correction”. In: *Phys. Rev. Lett.* 81 (10 Sept. 1998), pp. 2152–2155. [Link](#).
- [136] Seth Lloyd and Jean-Jacques E. Slotine. “Analog Quantum Error Correction”. In: *Phys. Rev. Lett.* 80 (18 May 1998), pp. 4088–4091. [Link](#).
- [137] Samuel L. Braunstein. “Quantum error correction for communication with linear optics”. In: *Nature* 394.6688 (July 1998), pp. 47–49. ISSN: 1476-4687. [Link](#).
- [138] Debbie Leung et al. “Experimental realization of a two-bit phase damping quantum code”. In: *Phys. Rev. A* 60 (3 Sept. 1999), pp. 1924–1943. [Link](#).
- [139] E. Knill et al. “Benchmarking Quantum Computers: The Five-Qubit Error Correcting Code”. In: *Phys. Rev. Lett.* 86 (25 June 2001), pp. 5811–5814. [Link](#).
- [140] J. Chiaverini et al. “Realization of quantum error correction”. In: *Nature* 432.7017 (Dec. 2004), pp. 602–605. ISSN: 1476-4687. [Link](#).
- [141] Nicolas Boulant et al. “Experimental Implementation of a Concatenated Quantum Error-Correcting Code”. In: *Phys. Rev. Lett.* 94 (13 Apr. 2005), p. 130501. [Link](#).
- [142] Takao Aoki et al. “Quantum error correction beyond qubits”. In: *Nature Physics* 5.8 (Aug. 2009), pp. 541–546. ISSN: 1745-2481. [Link](#).
- [143] Austin G. Fowler et al. “Surface codes: Towards practical large-scale quantum computation”. In: *Phys. Rev. A* 86 (3 Sept. 2012), p. 032324. [Link](#).
- [144] Barbara M. Terhal. “Quantum error correction for quantum memories”. In: *Rev. Mod. Phys.* 87 (2 Apr. 2015), pp. 307–346. [Link](#).
- [145] Earl T. Campbell, Barbara M. Terhal, and Christophe Vuillot. “Roads towards fault-tolerant universal quantum computation”. In: *Nature* 549.7671 (Sept. 2017), pp. 172–179. ISSN: 1476-4687. [Link](#).

- [146] Victor V. Albert et al. “Performance and structure of single-mode bosonic codes”. In: *Phys. Rev. A* 97 (3 Mar. 2018), p. 032346. [Link](#).
- [147] Jérémie Guillaud and Mazyar Mirrahimi. “Repetition Cat Qubits for Fault-Tolerant Quantum Computation”. In: *Phys. Rev. X* 9 (4 Dec. 2019), p. 041053. [Link](#).
- [148] Christophe Vuillot et al. “Quantum error correction with the toric Gottesman-Kitaev-Preskill code”. In: *Phys. Rev. A* 99 (3 Mar. 2019), p. 032344. [Link](#).
- [149] B M Terhal, J Conrad, and C Vuillot. “Towards scalable bosonic quantum error correction”. In: *Quantum Science and Technology* 5.4 (July 2020), p. 043001. [Link](#).
- [150] P. Campagne-Ibarcq et al. “Quantum error correction of a qubit encoded in grid states of an oscillator”. In: *Nature* 584.7821 (Aug. 2020), pp. 368–372. ISSN: 1476-4687. [Link](#).
- [151] Christian Kraglund Andersen et al. “Repeated quantum error detection in a surface code”. In: *Nature Physics* 16.8 (Aug. 2020), pp. 875–880. ISSN: 1745-2481. [Link](#).
- [152] Arne L. Grimsmo and Shruti Puri. “Quantum Error Correction with the Gottesman-Kitaev-Preskill Code”. In: *PRX Quantum* 2 (2 June 2021), p. 020101. [Link](#).
- [153] Sebastian Krinner et al. “Realizing repeated quantum error correction in a distance-three surface code”. In: *Nature* 605.7911 (May 2022), pp. 669–674. ISSN: 1476-4687. [Link](#).
- [154] William P. Livingston et al. “Experimental demonstration of continuous quantum error correction”. In: *Nature Communications* 13.1 (Apr. 2022), p. 2307. ISSN: 2041-1723. [Link](#).
- [155] Theerapat Tansuwannont and Debbie Leung. “Achieving Fault Tolerance on Capped Color Codes with Few Ancillas”. In: *PRX Quantum* 3 (3 Aug. 2022), p. 030322. [Link](#).
- [156] Rajeev Acharya et al. “Suppressing quantum errors by scaling a surface code logical qubit”. In: *Nature* 614.7949 (Feb. 2023), pp. 676–681. ISSN: 1476-4687. [Link](#).
- [157] Dany Lachance-Quirion et al. “Autonomous Quantum Error Correction of Gottesman-Kitaev-Preskill States”. In: *Phys. Rev. Lett.* 132 (15 Apr. 2024), p. 150607. [Link](#).
- [158] Shunya Konno et al. “Logical states for fault-tolerant quantum computation with propagating light”. In: *Science* 383.6680 (2024), pp. 289–293. [Link](#).
- [159] I. Newton. *Philosophiae naturalis principia mathematica*. Jussu Societatis Regiae ac Typis Josephi Streater. Prostat Venales apud Sam. Smith ad insignia Principis Walliae in Coemiterio D. Pauli, aliosq, nonnullos Bibliopolas, 1687. [Link](#).
- [160] R. Hooke. *Lectures de Potentia Restitutiva, Or of Spring Explaining the Power of Springing Bodies*. [Cutlerian lecture. John Martyn, 1678. [Link](#).
- [161] H. von Helmholtz and A.J. Ellis. *On the Sensations of Tone as a Physiological Basis for the Theory of Music*. Longmans, Green, 1885. [Link](#).
- [162] D.W. Jordan and P. Smith. *Nonlinear Ordinary Differential Equations: An Introduction to Dynamical Systems*. Oxford applied and engineering mathematics. Oxford University Press, 1999. ISBN: 9780198565628. [Link](#).
- [163] R.P. Feynman, R.B. Leighton, and M. Sands. *The Feynman Lectures on Physics, Vol. III: The New Millennium Edition: Quantum Mechanics*. The Feynman Lectures on Physics. Basic Books, 2011. ISBN: 9780465025015. [Link](#).
- [164] J. M. Raimond, M. Brune, and S. Haroche. “Manipulating quantum entanglement with atoms and photons in a cavity”. In: *Rev. Mod. Phys.* 73 (3 Aug. 2001), pp. 565–582. [Link](#).

- [165] H. Mabuchi and A. C. Doherty. "Cavity Quantum Electrodynamics: Coherence in Context". In: *Science* 298.5597 (2002), pp. 1372–1377. [Link](#).
- [166] Herbert Walther et al. "Cavity quantum electrodynamics". In: *Reports on Progress in Physics* 69.5 (Apr. 2006), p. 1325. [Link](#).
- [167] Alexandre Blais et al. "Quantum-information processing with circuit quantum electrodynamics". In: *Phys. Rev. A* 75 (3 Mar. 2007), p. 032329. [Link](#).
- [168] Hanhee Paik et al. "Observation of High Coherence in Josephson Junction Qubits Measured in a Three-Dimensional Circuit QED Architecture". In: *Phys. Rev. Lett.* 107 (24 Dec. 2011), p. 240501. [Link](#).
- [169] David M Pozar. *Microwave engineering; 3rd ed.* Hoboken, NJ: Wiley, 2005. [Link](#).
- [170] Inder Bahl and Prakash Bhartia. *Microwave solid state circuit design.* English. 2. ed. Hoboken: J. Wiley, 2003. ISBN: 0471207551; 9780471207559.
- [171] Koki Watanabe, Keiji Yoshida, and Takeshi Aoki Kohjiro. "Kinetic Inductance of Superconducting Coplanar Waveguides". In: *Japanese Journal of Applied Physics* 33.10R (Oct. 1994), p. 5708. [Link](#).
- [172] S. Gevorgian, L.J.P. Linner, and E.L. Kollberg. "CAD models for shielded multilayered CPW". In: *IEEE Transactions on Microwave Theory and Techniques* 43.4 (1995), pp. 772–779.
- [173] M. Göppl et al. "Coplanar waveguide resonators for circuit quantum electrodynamics". In: *Journal of Applied Physics* 104.11 (Dec. 2008), p. 113904. ISSN: 0021-8979. [Link](#).
- [174] Markus Aspelmeyer, Tobias J. Kippenberg, and Florian Marquardt. "Cavity optomechanics". In: *Rev. Mod. Phys.* 86 (4 Dec. 2014), pp. 1391–1452. [Link](#).
- [175] S. Probst et al. "Efficient and robust analysis of complex scattering data under noise in microwave resonators". In: *Review of Scientific Instruments* 86.2 (Feb. 2015), p. 024706. ISSN: 0034-6748. [Link](#).
- [176] U. Fano. "Effects of Configuration Interaction on Intensities and Phase Shifts". In: *Phys. Rev.* 124 (6 Dec. 1961), pp. 1866–1878. [Link](#).
- [177] D. Rieger et al. "Fano Interference in Microwave Resonator Measurements". In: *Phys. Rev. Appl.* 20 (1 July 2023), p. 014059. [Link](#).
- [178] T. Niemczyk et al. "Circuit quantum electrodynamics in the ultrastrong-coupling regime". In: *Nature Physics* 6.10 (Oct. 2010), pp. 772–776. ISSN: 1745-2481. [Link](#).
- [179] A. Baust et al. "Ultrastrong coupling in two-resonator circuit QED". In: *Phys. Rev. B* 93 (21 June 2016), p. 214501. [Link](#).
- [180] Sal J. Bosman et al. "Multi-mode ultra-strong coupling in circuit quantum electrodynamics". In: *npj Quantum Information* 3.1 (Oct. 2017), p. 46. ISSN: 2056-6387. [Link](#).
- [181] A. Wallraff et al. "Sideband Transitions and Two-Tone Spectroscopy of a Superconducting Qubit Strongly Coupled to an On-Chip Cavity". In: *Phys. Rev. Lett.* 99 (5 July 2007), p. 050501. [Link](#).
- [182] Mario F. Gely, Gary A. Steele, and Daniel Bothner. "Nature of the Lamb shift in weakly anharmonic atoms: From normal-mode splitting to quantum fluctuations". In: *Phys. Rev. A* 98 (5 Nov. 2018), p. 053808. [Link](#).

- [183] M. Brune et al. “Manipulation of photons in a cavity by dispersive atom-field coupling: Quantum-nondemolition measurements and generation of “Schrödinger cat” states”. In: *Phys. Rev. A* 45 (7 Apr. 1992), pp. 5193–5214. [Link](#).
- [184] Jay Gambetta et al. “Qubit-photon interactions in a cavity: Measurement-induced dephasing and number splitting”. In: *Phys. Rev. A* 74 (4 Oct. 2006), p. 042318. [Link](#).
- [185] Maxime Boissonneault, J. M. Gambetta, and Alexandre Blais. “Dispersive regime of circuit QED: Photon-dependent qubit dephasing and relaxation rates”. In: *Phys. Rev. A* 79 (1 Jan. 2009), p. 013819. [Link](#).
- [186] Lev S. Bishop, Eran Ginossar, and S. M. Girvin. “Response of the Strongly Driven Jaynes-Cummings Oscillator”. In: *Phys. Rev. Lett.* 105 (10 Sept. 2010), p. 100505. [Link](#).
- [187] D. I. Schuster. “Circuit Quantum Electrodynamics”. PhD thesis. Yale University (2007).
- [188] M. D. Reed et al. “High-Fidelity Readout in Circuit Quantum Electrodynamics Using the Jaynes-Cummings Nonlinearity”. In: *Phys. Rev. Lett.* 105 (17 Oct. 2010), p. 173601. [Link](#).
- [189] R. Dassonneville et al. “Transmon-qubit readout using an in situ bifurcation amplification in the mesoscopic regime”. In: *Phys. Rev. Appl.* 20 (4 Oct. 2023), p. 044050. [Link](#).
- [190] V. E. Manucharyan et al. “Microwave bifurcation of a Josephson junction: Embedding-circuit requirements”. In: *Phys. Rev. B* 76 (1 July 2007), p. 014524. [Link](#).
- [191] J. Bourassa et al. “Josephson-junction-embedded transmission-line resonators: From Kerr medium to in-line transmon”. In: *Phys. Rev. A* 86 (1 July 2012), p. 013814. [Link](#).
- [192] M.H. Devoret, Steven Girvin, and Robert Schoelkopf. “Circuit-QED: How strong can the coupling between a Josephson junction atom and a transmission line resonator be?” In: *Annalen der Physik* 519.10-11 (2007), pp. 767–779. [Link](#).
- [193] P. Winkel et al. “Nondegenerate Parametric Amplifiers Based on Dispersion-Engineered Josephson-Junction Arrays”. In: *Phys. Rev. Appl.* 13 (2 Feb. 2020), p. 024015. [Link](#).
- [194] C. Eichler et al. “Quantum-Limited Amplification and Entanglement in Coupled Nonlinear Resonators”. In: *Phys. Rev. Lett.* 113 (11 Sept. 2014), p. 110502. [Link](#).
- [195] N. E. Frattini et al. “3-wave mixing Josephson dipole element”. In: *Applied Physics Letters* 110.22 (May 2017), p. 222603. ISSN: 0003-6951. [Link](#).
- [196] D. Bothner, I. C. Rodrigues, and G. A. Steele. “Photon-pressure strong coupling between two superconducting circuits”. In: *Nature Physics* 17.1 (Jan. 2021), pp. 85–91. ISSN: 1745-2481. [Link](#).
- [197] Ines Corveira Rodrigues, Daniel Bothner, and Gary Alexander Steele. “Cooling photon-pressure circuits into the quantum regime”. In: *Science Advances* 7.42 (2021), eabg6653. [Link](#).
- [198] V.V. Sivak et al. “Kerr-Free Three-Wave Mixing in Superconducting Quantum Circuits”. In: *Phys. Rev. Appl.* 11 (5 May 2019), p. 054060. [Link](#).
- [199] Yong Lu et al. “Resolving Fock states near the Kerr-free point of a superconducting resonator”. In: *npj Quantum Information* 9.1 (Nov. 2023), p. 114. ISSN: 2056-6387. [Link](#).
- [200] N. E. Frattini et al. “Optimizing the Nonlinearity and Dissipation of a SNAIL Parametric Amplifier for Dynamic Range”. In: *Phys. Rev. Appl.* 10 (5 Nov. 2018), p. 054020. [Link](#).

- [201] D. Moskaleva et al. “Lumped-element SNAIL parametric amplifier with two-pole matching network”. In: *Applied Physics Letters* 125.16 (Oct. 2024), p. 164003. ISSN: 0003-6951. [Link](#).
- [202] Henry P. Kalmus. “The Inverted Pendulum”. In: *American Journal of Physics* 38.7 (July 1970), pp. 874–878. ISSN: 0002-9505. [Link](#).
- [203] F.J. Elmer. *The upside-down pendulum*. 1998. [Link](#).
- [204] F.J. Elmer. *Parametric Resonance*. 1998. [Link](#).
- [205] Eugene I. Butikov. “On the dynamic stabilization of an inverted pendulum”. In: *American Journal of Physics* 69.7 (July 2001), pp. 755–768. ISSN: 0002-9505. [Link](#).
- [206] M. V. Bartuccelli, G. Gentile, and K. V. Georgiou. “On the dynamics of a vertically driven damped planar pendulum”. In: *Proceedings of the Royal Society of London. Series A: Mathematical, Physical and Engineering Sciences* 457.2016 (Dec. 2001), pp. 3007–3022.
- [207] Émile Mathieu. “Mémoire sur le mouvement vibratoire d’une membrane de forme elliptique.” fre. In: *Journal de Mathématiques Pures et Appliquées* 13 (1868), pp. 137–203. [Link](#).
- [208] A.H. Nayfeh and D.T. Mook. *Nonlinear Oscillations*. Wiley Classics Library. Wiley, 2008. ISBN: 9783527617593. [Link](#).
- [209] F.M. Arscott et al. *Periodic Differential Equations: An Introduction to Mathieu, Lamé, and Allied Functions*. International series of monographs in pure and applied mathematics. Pergamon, 2014. ISBN: 9781483164885. [Link](#).
- [210] Eugene I. Butikov. “Analytical expressions for stability regions in the Ince–Strutt diagram of Mathieu equation”. In: *American Journal of Physics* 86.4 (Apr. 2018), pp. 257–267. ISSN: 0002-9505. [Link](#).
- [211] R. Cooke and V.I. Arnold. *Ordinary Differential Equations*. Springer Textbook. Springer Berlin Heidelberg, 1992. ISBN: 9783540548133. [Link](#).
- [212] Ivana Kovacic, Richard Rand, and Si Mohamed Sah. “Mathieu’s Equation and Its Generalizations: Overview of Stability Charts and Their Features”. In: *Applied Mechanics Reviews* 70.2 (Feb. 2018), p. 020802. ISSN: 0003-6900. [Link](#).
- [213] Mohsen Azimi. “Stability and bifurcation of Mathieu–Duffing equation”. In: *International Journal of Non-Linear Mechanics* 144 (2022), p. 104049. ISSN: 0020-7462. [Link](#).
- [214] T. L. Heugel. “Parametrons: From Sensing to Optimization Machines”. PhD thesis. ETH Zürich (2022), 2022.
- [215] Samuel Boutin et al. “Effect of Higher-Order Nonlinearities on Amplification and Squeezing in Josephson Parametric Amplifiers”. In: *Phys. Rev. Appl.* 8 (5 Nov. 2017), p. 054030. [Link](#).
- [216] S.H. Strogatz. *Nonlinear Dynamics and Chaos: With Applications to Physics, Biology, Chemistry, and Engineering*. CRC Press, 2018. ISBN: 9780429961113. [Link](#).
- [217] Archana Kamal, Adam Marblestone, and Michel Devoret. “Signal-to-pump back action and self-oscillation in double-pump Josephson parametric amplifier”. In: *Phys. Rev. B* 79 (18 May 2009), p. 184301. [Link](#).

- [218] J.R. Johansson, P.D. Nation, and Franco Nori. “QuTiP 2: A Python framework for the dynamics of open quantum systems”. In: *Computer Physics Communications* 184.4 (2013), pp. 1234–1240. ISSN: 0010-4655. [Link](#).
- [219] Mario F. Gely et al. “Observation and stabilization of photonic Fock states in a hot radio-frequency resonator”. In: *Science* 363.6431 (2019), pp. 1072–1075. [Link](#).
- [220] Mario F. Gely et al. “Apparent nonlinear damping triggered by quantum fluctuations”. In: *Nature Communications* 14.1 (Nov. 2023), p. 7566. ISSN: 2041-1723. [Link](#).
- [221] Shingo Kono. “Quantum Measurement of Itinerant Microwave Photons Using Superconducting Circuits”. PhD thesis. University of Tokyo, 2019. [Link](#).
- [222] C. A. Potts et al. *Parametric Light-Matter Interaction in the Single-Photon Strong Coupling Limit*. 2024. [Link](#).
- [223] E. Wigner. “On the Quantum Correction For Thermodynamic Equilibrium”. In: *Phys. Rev.* 40 (5 June 1932), pp. 749–759. [Link](#).
- [224] H.J. Groenewold. “On the principles of elementary quantum mechanics”. In: *Physica* 12.7 (1946), pp. 405–460. ISSN: 0031-8914. [Link](#).
- [225] Mario F Gely and Gary A Steele. “QuCAT: quantum circuit analyzer tool in Python”. In: *New Journal of Physics* 22.1 (Jan. 2020), p. 013025. [Link](#).
- [226] Zlatko K Minev et al. *Qiskit Metal: An Open-Source Framework for Quantum Device Design & Analysis*. 2021. [Link](#).
- [227] Ansys. *Ansys HFSS*. 2024. [Link](#).
- [228] Zlatko K. Minev et al. “Energy-participation quantization of Josephson circuits”. In: *npj Quantum Information* 7.1 (Aug. 2021), p. 131. ISSN: 2056-6387. [Link](#).
- [229] David Johannes Thoen et al. “Superconducting NbTiN Thin Films With Highly Uniform Properties Over a \varnothing 100 mm Wafer”. In: *IEEE Transactions on Applied Superconductivity* 27.4 (2017), pp. 1–5.
- [230] R. Barends et al. “Coherent Josephson Qubit Suitable for Scalable Quantum Integrated Circuits”. In: *Physical Review Letters* 111.8 (Aug. 2013), p. 080502. [Link](#).
- [231] Jay M. Gambetta et al. “Investigating Surface Loss Effects in Superconducting Transmon Qubits”. In: *IEEE Transactions on Applied Superconductivity* 27.1 (2017), pp. 1–5.
- [232] Steffen Schlör et al. “Correlating Decoherence in Transmon Qubits: Low Frequency Noise by Single Fluctuators”. In: *Phys. Rev. Lett.* 123 (19 Nov. 2019), p. 190502. [Link](#).
- [233] Jürgen Lisenfeld et al. “Electric field spectroscopy of material defects in transmon qubits”. In: *npj Quantum Information* 5.1 (Nov. 2019), p. 105. ISSN: 2056-6387. [Link](#).
- [234] Alexander Bilmes et al. “Resolving the positions of defects in superconducting quantum bits”. In: *Scientific Reports* 10.1 (Feb. 2020), p. 3090. ISSN: 2045-2322. [Link](#).
- [235] Conal E. Murray. “Material matters in superconducting qubits”. In: *Materials Science and Engineering: R: Reports* 146 (2021), p. 100646. ISSN: 0927-796X. [Link](#).
- [236] John M. Martinis. “Surface loss calculations and design of a superconducting transmon qubit with tapered wiring”. In: *npj Quantum Information* 8.1 (Mar. 2022), p. 26. ISSN: 2056-6387. [Link](#).

- [237] Kavli Nanolab Delft. [Link](#).
- [238] S. I. Raider, R. Flitsch, and M. J. Palmer. "Oxide Growth on Etched Silicon in Air at Room Temperature". In: *Journal of The Electrochemical Society* 122.3 (Mar. 1975), p. 413. [Link](#).
- [239] Aaron D. O'Connell et al. "Microwave dielectric loss at single photon energies and millikelvin temperatures". In: *Applied Physics Letters* 92.11 (Mar. 2008), p. 112903. ISSN: 0003-6951. [Link](#).
- [240] John M. Martinis and A. Megrant. *UCSB final report for the CSQ program: Review of decoherence and materials physics for superconducting qubits*. 2014. [Link](#).
- [241] C. Wang et al. "Surface participation and dielectric loss in superconducting qubits". In: *Applied Physics Letters* 107.16 (Oct. 2015), p. 162601. ISSN: 0003-6951. [Link](#).
- [242] Oliver Dial et al. "Bulk and surface loss in superconducting transmon qubits". In: *Superconductor Science and Technology* 29.4 (Mar. 2016), p. 044001. [Link](#).
- [243] Christian Bohling and Wolfgang Sigmund. "Self-Limitation of Native Oxides Explained". In: *Silicon* 8.3 (July 2016), pp. 339–343. ISSN: 1876-9918. [Link](#).
- [244] P. V. Klimov et al. "Fluctuations of Energy-Relaxation Times in Superconducting Qubits". In: *Phys. Rev. Lett.* 121 (9 Aug. 2018), p. 090502. [Link](#).
- [245] Lu Zhang et al. "Characterization of surface oxidation layers on ultrathin NbTiN films". In: *Physica C: Superconductivity and its Applications* 545 (2018), pp. 1–4. ISSN: 0921-4534. [Link](#).
- [246] Jonathan J. Burnett et al. "Decoherence benchmarking of superconducting qubits". In: *npj Quantum Information* 5.1 (June 2019), p. 54. ISSN: 2056-6387. [Link](#).
- [247] S. E. de Graaf et al. "Two-level systems in superconducting quantum devices due to trapped quasiparticles". In: *Science Advances* 6.51 (2020), eabc5055. [Link](#).
- [248] S E de Graaf et al. "Chemical and structural identification of material defects in superconducting quantum circuits". In: *Materials for Quantum Technology* 2.3 (July 2022), p. 032001. [Link](#).
- [249] Janka Biznárová et al. "Mitigation of interfacial dielectric loss in aluminum-on-silicon superconducting qubits". In: *npj Quantum Information* 10.1 (Aug. 2024), p. 78. ISSN: 2056-6387. [Link](#).
- [250] Mustafa Bal et al. "Systematic improvements in transmon qubit coherence enabled by niobium surface encapsulation". In: *npj Quantum Information* 10.1 (Apr. 2024), p. 43. ISSN: 2056-6387. [Link](#).
- [251] P. Graham Pritchard and James M. Rondinelli. *Suppressed paramagnetism in amorphous Ta₂O_{5-x} oxides and its link to superconducting qubit performance*. 2024. [Link](#).
- [252] William D. Oliver and Paul B. Welander. "Materials in superconducting quantum bits". In: *MRS Bulletin* 38.10 (Oct. 2013), pp. 816–825. ISSN: 1938-1425. [Link](#).
- [253] Anjali Premkumar et al. "Microscopic relaxation channels in materials for superconducting qubits". In: *Communications Materials* 2.1 (July 2021), p. 72. ISSN: 2662-4443. [Link](#).

- [254] Alexander P. M. Place et al. "New material platform for superconducting transmon qubits with coherence times exceeding 0.3 milliseconds". In: *Nature Communications* 12.1 (Mar. 2021), p. 1779. ISSN: 2041-1723. [Link](#).
- [255] Aditya Jayaraman et al. "Loss and decoherence in superconducting circuits on silicon: Insights from electron spin resonance". In: *Phys. Rev. Appl.* 22 (1 July 2024), p. 014030. [Link](#).
- [256] P. J. de Visser et al. "Number Fluctuations of Sparse Quasiparticles in a Superconductor". In: *Phys. Rev. Lett.* 106 (16 Apr. 2011), p. 167004. [Link](#).
- [257] Lukas Grünhaupt et al. "Loss Mechanisms and Quasiparticle Dynamics in Superconducting Microwave Resonators Made of Thin-Film Granular Aluminum". In: *Phys. Rev. Lett.* 121 (11 Sept. 2018), p. 117001. [Link](#).
- [258] R.N. Simons. *Coplanar Waveguide Circuits, Components, and Systems*. Wiley Series in Microwave and Optical Engineering. Wiley, 2004. ISBN: 9780471463931. [Link](#).
- [259] R.E. Collin. *Foundations for Microwave Engineering, 2nd Ed.* McGraw-Hill series in electrical engineering: Radar and antennas. Wiley India Pvt. Limited, 2007. ISBN: 9788126515288. [Link](#).
- [260] R. Barends. "Photon-detecting superconducting resonators". PhD thesis. TU Delft (2009).
- [261] Raith EBPG-5000+. [Link](#).
- [262] Allresist. *Positive E-Beam Resists AR-P 6200 (CSAR 62)*. [Link](#).
- [263] MicroChem. *NANO™PMMA and Copolymer*. [Link](#).
- [264] Sentech. *RIE Plasma Etching Open Lid System - Etchlab 200*. [Link](#).
- [265] A. Bruno et al. "Reducing intrinsic loss in superconducting resonators by surface treatment and deep etching of silicon substrates". In: *Applied Physics Letters* 106.18 (May 2015), p. 182601. ISSN: 0003-6951. [Link](#).
- [266] III Thomas J. H. and L. H. Hammer. "An x-ray photoelectron spectroscopy study of sulfur hexafluoride etchant residue on silicon and silicon dioxide". In: *Journal of Vacuum Science Technology B: Microelectronics Processing and Phenomena* 5.6 (Nov. 1987), pp. 1617–1621. ISSN: 0734-211X. [Link](#).
- [267] D Levko, L Garrigues, and G J M Hagelaar. "Chemical composition of SF6 low-pressure plasma in magnetic field". In: *Journal of Physics D: Applied Physics* 47.4 (Dec. 2013), p. 045205. [Link](#).
- [268] Huiliang Jin et al. "Research on the chemical reaction in CF4 plasma during fused silica processing". In: *Proceedings of the 2017 6th International Conference on Measurement, Instrumentation and Automation (ICMIA 2017)*. Atlantis Press, 2017/06, pp. 154–158. ISBN: 978-94-6252-387-6. [Link](#).
- [269] Hiroshi Fukumoto et al. "Plasma chemical behaviour of reactants and reaction products during inductively coupled CF4 plasma etching of SiO2". In: *Plasma Sources Science and Technology* 18.4 (Sept. 2009), p. 045027. [Link](#).
- [270] Alexander Anferov et al. "Improved coherence in optically defined niobium trilayer-junction qubits". In: *Phys. Rev. Appl.* 21 (2 Feb. 2024), p. 024047. [Link](#).

- [271] Alexander Anferov et al. “Superconducting Qubits above 20 GHz Operating over 200 mK”. In: *PRX Quantum* 5 (3 Sept. 2024), p. 030347. [Link](#).
- [272] Simon Gustavsson et al. “Dynamical Decoupling and Dephasing in Interacting Two-Level Systems”. In: *Phys. Rev. Lett.* 109 (1 July 2012), p. 010502. [Link](#).
- [273] Lunjie Zeng et al. “Atomic structure and oxygen deficiency of the ultrathin aluminium oxide barrier in Al/AlO_x/Al Josephson junctions”. In: *Scientific Reports* 6.1 (July 2016), p. 29679. ISSN: 2045-2322. [Link](#).
- [274] G. Catelani et al. “Relaxation and frequency shifts induced by quasiparticles in superconducting qubits”. In: *Phys. Rev. B* 84 (6 Aug. 2011), p. 064517. [Link](#).
- [275] G. Catelani et al. “Quasiparticle Relaxation of Superconducting Qubits in the Presence of Flux”. In: *Phys. Rev. Lett.* 106 (7 Feb. 2011), p. 077002. [Link](#).
- [276] C. Wang et al. “Measurement and control of quasiparticle dynamics in a superconducting qubit”. In: *Nature Communications* 5.1 (Dec. 2014), p. 5836. ISSN: 2041-1723. [Link](#).
- [277] E. M. Levenson-Falk et al. “Single-Quasiparticle Trapping in Aluminum Nanobridge Josephson Junctions”. In: *Phys. Rev. Lett.* 112 (4 Jan. 2014), p. 047002. [Link](#).
- [278] Alexander Bilmes et al. “Electronic decoherence of two-level systems in a Josephson junction”. In: *Phys. Rev. B* 96 (6 Aug. 2017), p. 064504. [Link](#).
- [279] K. Serniak et al. “Hot Nonequilibrium Quasiparticles in Transmon Qubits”. In: *Phys. Rev. Lett.* 121 (15 Oct. 2018), p. 157701. [Link](#).
- [280] Leonid I. Glazman and Gianluigi Catelani. “Bogoliubov quasiparticles in superconducting qubits”. In: *SciPost Phys. Lect. Notes* (2021), p. 31. [Link](#).
- [281] R. Benevides et al. “Quasiparticle Dynamics in a Superconducting Qubit Irradiated by a Localized Infrared Source”. In: *Phys. Rev. Lett.* 133 (6 Aug. 2024), p. 060602. [Link](#).
- [282] Joseph W. Fowler et al. “Spectroscopic Measurements and Models of Energy Deposition in the Substrate of Quantum Circuits by Natural Ionizing Radiation”. In: *PRX Quantum* 5 (4 Nov. 2024), p. 040323. [Link](#).
- [283] Ioan M. Pop et al. “Coherent suppression of electromagnetic dissipation due to superconducting quasiparticles”. In: *Nature* 508.7496 (Apr. 2014), pp. 369–372. ISSN: 1476-4687. [Link](#).
- [284] Simon Gustavsson et al. “Suppressing relaxation in superconducting qubits by quasiparticle pumping”. In: *Science* 354.6319 (2016), pp. 1573–1577. [Link](#).
- [285] Fabio Henriques et al. “Phonon traps reduce the quasiparticle density in superconducting circuits”. In: *Applied Physics Letters* 115.21 (Nov. 2019), p. 212601. ISSN: 0003-6951. [Link](#).
- [286] L. Cardani et al. “Reducing the impact of radioactivity on quantum circuits in a deep-underground facility”. In: *Nature Communications* 12.1 (May 2021), p. 2733. ISSN: 2041-1723. [Link](#).
- [287] Xianchuang Pan et al. “Engineering superconducting qubits to reduce quasiparticles and charge noise”. In: *Nature Communications* 13.1 (Nov. 2022), p. 7196. ISSN: 2041-1723. [Link](#).

- [288] G Catelani and J P Pekola. "Using materials for quasiparticle engineering". In: *Materials for Quantum Technology* 2.1 (Feb. 2022), p. 013001. [Link](#).
- [289] Arno Bargerbos et al. "Mitigation of Quasiparticle Loss in Superconducting Qubits by Phonon Scattering". In: *Phys. Rev. Appl.* 19 (2 Feb. 2023), p. 024014. [Link](#).
- [290] C. H. Liu et al. "Quasiparticle Poisoning of Superconducting Qubits from Resonant Absorption of Pair-Breaking Photons". In: *Phys. Rev. Lett.* 132 (1 Jan. 2024), p. 017001. [Link](#).
- [291] A. Potts et al. "CMOS compatible fabrication methods for submicron Josephson junction qubits". In: *IEE Proceedings - Science, Measurement and Technology* 148 (5 2001), pp. 225–228. [Link](#).
- [292] Marius V. Costache et al. "Lateral metallic devices made by a multiangle shadow evaporation technique". In: *Journal of Vacuum Science Technology B* 30.4 (May 2012), 04E105. ISSN: 2166-2746. [Link](#).
- [293] J M Kreikebaum et al. "Improving wafer-scale Josephson junction resistance variation in superconducting quantum coherent circuits". In: *Superconductor Science and Technology* 33.6 (Apr. 2020), 06LT02. [Link](#).
- [294] A. Osman et al. "Simplified Josephson-junction fabrication process for reproducibly high-performance superconducting qubits". In: *Applied Physics Letters* 118.6 (Feb. 2021), p. 064002. ISSN: 0003-6951. [Link](#).
- [295] Nandini Muthusubramanian et al. "Wafer-scale uniformity of Dolan-bridge and bridgeless Manhattan-style Josephson junctions for superconducting quantum processors". In: *Quantum Science and Technology* 9.2 (Feb. 2024), p. 025006. [Link](#).
- [296] Pie Scientific. *Plasma Cleaning and Etching*. [Link](#).
- [297] C T Earnest et al. "Substrate surface engineering for high-quality silicon/aluminum superconducting resonators". In: *Superconductor Science and Technology* 31.12 (Nov. 2018), p. 125013. [Link](#).
- [298] J. Verjauw et al. "Investigation of Microwave Loss Induced by Oxide Regrowth in High-Q Niobium Resonators". In: *Phys. Rev. Appl.* 16 (1 July 2021), p. 014018. [Link](#).
- [299] M. Virginia P. Altoé et al. "Localization and Mitigation of Loss in Niobium Superconducting Circuits". In: *PRX Quantum* 3 (2 Apr. 2022), p. 020312. [Link](#).
- [300] Zengqian Ding et al. "Stable and low loss oxide layer on -Ta (110) film for superconducting qubits". In: *Journal of Vacuum Science Technology B* 42.2 (Feb. 2024), p. 022209. ISSN: 2166-2746. [Link](#).
- [301] T. Schuhrke et al. "Investigation of surface amorphization of silicon wafers during ion-milling". In: *Ultramicroscopy* 41.4 (1992), pp. 429–433. ISSN: 0304-3991. [Link](#).
- [302] C. M. Quintana et al. "Characterization and reduction of microfabrication-induced decoherence in superconducting quantum circuits". In: *Applied Physics Letters* 105.6 (Aug. 2014), p. 062601. ISSN: 0003-6951. [Link](#).
- [303] A. Dunsworth et al. "Characterization and reduction of capacitive loss induced by submicron Josephson junction fabrication in superconducting qubits". In: *Applied Physics Letters* 111.2 (July 2017), p. 022601. ISSN: 0003-6951. [Link](#).

- [304] J. Van Damme et al. "Argon-Milling-Induced Decoherence Mechanisms in Superconducting Quantum Circuits". In: *Phys. Rev. Appl.* 20 (1 July 2023), p. 014034. [Link](#).
- [305] J.E Curran, J.S Page, and U Pick. "The influence of some evaporation parameters on the structure and properties of thin aluminium films". In: *Thin Solid Films* 97.3 (1982), pp. 259–276. ISSN: 0040-6090. [Link](#).
- [306] W.H. Mallison, R.E. Miller, and A.W. Kleinsasser. "Effect of growth conditions on the electrical properties of Nb/Al-oxide/Nb tunnel junctions". In: *IEEE Transactions on Applied Superconductivity* 5.2 (1995), pp. 2330–2333.
- [307] N.G. Semaltianos. "Thermally evaporated aluminium thin films". In: *Applied Surface Science* 183.3 (2001), pp. 223–229. ISSN: 0169-4332. [Link](#).
- [308] Na Cai et al. "Temperature and pressure dependent Mott potentials and their influence on self-limiting oxide film growth". In: *Applied Physics Letters* 101.17 (Oct. 2012), p. 171605. ISSN: 0003-6951. [Link](#).
- [309] S. Fritz et al. "Correlating the nanostructure of Al-oxide with deposition conditions and dielectric contributions of two-level systems in perspective of superconducting quantum circuits". In: *Scientific Reports* 8.1 (May 2018), p. 7956. ISSN: 2045-2322. [Link](#).
- [310] S. Fritz et al. "Structural and nanochemical properties of AlO_x layers in Al/ AlO_x /Al-layer systems for Josephson junctions". In: *Phys. Rev. Mater.* 3 (11 Nov. 2019), p. 114805. [Link](#).
- [311] Dmitry O. Moskalev et al. "Optimization of shadow evaporation and oxidation for reproducible quantum Josephson junction circuits". In: *Scientific Reports* 13.1 (Mar. 2023), p. 4174. ISSN: 2045-2322. [Link](#).
- [312] Chuanbing Han et al. "Molecular dynamics study of the effect of substrate temperature on the barrier behavior in aluminum oxide Josephson junctions". In: *Applied Surface Science* 615 (2023), p. 156369. ISSN: 0169-4332. [Link](#).
- [313] Xiaotao Liu et al. "Unveiling atomic structure and chemical composition of the Al/ AlO_x /Al Josephson junctions in qubits". In: *Applied Surface Science* 640 (2023), p. 158337. ISSN: 0169-4332. [Link](#).
- [314] Anastasiya A. Pishchimova et al. "Improving Josephson junction reproducibility for superconducting quantum circuits: junction area fluctuation". In: *Scientific Reports* 13.1 (Apr. 2023), p. 6772. ISSN: 2045-2322. [Link](#).
- [315] Yong Chen et al. "Distinguishing the impact of oxidation on the Josephson junction oxide barrier through the $1/f$ behavior". In: *Applied Physics Letters* 125.9 (Aug. 2024), p. 094001. ISSN: 0003-6951. [Link](#).
- [316] Vinay Ambegaokar and Alexis Baratoff. "Tunneling Between Superconductors". In: *Phys. Rev. Lett.* 10 (11 June 1963), pp. 486–489. [Link](#).
- [317] D. H. Douglass and R. Meservey. "Energy Gap Measurements by Tunneling Between Superconducting Films. I. Temperature Dependence". In: *Phys. Rev.* 135 (1A July 1964), A19–A23. [Link](#).
- [318] M. Tinkham. *Introduction to Superconductivity*. International series in pure and applied physics. McGraw Hill, 1996. ISBN: 9780070648784. [Link](#).

- [319] John F. Cochran and D. E. Mapother. “Superconducting Transition in Aluminum”. In: *Phys. Rev.* 111 (1 July 1958), pp. 132–142. [Link](#).
- [320] Yoshiaki Kogure et al. “Anisotropy of Superconducting Energy Gap in Aluminium Determined by Ultrasonic Method”. In: *Journal of the Physical Society of Japan* 54.9 (1985), pp. 3506–3513. [Link](#).
- [321] Jared B. Hertzberg et al. “Laser-annealing Josephson junctions for yielding scaled-up superconducting quantum processors”. In: *npj Quantum Information* 7.1 (Aug. 2021), p. 129. ISSN: 2056-6387. [Link](#).
- [322] Sihao Huang et al. “Microwave Package Design for Superconducting Quantum Processors”. In: *PRX Quantum* 2 (2 Apr. 2021), p. 020306. [Link](#).
- [323] P. J. J. O’Malley et al. “Scalable Quantum Simulation of Molecular Energies”. In: *Phys. Rev. X* 6 (3 July 2016), p. 031007. [Link](#).
- [324] Frank Arute et al. “Quantum supremacy using a programmable superconducting processor”. In: *Nature* 574.7779 (Oct. 2019), pp. 505–510. ISSN: 1476-4687. [Link](#).
- [325] I. M. Georgescu, S. Ashhab, and Franco Nori. “Quantum simulation”. In: *Rev. Mod. Phys.* 86 (1 Mar. 2014), pp. 153–185. [Link](#).
- [326] Michael J Hartmann. “Quantum simulation with interacting photons”. In: *Journal of Optics* 18.10 (Sept. 2016), p. 104005. [Link](#).
- [327] Kai Xu et al. “Emulating Many-Body Localization with a Superconducting Quantum Processor”. In: *Phys. Rev. Lett.* 120 (5 Feb. 2018), p. 050507. [Link](#).
- [328] M. Ganzhorn et al. “Gate-Efficient Simulation of Molecular Eigenstates on a Quantum Computer”. In: *Phys. Rev. Appl.* 11 (4 Apr. 2019), p. 044092. [Link](#).
- [329] M. Ganzhorn et al. “Benchmarking the noise sensitivity of different parametric two-qubit gates in a single superconducting quantum computing platform”. In: *Phys. Rev. Res.* 2 (3 Sept. 2020), p. 033447. [Link](#).
- [330] Antti O. Niskanen, Yasunobu Nakamura, and Jaw-Shen Tsai. “Tunable coupling scheme for flux qubits at the optimal point”. In: *Phys. Rev. B* 73 (9 Mar. 2006), p. 094506. [Link](#).
- [331] Yu Chen et al. “Qubit Architecture with High Coherence and Fast Tunable Coupling”. In: *Phys. Rev. Lett.* 113 (22 Nov. 2014), p. 220502. [Link](#).
- [332] M. D. Hutchings et al. “Tunable Superconducting Qubits with Flux-Independent Coherence”. In: *Phys. Rev. Appl.* 8 (4 Oct. 2017), p. 044003. [Link](#).
- [333] M. Kounalakis et al. “Tuneable hopping and nonlinear cross-Kerr interactions in a high-coherence superconducting circuit”. In: *npj Quantum Information* 4.1 (Aug. 2018), p. 38. ISSN: 2056-6387. [Link](#).
- [334] Fei Yan et al. “Tunable Coupling Scheme for Implementing High-Fidelity Two-Qubit Gates”. In: *Phys. Rev. Appl.* 10 (5 Nov. 2018), p. 054062. [Link](#).
- [335] Michele C. Collodo et al. “Implementation of Conditional Phase Gates Based on Tunable ZZ Interactions”. In: *Phys. Rev. Lett.* 125 (24 Dec. 2020), p. 240502. [Link](#).
- [336] Youngkyu Sung et al. “Realization of High-Fidelity CZ and ZZ -Free iSWAP Gates with a Tunable Coupler”. In: *Phys. Rev. X* 11 (2 June 2021), p. 021058. [Link](#).

- [337] Jiasen Jin et al. “Photon Solid Phases in Driven Arrays of Nonlinearly Coupled Cavities”. In: *Phys. Rev. Lett.* 110 (16 Apr. 2013), p. 163605. [Link](#).
- [338] Songbo Jin et al. “Phase transitions in the frustrated Ising model on the square lattice”. In: *Phys. Rev. B* 87 (14 Apr. 2013), p. 144406. [Link](#).
- [339] D. Marcos et al. “Superconducting Circuits for Quantum Simulation of Dynamical Gauge Fields”. In: *Phys. Rev. Lett.* 111 (11 Sept. 2013), p. 110504. [Link](#).
- [340] D. Marcos et al. “Two-dimensional lattice gauge theories with superconducting quantum circuits”. In: *Annals of Physics* 351 (2014), pp. 634–654. ISSN: 0003-4916. [Link](#).
- [341] A. S. Dehkharghani et al. “Quantum simulation of Abelian lattice gauge theories via state-dependent hopping”. In: *Phys. Rev. A* 96 (4 Oct. 2017), p. 043611. [Link](#).
- [342] Mahdi Sameti et al. “Superconducting quantum simulator for topological order and the toric code”. In: *Phys. Rev. A* 95 (4 Apr. 2017), p. 042330. [Link](#).
- [343] Mahdi Sameti and Michael J. Hartmann. “Floquet engineering in superconducting circuits: From arbitrary spin-spin interactions to the Kitaev honeycomb model”. In: *Phys. Rev. A* 99 (1 Jan. 2019), p. 012333. [Link](#).
- [344] Michael R. Geller et al. “Tunable coupler for superconducting Xmon qubits: Perturbative nonlinear model”. In: *Phys. Rev. A* 92 (1 July 2015), p. 012320. [Link](#).
- [345] David C. McKay et al. “Universal Gate for Fixed-Frequency Qubits via a Tunable Bus”. In: *Phys. Rev. Appl.* 6 (6 Dec. 2016), p. 064007. [Link](#).
- [346] Marco Roth et al. “Analysis of a parametrically driven exchange-type gate and a two-photon excitation gate between superconducting qubits”. In: *Phys. Rev. A* 96 (6 Dec. 2017), p. 062323. [Link](#).
- [347] X. Li et al. “Tunable Coupler for Realizing a Controlled-Phase Gate with Dynamically Decoupled Regime in a Superconducting Circuit”. In: *Phys. Rev. Appl.* 14 (2 Aug. 2020), p. 024070. [Link](#).
- [348] J. Stehlik et al. “Tunable Coupling Architecture for Fixed-Frequency Transmon Superconducting Qubits”. In: *Phys. Rev. Lett.* 127 (8 Aug. 2021), p. 080505. [Link](#).
- [349] Yangsen Ye et al. “Realization of High-Fidelity Controlled-Phase Gates in Extensible Superconducting Qubits Design with a Tunable Coupler”. In: *Chinese Physics Letters* 38.10 (Nov. 2021), p. 100301. [Link](#).
- [350] Ilya N. Moskaleenko et al. “High fidelity two-qubit gates on fluxoniums using a tunable coupler”. In: *npj Quantum Information* 8.1 (Nov. 2022), p. 130. ISSN: 2056-6387. [Link](#).
- [351] Hayato Goto. “Double-Transmon Coupler: Fast Two-Qubit Gate with No Residual Coupling for Highly Detuned Superconducting Qubits”. In: *Phys. Rev. Appl.* 18 (3 Sept. 2022), p. 034038. [Link](#).
- [352] Lukas Heunisch, Christopher Eichler, and Michael J. Hartmann. “Tunable coupler to fully decouple and maximally localize superconducting qubits”. In: *Phys. Rev. Appl.* 20 (6 Dec. 2023), p. 064037. [Link](#).
- [353] Daniel L. Campbell et al. “Modular Tunable Coupler for Superconducting Circuits”. In: *Phys. Rev. Appl.* 19 (6 June 2023), p. 064043. [Link](#).

- [354] Helin Zhang et al. “Tunable Inductive Coupler for High-Fidelity Gates Between Fluxonium Qubits”. In: *PRX Quantum* 5 (2 May 2024), p. 020326. [Link](#).
- [355] Giacomo Corrielli et al. “Fractional Bloch oscillations in photonic lattices”. In: *Nature Communications* 4.1 (Mar. 2013), p. 1555. ISSN: 2041-1723. [Link](#).
- [356] Ilan T. Rosen et al. “A synthetic magnetic vector potential in a 2D superconducting qubit array”. In: *Nature Physics* (Oct. 2024). ISSN: 1745-2481. [Link](#).
- [357] Y. Salathé et al. “Digital Quantum Simulation of Spin Models with Circuit Quantum Electrodynamics”. In: *Phys. Rev. X* 5 (2 June 2015), p. 021027. [Link](#).
- [358] Shruti Puri et al. “Quantum annealing with all-to-all connected nonlinear oscillators”. In: *Nature Communications* 8.1 (June 2017), p. 15785. ISSN: 2041-1723. [Link](#).
- [359] Hans Huebl et al. “High Cooperativity in Coupled Microwave Resonator Ferrimagnetic Insulator Hybrids”. In: *Phys. Rev. Lett.* 111 (12 Sept. 2013), p. 127003. [Link](#).
- [360] Nathan R. Bernier, Emanuele G. Dalla Torre, and Eugene Demler. “Unstable Avoided Crossing in Coupled Spinor Condensates”. In: *Phys. Rev. Lett.* 113 (6 Aug. 2014), p. 065303. [Link](#).
- [361] Hichem Eleuch and Ingrid Rotter. “Exceptional Points in Open and PT-Symmetric Systems”. In: *Acta Polytechnica* 54.2 (Apr. 2014), pp. 106–112. [Link](#).
- [362] A. Gloppe et al. “Bidimensional nano-optomechanics and topological backaction in a non-conservative radiation force field”. In: *Nature Nanotechnology* 9.11 (Nov. 2014), pp. 920–926. ISSN: 1748-3395. [Link](#).
- [363] H. Xu et al. “Topological energy transfer in an optomechanical system with exceptional points”. In: *Nature* 537.7618 (Sept. 2016), pp. 80–83. ISSN: 1476-4687. [Link](#).
- [364] Dengke Zhang et al. “Observation of the exceptional point in cavity magnon-polaritons”. In: *Nature Communications* 8.1 (Nov. 2017), p. 1368. ISSN: 2041-1723. [Link](#).
- [365] N. R. Bernier et al. “Level attraction in a microwave optomechanical circuit”. In: *Phys. Rev. A* 98 (2 Aug. 2018), p. 023841. [Link](#).
- [366] M. Harder et al. “Level Attraction Due to Dissipative Magnon-Photon Coupling”. In: *Phys. Rev. Lett.* 121 (13 Sept. 2018), p. 137203. [Link](#).
- [367] Vahram L. Grigoryan, Ka Shen, and Ke Xia. “Synchronized spin-photon coupling in a microwave cavity”. In: *Phys. Rev. B* 98 (2 July 2018), p. 024406. [Link](#).
- [368] Biswanath Bhoi et al. “Abnormal anticrossing effect in photon-magnon coupling”. In: *Phys. Rev. B* 99 (13 Apr. 2019), p. 134426. [Link](#).
- [369] Weichao Yu et al. “Prediction of Attractive Level Crossing via a Dissipative Mode”. In: *Phys. Rev. Lett.* 123 (22 Nov. 2019), p. 227201. [Link](#).
- [370] Y. Yang et al. “Control of the Magnon-Photon Level Attraction in a Planar Cavity”. In: *Phys. Rev. Appl.* 11 (5 May 2019), p. 054023. [Link](#).
- [371] Mohammad-Ali Miri and Andrea Alù. “Exceptional points in optics and photonics”. In: *Science* 363.6422 (2019), eaar7709. [Link](#).
- [372] Yi-Pu Wang et al. “Nonreciprocity and Unidirectional Invisibility in Cavity Magnonics”. In: *Phys. Rev. Lett.* 123 (12 Sept. 2019), p. 127202. [Link](#).

- [373] Yi-Pu Wang and Can-Ming Hu. “Dissipative couplings in cavity magnonics”. In: *Journal of Applied Physics* 127.13 (Apr. 2020), p. 130901. ISSN: 0021-8979. [Link](#).
- [374] F. Fani Sani et al. “Level attraction and idler resonance in a strongly driven Josephson cavity”. In: *Phys. Rev. Res.* 3 (4 Nov. 2021), p. 043111. [Link](#).
- [375] Tanmoy Bera et al. “Single-photon induced instabilities in a cavity electromechanical device”. In: *Nature Communications* 15.1 (Aug. 2024), p. 7115. ISSN: 2041-1723. [Link](#).
- [376] A. Metelmann and A. A. Clerk. “Quantum-Limited Amplification via Reservoir Engineering”. In: *Phys. Rev. Lett.* 112 (13 Apr. 2014), p. 133904. [Link](#).
- [377] Hilary M. Hurst and Benedetta Flebus. “Non-Hermitian physics in magnetic systems”. In: *Journal of Applied Physics* 132.22 (Dec. 2022), p. 220902. ISSN: 0021-8979. [Link](#).
- [378] Jonathan Kohler et al. “Negative-Mass Instability of the Spin and Motion of an Atomic Gas Driven by Optical Cavity Backaction”. In: *Phys. Rev. Lett.* 120 (1 Jan. 2018), p. 013601. [Link](#).
- [379] Bimu Yao et al. “The microscopic origin of magnon-photon level attraction by traveling waves: Theory and experiment”. In: *Phys. Rev. B* 100 (21 Dec. 2019), p. 214426. [Link](#).
- [380] S. Poletto et al. “Entanglement of Two Superconducting Qubits in a Waveguide Cavity via Monochromatic Two-Photon Excitation”. In: *Phys. Rev. Lett.* 109 (24 Dec. 2012), p. 240505. [Link](#).
- [381] Ken Xuan Wei et al. “Native Two-Qubit Gates in Fixed-Coupling, Fixed-Frequency Transmons Beyond Cross-Resonance Interaction”. In: *PRX Quantum* 5 (2 May 2024), p. 020338. [Link](#).
- [382] Layla Hormozi et al. “Nonstoquastic Hamiltonians and quantum annealing of an Ising spin glass”. In: *Phys. Rev. B* 95 (18 May 2017), p. 184416. [Link](#).
- [383] A. Ciani and B. M. Terhal. “Stoquasticity in circuit QED”. In: *Phys. Rev. A* 103 (4 Apr. 2021), p. 042401. [Link](#).
- [384] Andreas Bengtsson et al. “Nondegenerate parametric oscillations in a tunable superconducting resonator”. In: *Phys. Rev. B* 97 (14 Apr. 2018), p. 144502. [Link](#).
- [385] Waltraut Wustmann and Vitaly Shumeiko. “Parametric resonance in tunable superconducting cavities”. In: *Phys. Rev. B* 87 (18 May 2013), p. 184501. [Link](#).
- [386] Waltraut Wustmann and Vitaly Shumeiko. “Nondegenerate Parametric Resonance in a Tunable Superconducting Cavity”. In: *Phys. Rev. Appl.* 8 (2 Aug. 2017), p. 024018. [Link](#).
- [387] Waltraut Wustmann and Vitaly Shumeiko. “Parametric effects in circuit quantum electrodynamics”. In: *Low Temperature Physics* 45.8 (Aug. 2019), pp. 848–869. ISSN: 1063-777X. [Link](#).
- [388] R. Adler. “A Study of Locking Phenomena in Oscillators”. In: *Proceedings of the IRE* 34.6 (1946), pp. 351–357.
- [389] D. Marković et al. “Injection Locking and Parametric Locking in a Superconducting Circuit”. In: *Phys. Rev. Appl.* 12 (2 Aug. 2019), p. 024034. [Link](#).
- [390] Nicola Bartolo et al. “Exact steady state of a Kerr resonator with one- and two-photon driving and dissipation: Controllable Wigner-function multimodality and dissipative phase transitions”. In: *Phys. Rev. A* 94 (3 Sept. 2016), p. 033841. [Link](#).

- [391] Paul Brookes et al. “Critical slowing down in circuit quantum electrodynamics”. In: *Science Advances* 7.21 (2021), eabe9492. [Link](#).
- [392] M.J. Hartmann, F.G.S.L. Brandão, and M.B. Plenio. “Quantum many-body phenomena in coupled cavity arrays”. In: *Laser & Photonics Reviews* 2.6 (2008), pp. 527–556. [Link](#).
- [393] Yongqi Liang et al. *Floquet Engineering of Anisotropic Transverse Interactions in Superconducting Qubits*. 2024. [Link](#).
- [394] Yong Lu et al. *Resolving Fock states near the Kerr-free point of a superconducting resonator*. 2022. [Link](#).
- [395] Benjamin J. Chapman et al. “High-On-Off-Ratio Beam-Splitter Interaction for Gates on Bosonically Encoded Qubits”. In: *PRX Quantum* 4 (2 June 2023), p. 020355. [Link](#).
- [396] Bingcheng Qing et al. *Benchmarking Single-Qubit Gates on a Noise-Biased Qubit Beyond the Fault-Tolerant Threshold*. 2024. [Link](#).
- [397] M. Mamaev, L. C. G. Govia, and A. A. Clerk. “Dissipative stabilization of entangled cat states using a driven Bose-Hubbard dimer”. In: *Quantum* 2 (Mar. 2018), p. 58. ISSN: 2521-327X. [Link](#).
- [398] Samuel Aldana, Christoph Bruder, and Andreas Nunnenkamp. “Equivalence between an optomechanical system and a Kerr medium”. In: *Phys. Rev. A* 88 (4 Oct. 2013), p. 043826. [Link](#).
- [399] Nicolas Didier et al. “Analytical modeling of parametrically modulated transmon qubits”. In: *Phys. Rev. A* 97 (2 Feb. 2018), p. 022330. [Link](#).
- [400] S. A. Caldwell et al. “Parametrically Activated Entangling Gates Using Transmon Qubits”. In: *Phys. Rev. Appl.* 10 (3 Sept. 2018), p. 034050. [Link](#).
- [401] John Kerr. “XL. A new relation between electricity and light: Dielectrified media birefringent”. In: *The London, Edinburgh, and Dublin Philosophical Magazine and Journal of Science* 50.332 (1875), pp. 337–348. [Link](#).
- [402] Yoshisuke Ueda. “Survey of regular and chaotic phenomena in the forced Duffing oscillator”. In: *Chaos, Solitons Fractals* 1.3 (1991), pp. 199–231. ISSN: 0960-0779. [Link](#).
- [403] T. J. Kippenberg, S. M. Spillane, and K. J. Vahala. “Kerr-Nonlinearity Optical Parametric Oscillation in an Ultrahigh-Q Toroid Microcavity”. In: *Phys. Rev. Lett.* 93 (8 Aug. 2004), p. 083904. [Link](#).
- [404] Robin J. Dolleman et al. “High-Frequency Stochastic Switching of Graphene Resonators Near Room Temperature”. In: *Nano Letters* 19.2 (2019). PMID: 30681865, pp. 1282–1288. [Link](#).
- [405] M. X. Bi et al. “Tristability of cavity magnon polaritons”. In: *Phys. Rev. B* 103 (10 Mar. 2021), p. 104411. [Link](#).
- [406] Rui-Chang Shen et al. “Long-Time Memory and Ternary Logic Gate Using a Multistable Cavity Magnonic System”. In: *Phys. Rev. Lett.* 127 (18 Oct. 2021), p. 183202. [Link](#).
- [407] Ata Keşkekler et al. “Symmetry-Breaking-Induced Frequency Combs in Graphene Resonators”. In: *Nano Letters* 22.15 (2022). PMID: 35904442, pp. 6048–6054. [Link](#).

- [408] Edgar F. Perez et al. “High-performance Kerr microresonator optical parametric oscillator on a silicon chip”. In: *Nature Communications* 14.1 (Jan. 2023), p. 242. ISSN: 2041-1723. [Link](#).
- [409] Menglong He and Kambiz Jamshidi. “Conditions for dual-pumped optical parametric oscillation in Kerr microresonators”. In: *Phys. Rev. Appl.* 20 (5 Nov. 2023), p. 054036. [Link](#).
- [410] Tomás Manzaneeque et al. “Resolution Limits of Resonant Sensors”. In: *Phys. Rev. Appl.* 19 (5 May 2023), p. 054074. [Link](#).
- [411] Chunlei Zhang et al. “Van der Pol–Duffing oscillator and its application to gain-driven light-matter interaction”. In: *Phys. Rev. Appl.* 22 (1 July 2024), p. 014034. [Link](#).
- [412] Christian A. Rosiek et al. “Quadrature Squeezing Enhances Wigner Negativity in a Mechanical Duffing Oscillator”. In: *PRX Quantum* 5 (3 July 2024), p. 030312. [Link](#).
- [413] Zichao Li et al. “Strain engineering of nonlinear nanoresonators from hardening to softening”. In: *Communications Physics* 7.1 (Feb. 2024), p. 53. ISSN: 2399-3650. [Link](#).
- [414] A. Imamo ğlu et al. “Strongly Interacting Photons in a Nonlinear Cavity”. In: *Phys. Rev. Lett.* 79 (8 Aug. 1997), pp. 1467–1470. [Link](#).
- [415] B. Yurke et al. “Observation of 4.2-K equilibrium-noise squeezing via a Josephson-parametric amplifier”. In: *Phys. Rev. Lett.* 60 (9 Feb. 1988), pp. 764–767. [Link](#).
- [416] T. Yamamoto et al. “Flux-driven Josephson parametric amplifier”. In: *Applied Physics Letters* 93.4 (July 2008), p. 042510. ISSN: 0003-6951. [Link](#).
- [417] Max Hofheinz et al. “Synthesizing arbitrary quantum states in a superconducting resonator”. In: *Nature* 459.7246 (May 2009), pp. 546–549. ISSN: 1476-4687. [Link](#).
- [418] J. Y. Mutus et al. “Design and characterization of a lumped element single-ended superconducting microwave parametric amplifier with on-chip flux bias line”. In: *Applied Physics Letters* 103.12 (Sept. 2013), p. 122602. ISSN: 0003-6951. [Link](#).
- [419] M. H. Devoret and R. J. Schoelkopf. “Superconducting Circuits for Quantum Information: An Outlook”. In: *Science* 339.6124 (2013), pp. 1169–1174. [Link](#).
- [420] Gershon Kurizki et al. “Quantum technologies with hybrid systems”. In: *Proceedings of the National Academy of Sciences* 112.13 (2015), pp. 3866–3873. [Link](#).
- [421] A. Eichler et al. “Symmetry breaking in a mechanical resonator made from a carbon nanotube”. In: *Nature Communications* 4.1 (Nov. 2013), p. 2843. ISSN: 2041-1723. [Link](#).
- [422] Carlton M. Caves. “Quantum limits on noise in linear amplifiers”. In: *Phys. Rev. D* 26 (8 Oct. 1982), pp. 1817–1839. [Link](#).
- [423] M. A. Castellanos-Beltran et al. “Amplification and squeezing of quantum noise with a tunable Josephson metamaterial”. In: *Nature Physics* 4.12 (Dec. 2008), pp. 929–931. ISSN: 1745-2481. [Link](#).
- [424] Gerhard Kirchmair et al. “Observation of quantum state collapse and revival due to the single-photon Kerr effect”. In: *Nature* 495.7440 (Mar. 2013), pp. 205–209. ISSN: 1476-4687. [Link](#).
- [425] Hayato Goto. “Universal quantum computation with a nonlinear oscillator network”. In: *Phys. Rev. A* 93 (5 May 2016), p. 050301. [Link](#).

- [426] Shruti Puri, Samuel Boutin, and Alexandre Blais. “Engineering the quantum states of light in a Kerr-nonlinear resonator by two-photon driving”. In: *npj Quantum Information* 3.1 (Apr. 2017), p. 18. ISSN: 2056-6387. [Link](#).
- [427] Peng Zhao et al. “Two-Photon Driven Kerr Resonator for Quantum Annealing with Three-Dimensional Circuit QED”. In: *Phys. Rev. Appl.* 10 (2 Aug. 2018), p. 024019. [Link](#).
- [428] Christian Kraglund Andersen et al. “Quantum Versus Classical Switching Dynamics of Driven Dissipative Kerr Resonators”. In: *Phys. Rev. Appl.* 13 (4 Apr. 2020), p. 044017. [Link](#).
- [429] T. Yamaji et al. “Spectroscopic observation of the crossover from a classical Duffing oscillator to a Kerr parametric oscillator”. In: *Phys. Rev. A* 105 (2 Feb. 2022), p. 023519. [Link](#).
- [430] A. J. Leggett et al. “Dynamics of the dissipative two-state system”. In: *Rev. Mod. Phys.* 59 (1 Jan. 1987), pp. 1–85. [Link](#).
- [431] Itamar Katz et al. “Signatures for a Classical to Quantum Transition of a Driven Nonlinear Nanomechanical Resonator”. In: *Phys. Rev. Lett.* 99 (4 July 2007), p. 040404. [Link](#).
- [432] C. M. Wilson et al. “Photon Generation in an Electromagnetic Cavity with a Time-Dependent Boundary”. In: *Phys. Rev. Lett.* 105 (23 Dec. 2010), p. 233907. [Link](#).
- [433] Charles H. Meaney et al. “Quantum and classical nonlinear dynamics in a microwave cavity”. In: *EPJ Quantum Technology* 1.1 (June 2014), p. 7. ISSN: 2196-0763. [Link](#).
- [434] M. I. Dykman. *Classical and quantum dynamics of periodically driven nanomechanical systems*. 2017. [Link](#).
- [435] I. Pietikäinen et al. “Photon blockade and the quantum-to-classical transition in the driven-dissipative Josephson pendulum coupled to a resonator”. In: *Phys. Rev. A* 99 (6 June 2019), p. 063828. [Link](#).
- [436] Andrew D. Maris et al. “Chaos in the quantum Duffing oscillator in the semiclassical regime under parametrized dissipation”. In: *Phys. Rev. E* 104 (2 Aug. 2021), p. 024206. [Link](#).
- [437] Hayato Goto and Taro Kanao. “Chaos in coupled Kerr-nonlinear parametric oscillators”. In: *Phys. Rev. Res.* 3 (4 Dec. 2021), p. 043196. [Link](#).
- [438] Qi-Ming Chen et al. “Quantum behavior of the Duffing oscillator at the dissipative phase transition”. In: *Nature Communications* 14.1 (May 2023), p. 2896. ISSN: 2041-1723. [Link](#).
- [439] Guillaume Beaulieu et al. *Observation of first- and second-order dissipative phase transitions in a two-photon driven Kerr resonator*. 2023. [Link](#).
- [440] F. Hellbach et al. *Nonlinearity-induced symmetry breaking in a system of two parametrically driven Kerr-Duffing oscillators*. 2024. [Link](#).
- [441] D. K. J. Boneß, W. Belzig, and M. I. Dykman. “Resonant-force-induced symmetry breaking in a quantum parametric oscillator”. In: *Phys. Rev. Res.* 6 (3 Sept. 2024), p. 033240. [Link](#).
- [442] Leo Peyruchat et al. *Landau-Zener without a Qubit: Unveiling Multiphoton Interference, Synthetic Floquet Dimensions, and Dissipative Quantum Chaos*. 2024. [Link](#).
- [443] Yaxing Zhang and M. I. Dykman. “Preparing quasienergy states on demand: A parametric oscillator”. In: *Phys. Rev. A* 95 (5 May 2017), p. 053841. [Link](#).

- [444] Pablo Álvarez et al. “Biased Ising Model Using Two Coupled Kerr Parametric Oscillators with External Force”. In: *Phys. Rev. Lett.* 132 (20 May 2024), p. 207401. [Link](#).
- [445] Matteo Soriente et al. “Distinctive class of dissipation-induced phase transitions and their universal characteristics”. In: *Phys. Rev. Res.* 3 (2 May 2021), p. 023100. [Link](#).
- [446] Toni L. Heugel et al. “The role of fluctuations in quantum and classical time crystals”. In: *SciPost Phys. Core* 6 (2023), p. 053. [Link](#).
- [447] J. S. Ochs et al. “Amplification and spectral evidence of squeezing in the response of a strongly driven nanoresonator to a probe field”. In: *Phys. Rev. A* 103 (1 Jan. 2021), p. 013506. [Link](#).
- [448] Katarzyna Macieszczak et al. “Towards a Theory of Metastability in Open Quantum Dynamics”. In: *Phys. Rev. Lett.* 116 (24 June 2016), p. 240404. [Link](#).
- [449] I. C. Rodrigues, G. A. Steele, and D. Bothner. “Photon Pressure with an Effective Negative Mass Microwave Mode”. In: *Phys. Rev. Lett.* 132 (20 May 2024), p. 203603. [Link](#).
- [450] D. T. Smithey et al. “Measurement of the Wigner distribution and the density matrix of a light mode using optical homodyne tomography: Application to squeezed states and the vacuum”. In: *Phys. Rev. Lett.* 70 (9 Mar. 1993), pp. 1244–1247. [Link](#).
- [451] C. Eichler et al. “Experimental State Tomography of Itinerant Single Microwave Photons”. In: *Phys. Rev. Lett.* 106 (22 June 2011), p. 220503. [Link](#).
- [452] Zhaoyou Wang et al. “Quantum Dynamics of a Few-Photon Parametric Oscillator”. In: *Phys. Rev. X* 9 (2 June 2019), p. 021049. [Link](#).
- [453] M. Foss-Feig et al. “Emergent equilibrium in many-body optical bistability”. In: *Phys. Rev. A* 95 (4 Apr. 2017), p. 043826. [Link](#).
- [454] Filippo Vicentini et al. “Critical slowing down in driven-dissipative Bose-Hubbard lattices”. In: *Phys. Rev. A* 97 (1 Jan. 2018), p. 013853. [Link](#).
- [455] Fabrizio Minganti et al. “Spectral theory of Liouvillians for dissipative phase transitions”. In: *Phys. Rev. A* 98 (4 Oct. 2018), p. 042118. [Link](#).
- [456] Zejian Li et al. “Dissipative Phase Transition with Driving-Controlled Spatial Dimension and Diffusive Boundary Conditions”. In: *Phys. Rev. Lett.* 128 (9 Feb. 2022), p. 093601. [Link](#).
- [457] Y. Suzuki et al. “Quantum State Tomography for Kerr Parametric Oscillators”. In: *Phys. Rev. Appl.* 20 (3 Sept. 2023), p. 034031. [Link](#).
- [458] André Eckardt and Egidijus Anisimovas. “High-frequency approximation for periodically driven quantum systems from a Floquet-space perspective”. In: *New Journal of Physics* 17.9 (Sept. 2015), p. 093039. [Link](#).
- [459] Jayameenakshi Venkatraman et al. “Static Effective Hamiltonian of a Rapidly Driven Nonlinear System”. In: *Phys. Rev. Lett.* 129 (10 Aug. 2022), p. 100601. [Link](#).
- [460] Kilian Seibold, Orjan Ameye, and Oded Zilberberg. “Floquet Expansion by Counting Pump Photons”. In: *Phys. Rev. Lett.* 134 (6 Feb. 2025), p. 060401. [Link](#).
- [461] Jan Kořata et al. “HarmonicBalance.jl: A Julia suite for nonlinear dynamics using harmonic balance”. In: *SciPost Phys. Codebases* (2022), p. 6. [Link](#).
- [462] Louis N. Hand and Janet D. Finch. *Analytical Mechanics*. Cambridge University Press, 1998.

- [463] M. J. Collett and D. F. Walls. "Squeezing spectra for nonlinear optical systems". In: *Phys. Rev. A* 32 (5 Nov. 1985), pp. 2887–2892. [Link](#).
- [464] R. Movshovich et al. "Observation of zero-point noise squeezing via a Josephson-parametric amplifier". In: *Phys. Rev. Lett.* 65 (12 Sept. 1990), pp. 1419–1422. [Link](#).
- [465] I. Siddiqi et al. "RF-Driven Josephson Bifurcation Amplifier for Quantum Measurement". In: *Phys. Rev. Lett.* 93 (20 Nov. 2004), p. 207002. [Link](#).
- [466] P. Kinsler and P. D. Drummond. "Quantum dynamics of the parametric oscillator". In: *Phys. Rev. A* 43 (11 June 1991), pp. 6194–6208. [Link](#).
- [467] M. D. Reid and B. Yurke. "Effect of bistability and superpositions on quantum statistics in degenerate parametric oscillation". In: *Phys. Rev. A* 46 (7 Oct. 1992), pp. 4131–4137. [Link](#).
- [468] C. Stambaugh and H. B. Chan. "Supernarrow Spectral Peaks near a Kinetic Phase Transition in a Driven Nonlinear Micromechanical Oscillator". In: *Phys. Rev. Lett.* 97 (11 Sept. 2006), p. 110602. [Link](#).
- [469] Florian Marquardt, J. G. E. Harris, and S. M. Girvin. "Dynamical Multistability Induced by Radiation Pressure in High-Finesse Micromechanical Optical Cavities". In: *Phys. Rev. Lett.* 96 (10 Mar. 2006), p. 103901. [Link](#).
- [470] H. B. Chan and C. Stambaugh. "Activation Barrier Scaling and Crossover for Noise-Induced Switching in Micromechanical Parametric Oscillators". In: *Phys. Rev. Lett.* 99 (6 Aug. 2007), p. 060601. [Link](#).
- [471] H. B. Chan, M. I. Dykman, and C. Stambaugh. "Paths of Fluctuation Induced Switching". In: *Phys. Rev. Lett.* 100 (13 Apr. 2008), p. 130602. [Link](#).
- [472] Lin Zhang and Hong-Yan Kong. "Self-sustained oscillation and harmonic generation in optomechanical systems with quadratic couplings". In: *Phys. Rev. A* 89 (2 Feb. 2014), p. 023847. [Link](#).
- [473] Z. R. Lin et al. "Josephson parametric phase-locked oscillator and its application to dispersive readout of superconducting qubits". In: *Nature Communications* 5.1 (July 2014), p. 4480. ISSN: 2041-1723. [Link](#).
- [474] Alex G. Krause et al. "Nonlinear Radiation Pressure Dynamics in an Optomechanical Crystal". In: *Phys. Rev. Lett.* 115 (23 Dec. 2015), p. 233601. [Link](#).
- [475] F. Ricci et al. "Optically levitated nanoparticle as a model system for stochastic bistable dynamics". In: *Nature Communications* 8.1 (May 2017), p. 15141. ISSN: 2041-1723. [Link](#).
- [476] Loïc Rondin et al. "Direct measurement of Kramers turnover with a levitated nanoparticle". In: *Nature Nanotechnology* 12.12 (Dec. 2017), pp. 1130–1133. ISSN: 1748-3395. [Link](#).
- [477] Shiqian Ding et al. "Quantum Parametric Oscillator with Trapped Ions". In: *Phys. Rev. Lett.* 119 (15 Oct. 2017), p. 150404. [Link](#).
- [478] Andrew D. Armour, Björn Kubala, and Joachim Ankerhold. "Noise switching at a dynamical critical point in a cavity-conductor hybrid". In: *Phys. Rev. B* 96 (21 Dec. 2017), p. 214509. [Link](#).
- [479] J. M. Fink et al. "Observation of the Photon-Blockade Breakdown Phase Transition". In: *Phys. Rev. X* 7 (1 Jan. 2017), p. 011012. [Link](#).

- [480] P. R. Muppalla et al. “Bistability in a mesoscopic Josephson junction array resonator”. In: *Phys. Rev. B* 97 (2 Jan. 2018), p. 024518. [Link](#).
- [481] Martin Frimmer et al. “Rapid Flipping of Parametric Phase States”. In: *Phys. Rev. Lett.* 123 (25 Dec. 2019), p. 254102. [Link](#).
- [482] N. Carlon Zambon et al. “Parametric instability in coupled nonlinear microcavities”. In: *Phys. Rev. A* 102 (2 Aug. 2020), p. 023526. [Link](#).
- [483] Eyal Buks et al. “Driving-induced resonance narrowing in a strongly coupled cavity-qubit system”. In: *Phys. Rev. A* 102 (4 Oct. 2020), p. 043716. [Link](#).
- [484] Mehrdad Elyasi, Eiji Saitoh, and Gerrit E. W. Bauer. “Stochasticity of the magnon parametron”. In: *Phys. Rev. B* 105 (5 Feb. 2022), p. 054403. [Link](#).
- [485] Ata Ke şkekler et al. “Multimode Nonlinear Dynamics of Graphene Resonators”. In: *Phys. Rev. Appl.* 20 (6 Dec. 2023), p. 064020. [Link](#).
- [486] Ye Liu et al. “Mechanical cooling in the bistable regime of a dissipative optomechanical cavity with a Kerr medium”. In: *Phys. Rev. A* 108 (2 Aug. 2023), p. 023503. [Link](#).
- [487] Toni L. Heugel et al. “Proliferation of unstable states and their impact on stochastic out-of-equilibrium dynamics in two coupled Kerr parametric oscillators”. In: *Phys. Rev. E* 109 (6 June 2024), p. 064308. [Link](#).
- [488] B. Zhang et al. “Frequency stabilization of self-sustained oscillations in a sideband-driven electromechanical resonator”. In: *Phys. Rev. Appl.* 22 (3 Sept. 2024), p. 034072. [Link](#).
- [489] Shruti Puri et al. “Stabilized Cat in a Driven Nonlinear Cavity: A Fault-Tolerant Error Syndrome Detector”. In: *Phys. Rev. X* 9 (4 Oct. 2019), p. 041009. [Link](#).
- [490] A. Grimm et al. “Stabilization and operation of a Kerr-cat qubit”. In: *Nature* 584.7820 (Aug. 2020), pp. 205–209. ISSN: 1476-4687. [Link](#).
- [491] David Roberts and Aashish A. Clerk. “Driven-Dissipative Quantum Kerr Resonators: New Exact Solutions, Photon Blockade and Quantum Bistability”. In: *Phys. Rev. X* 10 (2 Apr. 2020), p. 021022. [Link](#).
- [492] Hiroomi Chono, Taro Kanao, and Hayato Goto. “Two-qubit gate using conditional driving for highly detuned Kerr nonlinear parametric oscillators”. In: *Phys. Rev. Res.* 4 (4 Oct. 2022), p. 043054. [Link](#).
- [493] Daisuke Iyama et al. “Observation and manipulation of quantum interference in a superconducting Kerr parametric oscillator”. In: *Nature Communications* 15.1 (Jan. 2024), p. 86. ISSN: 2041-1723. [Link](#).
- [494] Taro Kanao and Hayato Goto. “Fast elementary gates for universal quantum computation with Kerr parametric oscillator qubits”. In: *Phys. Rev. Res.* 6 (1 Feb. 2024), p. 013192. [Link](#).
- [495] Raphaël Lescanne et al. “Exponential suppression of bit-flips in a qubit encoded in an oscillator”. In: *Nature Physics* 16.5 (May 2020), pp. 509–513. ISSN: 1745-2481. [Link](#).
- [496] C. Berdou et al. “One Hundred Second Bit-Flip Time in a Two-Photon Dissipative Oscillator”. In: *PRX Quantum* 4 (2 June 2023), p. 020350. [Link](#).

- [497] M. I. Dykman, M. Marthaler, and V. Peano. “Quantum heating of a parametrically modulated oscillator: Spectral signatures”. In: *Phys. Rev. A* 83 (5 May 2011), p. 052115. [Link](#).
- [498] Gabriel Margiani et al. “Deterministic and stochastic sampling of two coupled Kerr parametric oscillators”. In: *Phys. Rev. Res.* 5 (1 Feb. 2023), p. L012029. [Link](#).
- [499] Peter Hanggi. “Escape from a metastable state”. In: *Journal of Statistical Physics* 42.1 (Jan. 1986), pp. 105–148. ISSN: 1572-9613. [Link](#).
- [500] B. Wielinga and G. J. Milburn. “Quantum tunneling in a Kerr medium with parametric pumping”. In: *Phys. Rev. A* 48 (3 Sept. 1993), pp. 2494–2496. [Link](#).
- [501] Z. R. Lin, Y. Nakamura, and M. I. Dykman. “Critical fluctuations and the rates of interstate switching near the excitation threshold of a quantum parametric oscillator”. In: *Phys. Rev. E* 92 (2 Aug. 2015), p. 022105. [Link](#).
- [502] M. I. Dykman. “Critical exponents in metastable decay via quantum activation”. In: *Phys. Rev. E* 75 (1 Jan. 2007), p. 011101. [Link](#).
- [503] H.A. Kramers. “Brownian motion in a field of force and the diffusion model of chemical reactions”. In: *Physica* 7.4 (1940), pp. 284–304. ISSN: 0031-8914. [Link](#).
- [504] Peter Hänggi, Peter Talkner, and Michal Borkovec. “Reaction-rate theory: fifty years after Kramers”. In: *Rev. Mod. Phys.* 62 (2 Apr. 1990), pp. 251–341. [Link](#).
- [505] F. R. Ong et al. “Quantum Heating of a Nonlinear Resonator Probed by a Superconducting Qubit”. In: *Phys. Rev. Lett.* 110 (4 Jan. 2013), p. 047001. [Link](#).
- [506] Maxime Boissonneault et al. “Superconducting qubit as a probe of squeezing in a nonlinear resonator”. In: *Phys. Rev. A* 89 (2 Feb. 2014), p. 022324. [Link](#).
- [507] M. Marthaler and M. I. Dykman. “Switching via quantum activation: A parametrically modulated oscillator”. In: *Phys. Rev. A* 73 (4 Apr. 2006), p. 042108. [Link](#).
- [508] Lingzhen Guo et al. “Quantum critical temperature of a modulated oscillator”. In: *Phys. Rev. A* 87 (6 June 2013), p. 062117. [Link](#).
- [509] Philip Krantz et al. “Single-shot read-out of a superconducting qubit using a Josephson parametric oscillator”. In: *Nature Communications* 7.1 (May 2016), p. 11417. ISSN: 2041-1723. [Link](#).
- [510] Gopika Lakshmi Bhai, Hiroto Mukai, and Jaw-Shen Tsai. “Mitigation of noise in Josephson parametric oscillator by injection locking”. In: *Applied Physics Letters* 122.5 (Feb. 2023), p. 054002. ISSN: 0003-6951. [Link](#).
- [511] D. Ryvkine and M. I. Dykman. “Resonant symmetry lifting in a parametrically modulated oscillator”. In: *Phys. Rev. E* 74 (6 Dec. 2006), p. 061118. [Link](#).
- [512] Anina Leuch et al. “Parametric Symmetry Breaking in a Nonlinear Resonator”. In: *Phys. Rev. Lett.* 117 (21 Nov. 2016), p. 214101. [Link](#).
- [513] Hayato Goto, Zhirong Lin, and Yasunobu Nakamura. “Boltzmann sampling from the Ising model using quantum heating of coupled nonlinear oscillators”. In: *Scientific Reports* 8.1 (May 2018), p. 7154. ISSN: 2045-2322. [Link](#).
- [514] Jennifer Gosner, Björn Kubala, and Joachim Ankerhold. “Quantum properties of a strongly driven Josephson junction”. In: *Phys. Rev. B* 99 (14 Apr. 2019), p. 144524. [Link](#).

- [515] Shumpei Masuda et al. “Controls of a superconducting quantum parametron under a strong pump field”. In: *Scientific Reports* 11.1 (June 2021), p. 11459. ISSN: 2045-2322. [Link](#).
- [516] Toni L. Heugel et al. “Ising machines with strong bilinear coupling”. In: *Phys. Rev. Res.* 4 (1 Feb. 2022), p. 013149. [Link](#).
- [517] Sergio O. Valenzuela et al. “Microwave-Induced Cooling of a Superconducting Qubit”. In: *Science* 314.5805 (2006), pp. 1589–1592. [Link](#).
- [518] Antonio D. Córcoles et al. “Protecting superconducting qubits from radiation”. In: *Applied Physics Letters* 99.18 (Nov. 2011), p. 181906. ISSN: 0003-6951. [Link](#).
- [519] Jen-Hao Yeh et al. “Microwave attenuators for use with quantum devices below 100 mK”. In: *Journal of Applied Physics* 121.22 (June 2017), p. 224501. ISSN: 0021-8979. [Link](#).
- [520] S. Krinner et al. “Engineering cryogenic setups for 100-qubit scale superconducting circuit systems”. In: *EPJ Quantum Technology* 6.1 (May 2019), p. 2. ISSN: 2196-0763. [Link](#).
- [521] Marco Scigliuzzo et al. “Primary Thermometry of Propagating Microwaves in the Quantum Regime”. In: *Phys. Rev. X* 10 (4 Dec. 2020), p. 041054. [Link](#).
- [522] Anatoly Kulikov, Rohit Navarathna, and Arkady Fedorov. “Measuring Effective Temperatures of Qubits Using Correlations”. In: *Phys. Rev. Lett.* 124 (24 June 2020), p. 240501. [Link](#).
- [523] Aidar Sultanov et al. “Protocol for temperature sensing using a three-level transmon circuit”. In: *Applied Physics Letters* 119.14 (Oct. 2021), p. 144002. ISSN: 0003-6951. [Link](#).
- [524] L. R. van Everdingen. *Fabrication and Characterization of a Dimer Josephson Junction Parametric Amplifier*. 2024. [Link](#).
- [525] Mitchell J. Feigenbaum. “Quantitative universality for a class of nonlinear transformations”. In: *Journal of Statistical Physics* 19.1 (July 1978), pp. 25–52. ISSN: 1572-9613. [Link](#).
- [526] B. A. Huberman and J. P. Crutchfield. “Chaotic States of Anharmonic Systems in Periodic Fields”. In: *Phys. Rev. Lett.* 43 (23 Dec. 1979), pp. 1743–1747. [Link](#).
- [527] Paul S. Linsay. “Period Doubling and Chaotic Behavior in a Driven Anharmonic Oscillator”. In: *Phys. Rev. Lett.* 47 (19 Nov. 1981), pp. 1349–1352. [Link](#).
- [528] Francis C. Moon. “Fractal Boundary for Chaos in a Two-State Mechanical Oscillator”. In: *Phys. Rev. Lett.* 53 (10 Sept. 1984), pp. 962–964. [Link](#).
- [529] Tomas Bohr, Per Bak, and Mogens Høgh Jensen. “Transition to chaos by interaction of resonances in dissipative systems. II. Josephson junctions, charge-density waves, and standard maps”. In: *Phys. Rev. A* 30 (4 Oct. 1984), pp. 1970–1981. [Link](#).
- [530] T. Matsumoto. “Chaos in electronic circuits”. In: *Proceedings of the IEEE* 75.8 (1987), pp. 1033–1057.
- [531] E. Kreuzer, M. Kleczka, and S. Schaub. “Chaotic dynamics of a simple oscillator — a pictorial introduction”. In: *Chaos, Solitons Fractals* 1.5 (1991), pp. 439–456. ISSN: 0960-0779. [Link](#).
- [532] C.-H. Lu and R.M. Evan-Iwanowski. “The nonstationary effects on a softening duffing oscillator”. In: *Mechanics Research Communications* 21.6 (1994), pp. 555–564. ISSN: 0093-6413. [Link](#).

- [533] P. K. Tien. "Parametric Amplification and Frequency Mixing in Propagating Circuits". In: *Journal of Applied Physics* 29.9 (Sept. 1958), pp. 1347–1357. ISSN: 0021-8979. [Link](#).
- [534] B. R. Mollow and R. J. Glauber. "Quantum Theory of Parametric Amplification. I". In: *Phys. Rev.* 160 (5 Aug. 1967), pp. 1076–1096. [Link](#).
- [535] B. R. Mollow and R. J. Glauber. "Quantum Theory of Parametric Amplification. II". In: *Phys. Rev.* 160 (5 Aug. 1967), pp. 1097–1108. [Link](#).
- [536] Bernard Yurke. "Use of cavities in squeezed-state generation". In: *Phys. Rev. A* 29 (1 Jan. 1984), pp. 408–410. [Link](#).
- [537] Kurt Wiesenfeld and Bruce McNamara. "Period-doubling systems as small-signal amplifiers". In: *Phys. Rev. Lett.* 55 (1 July 1985), pp. 13–16. [Link](#).
- [538] J.P. Crutchfield and B.A. Huberman. "Fluctuations and the onset of chaos". In: *Physics Letters A* 77.6 (1980), pp. 407–410. ISSN: 0375-9601. [Link](#).
- [539] S. Novak and R. G. Frehlich. "Transition to chaos in the Duffing oscillator". In: *Phys. Rev. A* 26 (6 Dec. 1982), pp. 3660–3663. [Link](#).
- [540] M. T. Levinsen. "Even and odd subharmonic frequencies and chaos in Josephson junctions: Impact on parametric amplifiers?" In: *Journal of Applied Physics* 53.6 (June 1982), pp. 4294–4299. ISSN: 0021-8979. [Link](#).
- [541] Carson Jeffries and Kurt Wiesenfeld. "Observation of noisy precursors of dynamical instabilities". In: *Phys. Rev. A* 31 (2 Feb. 1985), pp. 1077–1084. [Link](#).
- [542] R. Rätty, J. von Boehm, and H. M. Isomäki. "Chaotic motion of a periodically driven particle in an asymmetric potential well". In: *Phys. Rev. A* 34 (5 Nov. 1986), pp. 4310–4315. [Link](#).
- [543] Paul Bryant, Kurt Wiesenfeld, and Bruce McNamara. "Noise rise in parametric amplifiers". In: *Phys. Rev. B* 36 (1 July 1987), pp. 752–755. [Link](#).
- [544] L. A. Lugiato et al. "Bistability, self-pulsing and chaos in optical parametric oscillators". In: *Il Nuovo Cimento D* 10.8 (Aug. 1988), pp. 959–977. ISSN: 0392-6737. [Link](#).
- [545] Mark F. Bocko and James Battiato. "Phase-sensitive amplification and deamplification of noise and the noise rise in period-doubling systems near a bifurcation". In: *Phys. Rev. Lett.* 60 (17 Apr. 1988), pp. 1763–1766. [Link](#).
- [546] Jeffrey H. Baxter, Mark F. Bocko, and David H. Douglass. "Behavior of a nonlinear resonator driven at subharmonic frequencies". In: *Phys. Rev. A* 41 (2 Jan. 1990), pp. 619–625. [Link](#).
- [547] K. R. Schenk-Hoppé. "Bifurcation scenarios of the noisy duffing-van der pol oscillator". In: *Nonlinear Dynamics* 11.3 (Nov. 1996), pp. 255–274. ISSN: 1573-269X. [Link](#).
- [548] G.C. Layek. *An Introduction to Dynamical Systems and Chaos*. Springer India, 2015. ISBN: 9788132225560. [Link](#).
- [549] K. Murali and M. Lakshmanan. "Transmission of signals by synchronization in a chaotic Van der Pol–Duffing oscillator". In: *Phys. Rev. E* 48 (3 Sept. 1993), R1624–R1626. [Link](#).
- [550] Akira Kamimaki et al. "Chaos in spin-torque oscillator with feedback circuit". In: *Phys. Rev. Res.* 3 (4 Dec. 2021), p. 043216. [Link](#).

- [551] Claudio Guarcello et al. “Driving a Josephson Traveling Wave Parametric Amplifier into chaos: Effects of a non-sinusoidal current–phase relation”. In: *Chaos, Solitons Fractals* 189 (2024), p. 115598. ISSN: 0960-0779. [Link](#).
- [552] Mitchell J. Feigenbaum. “The onset spectrum of turbulence”. In: *Physics Letters A* 74.6 (1979), pp. 375–378. ISSN: 0375-9601. [Link](#).
- [553] James Testa, José Pérez, and Carson Jeffries. “Evidence for Universal Chaotic Behavior of a Driven Nonlinear Oscillator”. In: *Phys. Rev. Lett.* 48 (11 Mar. 1982), pp. 714–717. [Link](#).
- [554] F. A. Hopf et al. “Bifurcations to chaos in optical bistability”. In: *Phys. Rev. A* 25 (4 Apr. 1982), pp. 2172–2182. [Link](#).
- [555] Mitchell J. Feigenbaum. “Universal behavior in nonlinear systems”. In: *Physica D: Non-linear Phenomena* 7.1 (1983), pp. 16–39. ISSN: 0167-2789. [Link](#).
- [556] Kurt Wiesenfeld. “Noisy precursors of nonlinear instabilities”. In: *Journal of Statistical Physics* 38.5 (Mar. 1985), pp. 1071–1097. ISSN: 1572-9613. [Link](#).
- [557] Mitchell J. Feigenbaum. “The transition to aperiodic behavior in turbulent systems”. In: *Communications in Mathematical Physics* 77.1 (Feb. 1980), pp. 65–86. ISSN: 1432-0916. [Link](#).
- [558] J.P. Crutchfield, J.D. Farmer, and B.A. Huberman. “Fluctuations and simple chaotic dynamics”. In: *Physics Reports* 92.2 (1982), pp. 45–82. ISSN: 0370-1573. [Link](#).
- [559] J.N. Elgin, D. Forster, and Sarben Sarker. “Mechanism for chaos in the duffing equation”. In: *Physics Letters A* 94.5 (1983), pp. 195–197. ISSN: 0375-9601. [Link](#).
- [560] Nestor E. Sanchez and Ali H. Nayfeh. “Prediction of bifurcations in a parametrically excited duffing oscillator”. In: *International Journal of Non-Linear Mechanics* 25.2 (1990), pp. 163–176. ISSN: 0020-7462. [Link](#).
- [561] E. Ott. *Chaos in Dynamical Systems*. Cambridge University Press, 2002. ISBN: 9780521010849. [Link](#).
- [562] B. A. Huberman, J. P. Crutchfield, and N. H. Packard. “Noise phenomena in Josephson junctions”. In: *Applied Physics Letters* 37.8 (Oct. 1980), pp. 750–752. ISSN: 0003-6951. [Link](#).
- [563] N. F Pedersen and A. Davidson. “Chaos and noise rise in Josephson junctions”. In: *Applied Physics Letters* 39.10 (Nov. 1981), pp. 830–832. ISSN: 0003-6951. [Link](#).
- [564] D. D’Humieres et al. “Chaotic states and routes to chaos in the forced pendulum”. In: *Phys. Rev. A* 26 (6 Dec. 1982), pp. 3483–3496. [Link](#).
- [565] P. H. Bryant, R. Movshovich, and B. Yurke. “Noise rise in nondegenerate parametric amplifiers”. In: *Phys. Rev. Lett.* 66 (20 May 1991), pp. 2641–2644. [Link](#).
- [566] Tal Carmon, M. C. Cross, and Kerry J. Vahala. “Chaotic Quivering of Micron-Scaled On-Chip Resonators Excited by Centrifugal Optical Pressure”. In: *Phys. Rev. Lett.* 98 (16 Apr. 2007), p. 167203. [Link](#).
- [567] L. Bakemeier, A. Alvermann, and H. Fehske. “Route to Chaos in Optomechanics”. In: *Phys. Rev. Lett.* 114 (1 Jan. 2015), p. 013601. [Link](#).

- [568] F. C. Moon. “Experiments on Chaotic Motions of a Forced Nonlinear Oscillator: Strange Attractors”. In: *Journal of Applied Mechanics* 47.3 (Sept. 1980), pp. 638–644. ISSN: 0021-8936. [Link](#).
- [569] Wanda Szemplińska-Stupnicka. “The analytical predictive criteria for chaos and escape in nonlinear oscillators: A survey”. In: *Nonlinear Dynamics* 7.2 (Mar. 1995), pp. 129–147. ISSN: 1573-269X. [Link](#).
- [570] Vinicius Wiggers and Paulo C. Rech. “Multistability and organization of periodicity in a Van der Pol–Duffing oscillator”. In: *Chaos, Solitons Fractals* 103 (2017), pp. 632–637. ISSN: 0960-0779. [Link](#).
- [571] Tai-Ping Chang. “Chaotic Motion in Forced Duffing System Subject to Linear and Nonlinear Damping”. In: *Mathematical Problems in Engineering* 2017.1 (2017), p. 3769870. [Link](#).
- [572] Arianna Marchionne, Peter Ditlevsen, and Sebastian Wieczorek. “Synchronisation vs. resonance: Isolated resonances in damped nonlinear oscillators”. In: *Physica D: Nonlinear Phenomena* 380-381 (2018), pp. 8–16. ISSN: 0167-2789. [Link](#).
- [573] Md Nahid Hasan et al. “Fractal patterns in the parameter space of a bistable Duffing oscillator”. In: *Phys. Rev. E* 108 (2 Aug. 2023), p. L022201. [Link](#).
- [574] John Michael Tutill Thompson. “Chaotic phenomena triggering the escape from a potential well”. In: *Proceedings of the Royal Society of London. A. Mathematical and Physical Sciences* 421.1861 (1989), pp. 195–225. ISSN: 0080-4630. [Link](#).
- [575] Y Ueda et al. “Basin explosions and escape phenomena in the twin-well Duffing oscillator: compound global bifurcations organizing behaviour”. en. In: *Philos. Trans. Phys. Sci. Eng.* 332.1624 (July 1990), pp. 169–186.
- [576] Wanda Szemplińska-Stupnicka. “Cross-well chaos and escape phenomena in driven oscillators”. In: *Nonlinear Dynamics* 3.3 (May 1992), pp. 225–243. ISSN: 1573-269X. [Link](#).
- [577] Christian Hill. *Duffing*. <https://github.com/scipython/duffing>. 2013.
- [578] A. Schadschneider, D. Chowdhury, and K. Nishinari. *Stochastic Transport in Complex Systems: From Molecules to Vehicles*. Elsevier Science, 2010. ISBN: 9780080560526. [Link](#).
- [579] Xue-Juan Zhang, Hong Qian, and Min Qian. “Stochastic theory of nonequilibrium steady states and its applications. Part I”. In: *Physics Reports* 510.1 (2012). Stochastic Theory of Nonequilibrium Steady States and Its Applications: Part I, pp. 1–86. ISSN: 0370-1573. [Link](#).
- [580] Greta Villa et al. *Topological classification of driven-dissipative nonlinear systems*. 2024. [Link](#).
- [581] Letizia Catalini et al. *Adiabatic and diabatic responses in a Duffing resonator driven by two detuned tones*. 2024. [Link](#).
- [582] J. H. Shen et al. “Bifurcation and route-to-chaos analyses for Mathieu–Duffing oscillator by the incremental harmonic balance method”. In: *Nonlinear Dynamics* 52.4 (June 2008), pp. 403–414. ISSN: 1573-269X. [Link](#).
- [583] ALBERT C. J. LUO and JIANZHE HUANG. “ANALYTICAL DYNAMICS OF PERIOD- m FLOWS AND CHAOS IN NONLINEAR SYSTEMS”. In: *International Journal of Bifurcation and Chaos* 22.04 (2012), p. 1250093. [Link](#).

- [584] M. Dykman. *Fluctuating Nonlinear Oscillators: From Nanomechanics to Quantum Superconducting Circuits*. OUP Oxford, 2012. ISBN: 9780191637544. [Link](#).
- [585] Celso Grebogi, Edward Ott, and James A. Yorke. "Chaotic Attractors in Crisis". In: *Phys. Rev. Lett.* 48 (22 May 1982), pp. 1507–1510. [Link](#).
- [586] Celso Grebogi, Edward Ott, and James A. Yorke. "Chaos, Strange Attractors, and Fractal Basin Boundaries in Nonlinear Dynamics". In: *Science* 238.4827 (1987), pp. 632–638. [Link](#).
- [587] Martin Bier and Tassos C. Bountis. "Remerging Feigenbaum trees in dynamical systems". In: *Physics Letters A* 104.5 (1984), pp. 239–244. ISSN: 0375-9601. [Link](#).
- [588] Silvina P. Dawson et al. "Antimonotonicity: inevitable reversals of period-doubling cascades". In: *Physics Letters A* 162.3 (1992), pp. 249–254. ISSN: 0375-9601. [Link](#).
- [589] Lewi Stone. "Period-doubling reversals and chaos in simple ecological models". In: *Nature* 365.6447 (Oct. 1993), pp. 617–620. ISSN: 1476-4687. [Link](#).
- [590] John Vandermeer. "Period 'bubbling' in simple ecological models: Pattern and chaos formation in a quartic model". In: *Ecological Modelling* 95.2 (1997), pp. 311–317. ISSN: 0304-3800. [Link](#).
- [591] H. G. Solari and R. Gilmore. "Organization of periodic orbits in the driven Duffing oscillator". In: *Phys. Rev. A* 38 (3 Aug. 1988), pp. 1566–1572. [Link](#).
- [592] R. Gilmore and J. W. L. McCallum. "Structure in the bifurcation diagram of the Duffing oscillator". In: *Phys. Rev. E* 51 (2 Feb. 1995), pp. 935–956. [Link](#).
- [593] Ruiqi Wang, Jin Deng, and Zhujun Jing. "Chaos control in duffing system". In: *Chaos, Solitons Fractals* 27.1 (2006), pp. 249–257. ISSN: 0960-0779. [Link](#).
- [594] Albert C. J. Luo and Bo Yu. "Analytical routes of period-m motions to chaos in a parametric, quadratic nonlinear oscillator". In: *International Journal of Dynamics and Control* 4.1 (Mar. 2016), pp. 1–22. ISSN: 2195-2698. [Link](#).
- [595] Stephen Wiggins. "Chaos in the quasiperiodically forced duffing oscillator". In: *Physics Letters A* 124.3 (1987), pp. 138–142. ISSN: 0375-9601. [Link](#).
- [596] J. Heagy and W. L. Ditto. "Dynamics of a two-frequency parametrically driven duffing oscillator". In: *Journal of Nonlinear Science* 1.4 (Dec. 1991), pp. 423–455. ISSN: 1432-1467. [Link](#).
- [597] Andrey B. Belogortsev. "Quasiperiodic resonance and bifurcations of tori in the weakly nonlinear Duffing oscillator". In: *Physica D: Nonlinear Phenomena* 59.4 (1992), pp. 417–429. ISSN: 0167-2789. [Link](#).
- [598] Rainer Grobe, Fritz Haake, and Hans-Jürgen Sommers. "Quantum Distinction of Regular and Chaotic Dissipative Motion". In: *Phys. Rev. Lett.* 61 (17 Oct. 1988), pp. 1899–1902. [Link](#).
- [599] G. J. Milburn and C. A. Holmes. "Quantum coherence and classical chaos in a pulsed parametric oscillator with a Kerr nonlinearity". In: *Phys. Rev. A* 44 (7 Oct. 1991), pp. 4704–4711. [Link](#).
- [600] Salman Habib, Kosuke Shizume, and Wojciech Hubert Zurek. "Decoherence, Chaos, and the Correspondence Principle". In: *Phys. Rev. Lett.* 80 (20 May 1998), pp. 4361–4365. [Link](#).
- [601] Guanyu Wang et al. "The application of chaotic oscillators to weak signal detection". In: *IEEE Transactions on Industrial Electronics* 46.2 (1999), pp. 440–444.

- [602] Diana Monteoliva and Juan Pablo Paz. “Decoherence and the Rate of Entropy Production in Chaotic Quantum Systems”. In: *Phys. Rev. Lett.* 85 (16 Oct. 2000), pp. 3373–3376. [Link](#).
- [603] F. Haake. *Quantum Signatures of Chaos*. Physics and astronomy online library. Springer, 2001. ISBN: 9783540677239. [Link](#).
- [604] H. H. Adamyán, S. B. Manvelyan, and G. Yu. Kryuchkyan. “Chaos in a double driven dissipative nonlinear oscillator”. In: *Phys. Rev. E* 64 (4 Sept. 2001), p. 046219. [Link](#).
- [605] Jin Ying-Xin and He Kai-Fen. “Quantum Poincaré Section of a Two-Dimensional Hamiltonian in a Coherent State Representation”. In: *Chinese Physics Letters* 19.9 (Sept. 2002), p. 1264. [Link](#).
- [606] Tal Carmon et al. “Temporal Behavior of Radiation-Pressure-Induced Vibrations of an Optical Microcavity Phonon Mode”. In: *Phys. Rev. Lett.* 94 (22 June 2005), p. 223902. [Link](#).
- [607] Gabriela B. Lemos et al. “Experimental observation of quantum chaos in a beam of light”. In: *Nature Communications* 3.1 (Nov. 2012), p. 1211. ISSN: 2041-1723. [Link](#).
- [608] Diego A. Wisniacki and Peter Schlagheck. “Quantum manifestations of classical nonlinear resonances”. In: *Phys. Rev. E* 92 (6 Dec. 2015), p. 062923. [Link](#).
- [609] Jessica K. Eastman et al. “Controlling chaos in the quantum regime using adaptive measurements”. In: *Phys. Rev. A* 99 (1 Jan. 2019), p. 012111. [Link](#).
- [610] Gernot Akemann et al. “Universal Signature from Integrability to Chaos in Dissipative Open Quantum Systems”. In: *Phys. Rev. Lett.* 123 (25 Dec. 2019), p. 254101. [Link](#).
- [611] Tankut Can et al. “Spectral Gaps and Midgap States in Random Quantum Master Equations”. In: *Phys. Rev. Lett.* 123 (23 Dec. 2019), p. 234103. [Link](#).
- [612] Lucas Sá et al. “Spectral transitions and universal steady states in random Kraus maps and circuits”. In: *Phys. Rev. B* 102 (13 Oct. 2020), p. 134310. [Link](#).
- [613] Xin H. H. Zhang and Harold U. Baranger. “Driven-dissipative phase transition in a Kerr oscillator: From semiclassical \mathcal{PT} symmetry to quantum fluctuations”. In: *Phys. Rev. A* 103 (3 Mar. 2021), p. 033711. [Link](#).
- [614] Deng-Wei Zhang et al. “Nonreciprocal chaos in a spinning optomechanical resonator”. In: *Phys. Rev. A* 104 (3 Sept. 2021), p. 033522. [Link](#).
- [615] Daniel Dahan, Geva Arwas, and Eytan Grosfeld. “Classical and quantum chaos in chirally-driven, dissipative Bose-Hubbard systems”. In: *npj Quantum Information* 8.1 (Feb. 2022), p. 14. ISSN: 2056-6387. [Link](#).
- [616] Andrey R. Kolovsky. “Bistability and chaos-assisted tunneling in dissipative quantum systems”. In: *Phys. Rev. E* 106 (1 July 2022), p. 014209. [Link](#).
- [617] Filippo Ferrari et al. *Steady-state quantum chaos in open quantum systems*. 2023. [Link](#).
- [618] Joachim Cohen et al. “Reminiscence of Classical Chaos in Driven Transmons”. In: *PRX Quantum* 4 (2 Apr. 2023), p. 020312. [Link](#).
- [619] Kohei Kawabata et al. “Symmetry of Open Quantum Systems: Classification of Dissipative Quantum Chaos”. In: *PRX Quantum* 4 (3 Aug. 2023), p. 030328. [Link](#).
- [620] Ignacio García-Mata et al. *Chaos destroys the excited state quantum phase transition of the Kerr parametric oscillator*. 2024. [Link](#).

-
- [621] Deng-Wei Zhang et al. “Loss-induced chaos in a double-cavity optomechanical system”. In: *Phys. Rev. A* 109 (2 Feb. 2024), p. 023529. [Link](#).
 - [622] Lina Halef and Itay Shomroni. *Route to hyperchaos in quadratic optomechanics*. 2024. [Link](#).
 - [623] A. A. Clerk et al. “Hybrid quantum systems with circuit quantum electrodynamics”. In: *Nature Physics* 16.3 (Mar. 2020), pp. 257–267. ISSN: 1745-2481. [Link](#).
 - [624] Aaron Meurer et al. “SymPy: symbolic computing in Python”. In: *PeerJ Computer Science* 3 (Jan. 2017), e103. ISSN: 2376-5992. [Link](#).